Renewable Routes to Porous Aluminosilicate Materials

Emma Cecelia Cooper

PhD

University of York

Chemistry

December 2012

Abstract

The objectives of this project were to synthesise zeolites and aluminosilicate materials from silicon sources derived from biomass ashes. These materials will have great potential as catalysts and adsorbents.

In order to begin this study it was necessary to find and optimise a technique for extraction of silicon to an alkali silicate solution from biomass ashes. It was then necessary to develop a technique for analysis of the alkali silicate solutions. This was done using calibration of integrals from infrared spectra.

An optimisation of the synthesis of Zeolite X from a rice hull ash derived alkali silicate was developed and these materials were analysed and characterised using XRD, N_2 Adsorption porosimetry, X-Ray Fluorescence Spectroscopy, and X-Ray Photoelectron Spectroscopy. An in-depth study of the surface of the ash derived and reference Zeolite X was undertaken using *in situ* small molecule probing FT-IR. It was found that although the materials were similar there was a significant difference due to the presence of a strongly bonded carbonate species in the pores of the bio-derived zeolite.

Synthesis of a Miscanthus ash derived mesoporous silica, MCM-41, was successfully achieved which was comparable to its conventionally synthesised equivalent. Both displayed ordered hexagonal pores and high surface areas. A study on addition of different sources of aluminium found that it was possible to introduce aluminium into the structure successfully. Included in this study was the addition of the waste product 'red clay' as an aluminium source.

Another mesoporous silica, SBA-15 was synthesised from a Miscanthus ash derived alkali silicate. It was necessary to optimise the synthesis to adapt to the different pH systems of the conventional method and bio-derived alkali silicate solutions. This was achieved and a bio-derived SBA-15 material with ordered hexagonal pores was produced.

Table of Contents

List of Tables

List of Figures

Acknowledgements

Firstly, I would like to thank Dr. Duncan Macquarrie for providing me with the opportunity to work on this project. I am appreciative of his knowledge and patient supervision and for always being there if I had a problem.

I would like to thank Dr. Jennie Dodson for sharing her knowledge, time, enthusiasm, and friendship with me. Her patience and generosity of spirit have had a big impact on this work and I am truly grateful.

I am grateful to the EPSRC and the Department of Chemistry who funded this project.

I would also like to thank Paul Elliot and Owain Samuel for all their help in the laboratory, Dr Adrian Whitwood for his help with the X-Ray Diffractometer, Dr. Meg Stark for her help with SEM, Dr. David Apperley for the Solid State NMR service, and Dr. Vitaly Budarin and Dr. Steve Wainwright for their help with porosimetry.

Thanks must go to Alan Minihan at PQ Corporation for provision of alkali silicate solutions, Paul Vanden Branden at SciMed for loan of the XRF, Retsch for allowing use of their ball mill, Dr. Kris Milkowski for obtaining the rice hull ash, and the staff at Ely and Eccleshall power stations for providing samples of their ashes.

I have met many lovely and memorable people during my time at York. Thanks to everyone in Green Chemistry for keeping things fun and reminding me of the breadth and importance of the work we are all doing. I would like to extend thanks to all the administrative staff in Green Chemistry who keep the group running, in particular Alison Edmunds. Thanks to the Green Chemistry football team Andy M, Tom F, Tom A, Rob, Pete, Cinthia, *et al* for reminding me one can't always win but enjoying it anyway is what matters. Thanks to my office buddies including Nonti, Emily, Alice, Lucie, Gareth, Pete, Bernie, and Helen for fellow PhD advice and diversions.

On a more personal note I'd like to thank my friends and family and especially my parents Sue and Nick for their support throughout my time at York. Finally I'd like to thank Jasmine for her patience and support.

Declaration

I hereby declare that the work presented in this thesis is my own, except where otherwise acknowledged, and has not previously been submitted for a degree at this or any other university. This thesis includes one original paper that has been previously published in a peer reviewed journal, as follows: J R Dodson et al, Green Chem., 2013, 15 (5), 1203 – 1210.

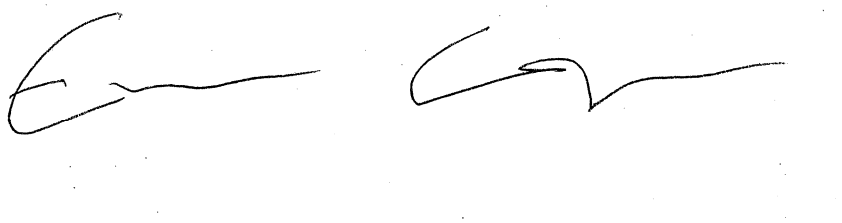

Emma Cecelia Cooper

December 2012

1 Introduction

1.1 Scope of project

This project aims to develop consistent and reliable methods for the synthesis of useful porous aluminosilicate solids using reagents sourced from waste products. The main reagent used will be alkali silicate solutions from biomass ashes. These porous aluminosilicate materials will then be compared with their counterparts synthesised from conventional reagents using various analytical techniques.

1.2 Context

1.2.1 Green Chemistry

"Green Chemistry is the utilisation of a set of principles that reduces or eliminates the use or generation of hazardous substances in the design, manufacture and application of chemical products."[1]

The popularity of Green Chemistry has grown exponentially in the last few decades. With the issues of climate change and the consumption of our natural resources coming to the fore in politics and the media there has been a greater awareness of green issues. The twelve principles of Green Chemistry, as outlined in 'Green Chemistry: Theory and Practice', have been developed as a tool to direct chemists and chemistry to a sustainable future. These principles are as follows:[1]

1. It is better to prevent waste than to treat or clean up waste after it has been created.
2. Synthetic methods should be designed to maximize the incorporation of all materials used in the process into the final product.
3. Wherever practicable, synthetic methods should be designed to use and generate substances that possess little or no toxicity to human health and the environment.
4. Chemical products should be designed to effect their desired function while minimizing their toxicity.
5. The use of auxiliary substances (e.g., solvents, separation agents, etc.) should be made unnecessary wherever possible and innocuous when used.

6. Energy requirements of chemical processes should be recognized for their environmental and economic impacts and should be minimized. If possible, synthetic methods should be conducted at ambient temperature and pressure.
7. A raw material or feedstock should be renewable rather than depleting whenever technically and economically practicable.
8. Unnecessary derivatization (use of blocking groups, protection/ deprotection, temporary modification of physical/chemical processes) should be minimized or avoided if possible, because such steps require additional reagents and can generate waste.
9. Catalytic reagents (as selective as possible) are superior to stoichiometric reagents.
10. Chemical products should be designed so that at the end of their function they break down into innocuous degradation products and do not persist in the environment.
11. Analytical methodologies need to be further developed to allow for real-time, in-process monitoring and control prior to the formation of hazardous substances.
12. Substances and the form of a substance used in a chemical process should be chosen to minimize the potential for chemical accidents, including releases, explosions, and fires.

These principles will be enacted as much as possible throughout this project. More specifically the raw materials used in this project are themselves waste products (principle 7) and the materials synthesised for this project will have great potential for catalysis (principle 9).

1.2.2 The Biorefinery and Biomass Power Plant

The project outline described above (Section 1.1) fits into a wider project developing research on the biorefinery both at the Green Chemistry Centre of Excellence at York and elsewhere. The concept of a Biorefinery as described by Audsley and Annetts is “an integrated factory to process crops into “refined” fractions”.[2] A biorefinery forms an alternative to a petrochemical refinery and could, in the future, sustainably provide the majority of our energy and chemical needs without compromising our provision of food. A simplified schematic diagram of the biorefinery process is shown in Figure 1.1.[3-4] In this

example an agricultural waste product such as rice hulls would be collected locally to minimise transport costs, it would be treated physically to optimise extraction, and then be chemically treated to obtain valuable chemicals and materials. The leftover material would then be combusted for energy and the resulting ash be treated to extract inorganic elements which are present in the biomass. Since ashes have often been shown to be very abundant in silicon, it would be an obvious choice for potential applications including the production of aqueous silicate solutions. In this project these extracted silicate solutions will be used as a starting material for the synthesis of porous silicate and aluminosilicate materials. Some work has been done previously researching potential uses for the ash post extraction such as in building or road building materials.[5]

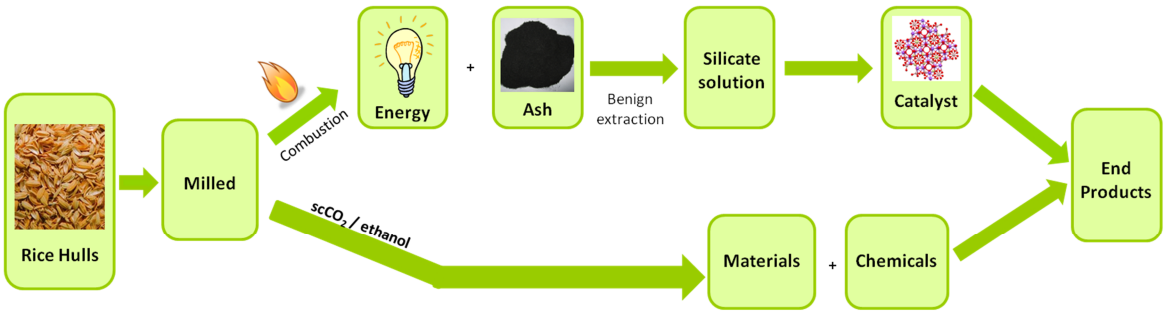

Figure 1.1 Schematic diagram showing a simplified biorefinery process from acquisition of agricultural waste (rice hulls) to production of high value chemicals, materials and energy

Another process which is relevant to this work is the custom built power station which combusts biomass on a large scale. This model of sustainable energy production relies on the agricultural production of 'energy crops' such as Miscanthus which are fast growing and efficient for combustion.[6] Although this idea is controversial in terms of competition with food growing crops and true carbon neutrality, there are some cases when it can be executed in a sustainable manner. A process is carbon neutral if its net carbon emissions are zero, for example if the process involves an uptake of CO_2 as well as emissions and they cancel themselves out.[7] The burning of biomass has been cited as an example of a carbon neutral process but it is important to incorporate all factors into those calculations including production of fertilizers, transport, and other resource uses. Ely Power Station is the largest straw burning power station in the world generating over 270GWh each year.[8] Miscanthus is one of the sources of straw burnt at Ely and the ash from this process is

used in the project. Approximately 3000 tonnes of fly ash and 10,000 tonnes of bottom ash is produced per annum.[5]

Coal fired power accounts for 20-40% of the UK electricity demand throughout the year with nuclear at between 15-20% and gas at 40-50%. Coal fired power stations are beginning to introduce biomass/coal mixes into their feedstocks as this reduces the amount of coal used and the overall environmental impact of the energy production.[9]

1.2.3 Legislation for Sustainability

In the last five years there has been increasing legislation worldwide, and in particular in the EU and USA, encouraging the increase in the combustion of biomass as a source of energy.[10-13]

1.3 Silicon and silicates

Silicon is the second most abundant element in the earth's crust after oxygen.[14] It is used in many applications in many different forms. Below is a discussion of commercial silicon sources such as TEOS and alkali silicate solutions, and alkali silicate solutions derived from biomass for synthesis of aluminosilicate materials.

1.3.1 Tetraethyl Orthosilicate (TEOS)

TEOS is an alkyl silicate which hydrolyses, condenses, and precipitates as silica in the presence of water (catalysed by acid/base) via a sol-gel mechanism.

TEOS is a common precursor to many sol-gel reactions and has a world production of between 23000 and 32000 tonnes. [15] There are environmental issues with the synthesis of TEOS. It is mainly synthesised from $SiCl_4$ and ethanol and produces large amounts of HCl during the process (Equation 1.1).[16] The HCl by-product is then removed by blowing air or nitrogen through the sample, using a vacuum, or solvent reflux.[16] The readily hydrolysable property of $SiCl_4$ to HCl also makes it difficult to store.[15] Silicon tetrachloride requires HCl in its synthesis which occurs at 250 ˚C (Equation 1.2).[16] Silicon can be used as a starting material but is itself produced by a very energy intensive process using carbon electrodes at temperatures exceeding 1700 °C.[15]

$$SiCl_4 + 4C_2H_5OH \rightarrow Si(OC_2H_5)_4 + 4HCl$$

Equation 1.1 Formation of tetraethyl orthosilicate from silicon tetrachloride and ethanol

$$7HCl + 2Si\ (Powdered\ Silicon) \rightarrow SiHCl_3 + SiCl_4 + 3H_2$$

Equation 1.2 Synthesis of silicon tetrachloride from silicon and hydrochloric acid

1.3.2 Commercial silicate solutions

Aqueous alkaline silicate solutions (also called waterglass) can be used as a source of silicon in the synthesis of aluminosilicates. The traditional process of making these solutions involves fusing silica sand with sodium or potassium carbonate at temperatures above 1300 °C.[14] This process is extremely energy intensive and although attempts have been made to improve the process, it remains very resource draining.[14]

In addition to Green Chemistry Principle 6 (referring to the minimisation of energy use in processes), rising energy costs worldwide and greater awareness of the environmental cost of energy use places greater emphasis on the problems in synthesising silicate solutions using present conventional methods. The proposed method adapted from Dr. Jennie Dodson will use a fraction of the energy in the synthesis of bio-derived alkali silicates from ashes.[5]

1.4 Analysis of alkali silicates

Conventionally, the most accurate method of silicon concentration determination is by Atomic Absorption Spectroscopy (AAS) but this requires dilute solutions and thus for concentrated solutions, error is introduced to the method on dilution as well as a lengthening in time taken for analysis. Dilution of silicate solutions also has an effect on the nature of the silicate ions in solutions. Dilution causes a reduction in concentration of hydroxyl ions and thus in pH. Hydrolysis then occurs and the silica can polymerise to higher polymeric species.[14]

Another method of finding the concentration is to obtain the specific gravity of the solution and combine this with the ratio of alkali metal to silicon. The ratio can be obtained using titration.[14]

Falcone *et al* describe a method of analysis of silicates using integrals of peaks in the infrared spectra. [17] This method will be developed for analysis of alkali silicate solutions extracted from ashes and is described in Chapter 2.

1.5 Extraction of Bio-Derived Alkali Silicate Solutions

The stage of the biorefinery process which will be focused on in this project is the final stage in treatment of waste biomass after combustion. Ashes formed from combustion of biomass will be the treated to extract silicon for use in the synthesis of zeolites. Dr. Jennie Dodson described the extraction of various biomass ashes to form alkali silicate solutions for use as binders in the production of composite boards.[5] The work on extraction of silicas from ash forms a significant basis on which the work described in this thesis is built.

The extraction of silicate solutions from ashes has been described in the literature for the synthesis of silica and aluminosilicate materials. Early papers by Shih describe synthesis of both zeolites and mesoporous silicas from coal fly ashes.[18-20] A fusion method is employed whereby ash is mixed with sodium hydroxide and heated to 550 ˚C for 1 hour in air. The powder was then mixed with water and aged to produce the solutions which were separated from any undissolved residue by centrifugation.[18] Kalapathy *et al* extracted alkali silicate solutions from rice hull ash for synthesis of silica xerogels by mixing the ashes with boiling 1M NaOH solution. Hui and Chao also studied the extraction of silicon into alkali silicate solutions from coal fly ash hydrothermally by mixing ash and 2M NaOH solution at 100 ˚C in a sealed polypropylene bottle.[21] They cited reasons such as energy efficiency and costs as reasons to not use fusion as previously.[21] Little work has been done on extraction of alkali silicate solutions from biomass for other purposes or from biomass ashes other than those obtained from coal or rice hulls. There has been very little research published either on studies on biomass ashes from large scale combustion or on Miscanthus ashes.

1.5.1 Microwave vs. Conventional Heating

In many cases heating using microwaves can be more energy efficient than conventional heating. Where there is a dipole in a molecule, that dipole will align with an electric field and since microwaves create an alternating oscillating electric field, the corresponding alternating dipole creates molecular friction and dielectric loss which in turn creates heat in the near environment of the molecule.[22] A dipole exists in water as well as other polar molecules. As can be seen from Figure 1.2 the heating from microwaves can be much more efficient than conventional heating as the heating is directed from the centre of the sample whereas heat must travel through the vessel and into the sample from the outside when conventionally heated in an oil bath, for example. Microwave heating within chemistry has gained much recognition as a quick heating technique and one that enables greener solvents such as water or even solvent free reactions.[22]

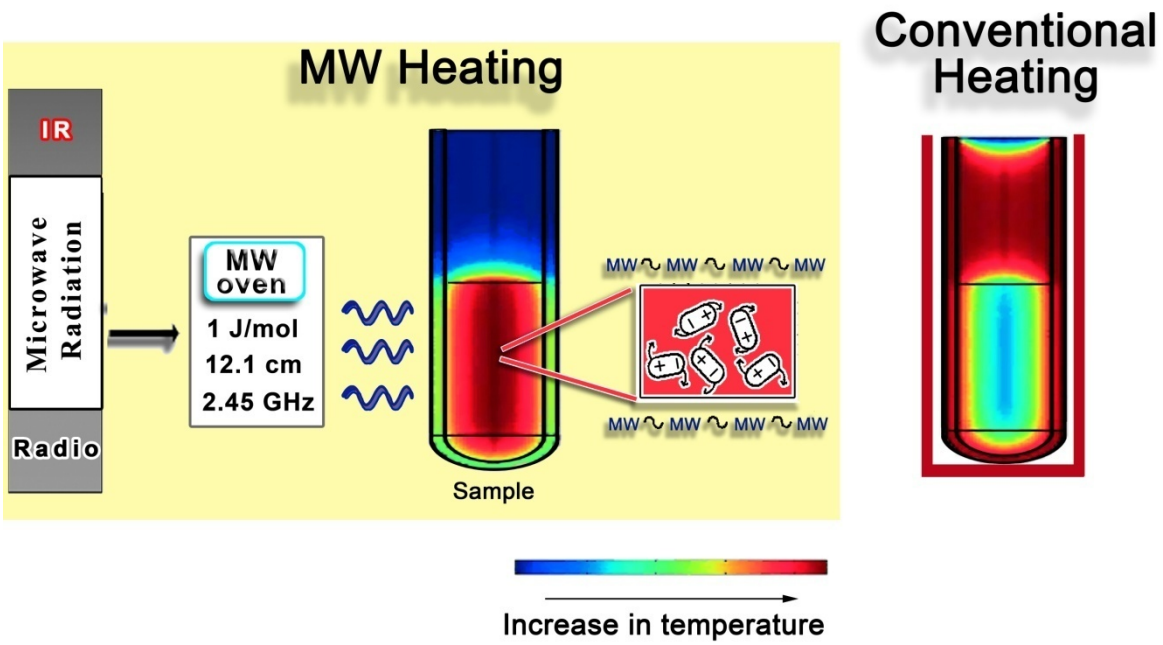

Figure 1.2 Process of microwave heating in comparison with conventional heating[23]

1.6 Microporous materials - Zeolites

Zeolites are a family of crystalline solids which occur both naturally, as minerals, and by synthesis.[24] Natural zeolites are found throughout the world as they are one of the most abundant mineral species. They are mined and utilised in large quantities for their sorbent and ion-exchanging properties such as in sewage treatment.[25]

Development of synthetic zeolites with reliable characterisation began in the 1940s and this work led to the first fully characterised zeolite (Zeolite A) without a corresponding natural structure.[25-26]

Zeolites are aluminosilicate materials of the form $M_{2/n}O\text{-}Al_2O_3\text{-}ySiO_2\text{-}wH_2O$ where M is a cation such as sodium, potassium, magnesium, or calcium, n is its charge, and y ranges from 2 to infinity. The water contained in the cavities are represented by the 'w'.[25] The presence of aluminium within the silica structure leads to a charge imbalance (+1) which is stabilised by the negatively charged cation 'M' and this relationship is reflected in the equivalence of the number of aluminium atoms and the number of cations.

1.6.1 Applications

Zeolites are used in large scales in industry. Major applications are in catalysis, especially in petroleum cracking, gas separation, and in ion exchange for purposes such as water softening.[24-25]

1.6.2 Geometry

The structure of the zeolites discussed in this thesis can be described beginning with the SiO_4 building block (Figure 1.3) which can polymerise with other SiO_4 tetrahedra through the covalent oxygen bond to form more complex geometries. When twenty four SiO_4 tetrahedra are combined, they form the octahedron shown in Figure 1.4, denoted the sodalite cage. The mineral sodalite is formed when the cages are arranged such that each square face joins two cages so each cage connects to six other cages (Figure 1.5). When the hexagonal faces of the sodalite cages join with four other cages through connecting units composed of six bridging oxygen ions, a hexagonal prism is formed with greater spacing than sodalite (Figure 1.6).[24] This structure is termed Faujasite and forms a family of zeolites which includes X and Y differentiated by their silicon to aluminium ratios. The largest cavity within this structure can fit a sphere of diameter 1.2 nm.[24]

Zeolites X and Y crystallise over different Si/Al ranges. For a typical Faujasite, the composition is $Na_j[(AlO_2)_j(SiO_2)_{192\text{-}j}].zH2O$ where z is around 260 and j is between 48 and

76 for Zeolite Y and between 77 and 96 for Zeolite X.[24] Therefore Zeolite X contains significantly more aluminium than Zeolite Y.

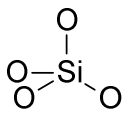

Figure 1.3 Silicon-oxygen tetrahedron

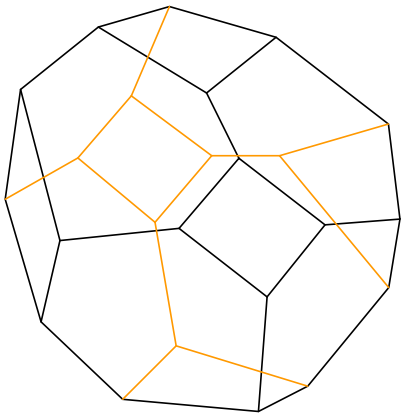

Figure 1.4 Sodalite cage with line intersections representing Silicon atoms and Oxygen atoms at the centre of each line

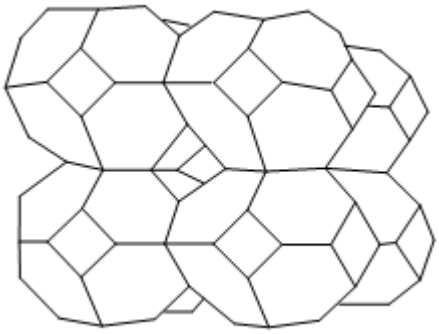

Figure 1.5 Sodalite structure[24]

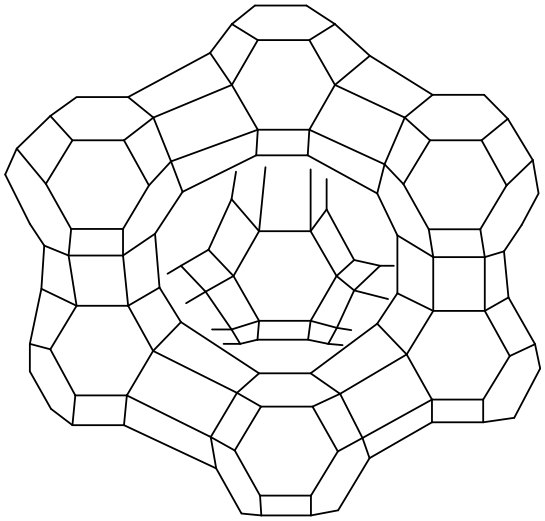

Figure 1.6 Faujasite structure with line intersections representing Silicon atoms and Oxygen atoms (not shown) at the centre of each line

Faujasite was chosen to be the target zeolite structure as the synthesis is simple and straightforward, no template is required and the crystallisation process does not require a pressurised system. Additionally, it has many applications in catalysis, particularly in the catalytic cracking of petroleum molecules due to its three dimensional pore structure which can admit long hydrocarbons. [24, 27]

Zeolites have been termed 'molecular sieves' as they have dimensions similar to the molecules converted in chemical reactions and therefore catalysis can be directed by the steric properties of the reagents and the pore size of the zeolitic catalyst.[24]

Zeolites exhibit both Brønsted and Lewis acidity. The number of catalytic sites increases with the concentration of aluminium in the structure and these potential sites where cations are located are shown in Figure 1.7 (determined from X-ray data).[24] There are four positions for the cation. Of particular interest are II and II' as they are accessible to reactants and thus relevant to catalysis. Sites I and I' are less accessible. Type I sites are located inside the hexagonal prisms, type I' sites are located inside the sodalite cages, and Type II and II' sites are located in the larger cavity (termed the supercage).

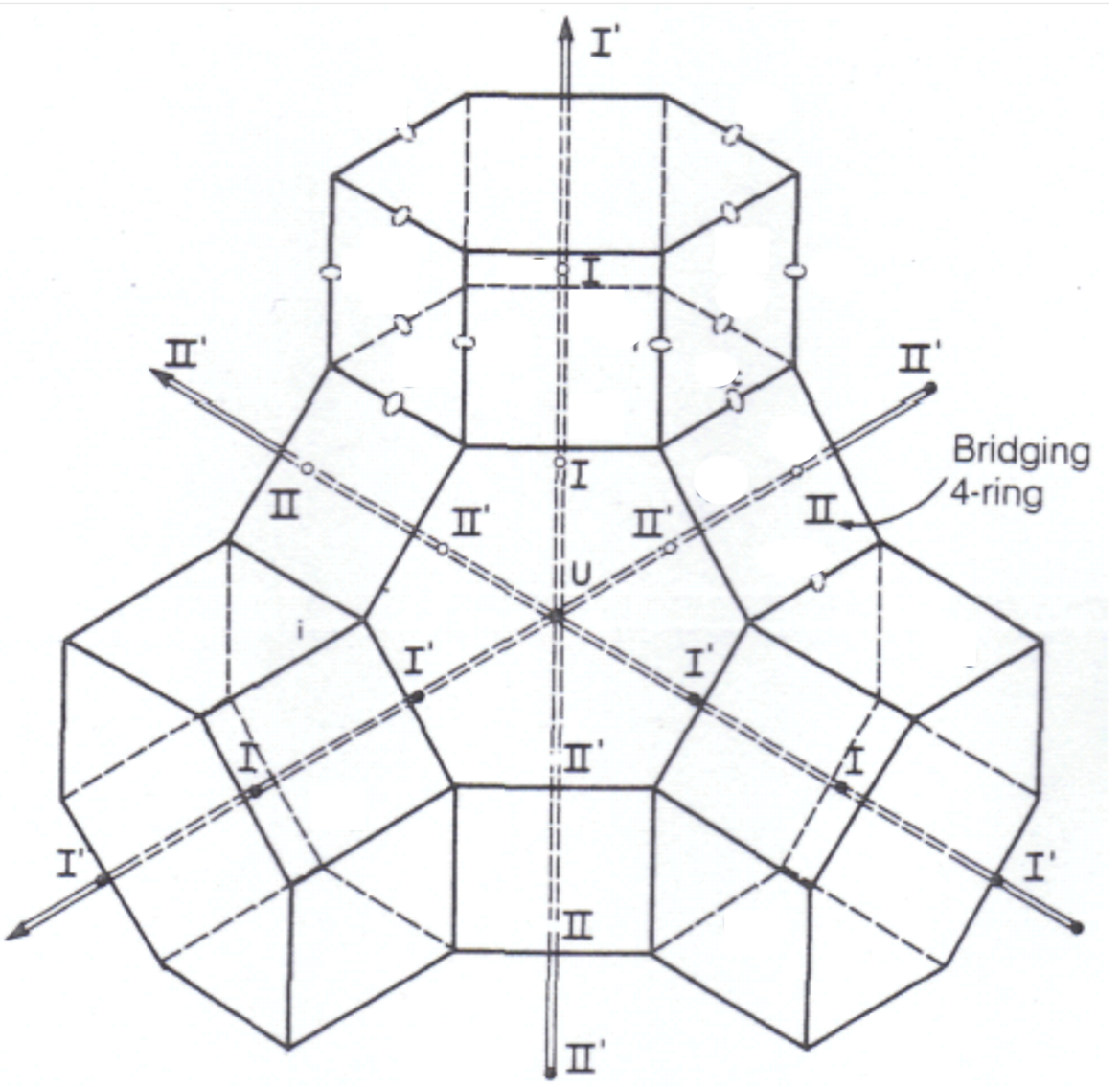

Figure 1.7 Locations of cation sites in X and Y Zeolites[24]

In order to generate Brønsted acidity, hydroxyl groups are needed on the surface to donate protons to a Brønsted base. Hydroxyl groups can be introduced by two methods; direct ion exchange with mineral acids, or exchange with ammonium or alkylammonium ions followed by calcination.[25] The exchange followed by calcination method can be less damaging to the structure, especially for high aluminium-containing zeolites, than treatment with mineral acids as silica structures are more vulnerable to pH changes than thermal effects. Lewis acidity is provided by the cations themselves as they have a positive charge and are susceptible to electron pair donation.[25]

As thermally stable heterogeneous catalysts and ion exchangers, zeolites are a useful and green tool in the development of more sustainable chemistry.

1.6.3 Synthesis of Zeolites from Ash

Ash can be used directly as a catalyst or catalyst support and has shown some activity in a range of reactions and processes.[28] Potential for catalysis in biodiesel production was described for a NaX Zeolite synthesised from coal fly ash.[29]

A large amount of research has been done synthesising zeolites from ashes for the last 30 years. Primarily focussing on using silicon from rice husk ash and coal fly and coal bottom ashes many papers have been published describing the synthesis of novel zeolites or a mimicking of zeolites formerly synthesised from commercial silicates.

Mixed phase zeolites were synthesised hydrothermally from coal fly ash[30-34] and in particular Faujasite zeolites were synthesised from coal fly ash as early as 1993.[35-38] A comparison using KOH and NaOH with coal fly ash was performed by Rios *et al* which found that no zeolitic materials were obtained when KOH was used.[39] Molina and Poole compared hydrothermal extraction with fusion prior to hydrothermal extraction of coal pulverised ash in the synthesis of zeolites and found a higher purity in yield of Zeolite X when using the fusion method.[40]

Other ashes have been used to synthesise zeolites such as ash from thermally treated sediment which was used by Wu *et al* to synthesise a range of zeolites including Faujasite.[41]

As early as 1985 a synthesis was described for NaX using rice husk ash with additional silica gel added.[42] Other zeolites such as Mordenite, ZSM-5, and Zeolite Beta were also synthesised from rice husk ash.[43-45]

1.7 Mesoporous Silica

Much more recently, from the early 1990s, silica derived molecular sieves with mesoporous pore structures with short-range order have been synthesised.[46-47] These materials offer the same advantages of zeolites such as thermal stability, high surface areas, and shape selective catalysis but with the addition that larger pores widen the number of molecules and chemical reactions which can be catalysed by these materials.

These mesoporous materials are synthesised using various templating techniques described below.[48-49] Molecular sieve type silica materials have a wide range of applications including as catalysts and catalyst supports, as adsorbents and particularly in CO_2 adsorption, and in separation.[50-53]

1.7.1 Micelle Templating

In order to synthesise ordered mesoporous materials it is often necessary to introduce a template for the silica to condense around. There are various mechanisms in which templates and silica interact. If the synthesis environment is aqueous, and this is the case for all materials synthesised in this thesis, template molecules with polar and non polar ends will form micelles with the polar end facing out and the non polar end in the centre. These micelles form the basis of the template and as they coordinate they form uniform arrays. Silica condenses around these templates and the required material precipitates out of solution. It is then necessary to remove the template by ion exchange, calcination, or solvent extraction to obtain the porous structure.

The various pathways of micelle templating are termed by using the nature of charge (positive or negative) on the structure directing agent (template surfactant), S, and the silicate precursor, I. For example, to synthesize MCM-41 the template CTAB (cetyl trimethylammonium bromide) (Figure 1.8 and Figure 1.9) is used and this has a positive amine group around which the negative silicate ions interact. This mechanism is termed S^+I^- (Figure 1.10).[46-47]

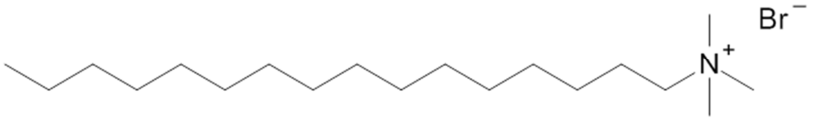

Figure 1.8 CTAB (cetyl trimethylammonium bromide)

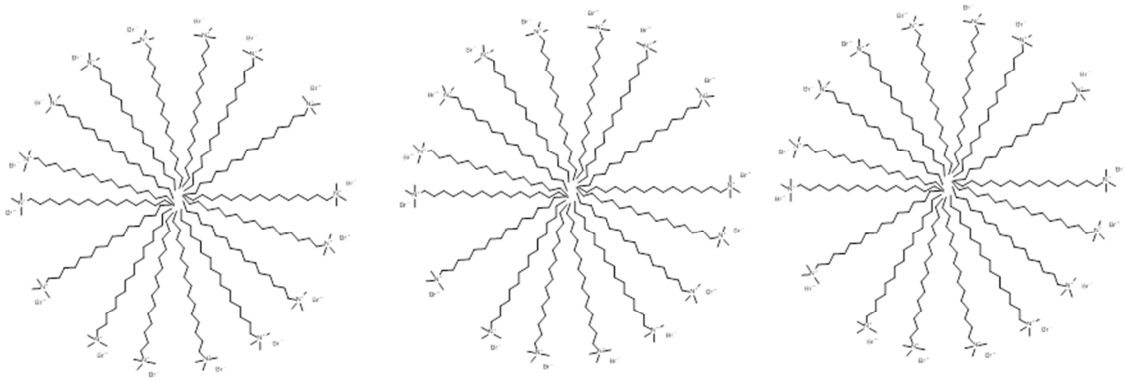

Figure 1.9 Three CTAB micelles with polar ends on outside and non polar end facing inwards

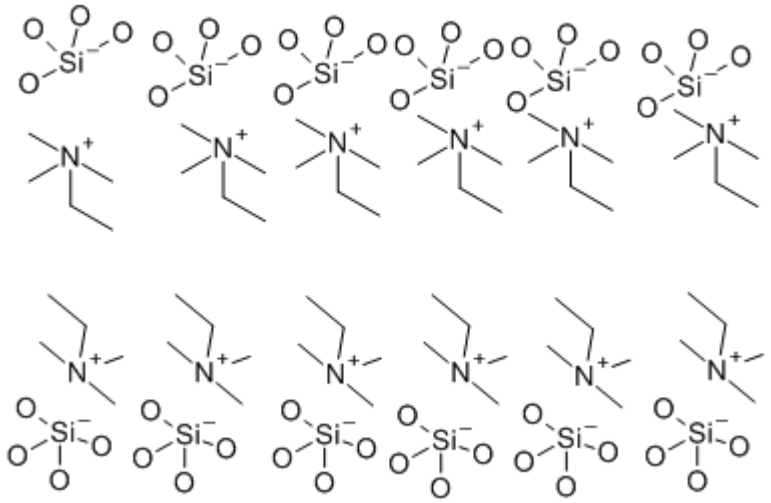

Figure 1.10 S^+I^- templating method for synthesis of mesoporous silica (where 'S' is surfactant and 'I' is inorganic). Positive nitrogen cations line the edge of the micelle arrays and silicate anions interact along the same axis

In order to synthesise SBA-15, the triblock copolymer Pluronic P123 (Figure 1.11, Figure 1.12, and Figure 1.13), is used as the template. Pluronic P123 forms micelles which self organise and have a positive surface charge once protonated under acidic conditions. A negatively charged anion then coordinates the positively charged micelle template surface with positively charge silica groups in an $S^+X^-I^+$ mechanism, where in this case the halide ion, X, is Chloride (Figure 1.14).[54-55]

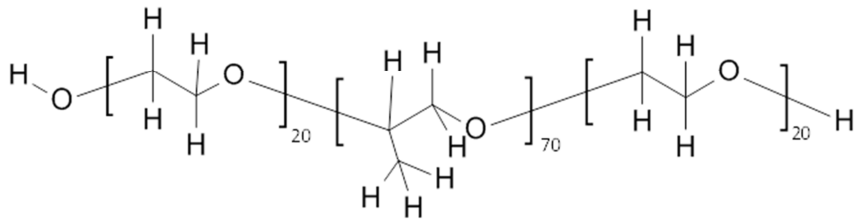

Figure 1.11 Simplified structure of the organic templating agent Pluronic P123

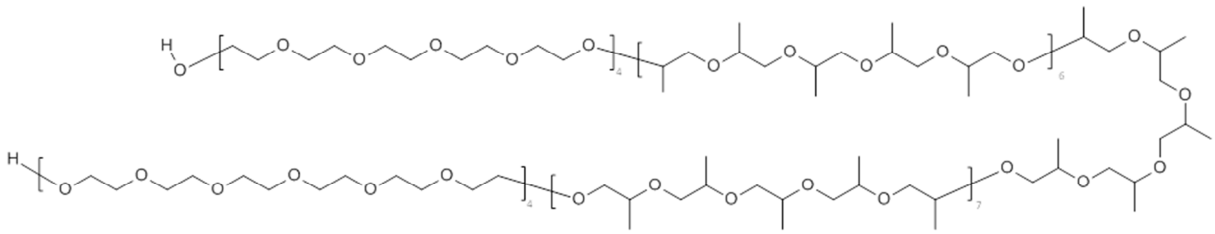

Figure 1.12 A Pluronic P123 molecule coordinated with polar groups at one end and the organic centre at the other end

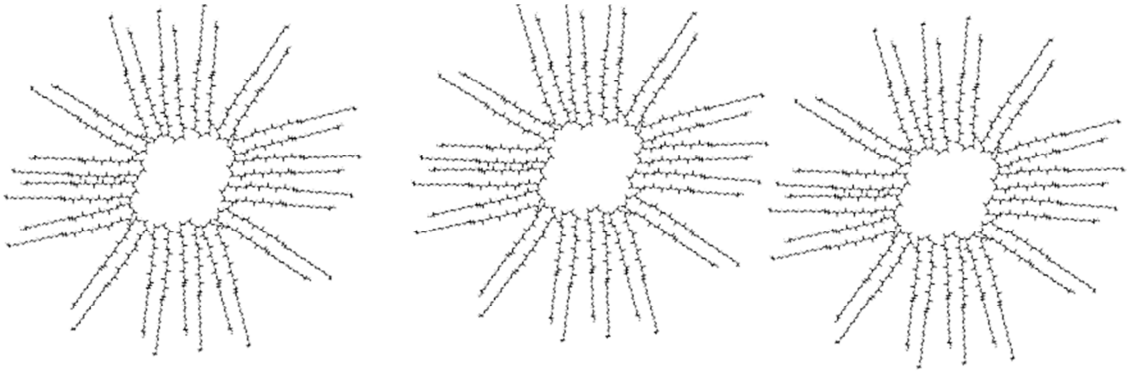

Figure 1.13 Three coordinated Pluronic P123 micelles with polar ends on outside and non polar end facing inwards

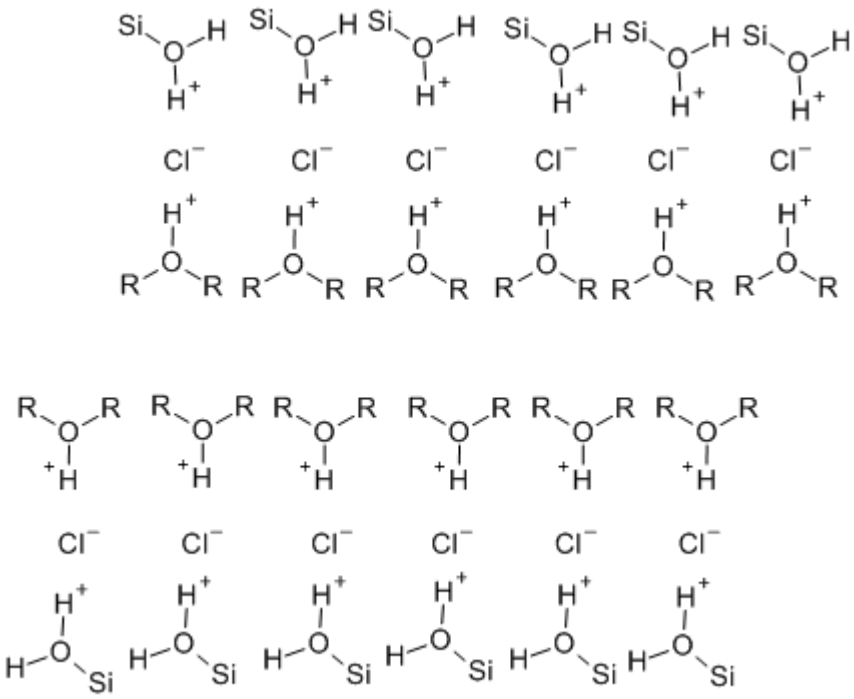

Figure 1.14 $S^+X^-I^+$ templating method for synthesis of mesoporous silica (where 'S' is surfactant, 'I' is inorganic, anion 'X' is Chloride ion, and R is H or alkyl chain). Protonated Pluronic P123 groups line the edge of the micelle arrays, chloride ions interact and form an intermediate between the micelle edge and protonated silicate cations

It will be useful to note that the nature of Pluronic P123, a surfactant template which has a very long chain and can arrange itself within 3 dimensional space, leads to condensation of silica at other points of the chain as well as merely on the edge of the micelle. The effect leads to microporosity in the final silicate structure which links the larger ordered mesopores.[56]

Another mechanism for synthesis of mesoporous molecular sieve silicas proceeds via a neutral route and utilises primary amines to form micelles (Figure 1.15) which then aggregate together and interact with silica via an S^0I^0 mechanism (Figure 1.16).[57-58] As there is no charge difference between the template and silicate, the interactions occur due to hydrogen bonding. A wide range of such materials have been synthesised using neutral amines which can be removed from the silicate materials via solvent extraction and reused.[59-60]

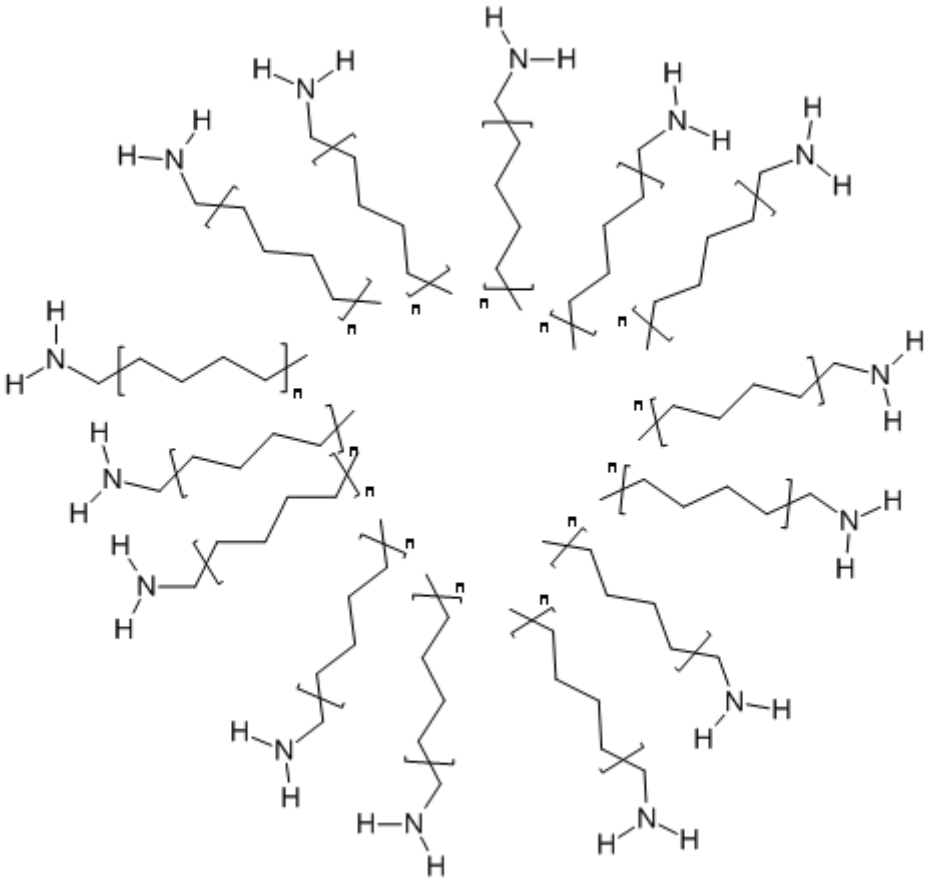

Figure 1.15 Primary amine template

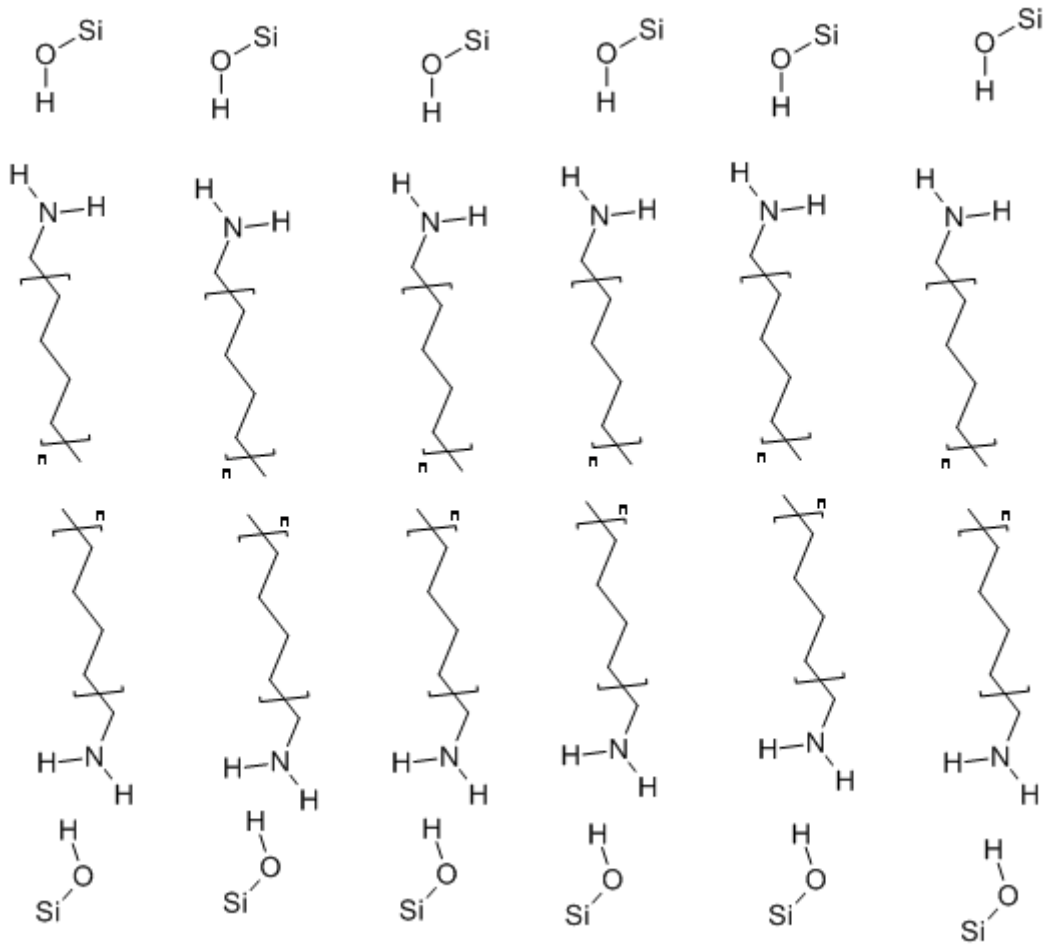

Figure 1.16 S^0I^0 neutral templating method for synthesis of mesoporous silica where the interaction between polar end groups and silica in hydrogen bonding ('S' is surfactant and 'I' is inorganic)

Ionic templating methods (Figure 1.10 and Figure 1.14) produce linear pores as the charge on the outer edge of the micelles prevents the pore arranging in a non-linear manner. When there is no charge density on the micelle surface, such as with neutral templating, there is no such constraint and there can exist 'wormhole porosity' where the micelles have arranged themselves in a non-linear fashion, an example of which is shown in Figure 1.17.

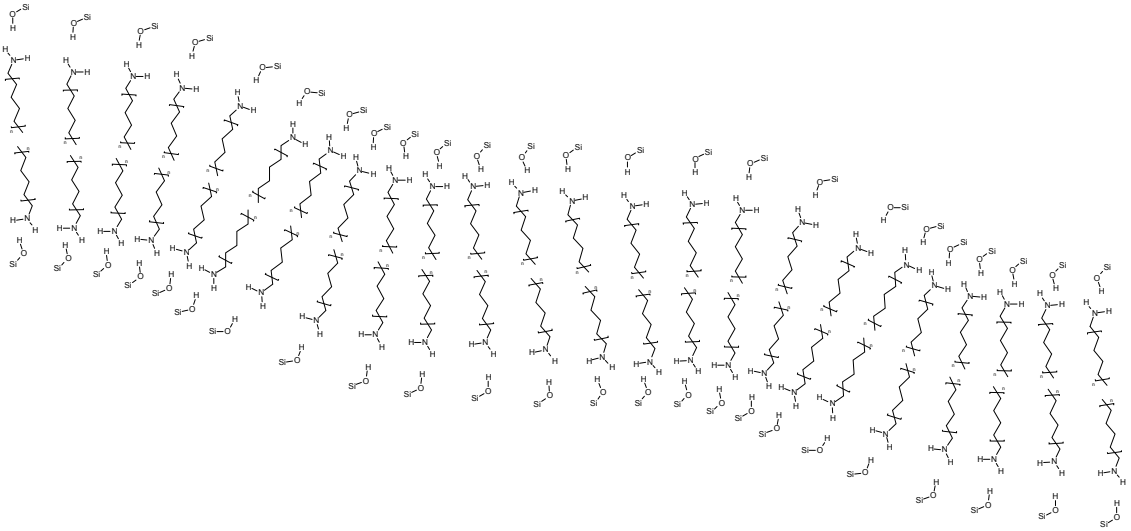

Figure 1.17 Wormhole porosity due to neutral S^0I^0 templating mechanism

The process described above uses micelle formation to create ordered structures for silica to condense around. This process has been termed liquid crystal templating (Figure 1.18).[61] A template is added to a particular pH environment and forms micelles. A silica source is added which interacts with the micelles and condenses to form the desired structure. The material is filtered and calcined in order to remove the template.

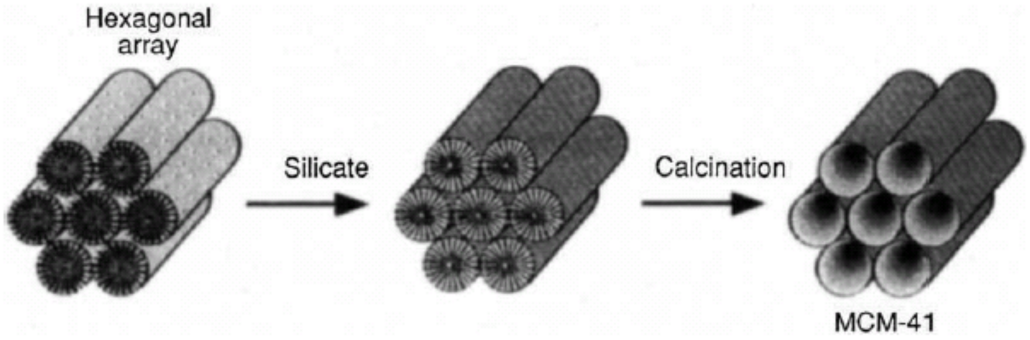

Figure 1.18 Schematic drawing of the liquid-crystal templating mechanism [46]

1.7.2 MCM-41

In 1992 a new family of materials were synthesised by scientists at Mobil named M41S.[46-47] These materials were the first mesoporous materials containing regular arrays of uniform channels (between 16-100 Å depending on synthesis conditions) to be synthesised via the calcination of silicate gels in the presence of surfactants.

MCM-41 (Mobil Composition of Matter number 41) was chosen for synthesis from bio-derived silicates since promising work had been published (Section 1.7.4) in which MCM-41 was synthesised from alkali silicate solutions derived from coal ashes under ambient conditions (room temperature and atmospheric pressure).

One of the less green aspects of the synthesis is the use of CTAB (cetyl trimethylammonium bromide) which is poorly biodegradable and has "high acute and chronic toxicity".[15] Since the template is calcined this becomes an issue of any wasted template unused in the synthesis. Negative environmental impacts of the use of CTAB are also the calcination of the template causing gases to be released to the atmosphere and also the single use nature of the template.

1.7.3 SBA-15

In 1998 a new family of mesoporous silicas named SBA, with larger pores and thicker walls than the MCM family were synthesised from TEOS. These materials were synthesised via a micelle templated method (as described above) in an acidic aqueous environment (pH around 1). The template used for SBA-15 is Pluronic P123, and is an organic triblock copolymer (polyethylene glycol – polypropylene glycol – polyethylene glycol) which has surfactant properties.[54-55]

As with the template for synthesis of MCM-41, the template for synthesis of SBA-15, Pluronic P123, is not readily biodegradable and can have "acute and prolonged toxicity to aquatic systems".[15] Again, since it is calcined this becomes less of an issue in itself but the calcination causes gases to be released to the atmosphere which is in itself a problem.

1.7.4 Mesoporous materials synthesised from ashes

In the last 13 years SBA-15 and MCM-41, alongside other mesoporous silica materials, have been synthesised from ashes. Coal and rice husk appear to be the main sources of silicon for ash based synthesis of these mesoporous materials (rice hulls are the only biomass to have been researched in this way to date).

Shih *et al* appear to have been the first to synthesise the mesoporous aluminosilicate material MCM-41 from fused fly ash solutions.[19] They describe a method to extract the silicate solutions for use in synthesis as a high temperature (550 ˚C) fusion of the ashes with sodium hydroxide followed by mixing with water at room temperature to extract the inorganic species.

Kumar *et al* synthesised Al-MCM-41 and SBA-15 from coal fly ash. Fusion was utilised to extract the supernatant solutions (aluminium and silica) for use in synthesis of the materials. Sodium metasilicate was added to the SBA-15 synthesis and no aluminium from the supernatant solution was incorporated. Porosity was found to be lower for the ash derived materials.[62] Hui and Chao studied the effect of pH on the uptake of aluminium into an MCM-41 material synthesised from coal fly ash. The silicate solution used for this work was extracted hydrothermally citing reasons such as energy efficiency and costs as reasons to not use fusion as previously.[21] Misran *et al* also describe a synthesis of MCM-41 from coal fly ash using fusion extraction.[63] Ahn *et al* synthesised SBA-15, MCM-41 and other mesoporous materials from coal bottom ash and fly ash.[64-67] Aluminium from bottom ash was incorporated into the MCM-41 structure which destabilised it. Sodium metasilicate was added to reduce this effect and increase the porosity.[64]Addition of sodium metasilicate to the synthesis of SBA-15 is described in order to strengthen the structures of the materials.[64, 66] Coal fly ash was found to contain lower amounts of silicon but synthesis of SBA-15 was achieved with some inferior properties to a TEOS derived SBA-15. It was found that once these materials were impregnated with polyethyleneimine (PEI), their CO_2 sorption capacities were similar.[66] Majchrzak-Kucęba and Nowak studied the reproducibility of the synthesis of MCM-41 from coal fly ashes from different power stations in Poland. It was found that the successful synthesis of the material depended on the Si/Al ratio of the supernatant.[68]

Grisdanurak and Chiarakorn *et al* describe syntheses of MCM-41 from washed rice husks and rice husk ashes in acidic conditions.[69-70] The silicate solutions used in the syntheses were hydrothermally extracted. The materials were tested for sorption of chlorinated volatile organic compounds (CVOCs) and hydrophobicity properties. Chidthaisong *et al* synthesised MCM-41 from rice husk using the same technique as Chiarakorn *et al* and tested it for sorption of CO_2.[71] Jang *et al* synthesised MCM-41 and SBA-15 from rice husk ash (basic pH solution) and grafted amine compounds onto the surface in order to test the materials for sorption of CO_2.[53]

All rice husk and rice husk ash syntheses described in the literature have been conducted using ash produced on a lab scale and therefore not only is the use of Miscanthus ash a novel source of mesoporous silica materials, the fact that the Miscanthus ash was collected from large scale combustion at a power plant also makes the studies in the thesis unique.

1.8 Red Clay Aluminium Extraction

More than 70 million tonnes of dry Bauxite Residue (red clay) was produced annually worldwide in 2000 and production has increased by 65% between then and 2010.[72-73] Red clay is a waste product of the large scale Bayer process of aluminium production. It is formed from the insoluble residue left after digestion of bauxite ore in hot caustic soda and is a heterogeneous mixture of oxides.[74] Below in Table 1.1 are some examples of the composition of the material. [75] It has a high concentration of silicon, aluminium and iron which can be used as a source for synthesis of aluminosilicate materials. Red clay has been studied as a catalyst for methane decomposition.[76] Due to the large amounts of this material being produced and its high concentration of aluminium and iron it was decided to test the potential of this material as an aluminium source in the synthesis of MCM-41. This possibility has not been suggested or published as yet elsewhere.

Table 1.1 Elemental composition (ICP-AES) of red clay samples (wt%) from Hargreaves *et al*. [75]

Sample Code	Major Elements										
	SiO_2	Al_2O_3	Fe_2O_3	TiO_2	CaO	MgO	Na_2O	K_2O	P_2O_5	MnO	LOI
RM4[53]	16.40	10.44	42.70	6.44	2.85	1.56	3.72	0.05	0.02	-	15.30
RM6[53]	12.40	10.12	36.40	18.70	2.65	2.52	3.85	0.09	0.02	-	12.80
RM7[53]	14.60	23.51	36.79	0.74	1.18	0.07	6.08	0.02	0.15	0.12	16.47

1.9 Techniques

A brief overview of the techniques used in this project are described below. All techniques are methods used to analyse materials synthesised in this project. Further details about the exact methods used are given in Chapter 6 Section 6.5.

1.9.1 X-Ray Techniques

X-rays were discovered in 1895 by Wilhelm Röntgen and various techniques have since been developed to characterise materials.[77]

1.9.1.1 X-Ray Diffraction Spectroscopy (XRD)

The type of XRD spectroscopy used in this project is Powder X-Ray Diffraction but will be referred to as simply XRD.

This technique has developed over the last 100 years and is based on the discovery that the wavelength of x-rays is of the order of 1 Å (= 1 x 10^{-10} m) and that this is comparable to the separation of atoms in a crystalline lattice. When x-rays are scattered by electrons bound to atoms the interference leads to a phase shift in their wave. When this effect occurs for atoms in repeating planes the phase shift can form constructive interference. This constructive interference occurs when Bragg's equation (Equation 1.3) is satisfied and gives a peak of intensity which can give information on the crystalline structure of the material.[78]

$$n\lambda = 2d\sin\theta$$

Equation 1.3 Bragg's Equation where n = 0, ±1, ±2, ... λ = wavelength of X-ray, and 2θ is the angle between incoming and outgoing x-rays (diffraction angle)

The technique is incredibly useful for identifying crystalline materials as each different structure has its own unique pattern (set of peaks at specific 2θ values), much like a fingerprint, which can be compared with a library of such patterns to quickly identify the crystalline phase. It is also possible to analyse a material if it is a mix of crystalline phases as patterns for each unique phase can be identified from the sample's pattern.

1.9.1.2 X-Ray Fluorescence Spectroscopy (XRF)

Where XRD detects diffracted X-rays at different angles to identify a material, XRF detects fluorescence energy caused by x-rays hitting a sample. When an x-ray photon of high enough energy strikes an atom it can expel an electron from one of that atom's shells. An electron from an outer shell (higher energy) then transfers to the shell with the vacancy (lower energy) and this process produces emitted energy at a certain radiation characteristic of that element. An atom will emit more than one single energy as there are multiple shells for an electron to be expelled from and for an electron to transfer from. This creates an element specific fingerprint which can be added to a library for all elements that the XRF spectrometer detects.[79]

XRF can give the elemental composition of the bulk of a material for all elements heavier than Neon in the periodic table. Therefore it cannot give information on any organic content of a material but it can give precise concentrations of any inorganic or metal elements, especially when combined with similar reference samples.

1.9.1.3 X-Ray Photoemission Spectroscopy (XPS)

XPS is another X-ray technique which gives information on the elemental composition of a material's surface. This technique covers all elements from the periodic table, except Hydrogen and Helium, and needs to be carried out under vacuum. XPS can give elemental composition of the surface up to a depth of 10 nm which is important as this is the active area which will be involved in catalysis. XPS can provide information on the molecular

environment of the elements on the surface such as oxidation state. The technique monitors the energy of electrons which are emitted when the material is subjected to x-ray photons. This information can then be related to the element and its molecular environment which is especially important for understanding potential applications such as in catalysis.

1.9.2 Porosity and Porosimetry

Porosimetry is an analytical technique which can give information about a material's surface structure. In particular, the technique can characterise pore structures of a material. The technique used in this thesis is N_2 porosimetry and utilises the properties of nitrogen such as its size and boiling temperature to study the surfaces of materials. By varying the partial pressure of nitrogen in a nitrogen/helium mixed atmosphere, an isotherm can be produced which examines the adsorption of nitrogen on the surface of a material.[80] Adsorption is defined as the strictly physical effect of enrichment of one or more components in an interfacial layer.[81] Nitrogen porosimetry, thus, uses the nature of the condensation of nitrogen onto the surface of the pores of a structure in order to characterise it. This characterisation is useful in characterising a material's pore structure, i.e. pore size, pore volume, and pore geometry, which is in turn useful in understanding its behaviour in various applications such as in catalysis.

Figure 1.19 shows the six types of adsorption isotherms classified by IUPAC.[81] The most relevant ones for this thesis will be Types I, II, and IV which relate to microporous, nonporous, and mesoporous materials respectively.[80]

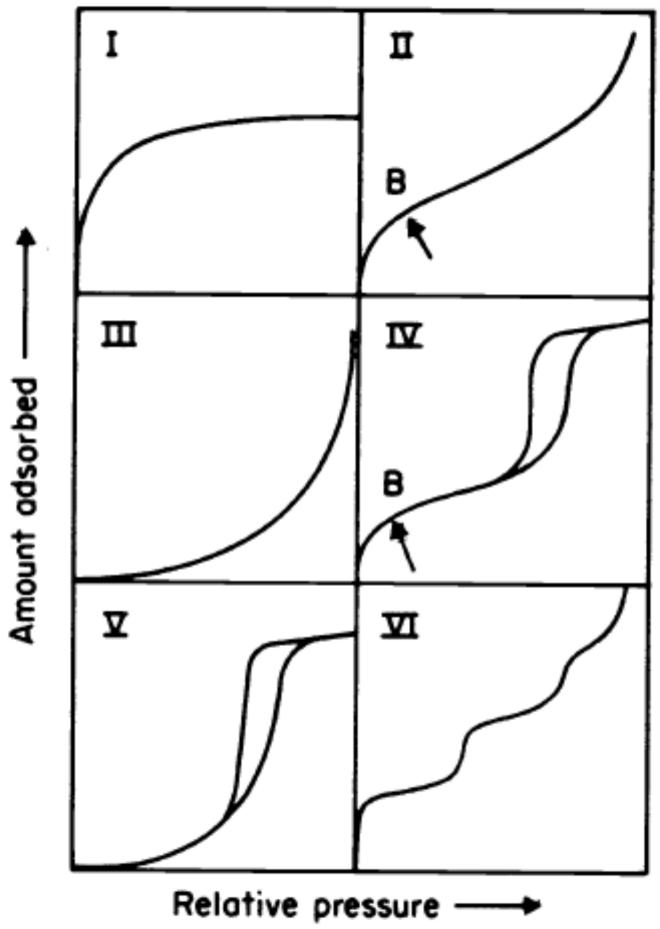

Figure 1.19 The six types of adsorption isotherm[81]

The Type II isotherm which most often refers to a non-porous material, gives information on the monolayer capacity (amount of adsorbate which can be accommodated in a single molecular layer of 1 g of the solid) of that solid. This information can be used to calculate the surface area by multiplying the number of molecules adsorbed by the area taken up by each molecule.[80]

Below in Table 1.2 are the IUPAC definitions of pore width.[81]

Table 1.2 Pore size definitions.[81] 1 Å = 10^{-10} m

	Pore Width Å
Micropore	**Less than ~ 20**
Mesopore	**Between ~ 20 and ~ 500**
Macropore	**More than ~ 500**

Microporous materials, represented by the Type I isotherm, adsorb a high volume of nitrogen at very low relative pressure. This is because the pores are no more than a few molecular diameters in width and so the potential field from neighbouring pore walls will overlap causing an enhancement of the interaction energy of the solid with the gas molecule and thus cause filling of the pores at quite low relative pressures.[80]

Mesoporous materials exhibit a Type IV isotherm (Figure 1.20) which follows a similar path to the Type II isotherm but at a certain point after 'C' rises upwards until at higher pressures the slope decreases.[80]

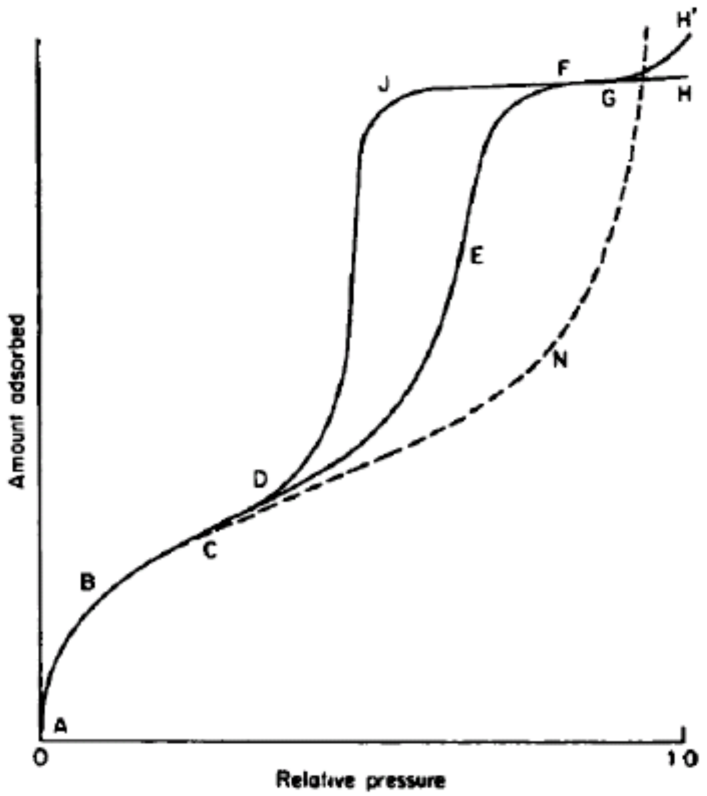

Figure 1.20 A type IV isotherm[80]

The Type IV isotherm has a characteristic hysteresis loop (Figure 1.20), during which the volume adsorbed at a given partial pressure is always greater along the desorption branch.[80]

For a mesoporous material adsorption of nitrogen is in two stages. Initially a monolayer of the adsorbate is formed across a surface and this relates to the initial rise in volume adsorbed of its isotherm. The secondary step is termed Capillary Condensation and is

defined as a transformation of a vapour to a liquid within a pore. The effect occurs at a pressure which is related to the pore size (in turn related to the core radius which is the pore size minus adsorbed film) and is lower than the saturation vapour pressure when there exists a concave meniscus within that pore. Within a pore, the initial monolayer acts as a seed for the condensation to take place. When the adsorbate evaporates the process spontaneously occurs once the relative pressure is low enough to destabilise the meniscus.

The process of hysteresis occurs only for some pore shapes. For a cylinder closed at one end the condensation begins at that end to form a hemispherical meniscus which then expands to the end of the pore. The process of evaporation then commences at the pore face and continues to the end of the pore. These processes occur at the same relative pressures and so a hysteresis loop is not observed. When examining a cylindrical pore open at both ends, condensation occurs from the film on the walls and a cylindrical meniscus is formed until the pore is full whereas a hemispherical meniscus is formed on evaporation. Since this difference in meniscus affects the core radius of the pore these two processes occur at different relative pressure and this creates the hysteresis loop.

1.9.2.1 BET calculation

Brunauer, Emmett, and Teller formulated an equation to obtain a surface area value of a material. This involves plotting relative pressure and volume adsorbed with a constant derived from temperatures related to the adsorption. The gradient of this plot then provides the monolayer capacity which can then be converted to the surface area by incorporating the diameter of the adsorbate.

$$\frac{p/p^0}{n(1-p/p^0)} = \frac{1}{n_m c} + \frac{c-1}{n_m c}\frac{p}{p^0}$$

Equation 1.4 BET equation where n is number of moles adsorbed at p/p^0 relative pressure, n_m is the monolayer capacity

$$c = e^{(q_1 - q_l)/RT}$$

Equation 1.5 Equation for parameter C of BET equation. $q_1 - q_l$ is net heat of adsorption (q_1 is heat of adsorption and q_l is molar heat of condensation), R is molar gas constant, T is temperature

All surface area values calculated in this thesis have used the BET calculation.

1.9.2.2 BJH Calculation

All mesopore size distributions in the work are calculated using a calculation derived from BJH calculations (Equation 1.7 and Equation 1.8) which is in turn based on the Kelvin equation (Equation 1.6).[82-83]

$$Rc_I = \frac{-A}{(1+F)\left[\ln(Pr_I)\right]}$$

Equation 1.6 Kelvin Equation to obtain core radius Rc_I. A is a given constant, F is the fraction of pores open at both ends which is 0 on desorption, and Pr_I is the relative pressure which is assumed to be close to unity such that nearly all pores are filled

$$\frac{dV}{dD_I} = \frac{Vp_I}{Dp_I - Dp_{I+1}}$$

Equation 1.7 BJH equation for pore size distribution where *Dp* is pore (or core) diameter and V is volume adsorbed

$$Dp_I = 2(Rc_I + t)$$

Equation 1.8 Calculation for Pore of Core diameter, Dp_I, using Rc_I and $t = 3.54 \times [-5/(\ln(P/P_0))]^{0.333}$

1.9.3 Fourier Transform Infrared spectroscopy (FT-IR)

A diatomic molecule will absorb infrared radiation if its vibration creates a changing dipole and is of the same frequency as the radiation.[84] Infrared spectroscopy subjects a sample to infrared radiation and studies the frequency of the radiation which is absorbed. The signal detected can be analysed using a Fourier Transform technique which then produces a spectrum from which bond rotations and vibrations can be identified.

1.9.3.1 In Situ FT-IR

In Situ FT-IR is a technique which combines FT-IR with a vacuum system which enables analysis of a surface of a material without any atmospheric molecules adsorbed to it. It is also possible to add specific pressures of pure probe gases in order to study the interactions of the surface with the probe molecules.

For example the introduction of CO or CO_2 can provide information on the acidity and basicity of any surface groups such as metal cations or hydroxyl groups by monitoring the shifts in CO or CO_2 vibrations caused by interactions with surface species.[85-89]

1.9.4 Transmission Electron Microscopy (TEM)

TEM is a microscopy technique, analogous to optical microscopy, which studies the scattering and diffraction of electrons as they travel through a material. An image is produced which then shows the electrons which have not been changed in velocity or direction and some that have been changed either way or both ways.[90] Denser areas of atoms and heavier elements appear darker due to increased scattering of electrons. The technique can produce images with nanometer scales enabling even individual atoms to be seen. A small amount of sample is placed on a carbon grid after being suspended in ethanol. The grid is then placed in the chamber under vacuum for analysis.

1.9.5 Solid State Nuclear Magnetic Resonance Spectroscopy (NMR)

A useful technique for obtaining information about bonding between elements in a material is NMR. The technique analyses the frequency of the resonant electromagnetic field which is produced when a magnetic field is applied to a molecule which contains a magnetic nucleus. NMR can only be conducted on materials which have an odd number

of protons and neutrons such as ^{29}Si and ^{27}Al as this property enables a spin, or magnetic moment which can interact with a magnetic field. The interactions can then be interpreted to obtain spectra where characteristic peaks are shifted depending on their local magnetic field which is in turn affected by the type of atoms and bonding.[77]

1.9.6 Thermogravimetric analysis with infrared absorption spectroscopy (TGA-IR)

TGA studies the variation in weight of a sample as a function of time or temperature during which the sample is subjected to a controlled heat treatment in a controlled atmosphere.[91]

1.9.7 Atomic Absorption Spectroscopy (AAS) Inductively Coupled Plasma Atomic Emission Spectroscopy (ICP-AES)

Both techniques study the energy of a change in orbital of an electron. AAS detects the absorption of radiation as the electrons are promoted to a higher energy orbital. This absorption occurs at a characteristic wavelength and this is provided by element specific lamps. The analysis occurs on free atoms which have been atomised by a particular flame. The technique requires accurate standards in order to calibrate the results. ICP-AES studies the emission of photons as electrons drop to a lower energy orbital. The technique uses plasma (partly ionised gas or vapour) to atomise and excite the material being studied.[92]

1.10 Summary of Project Objectives

The main objectives and what is covered in each chapter is outlined below;

- Extraction of alkali silicate solutions from rice hull and Miscanthus ashes
- Development of a quick and easy method to obtain silicon concentrations of alkali silicate solutions using the integrals of their FT-IR peaks
- Synthesis of a Faujasite zeolite from an ash derived alkali silicate solution and comparison with a Faujasite zeolite synthesised using a commercial alkali silicate solution
- Synthesis of a mesoporous MCM-41 aluminosilicate material from an ash derived alkali silicate solution and comparison with commercial alkali silicate derived MCM-41
- Introduction of aluminium into bio-derived MCM-41 using the waste product red clay
- Synthesis of a mesoporous SBA-15 material from an ash derived alkali silicate solution and comparison with that derived from tetraethyl orthosilicate (TEOS)

2 Biomass Ashes and Silicate extraction and Analysis

2.1 Introduction

This chapter introduces and discusses the ashes used for the research carried out in later chapters. This includes the analysis performed on the materials prior to extraction in order to gain an understanding of the potential for the extraction and formation of alkali silicates.

The second section goes on to describe an optimisation of extraction of silicon from ashes to produce alkali silicate solutions. The use of microwaves as an alternative heating source is explored and shown to be not only just as effective but also much more energy efficient. The comparison of these solutions with commercial alkali silicates is presented and the development of a technique with which to quickly and easily characterise the concentration of silica in the solutions from the integrals of their infrared peaks is explained.

2.2 Biomass Ashes

Various biomass ashes were obtained for this project and are described below.

2.2.1 Rice Hull Ashes

The first biomass ashes to be obtained for this project were from Canada and were ashes from the combustion of Rice Hulls. Annual rice production around the world is forecast to be 729 million tonnes in 2012 and 20% by weight of this is husk or hull.[93-94] The majority of these rice hulls are dumped or burnt on-site as they are mostly considered a waste product of rice production.[94] The combustion of rice hulls can be utilised for energy on small and larger scales and even to power the milling process itself, but rice hulls have a high ash content, around 17-26%, which is a lot higher than conventional fuels and can cause problems in the combustion furnace.[94]

There were two grades of ash obtained for this project, one high in silica (RHA 90%) and the other less so (RHA 55%). The lower silica content is due to a higher unburnt carbon content from the gasification of the hulls as opposed to combustion (heating with much less oxygen). The non-organic components of these ashes are shown in Table 2.1.

RHA90% and RHA55% both contain silica and trace amounts of other metals with any remaining content due to carbonaceous materials.

Table 2.1 X-Ray Fluorescence Spectroscopic (XRF) analysis of Rice Hull Ashes. Elemental composition in wt%

Compound	RHA90%	RHA55%
Na_2O	0.09	0.05
MgO	0.39	0.18
SiO_2	93.19	54.96
P_2O_5	0.94	0.23
SO_3	0.02	0.08
K_2O	1.26	0.84
CaO	1.17	0.24
Mn_3O_4	0.14	0.06
Fe_2O_3	0.04	0.00
ZnO	0.01	0.00
Total	97.24	56.64

A comparison with rice hull ash compositions from the literature is shown in Table 2.2. All samples were analysed using XRF which is an accurate and useful technique for studying the inorganic elemental composition of materials. It is clear that there is consistently a very high concentration of silica and only trace amounts of other elements present. This means that 'RHA 90%' should make a good ash for extracting a pure alkali silicate solution. The unlabelled component (2.76% for RHA90% in Table 2.1) is likely to be carbonaceous materials from incomplete combustion which is not directly registered using XRF and also colours the ashes to varied shades of grey.

Table 2.2 XRF % Composition of RHA 90% ash compared with values from the literature.[45, 95] Elemental composition in wt%

		Prasetyoko *et al*[45]	Sanchez Flores *et al*[95]
Compound	**RHA90%**	**Rice Husk Ash**	**Rice Hull Ash**
Na_2O	**0.09**	**not given**	**0.074**
MgO	**0.39**	**not given**	**0.171**
Al_2O_3	**0.00**	**0.19**	**0.414**
SiO_2	**93.19**	**94**	**93.914**
P_2O_5	**0.94**	**not given**	**0.314**
SO_3	**0.02**	**not given**	**not given**
K_2O	**1.26**	**1.64**	**1.304**
CaO	**1.17**	**0.32**	**0.493**
TiO_2	**0.00**	**not given**	**0.014**
Mn_3O_4	**0.14**	**not given**	**0.067**
Fe_2O_3	**0.04**	**not given**	**0.136**
ZnO	**0.01**	**not given**	**not given**
Total	**97.23**	**96.15**	**96.90**

2.2.2 Ely Ashes (Miscanthus)

The second set of ashes to be obtained for this project were from Ely Power Station and were obtained from the large scale combustion of bales of miscanthus.[8]

Miscanthus is one of the two main dedicated energy crops growing in the UK.[96] Its properties such as high yields, hardiness, and efficient solar energy conversion and use of water and nitrogen have made it widely touted as a future major bioenergy resource.[6] Within England the planting of miscanthus is encouraged through the Energy Crops Scheme resulting in nearly 7500 hectares of miscanthus being planted between 2000-2011. Some recent work has studied the effects of inorganic species within the fuel on the lab-scale combustion of miscanthus and the composition of the ash formed but no previous work has studied the production of ash from a commercial biomass combustion power plant.[96]

Research studying miscanthus combustion residues is important and useful due to its potential as a major bioenergy resource and its unique ash composition differing from the more widely studied coal, wood and cereal straw ashes.

Two types of ash were obtained for this project; bottom (EBA) and fly ash (EFA) (as shown in Figure 2.1). They are differentiated by their collection locations. The fly ash is carried along by the combustion gases and collected before the gases exit through the chimney. The bottom ash is collected from the bottom of the combustion chamber and quenched in water. Typically there is a fractionation of the elements between the fly ash and the bottom ash during the combustion of the biomass, dependent on the volatility of the elements. Potassium, chlorine, sulfur, sodium and phosphorus are enriched in the fly ash, whilst the bottom ash is predominantly composed of silica.[97] This process will likely lead to the extraction of some silicon, potassium, calcium, and chlorine into the quenching waters as this was found to occur on the lab scale.[5] The ashes were obtained on a large scale, dried, milled, and sieved to a fine powder (<125 μm).

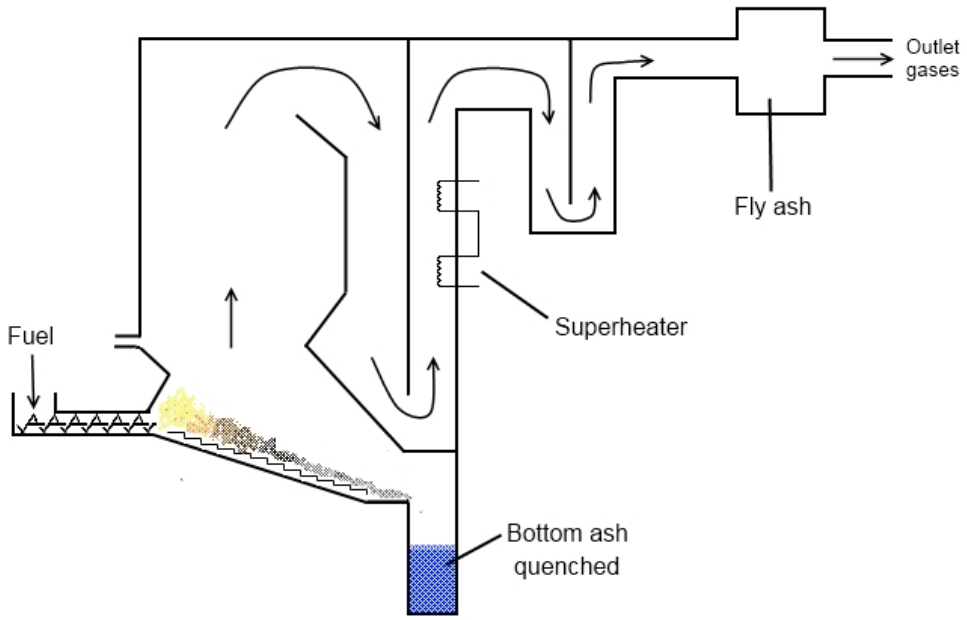

Figure 2.1 Schematic of diagram of the combustion process at a power station.[5] The locations where the two ash types were collected are also labelled

The elemental composition of these ashes is shown in Table 2.3. It is clear that the majority of silica is to be found in the bottom ash whereas the fly ash contains the

majority of the sulfur, potassium, and calcium as explained above. In this case the bottom ash would be more suitable for extraction as the yield should theoretically be higher.[98]

Table 2.3 X-Ray Fluorescence Spectroscopic (XRF) analysis of Ely Fly and Bottom ashes. Elemental composition in wt%

Compound	Ely Fly Ash	Ely Bottom Ash
Na_2O	2.45	0.16
MgO	1.02	2.82
Al_2O_3	0.19	0.76
SiO_2	6.59	63.0
P_2O_5	3.02	2.74
SO_3	18.30	4.37
K_2O	32.0	14.6
CaO	16.8	8.28
Mn_3O_4	0.05	0.14
Fe_2O_3	0.12	0.50
ZnO	0.08	0.02
SrO	0.03	0.02
BaO	0.02	0.06
CuO	0.01	0.02
SnO_2	0	0.09
Cl	19.1	0.05
Br	0.53	0
PbO	0.006	0
Rb_2O	0.023	0
Nb_2O_5	0	0.038
In_2O_3	0	0.031
Total	100	97.7

2.2.3 Eccleshall (wood chip) ashes

A third ash that was acquired for potential use in the project was ash from the large scale combustion of wood chips at a power station in Eccleshall.[99] Wood is one of the oldest biomass sources used for energy production and can be a sustainable fuel source if managed correctly.

The XRF analysis of this material is shown in Table 2.4. Since the total wt% is low this implies these ashes contain more organic components. Again the bottom ash contains the higher silica content but for both ashes this is significantly lower than EBA or RHA90% (20.2% for the bottom ash and 6.84% for the fly ash).

Table 2.4 XRF analysis of Eccleshall Bottom and Fly ashes. Elemental composition in wt% ND is not detected

	Bottom Ash	Fly Ash
SiO_2	26.2	6.84
K	3.92	22.1
Cl	0.024	20.4
Al_2O_3	1.91	ND
Na	ND	8.44
Mg	1.03	0.64
P	0.66	0.33
S	0.077	3.29
Ca	18.4	12.2
Ti	0.035	0.066
Cr	ND	0.0086
Mn	0.0967	0.15
Fe	1.21	1.36
Co	0.013	ND
Ni	0.0024	0.0011
Cu	0.021	0.0532
Zn	0.013	1.1
Ga	ND	0.0013
As	ND	0.031
Se	ND	0.0007
Br	ND	0.083
Rb	0.0059	0.023
Sr	0.05	0.042
Y	0.0014	0.0026
Mo	ND	0.0062
Cd	ND	0.012
Sn	0.005	0.03
Sb	ND	0.026
Ba	0.04	0.045
W	0.095	ND
Ir	ND	0.0092
Pt	ND	0.002
Au	0.0015	ND
Hg	0.0012	0.0011
Pb	0.0217	0.362
Total	53.83	77.67

2.3 Alkali Silicate Extraction

In order to produce zeolites and other ordered porous silica materials it was necessary to have an alkali silicate solution with which to begin the synthesis.

All ashes described in this chapter were tested for alkali silicate extraction. It was found that the Ely Fly Ash, Eccleshall ashes, and Rice Hull Ash (55%) were not efficient for the extraction. This is unsurprising since these ashes contained much lower concentrations of silicon as shown in their XRF analyses (Table 2.1, Table 2.3, and Table 2.4). Therefore RHA95% (RHA) and Ely Bottom Ash (EBA) were chosen for extraction of alkali silicate for use in synthesis of zeolites and aluminosilicate materials.

Two methods were employed to extract the silica from the ashes. One used conventional heating, the other microwave heating.

2.3.1 Microwave

Initial extractions were performed on RHA90% on a small scale. Since the objective was to obtain a large amount of alkali silicate solution as a starting material (in order to carry out syntheses of zeolites and other aluminosilicate materials) this process was soon scaled up. Microwave heating was found to be the more energy and time efficient method. Extractions were carried out at temperatures of 150 ˚C for 2-10 minutes. At a small scale the technique worked well to extract silicon from the ashes into solution. The alkali silicate solutions extracted using this method were of a similar concentration and ratio to those extracted conventionally (Figure 2.2). There is some slight difference in the two bands which may be due to variations in speciation of the silicate ions. An issue arose at the larger scale in the microwave as it was impossible to stir the solution inside the polypropylene vessels in which the extraction was taking place. A lack of mixing led to hot spots occurring in the mixture where metals from the ash were excited by the microwaves and this effect combined with high pressure caused such damage to the vessels that they exploded. A system with stronger vessels, such as TEFLON, and which enabled agitation and mixing of the solution would solve this issue in future and make extraction using microwaves a viable and more preferable option.

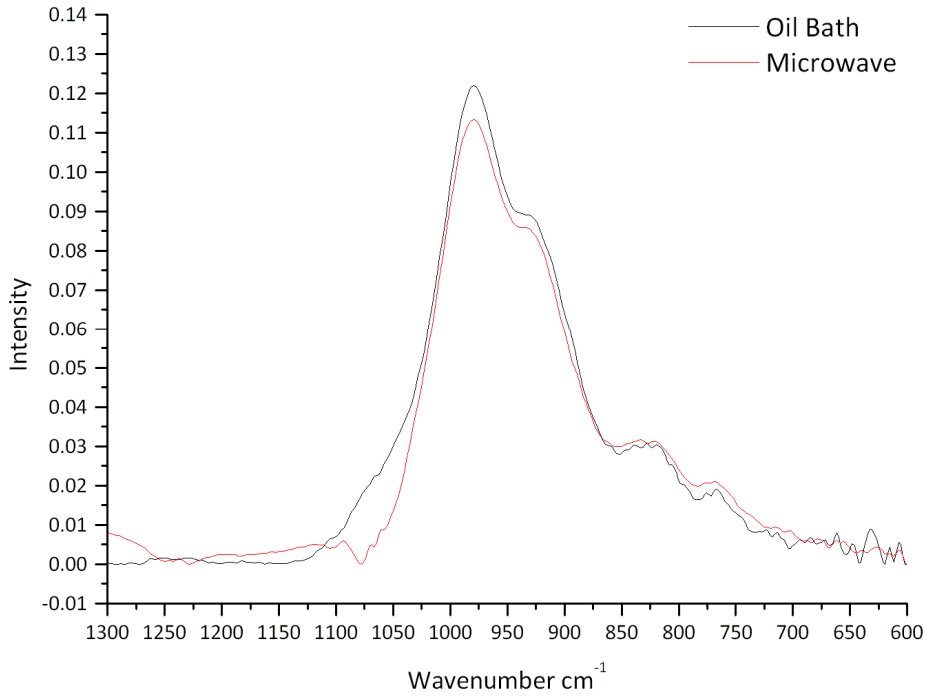

Figure 2.2 Infrared Spectra of bio-derived alkali silicates extracted from Rice Hull Ash using an oil bath and microwave

2.3.2 Heating Mantle

A method was devised by Dr. Jennie Dodson to extract alkali silicate solutions from ash using a reflux system, oil bath, and heating mantle over a 16 hour period.[5] It was found that there was not enough inherent alkalinity within the rice hull or miscanthus bottom ashes to enable extraction and so it was necessary to add either sodium or potassium hydroxide to the extraction without additives.[5] This method was employed to obtain a stock amount of bio-derived alkali silicate solutions for use in the synthesis of the silica and aluminosilicate materials for this project. The rice hull ash (RHA) was extracted using sodium hydroxide whilst the Ely Bottom Ashe (EBA) was extracted using potassium hydroxide. The choice of sodium for RHA was because zeolites are commonly synthesised with sodium cations. The choice of potassium, for EBA was because potassium was present in the ashes and therefore there is potential to develop the extraction technique in order for it not to require addition of extra alkali. The results clearly show the extraction of silica along with significant concentrations of sodium and potassium from the relevant alkali solutions. The yield of extraction of silica from the ashes into solution is much higher for RHA (66.5%) than for EBA (16%) and this is partly due the higher

concentration of cation used for the RHA extraction. There are also trace amounts of other inorganic elements present such as aluminium, phosphorus, and iron (Table 2.5).

Table 2.5 XRF EBA and RHA Alkali Silicate. Elemental composition in ppm

Elemental concentration (ppm)	RHA	EBA
Si	44200	89500
Al	173	335
Na	164000	0
K	1060	159000
Fe	19	31.4
Cu	5.3	9.82
Zn	6.09	9.97
S	59.4	2400
P	380	3460
Mn	265	0
Ca	30.6	0
Ti	4.74	0
Cl	0	480
Br	0	8.96
Ni	0	5.88
Ge	0	18.4
Se	0	3.08

2.4 Commercial Alkali Silicates

Six commercial alkali silicate solutions were used in this project as 'standards' and are described in this thesis as commercial or conventional alkali silicate solutions. The solutions were all obtained from PQ Corporation and were called C501, C503, C75, K120, K78, and K53. These alkali silicate solutions are often described in the methods section of relevant zeolite and aluminosilicate materials synthesis literature. Their silica to cation ratios, silica concentrations, and cation type are shown in Table 2.6. XRF elemental analysis of two of the commercial alkali silicates is shown in Table 2.7.

Table 2.6 Details of commercial alkali silicate solutions used for alkali silicate analysis development[5]

Name	Mean specific gravity	Mean wt ratio	Mean molar ratio	Mean M_2O	Mean SiO_2	Mean total solids
(Counter-ion)	g cm^{-3} at 20 °C	SiO_2: M_2O	SiO_2: M_2O	wt%	wt%	wt%
C501 (Na)	1.6	1.6	1.65	18.0	28.8	46.7
C503 (Na)	1.5	2.5	2.58	12.5	31.1	43.6
C75 (Na)	1.38	3.2	3.3	8.6	27.6	36.2
K120 (K)	1.6	1.43	2.24	21.6	20.8	52.4
K78 (K)	1.39	2.09	3.27	13.0	27.1	40.1
K53 (K)	1.26	2.48	3.89	8.6	21.3	29.9

Table 2.7 XRF elemental analysis of two commercial alkali silicate solutions. Elemental composition in ppm

	C501	K120
NiO	0	7
Cl	0	1780
Na_2O	268000	0
Al_2O_3	1090	1140
SiO_2	384000	383000
SO_3	64	1160
ZnO	4	7
CuO	8	14
Fe_2O_3	160	188
V_2O_5	10	0
TiO_2	81	0
CaO	42	0
K_2O	592	239000
SrO	5	0
ZrO_2	488	0

2.5 Silica Concentration IR Calibration

In order to carry out effective research in the synthesis of alkali silicate solutions it is necessary to obtain accurate concentrations of silica in these solutions. The current most common methods are limited to serial dilution followed by Atomic Absorption Spectroscopy, XRF, or a combination of density measurements and titrations. All methods are subject to large margins of error and/or are time and resource intensive.

A method was developed, in conjunction with Dr. Jennie Dodson, to obtain reliable alkali silicate concentrations using Fourier-Transform Infrared Spectroscopy. The method involves using calibration curves obtained from dilutions of commercial alkali silicate solutions. The reliability of the method was tested by comparing the values obtained by the FT-IR integral method with those obtained using atomic absorption spectroscopy.

As can be seen from the IR spectra of the commercial alkali silicate solutions in Figure 2.3 and the close up of the silicate region (Figure 2.4) the shape and intensity of the silicate peak varies according to their silica concentration and their specific cation-to-silicon ratios. The silicate band area is within the 1250 – 650 cm^{-1} region so this was tested to study whether the integration of this peak region was suitable for analysing the concentration of silica in the solutions.

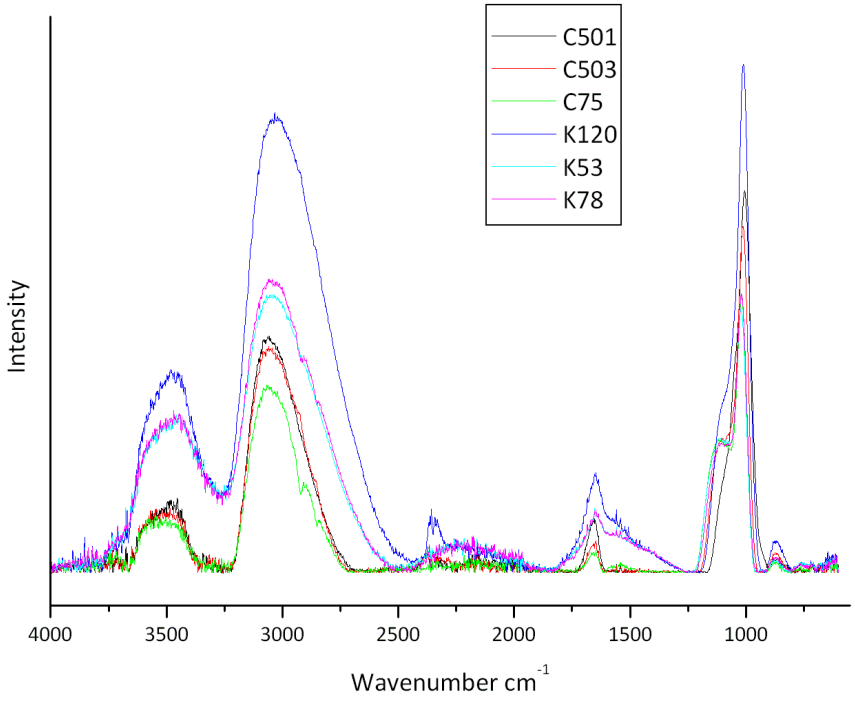

Figure 2.3 IR absorption spectra of commercial alkali silicates

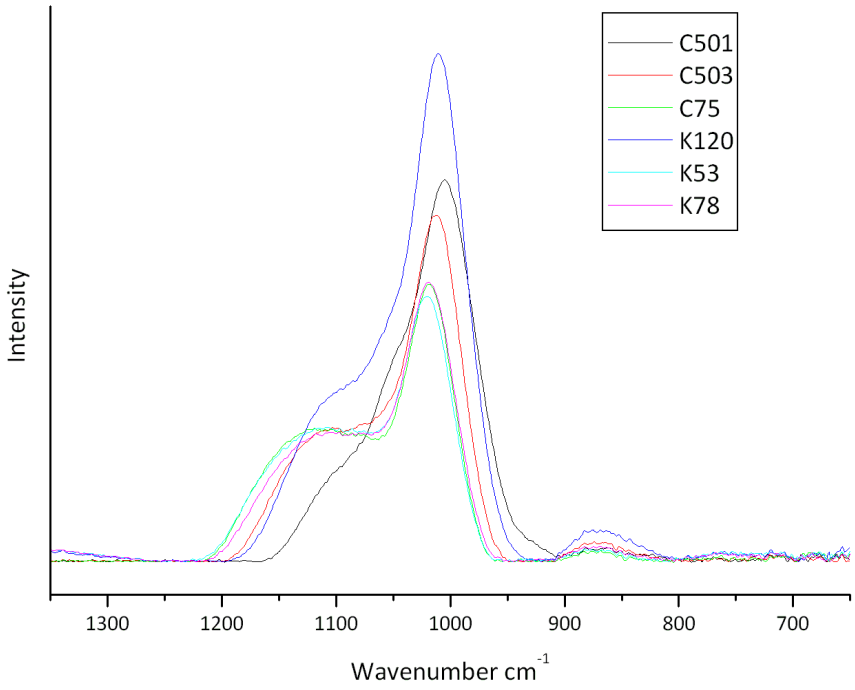

Figure 2.4 Silica region of IR absorption spectra of commercial alkali silicates

It is also important that the spectrum of an alkali silicate solution is not affected by dilution as this may affect the calibration. As can be seen from Figure 2.5 the spectrum remains unchanged for the commercial alkali silicate solution K120, on dilution the spectrum merely decreases in intensity. This was found to be the case for all commercial alkali silicate solutions tested.

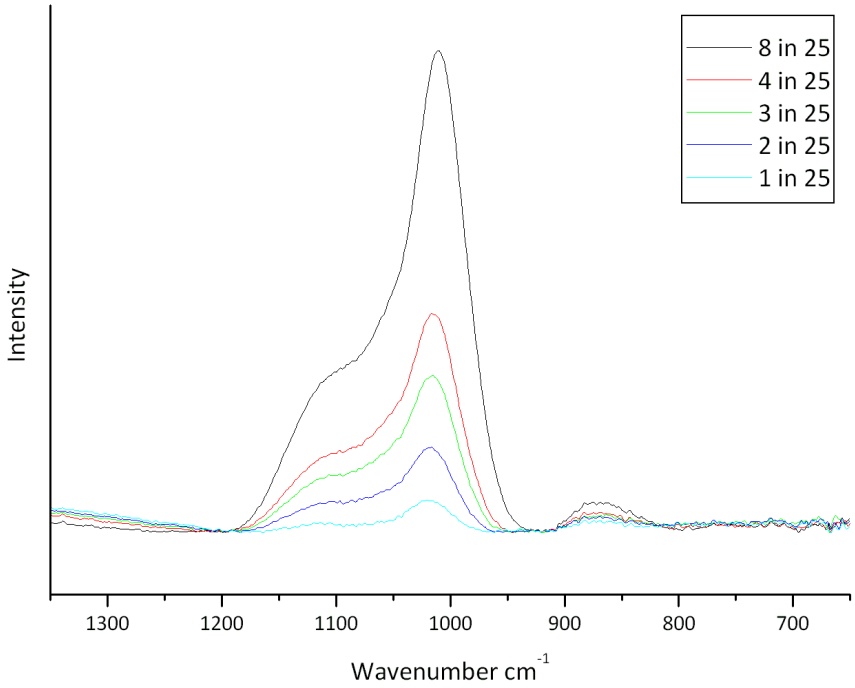

Figure 2.5 IR spectra of K120 Alkali Silicate Solutions at varied dilutions

The six commercial alkali silicate solutions were diluted to five separate concentrations and analysed (with further dilution) by Atomic Absorption Spectroscopy (AAS). The same solutions were then analysed using Fourier Transform Infrared Spectroscopy (FT-IR) based on the method by Falcone *et al.*[17] A water spectrum was subtracted from the sample spectra followed by a baseline correction to obtain consistency, then an integral of the spectra between 1250 and 650 cm^{-1} was taken. These two values (AAS and FT-IR integrals) were compared for the different dilutions in order to analyse the consistency of the FT-IR technique. Table 2.8 shows the values obtained for the silicon concentration of the commercial alkali silicate solution K120 at five different dilutions using AAS and the integral values of their silicate peaks using FT-IR. Figure 2.6 shows the correlation between these two values (R^2 = 0.9995).

Table 2.8 Concentrations (ppm) of the commercial potassium silicate solution 'K120' at different dilutions using AAS and FT-IR integral method

Dilution	Concentration of Silicon (AAS) ppm	FT-IR Integral Value
1 in 25	6765	1.507
2 in 25	13530	3.298
3 in 25	20295	5.593
4 in 25	27060	7.376
8 in 25	54120	15.574

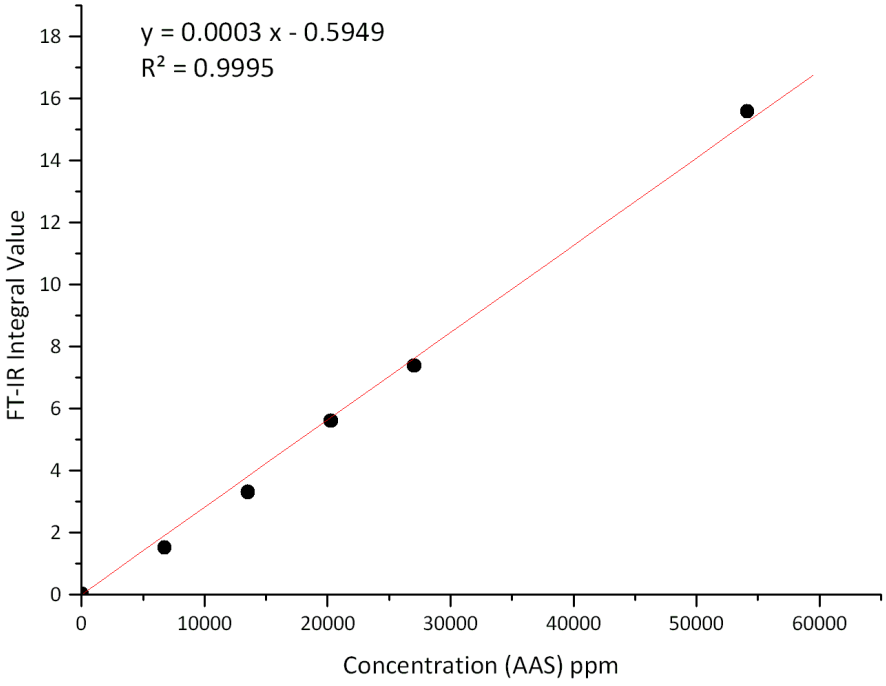

Figure 2.6 Graph comparing silicon concentrations derived from AAS with FT-IR integrals for K120 commercial alkali silicate solution at five different dilutions

As can be seen from Figure 2.7, this consistency remains when comparing all six commercial alkali silicate solutions. Each alkali silicate solution has a very specific linear correlation but these vary between the alkali silicate solutions as they have different alkali to silica ratios. The ratio affects the solution environment and an increased polarity of bonds leads to an increase in intensity. Therefore if an unknown alkali silicate solution was analysed using a calibration curve obtained from the average of all alkali silicate

solutions there would be a greater margin of error than if the commercial alkali silicate solution with the most closely resembling infrared spectrum was chosen and that calibration curve used.

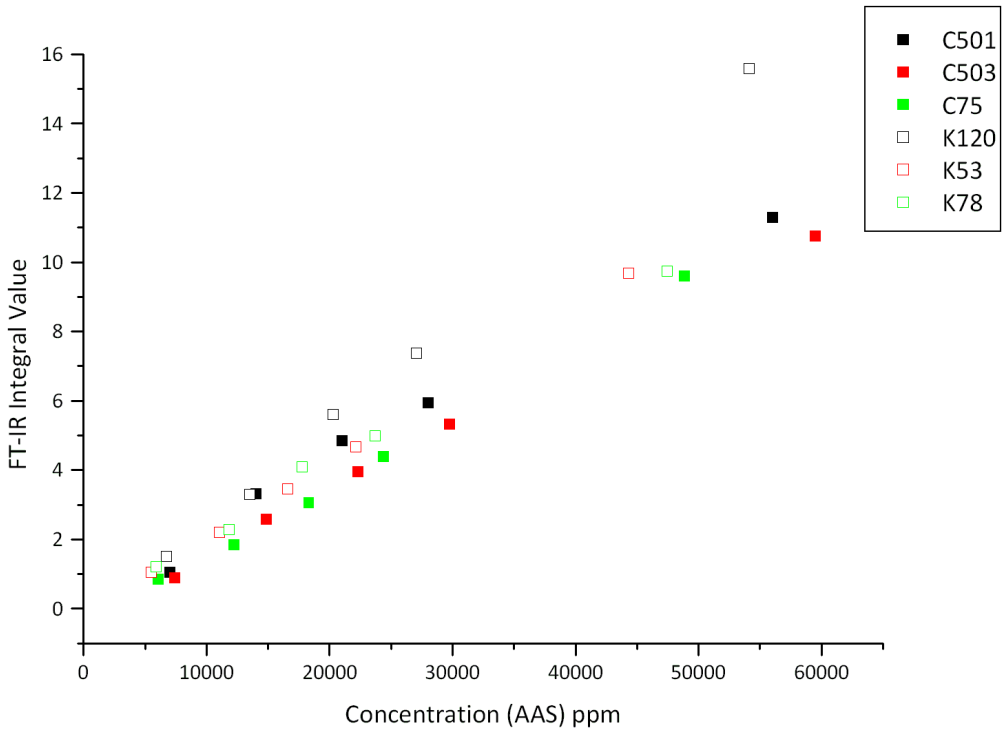

Figure 2.7 Graph comparing silicon concentrations derived from AAS with FT-IR integrals for 6 commercial alkali silicate solutions at five different dilutions

2.5.1 Bio-derived alkali silicate analysis

The technique described above was developed in order to have accurate silicon concentrations of unknown alkali silicate solutions. Below, in Figure 2.8, is the infrared spectra of the alkali silicate solution extracted from Ely Bottom Ash and the commercial alkali silicate solution K120. It is clear they are similar in shape and therefore an analysis using a calibration obtained from K120 can be assumed to be reasonably accurate. An integral was taken between 1250 and 650 cm^{-1} after a water spectrum subtraction and baseline correction. The integral was found to be 34.6849 and when using the calibration curve shown in Figure 2.6, the concentration of silicon was calculated to be 1.2 x 10^5 ppm. For comparison, the spectrum shown in Figure 2.9 for rice hull ash had a calculated concentration of 0.34 x 10^5 ppm.

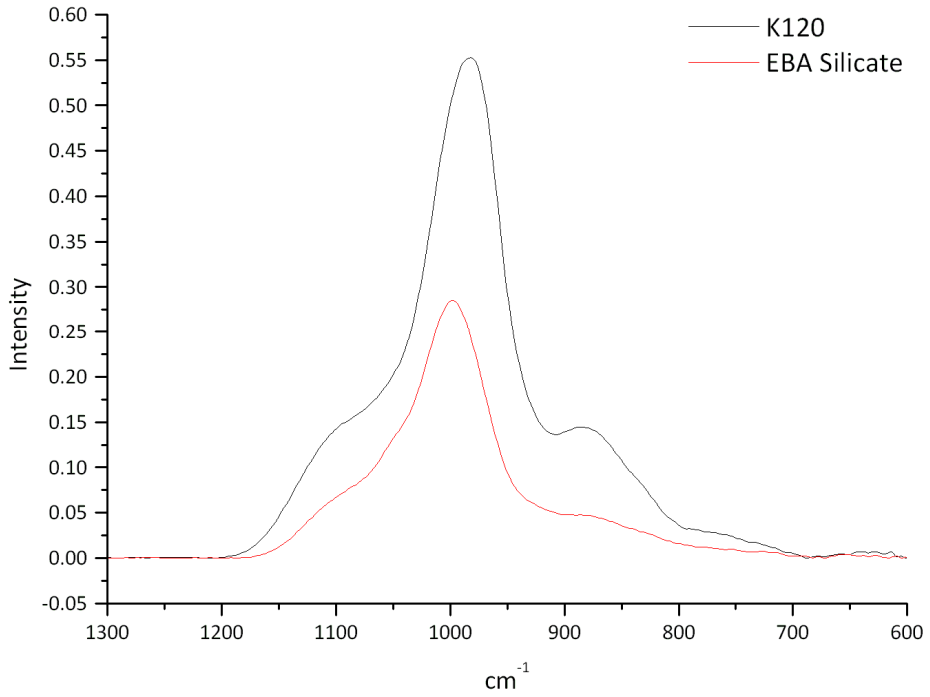

Figure 2.8 Silicate region of Infrared Spectra of commercial alkali silicate K120 (diluted) and bio-derived silicate EBA

The bio-derived alkali silicate derived from Rice Hull Ash has a pattern which is more difficult to match with the six commercial alkali silicate solutions. This is due to a much lower silica-to-alkali ratio which causes a shift to the main peak and other lower wavenumber peaks to appear. The sodium silicate solution C501 appears to most closely resemble it (Figure 2.9) and thus was used for the concentration calibration and calculations.

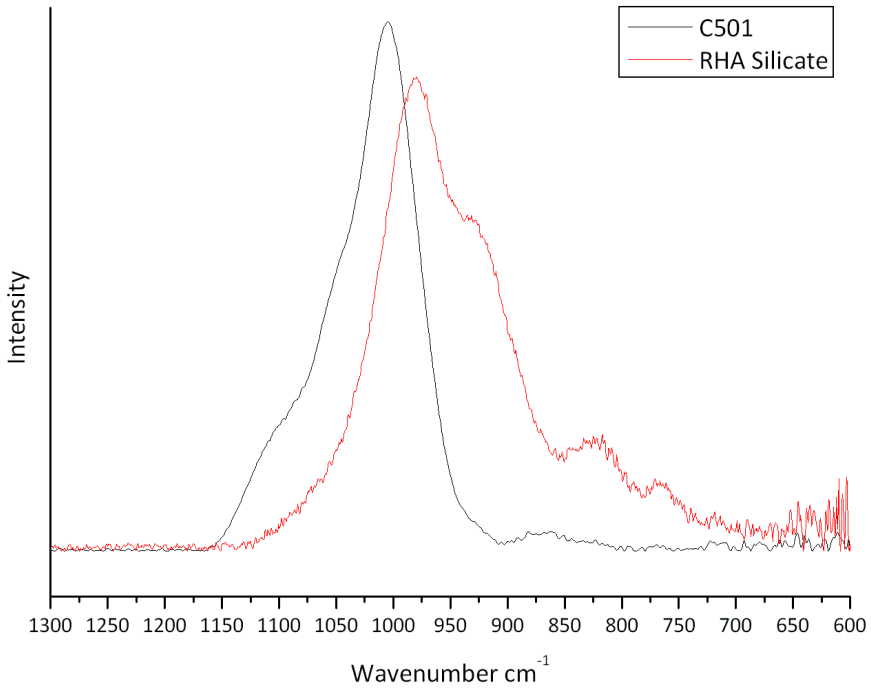

Figure 2.9 Silicate region of Infrared spectra of commercial alkali silicate C501 (diluted) and bio-derived alkali silicate derived from Rice Hull Ash

2.6 Alkali Silicates Used in Synthesis of Zeolites and Aluminosilicate materials

The alkali silicate solutions used in the following chapters are shown in Table 2.9 along with their silicon concentrations derived from their FT-IR peak integrals and their silica-to-alkali ratios obtained from XRF. Bio-derived alkali silicate solutions have much lower concentrations of silica and this is allowed for in the syntheses of zeolites and aluminosilicate materials in later chapters. They also have much lower silica-to-alkali ratio and this is due to the necessity of a strongly basic solution to extract the silica at low temperatures. The FT-IR integral technique correlates with the XRF concentrations reasonably well.

Table 2.9 Collated XRF, FT-IR Integral and PQ Corp data for alkali silicate solutions used in this project

	XRF			IR Integral	PQ Corp	
	SiO_2 ppm	M_2O ppm	SiO_2/M_2O	SiO_2 ppm	SiO_2 wt%	SiO_2/M_2O
EBA	0.9×10^5	1.6×10^5	0.56	1.2×10^5	-	-
RHA	0.44×10^5	1.6×10^5	0.27	0.34×10^5	-	-
C501	3.84×10^5	2.68×10^5	1.4	2.5×10^5	28.8	1.6
K120	3.83×10^5	2.39×10^5	1.6	2.7×10^5	20.8	1.43

2.7 Conclusion

The ashes obtained and used in this project have been analysed using various spectroscopic techniques and found to be high in silicon. In particular, the ashes RHA 95% and EBA were found to be extremely high in silicon and were chosen for extraction treatment. Methods of extraction of silicon into alkali silicate solutions from biomass ashes have been discussed, especially with respect to the comparison of microwave and conventional heating. Microwave heating was found to be more time and energy efficient but had issues with vessel strength so extraction using conventional heating mantle and oil bath was utilised for production of alkali silicates from ashes. This is the first step in the synthesis of aluminosilicate materials from biomass ashes described in the following chapters.

A method for obtaining reliable concentrations of silicon in alkali silicate solutions was described. This technique used the integrals from infrared peaks and commercial alkali silicate solutions for calibration. This method is consistent, quick and straightforward. This will be an important tool for designing the syntheses of materials described in this thesis.

3 Synthesis of Zeolites from Biomass Ashes

3.1 Choice of Zeolite

The initial aluminosilicate material chosen for synthesis was a microporous zeolite of the Faujasite family called Zeolite X. This material requires no template or high pressure in its synthesis and is used in high quantities for many applications as described in the Introduction Section 1.6.[27]

3.2 Synthesis of reference Zeolite

Initially Zeolite X was synthesised from commercial alkali silicate 'C501' in order to provide a standard for comparison with zeolites synthesised from bio-derived ashes. C501 sodium silicate solution was chosen as it most closely resembled RHA sodium silicate.

Zeolite X was synthesised according to the method described by the International Zeolite Association (IZA).[27] X-ray Diffraction (XRD) analysis of the material formed (Figure 3.1) indicates that the desired Zeolite X was synthesised using this procedure , matching that found in the literature well (Figure 3.2).[100] Zeolite X, formed 'conventionally' using a commercial alkali silicate solution has a silica to aluminium ratio of 7.5 and will be termed 'Conv-Zeo' throughout this chapter.

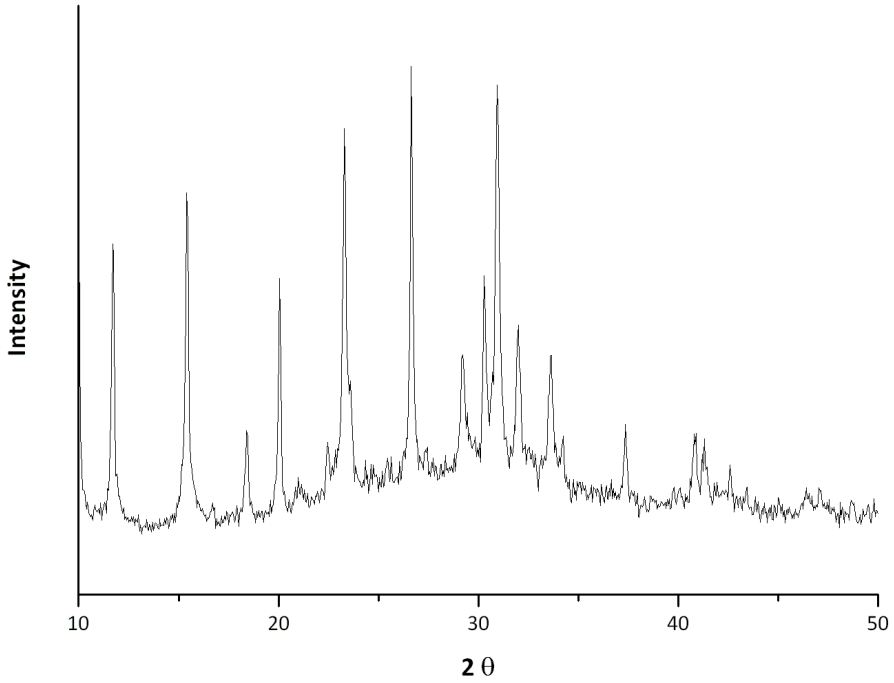

Figure 3.1 XRD pattern of Zeolite X ('Conv Zeo') using a 'C501' alkali silicate solution

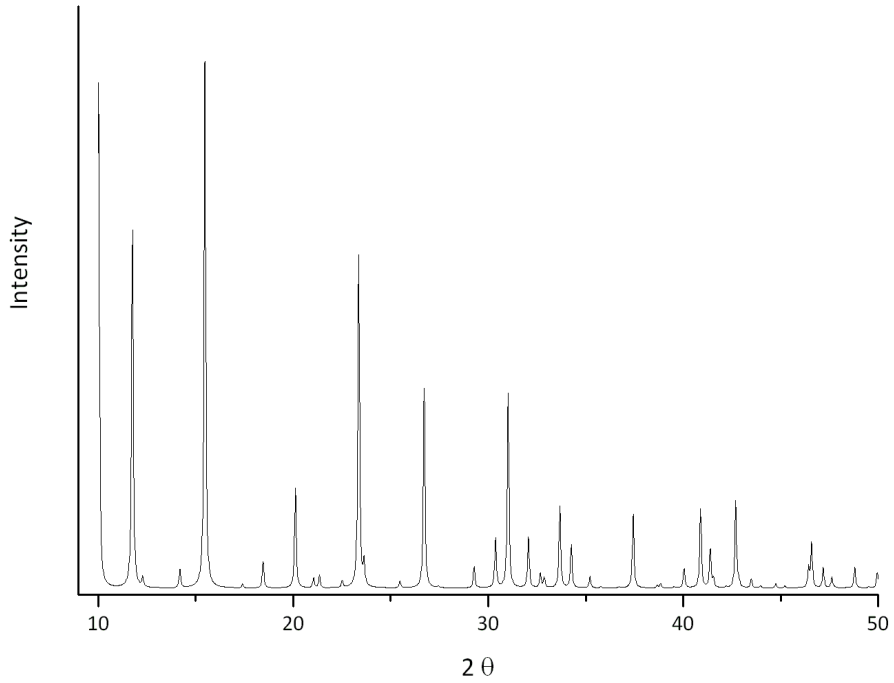

Figure 3.2 Reference XRD Pattern of Faujasite structure[100]

The Faujasite structure typically contains cavities 11 Å in diameter, connected via 12-membered rings with diameters of 7.4 Å.[25] Therefore the majority of porosity should be in the microporous range. The N_2 adsorption/desorption Isotherm for Conv-Zeo is comparable with that expected for an ordered microporous Faujasite Zeolite X (Figure 3.3).[101-102] The isotherm shows substantial adsorption of nitrogen at low relative pressure (vertical increase up to 170 cm^3g^{-1} beginning at $P/P_0=0$), confirming the presence of significant microporosity. There is some adsorption at higher relative pressure which relates to amorphous textural meso- and macro-porosity. The calculated BET surface area is 658 m^2g^{-1} and this is comparable to measurements in the literature (Table 3.1).[101-102]

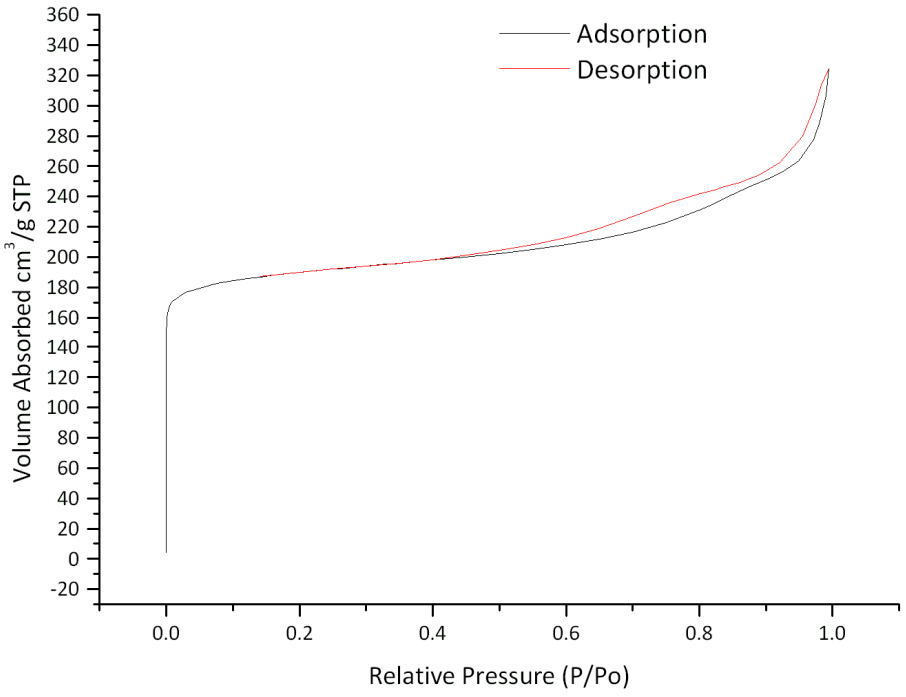

Figure 3.3 Adsorption desorption isotherm for Conv-Zeolite X

Table 3.1 Porosimetry data for Conv-Zeolite X and literature values for comparison

Sample	Surface Area (m^2g^{-1})
Conv-Zeo	658
Du & Wu[102]	565
Langmi *et al*[101]	662

3.3 Synthesis of Zeolites from Biomass Ash

The next stage was to attempt to synthesise Zeolite X from bio-derived alkali silicates derived from biomass ashes which, in this case, was rice hull ash (RHA) as it contained an extremely high silicon concentration (Chapter 2 Section 2.2.1). Samples synthesised from alkali silicate solutions extracted from these rice hull ashes are prefixed with RHA. The synthesis was optimised to produce a stable porous crystalline Zeolite X which is comparable with that synthesised from commercial alkali silicate.

3.3.1 Initial Synthesis of Zeolites from Biomass Ashes

Initially a synthesis was derived which assumed that all of the silica in the rice hull ash would be extracted from the ash as silicate and thus the recipe from the IZA would be directly transferrable. The very low surface area (8 m^2g^{-1}) and porosity found for the material formed following extraction, crystallisation and calcination (Figure 3.4) implies that a large majority of the precipitate did not crystallise into the microporous structure required for Zeolite X. XRD analysis (Figure 3.5) identified the only crystalline phase as sodalite. A reference XRD pattern for Sodalite is shown and all peaks match except that they appear to be shifted to slightly higher 2θ values which could be due to a slightly smaller unit cell. Sodalite is an ordered microporous aluminosilicate material but does not display a large N_2 adsorption BET surface area here or in the literature.[103] Sodalite has a six membered ring with a pore size of 2.8 Å and N_2 has a Van Der Waals radius of up to 1.7 Å therefore nitrogen molecules should be able to enter the pores.[25, 104] The fact that they don't to the extent that barely any adsorption is registered could be due to the cations blocking the pores or other kinetic issues preventing the N_2 entering the pores quickly enough for equilibration in the porosimeter. Since the product showed little porosity and the crystalline material formed was sodalite it was clear that the synthesis needed to be optimised to encourage the crystallisation of Zeolite X. Sodalite cages can go on to form the Faujasite structure but this involved further crystallisation.[25] Sodalite forms more readily than Zeolite X so the method of synthesis methodology needed improvement to complete the crystallisation process to form the desired product.

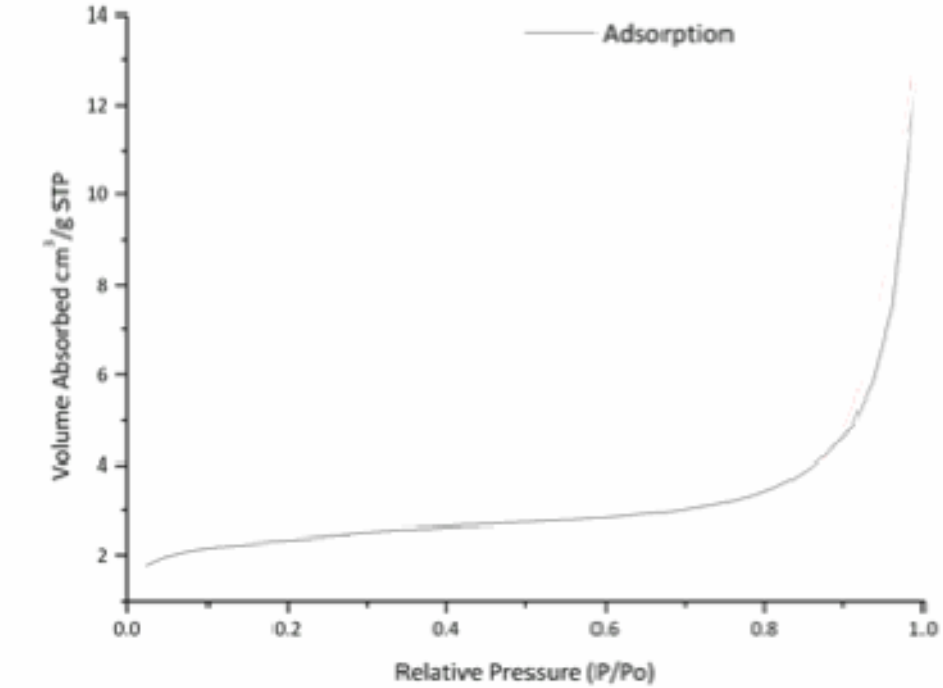

Figure 3.4 N_2 Adsorption Isotherm of initial RHA-Zeolite

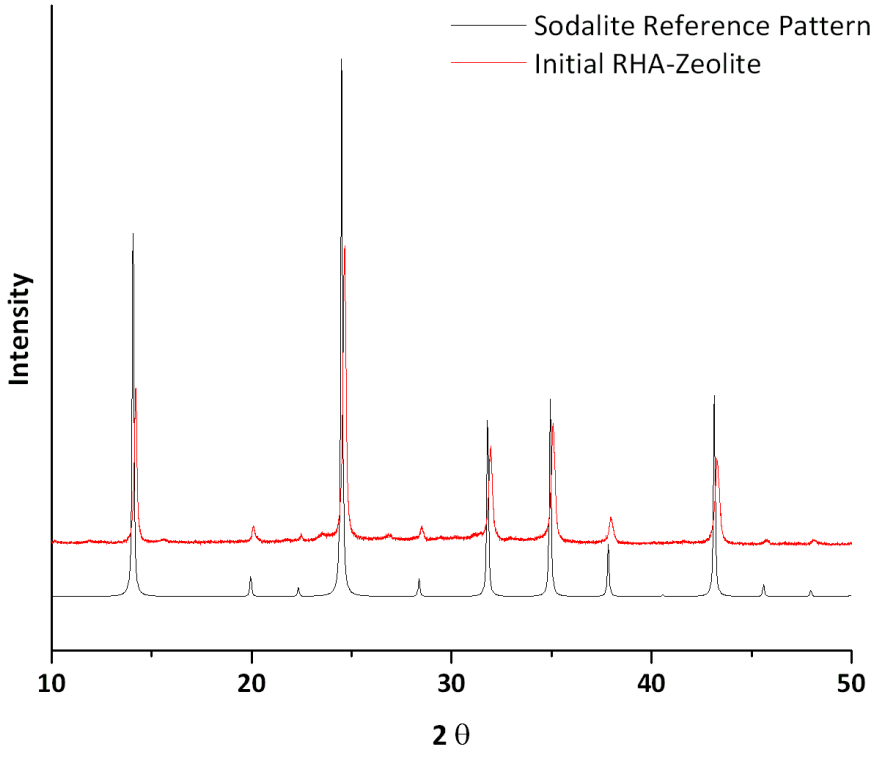

Figure 3.5 XRD pattern of initial RHA Zeolite and sodalite reference spectra [105-106]

3.3.2 Synthesis of RHA Zeolites with Different Si/Al ratios

The first variable tested in the optimisation of the synthesis conditions was the ratio of silicon to aluminium. This was calculated from assumptions about the silica extraction yield as described in Chapter 2. The BET surface areas found via N_2(g) adsorption porosimetry measurements for these products showed very low surface areas in comparison with Conv-Zeo but higher than the initial synthesis (Table 3.2). The adsorption isotherm for the zeolite synthesised with a Si/Al ratio of 6.3 shows there has been very little adsorption in the micropore range. Although a greater quantity of N_2(g) is adsorbed, this is due to textural porosity and not to ordered zeolitic micropores as it occurs at much higher relative pressures and over a large range. This isotherm is typical of the other materials synthesised in this experiment.

Table 3.2 Porosimetry results for RHA alkali silicate derived zeolites with different Si:Al

Si/Al	Surface Area m^2g^{-1}
6.3	34
3	50
1.7	45
1.2	17
0.9	9

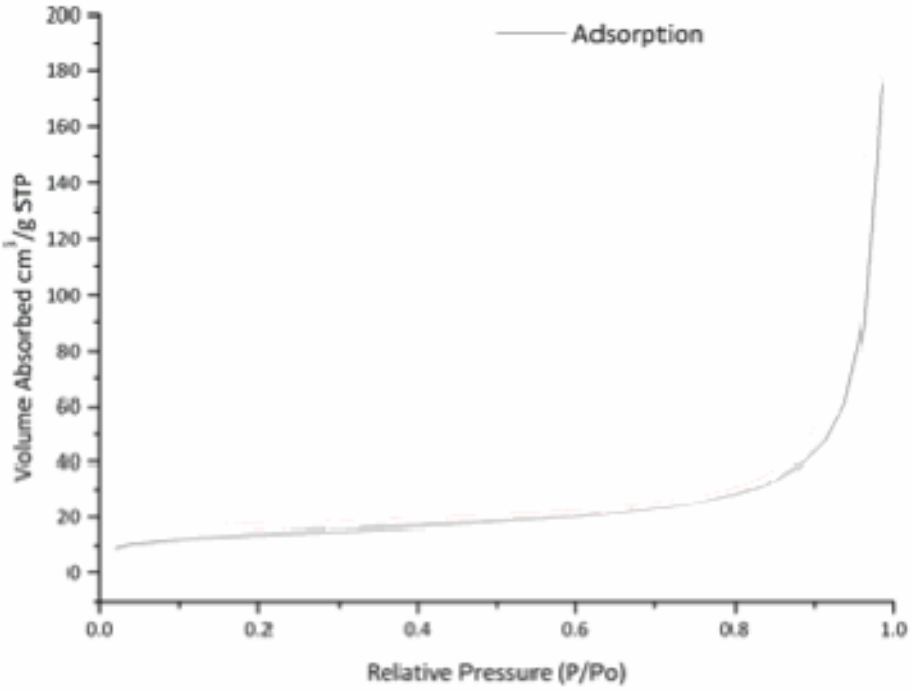

Figure 3.6 N_2 Adsorption Isotherm for RHA-Zeolite with a Si:Al ratio of 6.3

XRD patterns for the synthesised materials show the presence of both Zeolite X and sodalite (Figure 3.7). All of the patterns display mostly the same peaks which can be attributed to sodalite and X but at different intensities. The materials that have XRD patterns which are most clearly defined are those with the lowest Si/Al ratios. This is because these materials are composed primarily of sodalite which crystallises under all Si/Al ratios greater than 1.[25] As the ratio increases to 6.3, and becomes more in the range where Zeolite X can crystallise, the Zeolite X pattern begins to appear more prominently but this effect appears to coincide with a decrease in overall peak intensity. The materials with Si/Al of 6.3 and 3 had the highest surface areas but since all materials had surface areas lower than 50 m^2g^{-1} it would be difficult to draw conclusions on the level of porosity achieved for the different ratios of silicon to aluminium.

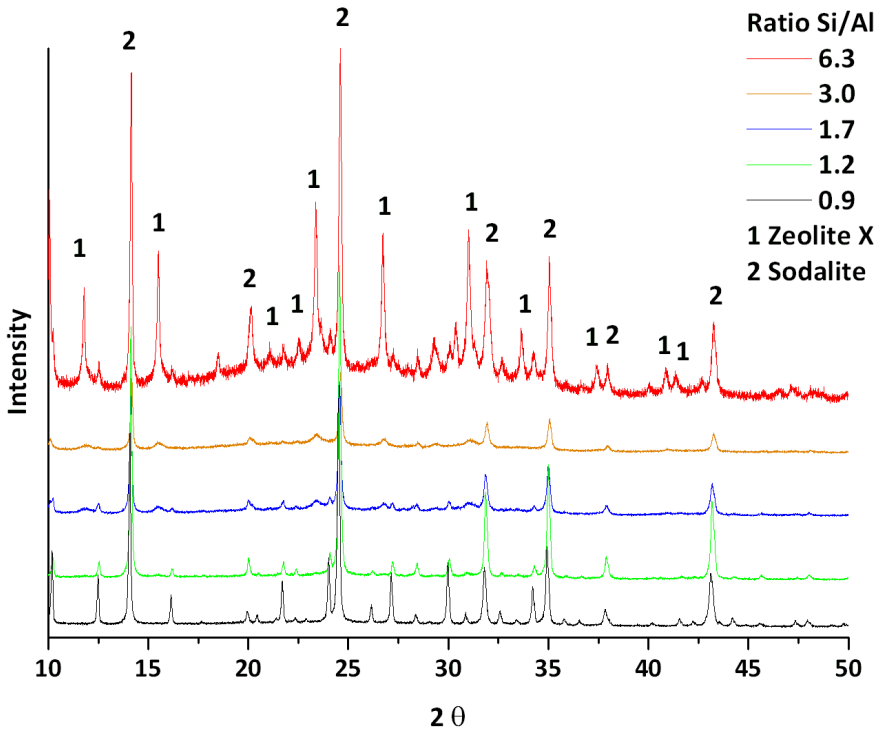

Figure 3.7 XRD Patterns for RHA alkali silicate derived zeolites with varied ratios of silica to aluminium with peaks labelled using reference patterns for Zeolite X and Sodalite[106]

3.3.3 Synthesis of RHA Zeolites with Further Different Si/Al ratios

Zeolites with lower aluminium content from the previous experiment showed highest crystallinity and porosity, and therefore higher silica to aluminium ratios were investigated in the zeolite synthesis. Surface areas of over 100 m^2g^{-1} were obtained for the samples with Si/Al of 3.6 and 4.6 (Table 3.3). The adsorption isotherm for the zeolite with a Si/Al of 3.6 is shown in Figure 3.8 and shows some absorption at low relative pressure which relates to some microporous structure as well as the textural surface area which appears at higher relative pressures. Calcination at 600 ˚C appears to have collapsed some of the structure as the surface area values have halved after this treatment. This implies the crystalline structures which have synthesised have not been thermally stable enough to withstand these temperatures.

Table 3.3 Porosimetry results for RHA alkali silicate derived zeolites with further varied Si:Al

Si/Al	Calcined at:	Surface Area m^2g^{-1}
2.7	150 ˚C	66
3.6	150 ˚C	113
4.6	150 ˚C	111
5.6	150 ˚C	85
6.6	150 ˚C	55
2.7	600 ˚C	28
3.6	600 ˚C	33
4.6	600 ˚C	43
5.6	600 ˚C	46
6.6	600 ˚C	46

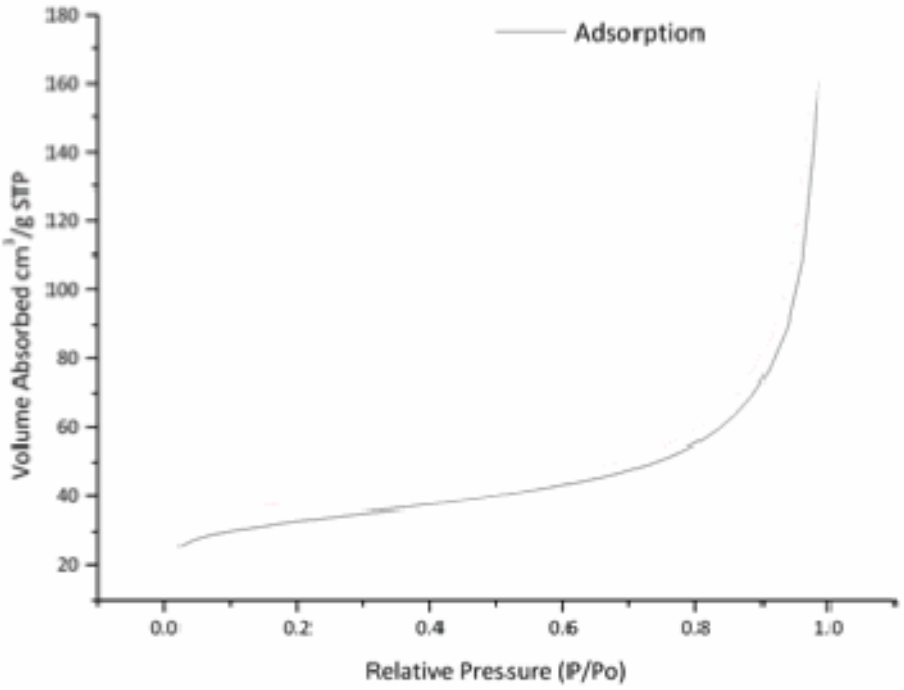

Figure 3.8 N_2 Adsorption Isotherm for RHA-Zeolite with Si/Al of 3.6

These samples also showed evidence of crystallinity in their XRD patterns and these matched those of a mixture of Zeolite X and Sodalite (Figure 3.9). Figure 3.10 shows the XRD patterns of the RHA-Zeolite (Si/Al = 3.6) before and after calcination. The patterns are almost identical except for a slight shift to lower 2θ on calcinations. This relates to an enlargement of the unit cell on heat treatment. Zeolites such as X crystallize in a narrow Si/Al atomic ratio range whereas Sodalite is the only material known to crystallize over

the full compositional range Si/Al = 1 to infinity.[25] Therefore it is to be expected that Sodalite will appear at Si/Al compositions which fall out of the standard X range. As this is a new silica source the range may be different and has to be found experimentally.

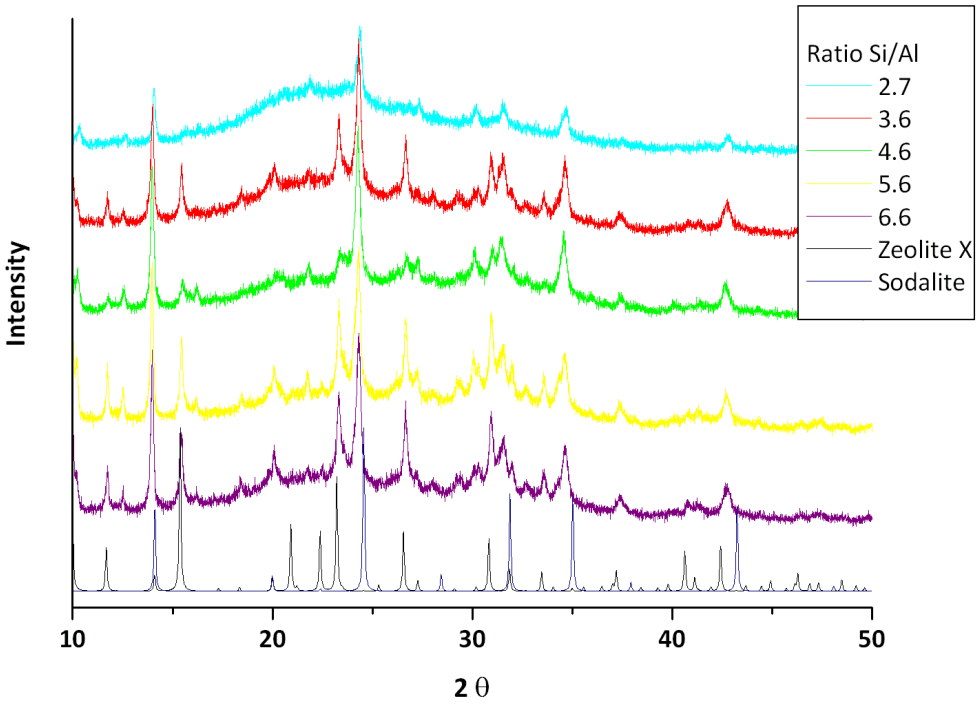

Figure 3.9 XRD Patterns for RHA alkali silicate derived zeolites with further varied ratios of silica to aluminium

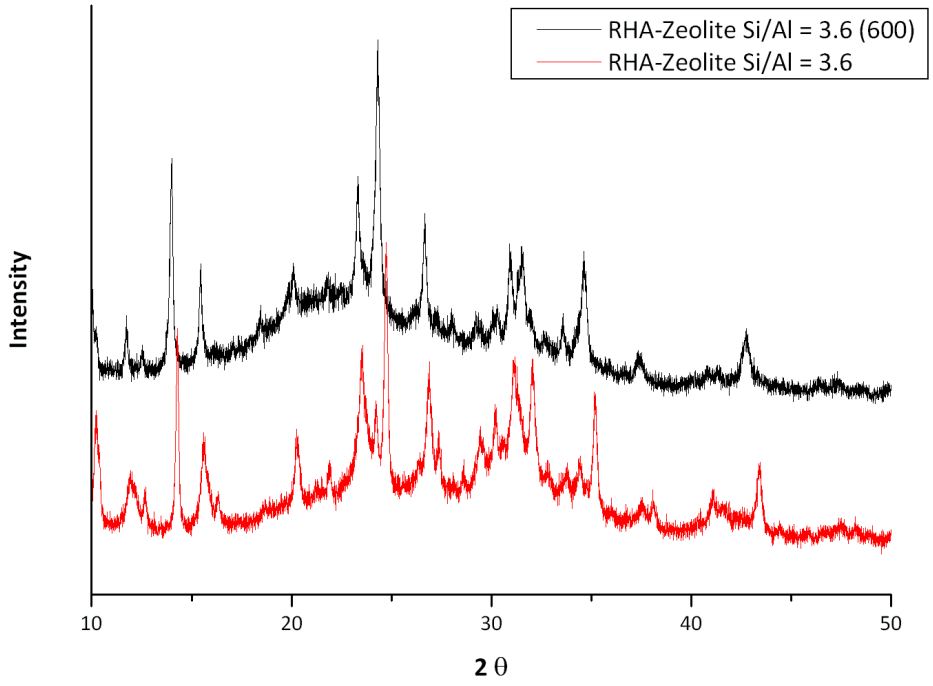

Figure 3.10 XRD Patterns for RHA-Zeolite (Si/Al = 3.6) before and after calcinations at 600 ˚C

3.3.4 Investigation into methods of cooling

The effect of cooling and filtration was investigated to explore the potential effect on the kinetics of crystallisation of the different phases which precipitated from the solution. This was done by taking RHA-Zeolite (Si/Al = 4.6) samples after the synthesis and subjecting them to either rapid cooling followed by filtration, hot filtration, or slow cooling in the oil bath used for crystallisation. All samples had much higher porosity (

Table 3.4) than previous measurements and high crystallinity, again of a mix of Zeolite X and Sodalite structures (Figure 3.12). There did not seem to be an effect on the materials synthesised by these changes in synthesis technique. The N_2 adsorption isotherm for RHA-Zeolite (filtered hot) shows some adsorption at higher relative pressure but this is in the textural porosity region and does not provide information on the microporosity which is shown in the high adsorption of N_2 at low relative pressure.

Part of the increase in porosity and crystallinity of the materials synthesised can be attributed to increased familiarity with the laboratory procedures and analysis techniques.

Table 3.4 Porosimetry results for RHA alkali silicate derived zeolites after different methods of cooling

Process after crystallisation	Surface Area m^2g^{-1}
Ice bath	82.6
Filter hot	147
Let cool slowly then filter	123

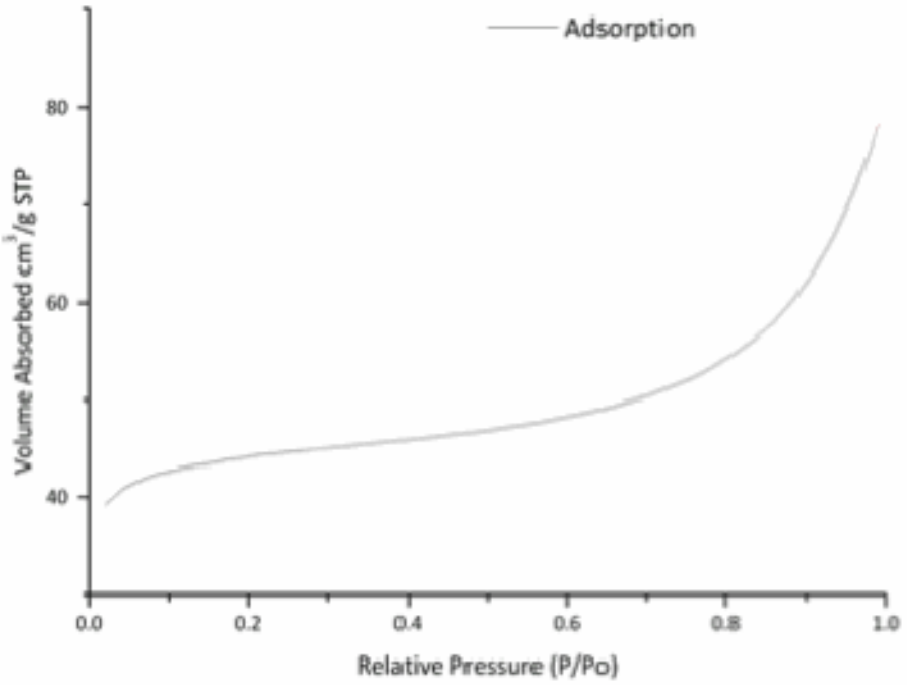

Figure 3.11 Adsorption Isotherm for RHA-Zeolite (filtered hot)

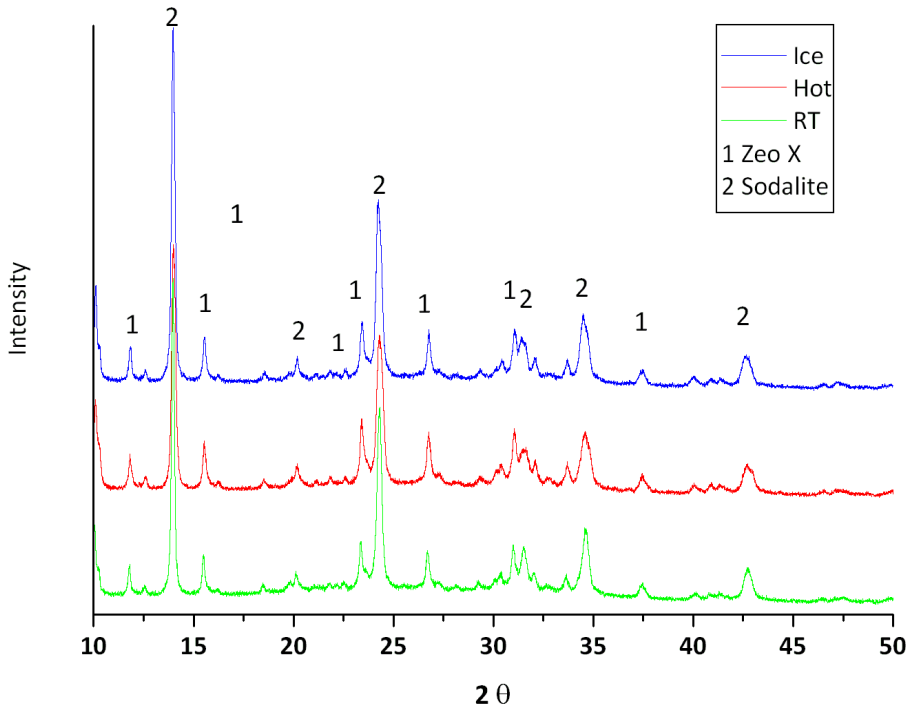

Figure 3.12 XRD Patterns for RHA-Zeolite (Si/Al = 4.6) after different methods of cooling

The RHA-Zeolite synthesised with a Si/Al of 4.6 and filtered hot produced the highest porosity and surface area, and similar high crystallinity to the other materials. It was also the easiest and quickest method for filtration. Therefore it was chosen for in-depth comparison with a conventionally synthesised zeolite using *in situ* Fourier Transform Infrared (FT-IR) analysis. The Si/Al of 3.6 zeolite also shared these physical properties but this synthesis used more aluminium with no obvious gain and in order to make the synthesis as efficient as possible the ratio with the lower aluminium content was chosen. For the following work, Conv-Zeolite will refer to the conventionally synthesised Zeolite X and RHA-Zeolite will refer to the RHA-Zeolite as described above. Some results have been repeated with a further material 'RHA-Zeolite (lower Al)' which was synthesised as with RHA-Zeolite but with a calculated ratio of 9.0. This material was synthesised to further investigate the cause of the properties found for RHA-Zeolite with Si/Al = 4.6.

3.4 Optimised RHA-Zeolite Synthesis and comparison with Conv-Zeolite

The comparison of RHA-Zeolite and Conv-Zeolite is important if bio-derived alkali silicates are going to be accepted more generally for the synthesis of microporous aluminosilicate materials. Materials synthesised from bio-derived alkali silicates must be shown to have comparable properties to prove the synthesis is robust and that the bio-derived element of the starting material does not negatively influence the final product. This comparison was conducted using various techniques including; X-Ray Diffraction to provide information on the crystalline composition of the materials, XRF and XPS to provide information on the elemental composition, N_2 Adsorption porosimetry for porosity and surface area information, NMR spectroscopy for information on the location and bonding of silica and aluminium within the structure, TGA-IR for information on the thermal decomposition of the materials, and In-Situ infrared spectroscopic analysis with CO and CO_2 gas dosing in order to provide information on the surface groups and their acidity and basicity.

3.4.1 XRF

XRF analysis showed the materials which were both mainly composed of sodium, silicon, and aluminium but there were differences in amounts of their trace elements (Table 3.5). All three samples contained small amounts of potassium, calcium, and iron. Conv-Zeolite contained much less potassium than the two RHA derived zeolites. RHA-Zeolite had a higher concentration of calcium than the other two materials. This presence of calcium and potassium could mean a presence of corresponding carbonate in the materials. Although the elemental composition appears to be similar the structures formed are significantly different as shown by X-Ray Diffraction below (Section 0).

Table 3.5 XRF % elemental composition of RHA-Zeolite and Conv-Zeolite and RHA-Zeolite(Lower Al)

	Conv-Zeo	RHA-Zeolite (Lower Al)	RHA-Zeolite
Na_2O	16.20	19.30	11.70
K_2O	0.01	0.13	0.09
CaO	0.01	0.01	0.04
Fe_2O_3	0.04	0.03	0.02
Al_2O_3	23.30	24.20	16.20
SiO_2	30.60	28.80	20.19

Calculated and observed ratios of silicon to aluminium are shown in Table 3.6 and it is clear that the assumed amount of silica from the synthesis mixture was highly overestimated. The ratios of Conv-Zeolite, RHA-Zeolite, and RHA-Zeolite (Lower Al) are all seemingly comparable from XRF data.

Table 3.6 Si/Al ratio Conv-Zeolite, RHA-Zeolite, and RHA-Zeolite (lower Al) from XRF elemental analysis and calculated using values from the synthesis mixtures

	Si/Al	
	Calculated	XRF
Conv-Zeolite	7.5	1.15
RHA-Zeolite	3.7	1.1
RHA-Zeolite (Lower Al)	9	1.05

3.4.2 XPS

XPS analysis showed a composition of oxygen, sodium, silicon, and aluminium as the major elements on the surface of both samples which agrees with the XRF analysis (Table 3.7). Since the XRF analysis cannot detect carbon, it is useful to note from XPS data on the surface of the materials there is a significant presence of carbon. This is most likely to be atmospheric CO_2 which has bonded to the surface as carbonate. There was no signal detected using this technique for the other trace elements detected using XRF such as potassium or calcium. Therefore the trace elements must be located within the framework structure and are not on or near the surface of the materials. There appears to be a higher relative concentration of sodium on the surface in relation to silicon and aluminium than in the bulk of the material for both samples. Surface Si/Al ratios are 1.18 for RHA-Zeolite and 1.2 for Conv-Zeolite.

Table 3.7 XPS % surface elemental composition of RHA-Zeolite and Conv-Zeolite

	O	C	Na	Si	Al
RHA-Zeolite	**49.59**	**17.5**	**10.92**	**11.91**	**10.08**
Conv-Zeolite	**44.11**	**26.5**	**10.39**	**10.36**	**8.64**

3.4.3 X-Ray Diffraction

From the XRD patterns it is clear the synthesised Conv-Zeolite material has a lot of the same peaks as the RHA-Zeolite. All of the main peaks can be attributed to either the Faujasite pattern or the Sodalite pattern but Conv-Zeolite only contains the Faujasite peaks. Thus both materials contain the crystalline phase of Faujasite but RHA-Zeolite also contains sodalite. The pattern for RHA-Zeolite (lower Al) also shares peaks with Conv-Zeolite but there is significant noise in the pattern. RHA-Zeolite (lower Al) exhibits no sign of the sodalite crystalline phase and therefore must have a composition which falls more within the range for Faujasite crystallisation.

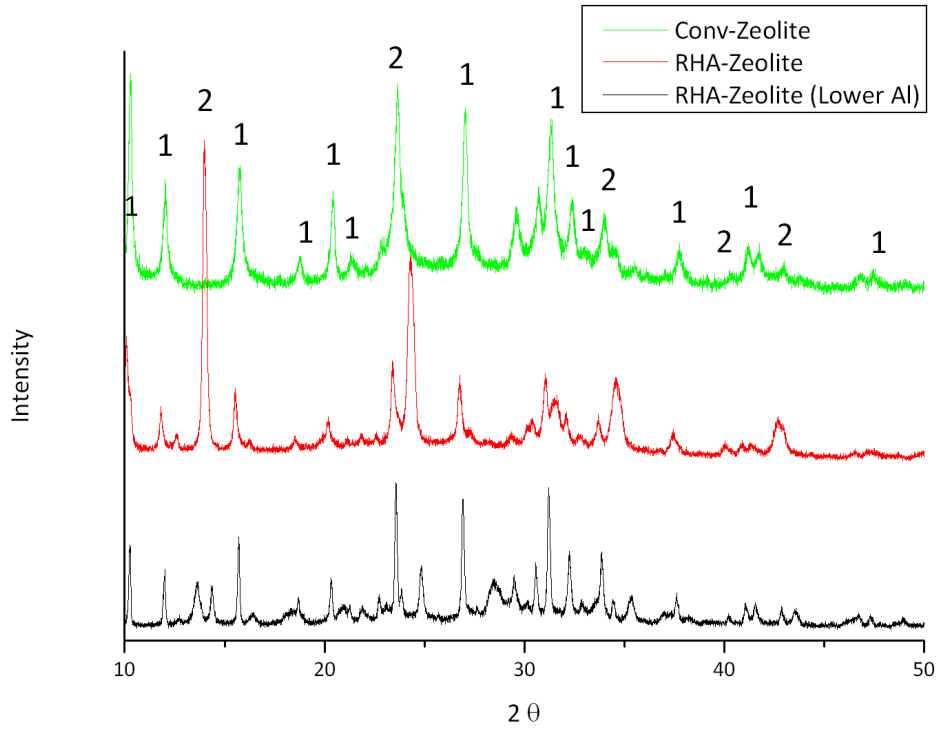

Figure 3.13 XRD Patterns of RHA-Zeolite and Conv-Zeolite with labelling of 1 (Faujasite) and 2 (Sodalite) peaks

Since Sodalite cages form part of the Faujasite structure this means the RHA-Zeolite is crystallising into the building blocks for the Faujasite structure from the silicate but the process is not continuing to form the larger more complex final structure.[25] This could be due to an incorrect amount of aluminium being added to the synthesis and therefore forcing the ratio outside of the range within which Zeolite X forms. According to the IZA, Zeolite X crystallises within the Si/Al range 1.4 – 5 but this also depends on the concentration of NaOH in the solution.[27]

Alternatively there may be an issue with the presence of impurities from the ash derived alkali silicate solution preventing the sodalite blocks from fusing together correctly. The Conv-Zeolite sample contained only the Faujasite pattern and thus any crystalline element in the sample is pure Faujasite. Thus the conventional synthesis is confirmed as effective for commercial alkali silicates and shows promise for synthesis from RHA derived alkali silicate.

3.4.4 N_2 Adsorption Porosimetry

Nitrogen adsorption analyses (Table 3.8) showed the RHA-Zeolite sample has a surface area of 149 m^2g^{-1} and this is significantly lower than that of the Conv-Zeolite result at 406 m^2g^{-1}. This implies that there are materials within the RHA-Zeolite sample which are amorphous and have no surface area and/or that some of the porosity in the RHA-Zeolite sample is inaccessible to the N_2 molecules. This inaccessibility could be due to the high concentration of the sodalite phase (XRD patterns, Section 0) which has very small pores and/or the presence of carbonate within the pores which is explored in more detail in Section 3.4.7. Faujasite is made up of sodalite cages forming together to form larger pores and this porosity is what adsorbs the majority of the N_2(g) in the Conv-Zeolite sample. RHA-Zeolite (lower aluminium) registered a surface area of 0.65 m^2g^{-1} which is likely to be due to pore blocking with carbonate and water.

Table 3.8 Porosimetry data for Zeolite X synthesised from Rice Hull Ash Alkali Silicate and Commercial Alkali Silicate

	Surface Area
Sample	**m^2g^{-1}**
Conv-Zeolite	**591**
RHA-Zeolite	**168**
RHA-Zeolite (lower Al)	**0.65**

3.4.5 NMR

Aluminium NMR spectra (Figure 3.14) for Conv-Zeolite, RHA-Zeolite, and RHA-Zeolite (Lower Al) showed one major peak at 60 ppm attributable to framework tetrahedral aluminium and a weak spinning sideband manifold associated with this species.[107] This result implies all aluminium was taken into the structure as there is no evidence that extra-framework 6-coordinate aluminium species have precipitated.

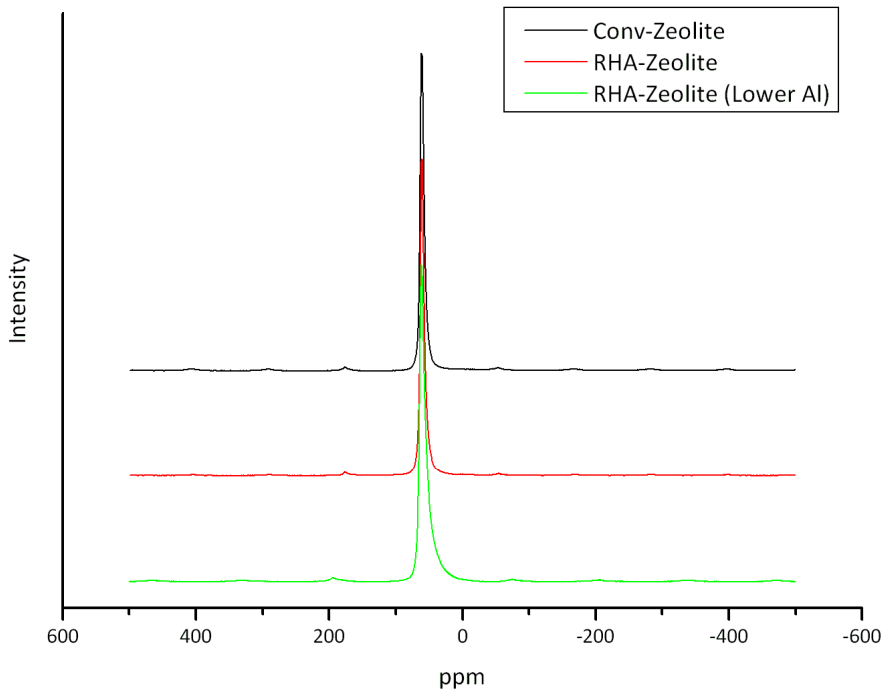

Figure 3.14 Aluminium NMR traces for Conv-Zeolite, RHA-Zeolite, and RHA-Zeolite (Lower Al)

3.4.6 Thermogravimetric analysis with infrared absorption spectroscopy (TGA-IR)

Thermogravimetric analysis with infrared absorption spectroscopy of the exit gases (TGA-IR analysis) (Figure 3.15) was performed on RHA-Zeolite in order to examine what non-zeolitic materials were present. The thermal treatment went up to a temperature of 1000 ˚C and showed a weight loss of 12.2%. No main components of the solid were shown (by infrared spectroscopy) to be lost during the analysis in the exit gases. It is likely that between 100 ˚C and 300 ˚C the majority of mass loss was water and this can be seen in the infrared spectra of the exit gases. It can be seen from infrared spectra (Figure 3.16) taken before and after the thermal analysis that there was a loss of water/hydroxyl groups in the range 3700-2900 cm^{-1} and the loss of a low intensity peak at 657 cm^{-1} which was attributed to an OH bending vibration by Komadel *et al.*[108-109] There is also a band associated with carbonate (at 1645 cm^{-1} and 1445 cm^{-1}) which disappeared following thermal treatment. Since there is no sign of a significant mass loss it can be assumed that this carbonate is lost as a small concentration of CO_2(g) over a wide range of temperatures and this is corroborated by the presence of CO_2(g) in the infrared spectra of

the exit gases (Figure 3.17). The presence of strongly bonded carbonate which decomposes over the temperature region up to 1000 ˚C could affect recorded porosity for the RHA-Zeolite and may explain other properties noted in the *in situ* FT-IR work below. The overall effect of the thermal treatment on the material was shown to be dehydration and dehydroxylation as well as the loss of carbonate. This carbonate may have come from K_2CO_3 or Na_2CO_3 absorbed from the RHA derived alkali silicate solution.

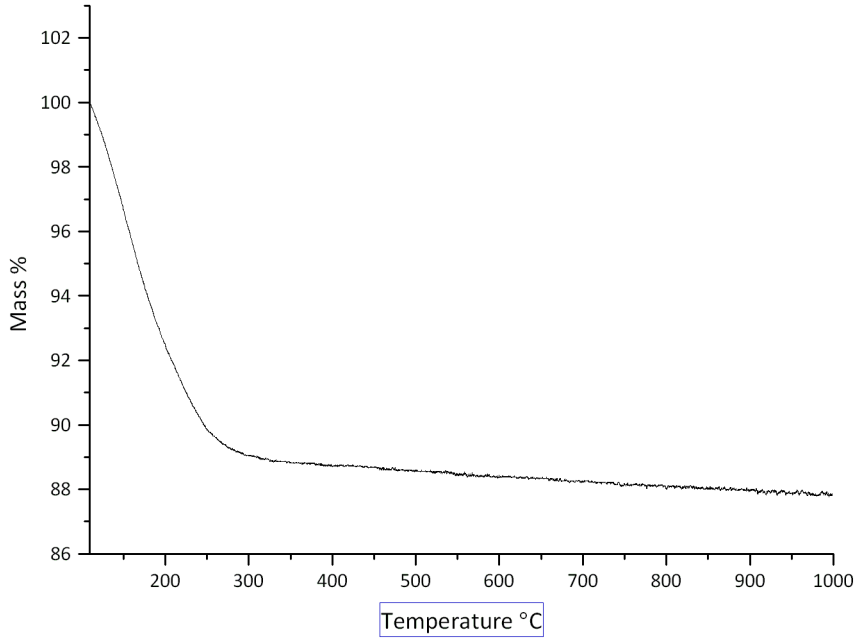

Figure 3.15 Thermogravimetric graph showing mass loss over time and with increasing temperature

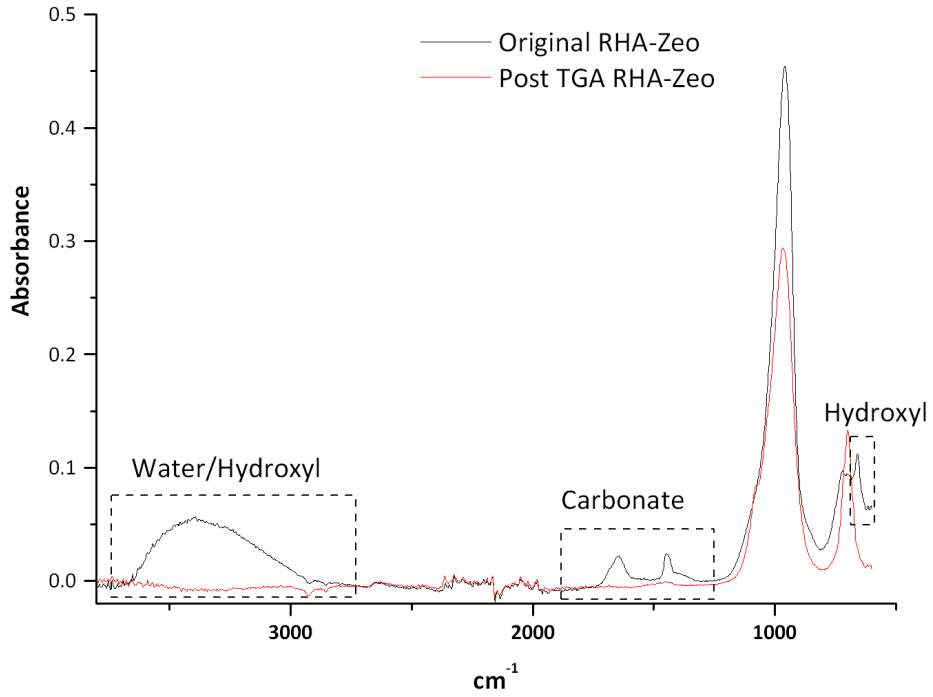

Figure 3.16 Infrared spectra for RHA-Zeolite before and after Thermogravimetric Analysis

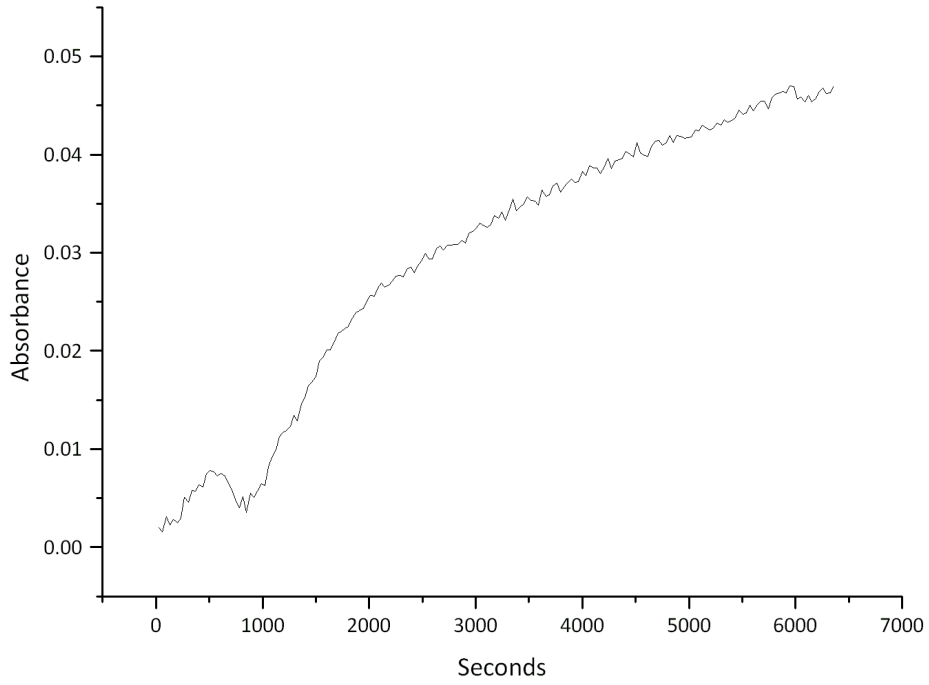

Figure 3.17 Graph showing increase in absorbance at 2350 cm^{-1} which corresponds to concentration of CO_2(g) in the exit gases of the thermogravimetric analysis

3.4.7 *In Situ FT*-IR Probing Using Small Molecules

Another technique which could shed light on the differences and similarities of the two zeolites prepared from commercial alkali silicate and bio-derived alkali silicate is *in situ* Fourier Transform-Infrared (FT-IR) spectroscopy. This technique explores functional groups on the surface and uses the interactions with dosed gas molecules to further study the activity of these surface functional groups. The dosing with carbon monoxide (CO) and carbon dioxide (CO_2) can provide information on the basicity and acidity of the surface respectively which is important in order to investigate applications of these materials. The method consists of a process which enables infrared spectroscopy of a sample under vacuum and after heat treatments. A sample is pressed into a disc and transferred to a sealed glass vessel which is then subjected to heat treatments under vacuum in order to eradicate any adsorbed molecules from the surface. A high-resolution infrared spectrum can then be taken of the surface in its simplest state. Different probe gases can then be dosed into the vessel at increasing pressures using a sealed glassware

setup and a number of taps. This happens *in situ* of the infrared spectrometer and spectra are taken throughout the process. This process occurs in order to study the effect on the surface of the increasing interactions with the molecule. The partial pressures of the probe gas can then be decreased using a vacuum and the resultant effects studied. For the materials in this project, heat treatments of up to 500 ˚C and studies using CO and CO_2 were conducted.

Visible from the *in situ* Infrared spectra of the RHA-Zeolite X, after heat treatment at 500 ˚C under vacuum (Figure 3.18 and Figure 3.19), are hydroxyl groups on silicon and aluminium, water, and carbonate. It is notable that the carbonate band (1500 – 1350 cm^{-1}) is still present after the 500 ˚C thermal treatment as this signifies that this impurity is strongly bonded to the material or very thermally stable. The carbonate band is singular implying the species is symmetric. Asymmetric carbonate is discussed later in the chapter in the *In Situ* dosing of CO_2 Section 3.4.7.2. The continued presence of carbonate complements observations from the TG-IR data and implies the decomposition of the carbonate to CO_2(g) continues to occur at temperatures above 500 ˚C and up to 1000 ˚C. The high concentration of stable non-crystalline carbonate in the pores could explain the lower surface area and porosity measurements observed from N_2 adsorption porosimetry. This carbonate is likely to be in the form $CaCO_3$ as there was a presence of calcium found using XRF analysis in the bulk solid of RHA-Zeolite and in the rice hull ash. Most water/hydroxyls are lost from the surface after thermal treatment although some still remain and this is shown in the decrease in intensity but not extinction of the water/hydroxyl band (3800 – 3000 cm^{-1}) as the temperature of the thermal treatment increases.

After all three heat treatments there remains two peaks at 2930 cm^{-1} and 2850 cm^{-1} which represent CH_2 anti- and symmetrical stretching respectively. These peaks are due to an impurity such as vacuum grease and this does not affect the results of the materials being analysed.

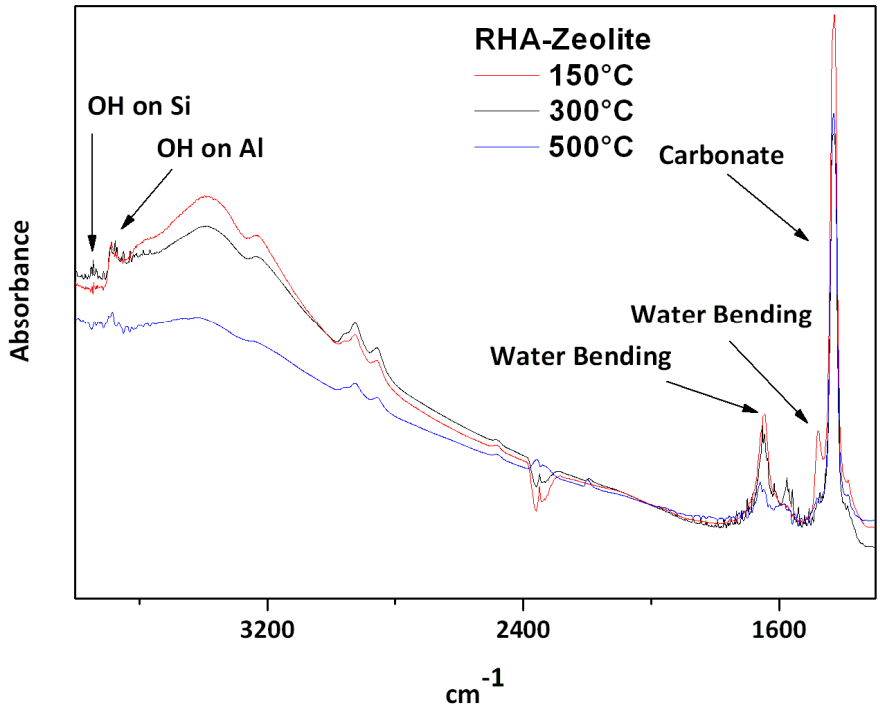

Figure 3.18 **Infrared Spectrum of Rice Hull Ash derived Zeolite under vacuum and after heat treatments up to 150 ˚C, 300 ˚C, and 500 ˚C**

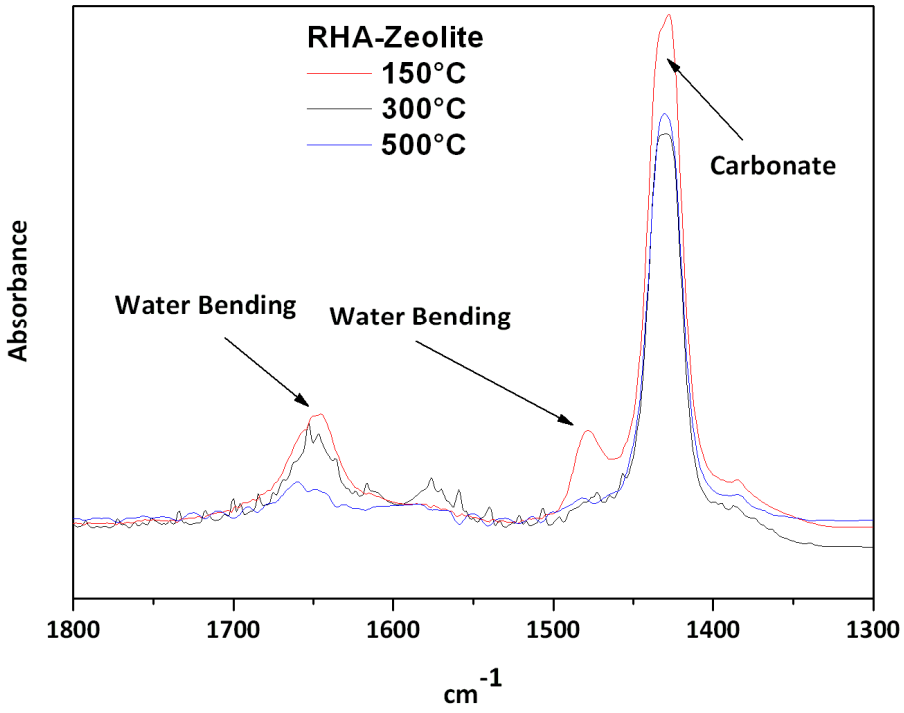

Figure 3.19 Close up of the region 1300-1800 cm^{-1} of the Infrared Spectrum of Rice Hull Ash derived zeolite under vacuum and after heat treatments up to 150 ˚C, 300 ˚C, and 500 ˚C

The FT-IR spectra of the Conv-Zeolite (Figure 3.20) sample similarly showed the presence of hydroxyl groups on silicon and aluminium, water, and some carbonate on the surface. After increasing heat treatments the bands in the water/hydroxyl region (3800-3000 cm^{-1}) almost completely disappear as do the water bending bands at 1700-1500 cm^{-1}. The carbonate band decreases in intensity on increasing heat treatments (Figure 3.21) implying that the carbonate on Conv-Zeolite is less strongly bonded to the surface and is more easily decomposed to CO_2(g). After the heat treatment at 500 ˚C almost all water, hydroxyl, and carbonate groups have gone from the surface of the Conv-Zeolite.

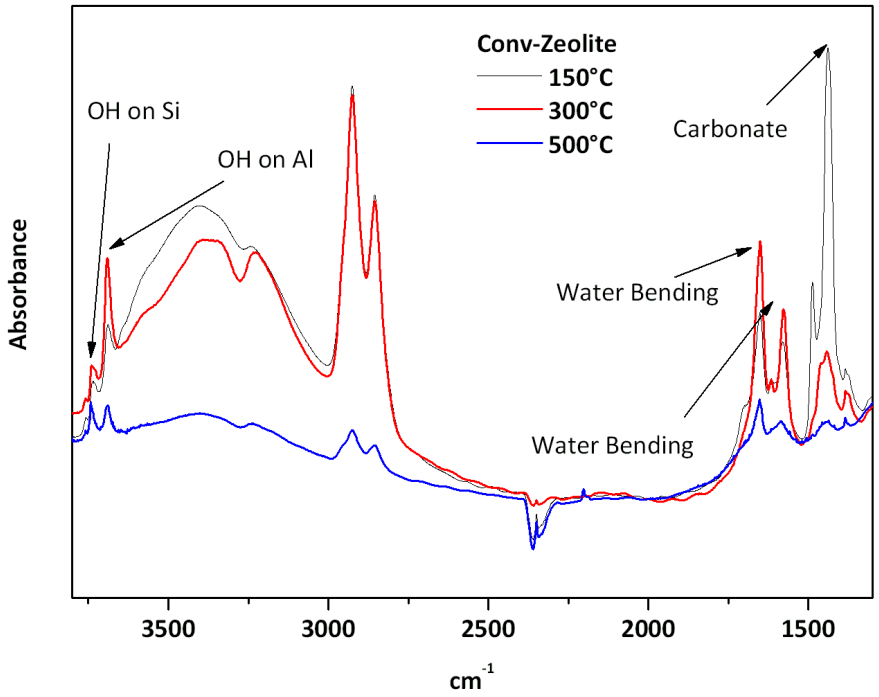

Figure 3.20 Infrared Spectrum of Zeolite synthesised from commercial alkali silicate under vacuum and after heat treatments up to 150 ˚C, 300 ˚C, and 500 ˚C

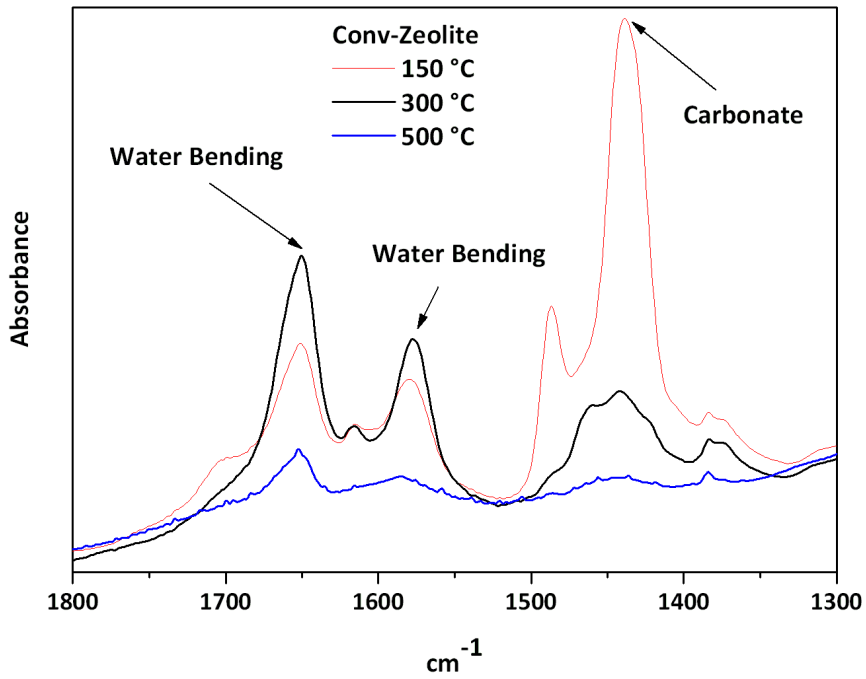

Figure 3.21 Close up of the region 1300-1800 cm^{-1} of the Infrared Spectrum of Conv-Zeolite under vacuum and after heat treatments up to 150 ˚C, 300 ˚C, and 500 ˚C

Comparing the effects of heat treatment under vacuum at increasing temperatures on the IR spectra of the two materials the main differences are in the carbonate region. Even after heat treatments a strong carbonate peak is present in the RHA-Zeolite FT-IR spectra whereas it disappears with increasing heat treatments for the Conv-Zeolite. This would imply there is either substantial carbonate material within the pores of the RHA-Zeolite, that the carbonate present absorbs unusually strongly in the infrared region, or, that the carbonates are different in nature. The difference in nature of carbonate for the materials could be explained by a difference in the way the carbonate forms in the two materials. If there is carbonate present in the alkali silicate solution extracted from the rice hull ash then the carbonate may form inside the structure in closed pores as it is crystallising in such a way that when the carbonate decomposes at higher temperatures in the pores it is not able to escape and thus it reforms into carbonate when the sample returns to room temperature and the IR spectra is taken. The Conv-Zeolite sample, having no carbonate in the starting alkali silicate material, would then only form carbonate, in the pores or on the surface, from atmospheric CO_2 after the structure had been formed and this carbonate would decompose and leave the materials on heat treatment under vacuum. The porosimetry data reports a high surface area for Conv-Zeolite and a much lower surface area for RHA-Zeolite which may confirm the theory that carbonate is structurally integral for the RHA-Zeolite sample whereas it is not for the Conv-Zeolite.

RHA-Zeolite(lower aluminium) showed a small reduction in carbonate presence for heat treatment under vacuum at 150 ˚C and 300 ˚C but the peak remained high (Figure 3.22). Water disappears from all materials on heat treatment.

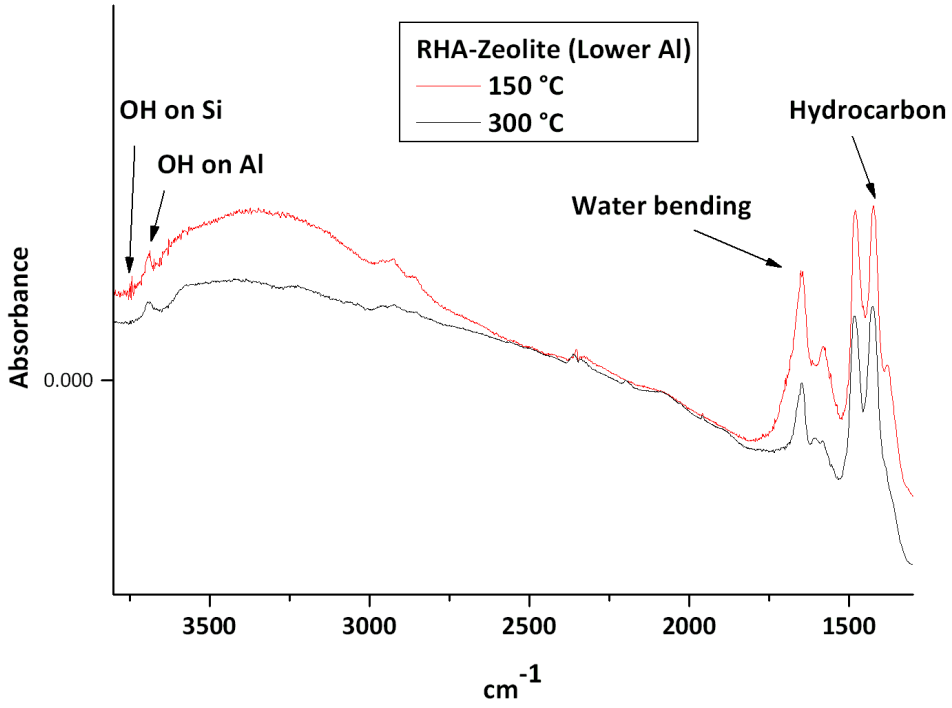

Figure 3.22 Infrared Spectrum of RHA-Zeolite with lower aluminium under vacuum and after heat treatments up to 150 ˚C and 300 ˚C

In order to investigate the surface further, carbon dioxide and carbon monoxide were dosed onto the surface *in situ* and the effects analysed using IR spectroscopy.

3.4.7.1 In Situ Dosing of Carbon Monoxide (CO)

Examining the location and nature of peaks in an infrared spectrum as the concentration of CO changes can give information on the basic sites on the surface. The process proceeds by first taking a spectrum of the sample under vacuum and then dosing the vessel with a certain concentration of CO and finally by slowly lowering the partial pressure gradually, in stages, (thus creating an expansion) of CO using vacuum and a system of airtight glassware. Spectra are taken at intervals throughout the process. The sample is formed into a self-supporting wafer using a press and is then held in a foil envelope.[110]

CO chemisorbs on basic sites and this bonding is stronger than the physisorption that occurs more generally over a surface. The chemisorption affects the symmetry of the CO molecule and the group(s) it is interacting with and this effect appears in the infrared

spectrum at the peak locations of the relative molecules. For example any OH groups that bond with a CO molecule will provide absorption in the IR spectrum at around 3800-3000 cm^{-1} and the CO molecule itself appears at around 2200-2100 cm^{-1}.[111]

Below in Figure 3.23 are the spectra of the incremental expansions of CO gas after dosing of the RHA-Zeolite surface. These spectra are subtracted from the initial spectrum and termed 'the difference spectra'. In this format positive peaks indicate the formation of a species and negative peaks indicate the loss of a species. If there is no effect on a functional group and thus no change to an infrared absorption peak in the original spectrum, this effect is manifested by a lack of a peak in the different spectra. The conversion of the peak from one main peak at 2158 cm^{-1} to two peaks at 2164 cm^{-1} and 2173 cm^{-1} is an effect which occurs for all materials analysed and is discussed later in the chapter.

There are some negative peaks in the water/hydroxyl region in the difference spectra which could be due to extraction of water under the vacuum during the experiment. It is unlikely that they are due to interactions with the CO probing gas as this would involve the creation of a peak in the region alongside the negative peaks forming and this does not occur.

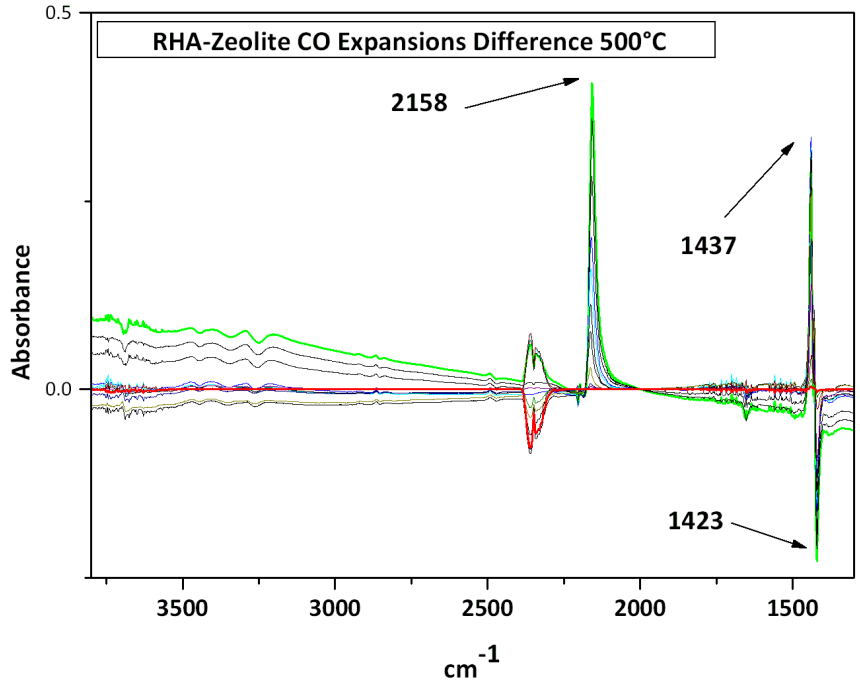

Figure 3.23 **Full IR difference Spectra during expansion of CO gas on RHA-Zeolite after heat treatment at 500 ˚C under vacuum**

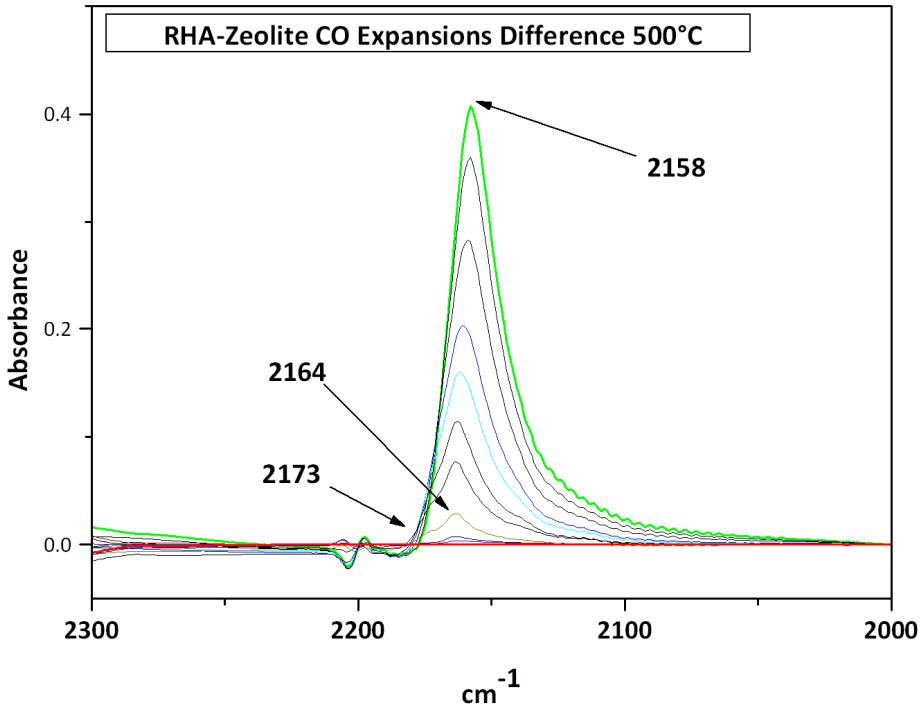

Figure 3.24 **IR Spectra of CO peak change during expansion of CO gas on RHA-Zeolite after heat treatment at 500 ˚C under vacuum**

The negative and positive peaks appearing in the carbonate region of the IR spectra shown below in Figure 3.25 suggest that there is a presence of carbonate on the surface and that the nature of this species changes to form a new species on addition and then expansion of CO(g).

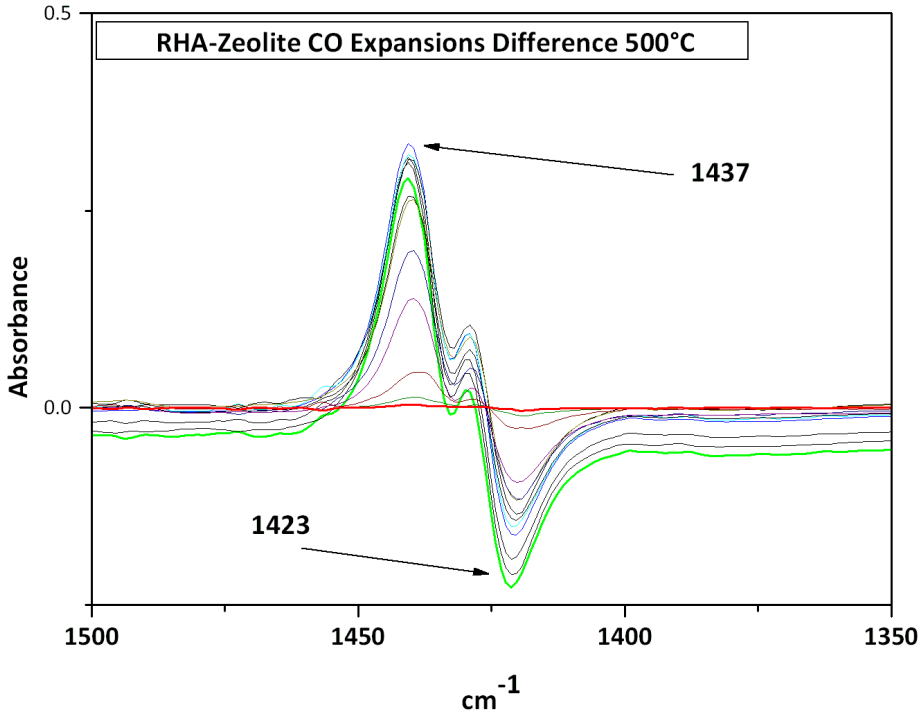

Figure 3.25 IR Spectra of carbonate peak area change during expansion of CO gas on RHA-Zeolite after heat treatment at 500 ˚C under vacuum

Below, in Figure 3.26, are the difference spectra for the Conv-Zeolite material at 500 ˚C. No significant effects are apparent in changes to the IR spectra. This implies the CO interacts solely with the sodium cations on the surface.

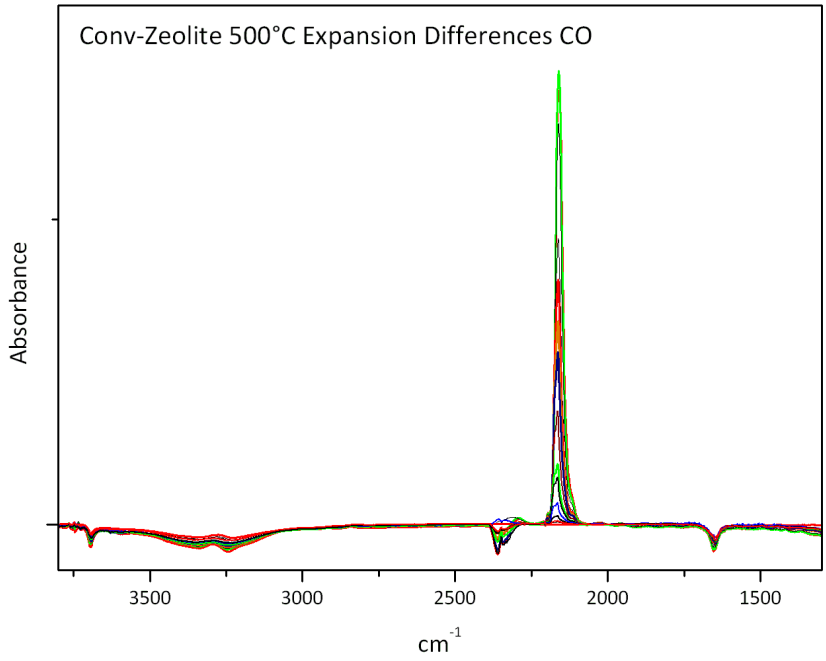

Figure 3.26 Full IR Spectra during expansion of CO gas on Conv-Zeolite after heat treatment at 500 ˚C under vacuum

There are clearly two peaks forming from the single CO peak on expansion of CO gas on the conv-Zeolite surface (Figure 3.27), the main peak changes from 2162 cm^{-1} to two peaks at 2165 cm^{-1} and 2174 cm^{-1}. Two smaller peaks at 2198 cm^{-1} and 2116 cm^{-1} also appear at lower concentrations.

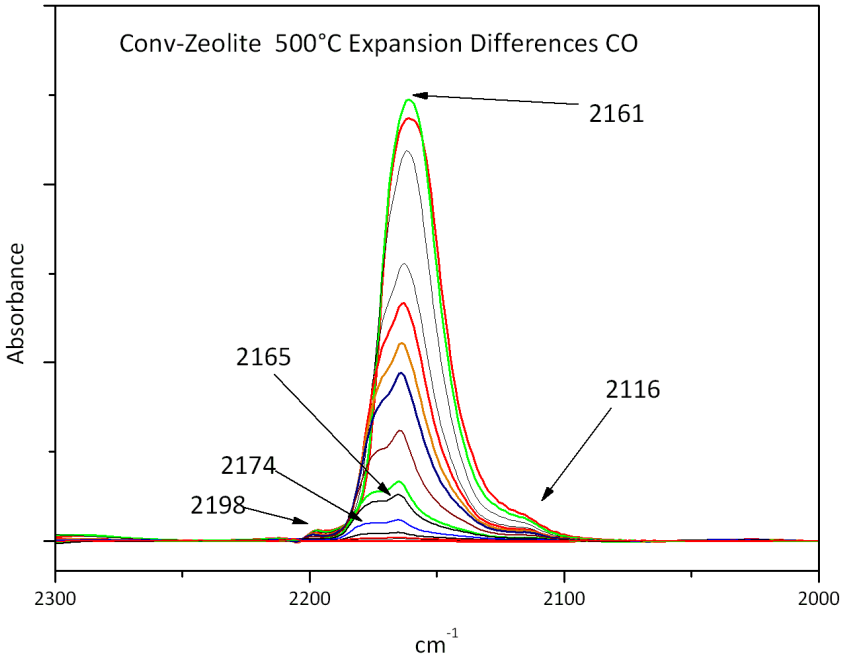

Figure 3.27 IR Spectra of CO peak change during expansion of CO gas on Conv-Zeolite after heat treatment at 500˚C under vacuum

The equivalent spectra for RHA-Zeolite(lower aluminium) (Figure 3.28) is more difficult to analyse due to more significant background noise and interference. The band may be weaker in intensity due to a lower concentration of sodium cations in the structure which is due to the higher Si/Al ratio. It is clear that the main CO peak at 2160 cm^{-1} at high coverage splits into two peaks at 2165 cm^{-1} and 2151 cm^{-1} as the concentration of CO decreases. Two smaller peaks at 2191 cm^{-1} and 2126 cm^{-1} also appear at lower concentrations which is similar to Conv-Zeolite but different to RHA-Zeolite. The new peak locations for the three samples are collated in Table 3.9. The peak at 2350 cm^{-1} is CO_2 gas contamination. This should not affect the CO interactions with the surface because the CO study occurs at 77K and at this temperature CO_2 is a solid (melts at 194.7K) and thus would not be able to integrate into the material or interact with it.

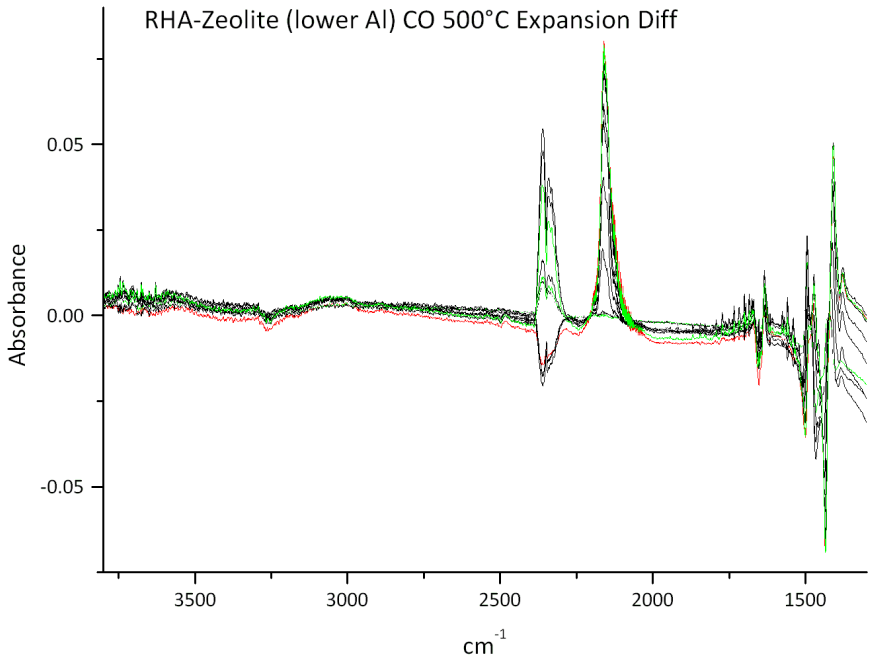

Figure 3.28 Full IR Spectra during expansion of CO gas on RHA-Zeolite (lower Al) after heat treatment at 500 ˚C under vacuum

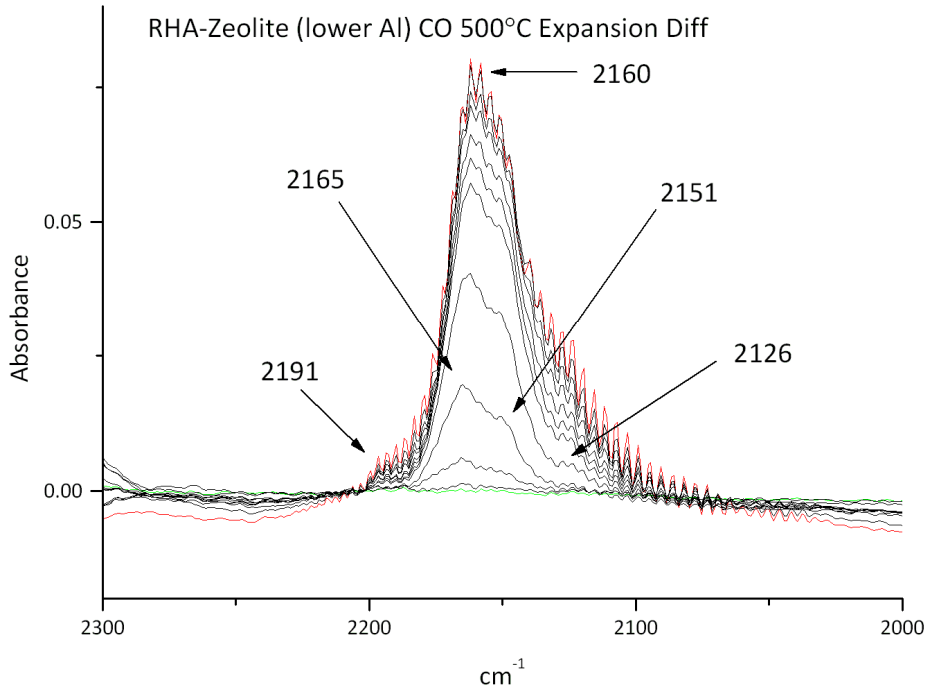

Figure 3.29 IR Spectra of CO peak change during expansion of CO gas on RHA-Zeolite (lower Al) after heat treatment at 500˚C under vacuum

Table 3.9 Infrared peaks (cm^{-1}) formed from initial CO peaks for RHA-Zeolite, Conv-Zeolite, and RHA-Zeolite(lower Al)

	Initial peak	New Peaks formed on expansion of CO			
RHA-Zeolite	2158		2173	2164	
Conv-Zeolite	2161	2198	2174	2165	2116
RHA-Zeolite(lower Al)	2160	2191	2165	2151	2126

There are various different interpretations within the literature for the location and shifting of the CO peak found in these results.

According to Martra the large peak at 2160-2145 cm^{-1}, which is measured at high concentrations of CO, is associated with the dicarbonylic adduct (Figure 3.30).[112] This is then converted to two monocarbonylic adducts as the concentration decreases and these two new species correspond to peaks at 2174 cm^{-1} and 2165 cm^{-1}.

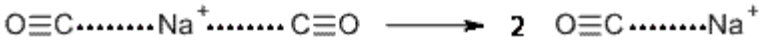

Figure 3.30 Conversion of dicarbonylic adduct to monocarbonylic adduct on a sodium cation

That there are two distinct peaks signifies there are two unique positions within the Faujasite structure where the positive sodium cation polarises the CO. As the peaks are at higher wavenumbers than the absorption of free CO (2143 cm^{-1}) the polarisation must occur through the carbon end.[112] These peaks at 2174 cm^{-1} and 2165 cm^{-1} represent a CO molecule bonding on a positive sodium cation which is in an S_{III} position (within the four-membered ring) and an S_{II} position (within the hexagonal ring) respectively (Figure 3.31). The electric field produced from the extra framework sodium cations decreases as the number of neighbouring oxygen atoms increases. The CO stretching frequency increases as the strength of the positive field increases. The relative intensities of the two peaks reflects the relative population of sodium cations in the two extra framework positions. Comparing a low silicon to aluminium ratio Zeolite to a higher silicon to aluminium ratio Zeolite, although there is the same number of surrounding framework oxygens, the sodium cation is affected more by oxygens with a higher electron density (if interacting with more aluminiums) and this causes a larger shielding of the positive electric field in the proximity of the cation which in turn causes less of a shift in the infrared spectrum.

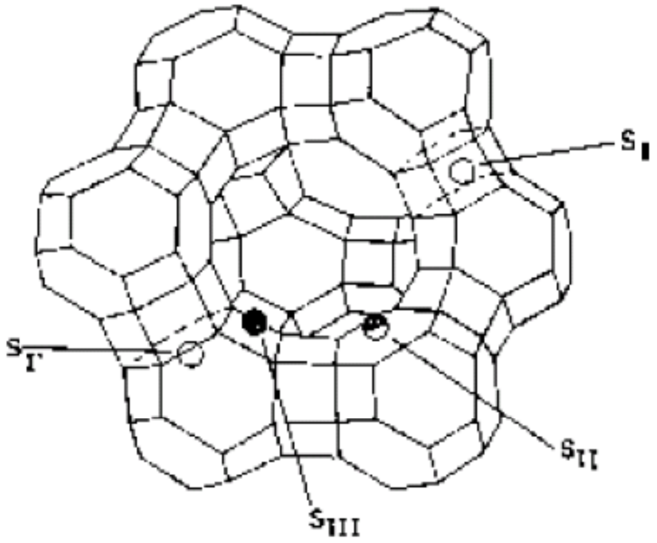

Figure 3.31 Location of extra-framework sites in a Faujasite structure which may accommodate cations[112]

Knözinger and Huber, on the other hand, describe a system whereby the location of the peaks is dependent on the nature of interactions with positive sodium cations. A dominant peak occurring at 2172 cm^{-1} represents the interaction, by σ-donor bond, of the C end of the CO molecule with a single positive sodium cation evidenced by the shift of the band to high wavenumbers.[113] This peak was deconvoluted and a further four peaks with frequencies of 2183, 2172, 2166, and 2157 cm^{-1} were identified. Information gathered from XRD and Na-NMR-spectroscopy implies the only accessible sodium cations for NaY are located in sites S_{II}.[23] The Si/Al ratio for NaY described in the paper was 2.6 and thus the likely arrangements of silicon and aluminium in the 6-rings near S_{II} sites are shown in Figure 3.32. There are four potential arrangements which would contain a sodium cation in the plane and these correspond with the four peaks. The magnitude of shift in wavenumbers of the carbonyl peak reflects the sodium location which is least shielded by the electric field of its neighbouring framework oxygens. On increasing the number of aluminiums in the ring, the negative charge density of the oxygens increases and thus the highest peak at 2183 cm^{-1} relates to the S_{II} site containing only one aluminium and the lowest peak at 2157 cm^{-1} the S_{II} site containing three aluminiums (Figure 3.32).

For the NaX Zeolite described with a Si/Al ratio of 1.3 the majority of S_{II} sites contained the maximum of three aluminiums and S_{III} sites (4-rings) contained the maximum of two aluminiums. Therefore both S_{III} and S_{II} sites will contain sodium cations. Two peaks were registered on the FT-IR spectra of CO adsorption on NaX, 2166 cm^{-1} and 2157 cm^{-1}, and since there is a greater negative charge on the S_{II} site, the sodium cation is more shielded and therefore a lower electric field strength compared with the sodium cation on the S_{III} site and therefore the peaks can be attributed such that the 2166 cm^{-1} peak relates to the S_{III} sited cation and the 2157 cm^{-1} peak the S_{II} sited cation.

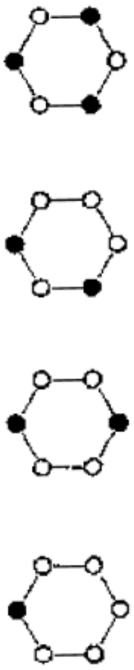

Figure 3.32 Possible distributions of Al atoms in 6-rings (S_{II} sites)[113]

Busca reports four peaks at 2174 cm^{-1}, 2165cm^{-1}, 2138 cm^{-1}, and 2113cm^{-1} for NaX with Si/Al ratio of 1.31. The peak at 2113 cm^{-1} is assigned to O-bonded CO although there may be an element of ^{13}C-bonded CO as suggested by Martra. 2138cm^{-1} is identified as the pseudo liquid form of CO inside the pores. Peaks at 2174 cm^{-1} and 2165 cm^{-1} were assigned to carbonyls on S_{III} and S_{II} cations respectively.

Further explanation for the relation between the nature of the interactions of CO with cations and their vibration frequencies can be found by referring to the molecular orbital diagram shown in Figure 3.33. As can be seen, there is one pair of electrons in the highest occupied molecular orbital (HOMO) and this orbital (5σ) is a combination of the C 2*s* orbital and *O*-centred *p*-orbitals, and has slight antibonding character. As the C 2*s* orbital is at a slightly higher energy than the O *p*-orbital, there is a prevalence of electron density at the C end, and this is why, along with better overlap, CO bonds predominantly at the C end. When the CO molecule donates electrons to a Lewis acid and in the absence of any π back bonding (not present in this case), the electron density in this antibonding 5σ orbital is reduced and thus causes a slight increase in bond strength, leading to an increased vibrational frequency for the CO bond.

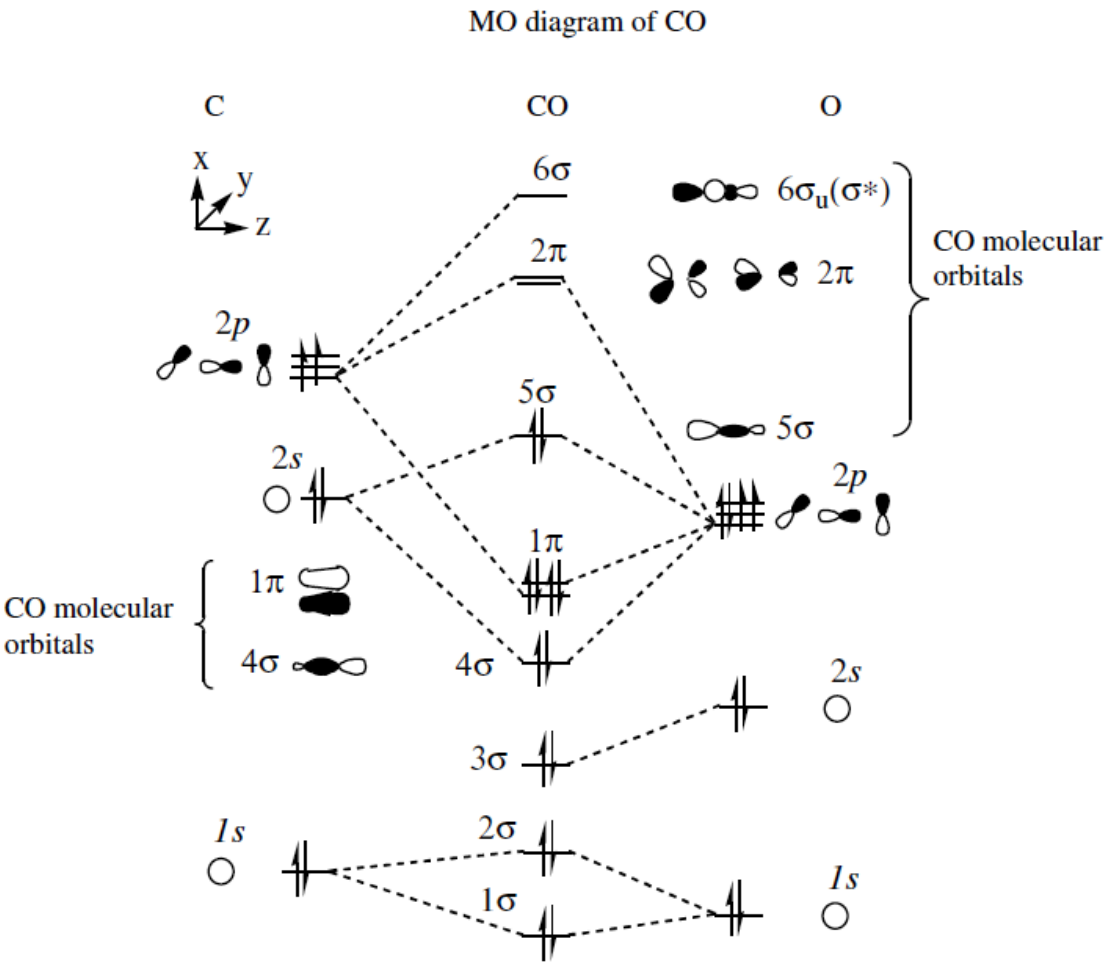

Figure 3.33 Molecular Orbital Diagram of CO[124]

Shown below in Table 3.10 are the collated results of these papers.

Table 3.10 Collated literature results for FT-IR peak locations of CO adsorbed onto Zeolites NaX and NaY. CO molecule is C-bonded except where noted.

	Zeolite	Si/Al	Site name	site type	In/Off ring	CO frequency	
						cm^{-1}	
Busca	**NaX**	**1.31**	**S_{II}**	**6 ring**	**in**	**2165**	
			S_{III}	**4 ring**	**off**	**2176**	
	NaY	**2.56**	**S_{II}**	**6 ring**	**in**	**2172**	
			S_{III}	**4 ring**	**off**	**2182**	
						2113	**O-bonded**
						2138	**Liquid CO**
Knözinger	**NaX**	**1.3**	**S_{II}**	**6 ring**		**2157**	
			S_{III}	**4 ring**		**2166**	
	NaY	**2.6**	**S_{II}**	**6 ring**		**2183**	**1 Al**
						2172	**2 Al**
						2166	**2 Al**
						2157	**3 Al**
Martra	**NaX**					**2160-2145**	**dicarbonylic adduct**
			S_{II}	**6 ring**		**2165**	
			S_{III}	**4 ring**		**2174**	
						2143	**Free CO**

Below in Table 3.11 are the collated results from this work and proposed interactions with sodium cations. The RHA-Zeolite FT-IR spectrum contains peaks which most closely match all papers for CO interactions on NaX at the two available sites. Both the conv-Zeolite and the RHA-Zeolite(lower Al) have peaks at 2198 cm^{-1} and 2191 cm^{-1} respectively which are significantly higher than peaks found in the literature for interactions of CO on sodium. A possible explanation could be that the CO is interacting with another species. The CO cannot be interacting with aluminium cations as it is all tetrahedrally bonded within the structure (known from NMR analysis - Figure 3.14). Potassium, in K-ZSM-5 (Zeolite), interacts with CO(g) through the carbon and oxygen ends and this appears in the IR spectrum at 2166 cm^{-1} and 2117 cm^{-1} respectively.[114] Calcium interacts with CO(g) through the carbon end in calcium hydroxyapatite to produce a band at 2168cm^{-1}.[115] As

shown from XRF analysis (3.4.1) there are trace amounts of potassium (0.09%) and calcium (0.04%) in the RHA-Zeolite sample compared with 0.01% potassium and 0.01% calcium in the Conv-Zeolite material, although these did not appear in the XPS analysis (Section 3.4.2) which describes the elemental composition of the top surface layers. Therefore the presence of potassium or calcium could not be the cause of these higher wavenumber peaks appearing in spectra for Conv-Zeolite and RHA-Zeolite (lower Al) because there are slightly higher concentrations of potassium and calcium in RHA-Zeolite. The large shift could imply a CO molecule interacting through the carbon end on a sodium cation which is least shielded and is in an environment which has a high positive electric field strength. The electric field may be affected by the presence of Ca^{2+} ions but since the concentration of calcium is high for RHA-Zeolite then this should produce the peak in that sample as well as Conv-Zeolite and RHA-Zeolite(lower Al). A CO molecule might be interacting with multiple sodium cations prompting an environment with a higher electric field than that produced by one sodium cation but since all materials have similar Si/Al ratios the lack of peak in the RHA-Zeolite sample contradicts this. Since both Conv-Zeolite and RHA-Zeolite (lower Al) are structurally more like Zeolite X whereas RHA-Zeolite has a significant presence of sodalite (known from XRD) it may be possible that there is a sodium cation within the large pore of the structure which is distanced from the aluminium bonded oxygen atoms and therefore shielded least and thus producing higher positive field which in turn would shift the CO peak to higher wavenumber. This would occur to a much lesser extent for the RHA-Zeolite sample which contains a significant amount of Sodalite in which there is no large pore in the structure of the truncated octahedral as shown in Figure 1.5.

The further two peaks for each sample can be ascribed as the two cation sites S_{II} and S_{III} as with the NaX described in the literature. The Conv-Zeolite sample peaks are more similar to Busca and Martra's observations whereas the RHA-Zeolite peak locations fit with those found by Knözinger. The low frequency peaks at 2116 cm^{-1} for Conv-Zeolite and 2126 cm^{-1} for RHA-Zeolite (lower Al) could be ascribed to CO bonding on a sodium cation through its oxygen end.

From these results it can be concluded that all three materials contain the S_{II} and S_{III} sites shown in Figure 3.31 which are the same as the sites in a sodalite structure. The difference in the materials occurs with the presence of the extra peaks for Conv-Zeolite

and RHA-Zeolite (lower Al). For these samples there is an O-bonded interaction at low wavenumber and a higher wavenumber interaction which has been difficult to assign but could be a sodium cation distanced from the aluminium bonded oxygen in a large pore. Therefore these extra interactions are enabled by a difference in structure to the RHA-Zeolite. These results show that the RHA-Zeolite (lower Al) more closely resembles the Conv-Zeolite in structure and that the RHA-Zeolite may not contain a sodium cation in the large pores of its Faujasite crystalline phase.

Table 3.11 Results obtained for this project

Zeolite	CO frequency		Site name	site type
	cm^{-1}			
Conv-Zeolite	2161	high concs		
	2198			
	2174	fits NaX	S_{II}	4 ring
	2165	fits NaX	S_{III}	6 ring
	2116	O bonded		
RHA-Zeolite	2158	high concs		
	2173	fits NaX	S_{II}	4 ring
	2164	fits NaX	S_{III}	6 ring
RHA-Zeolite(lower Al)	2160	high concs		
	2191			
	2165	fits NaX	S_{II}	4 ring
	2151	fits NaX	S_{III}	6 ring
	2126	O bonded		

3.4.7.2 In Situ Dosing of Carbon Dioxide (CO_2)

The study of the effects in FT-IR spectra on the interactions of carbon dioxide with a surface is a well used technique for providing information on metal cation sites and on basic sites on a zeolite surface. It can also provide information on carbonate species as described later.

As can be seen from the difference spectra shown in Figure 3.34, Figure 3.35, and Figure 3.36, there are three main regions where there has been an effect produced from the

dosing of carbon dioxide on the materials. Firstly, there is a small perturbation in the water/hydroxyl region where the intensity of a peak increases on increased concentration of CO_2 and this is caused by the presence of carbon dioxide increasing the polarity of the small concentration of hydroxyl groups present on the surface and thus making their signal increase. There are also changes in the new carbon dioxide peak as the CO_2 interacts with the sodium cations, forms carbonate, and affects any pre-existing carbonate as discussed below.

The process of dosing of carbon dioxide has an irreversible effect on the surface. The single carbonate peak (Figure 3.18, Figure 3.21, and Figure 3.22) splits once dosing has occurred and this double peak then recedes to form another double peak which is more stable as discussed below. This effect occurs for all three samples (Figure 3.43, Figure 3.44, and Figure 3.45).

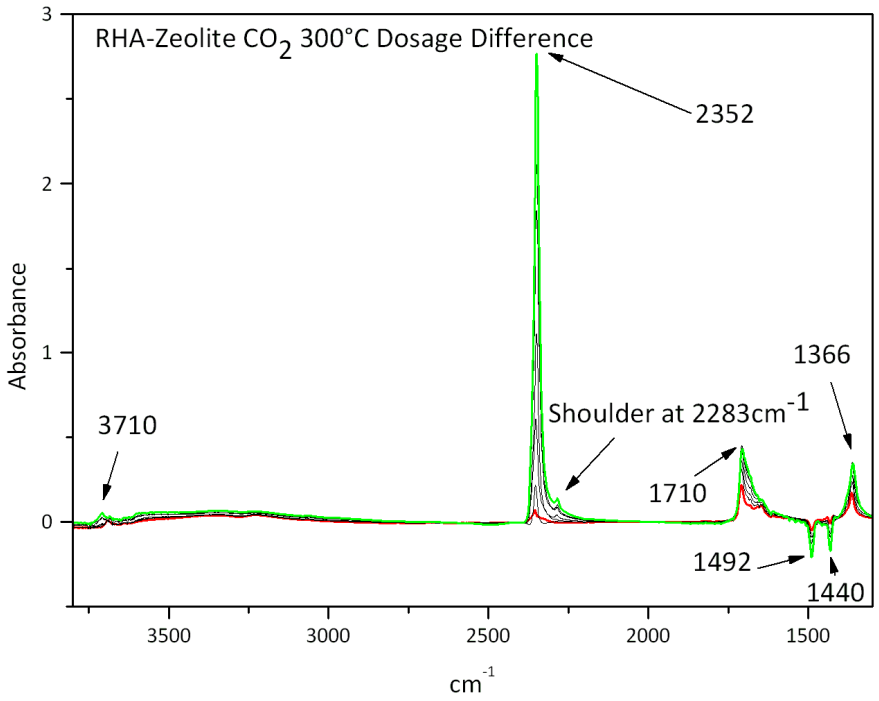

Figure 3.34 Difference spectra for dosing of CO_2 on RHA-Zeolite

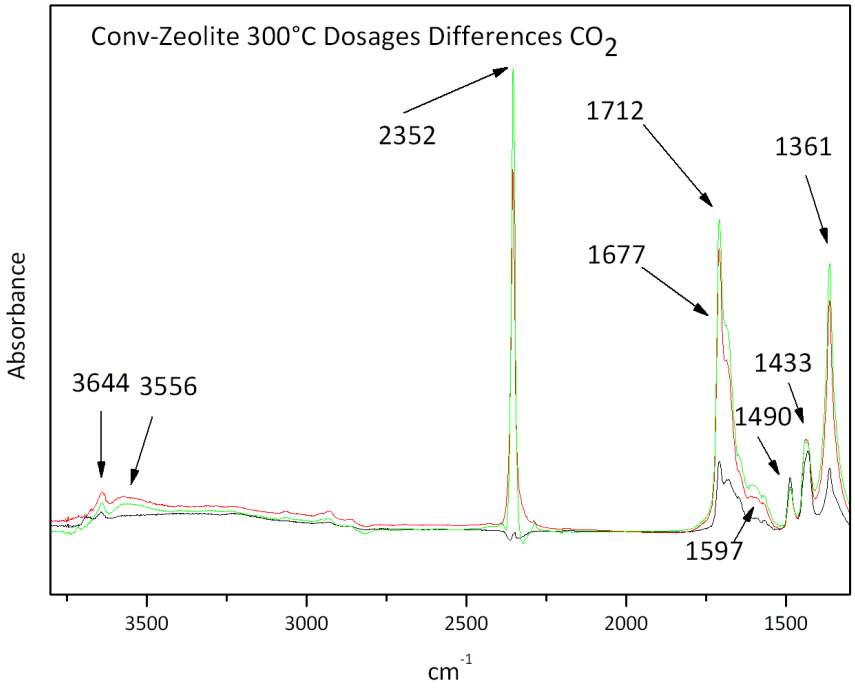

Figure 3.35 Difference spectra for dosing of CO_2 on Conv-Zeolite

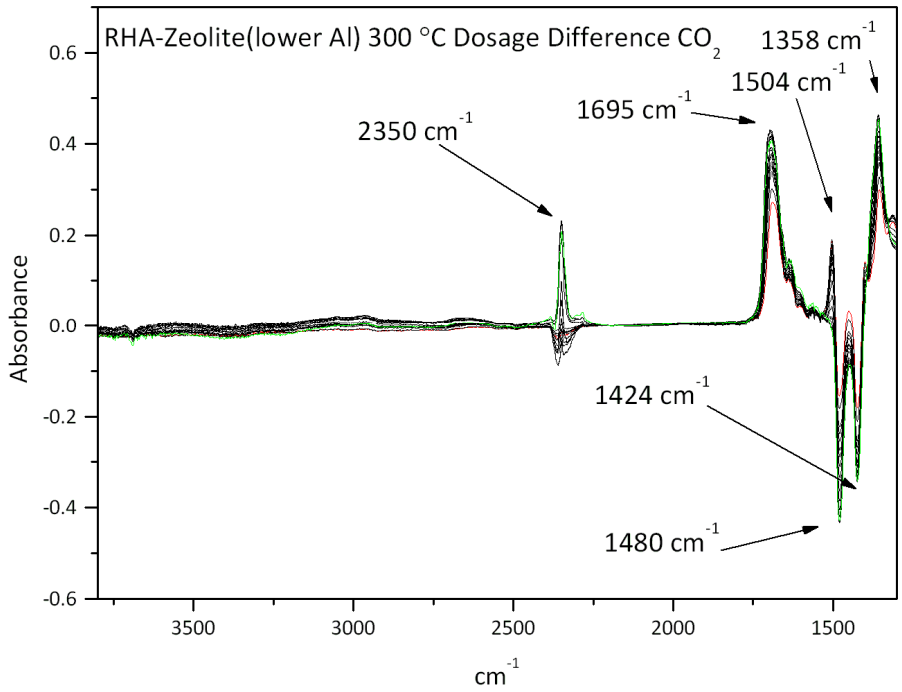

Figure 3.36 Difference spectra for dosing of CO_2 on RHA-Zeolite(lower Al)

CO_2 adsorbs onto cations in Zeolites and a peak appears at around 2360 cm^{-1} designated as the asymmetric stretching vibration ν_3. This peak increases in wavenumber on increased polarization strength ($Li^+ > Na^+ > K^+ > Rb^+ > Cs^+$). For a linear CO_2 (base) interacting with one positive sodium cation (acid) this peak is around 2355 cm^{-1} (Figure 3.37).[112] Shown below are the infrared difference spectra for RHA-Zeolite on dosing with CO_2 (Figure 3.38). There is a clear peak at 2354 cm^{-1} which shifts to 2350 cm^{-1} on increased dosing of CO_2. For the comparable Conv-Zeolite (Figure 3.39) there is a much smaller shift of the peak from 2355 cm^{-1} to 2354 cm^{-1}. There is no shift in the carbon dioxide peak at 2350 cm^{-1} for the RHA-Zeolite (Lower aluminium) sample (Figure 3.40).

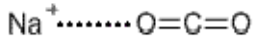

Figure 3.37 Interaction of M^+ acid such as sodium with carbon dioxide (base)

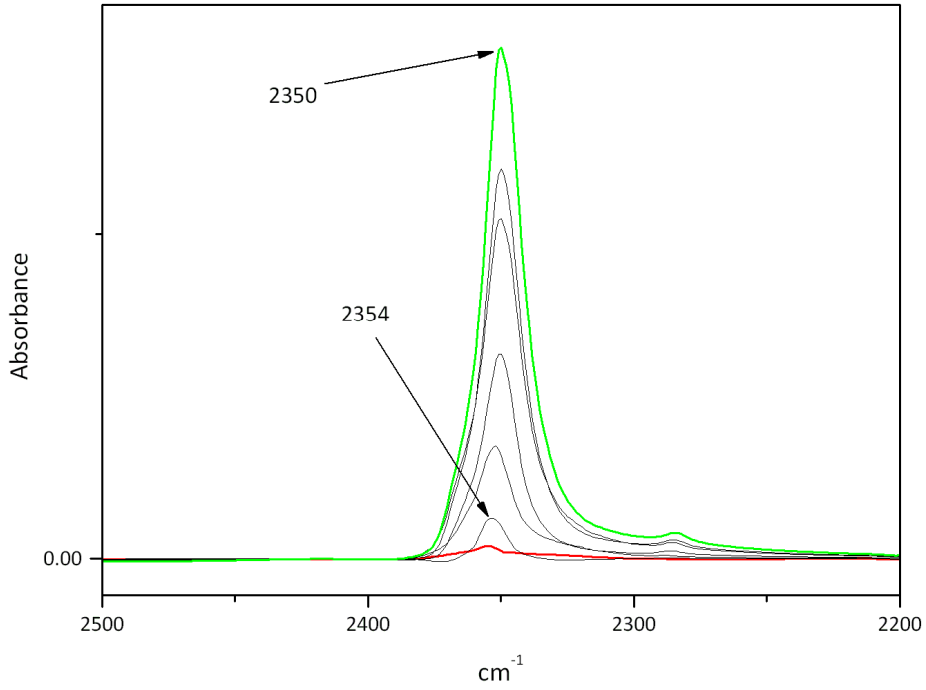

Figure 3.38 Infrared spectra of RHA-Zeolite during dosing with CO_2 in the CO_2 peak region. Spectra were subtracted from initial spectra in order to see only changes in peaks caused by the dosing

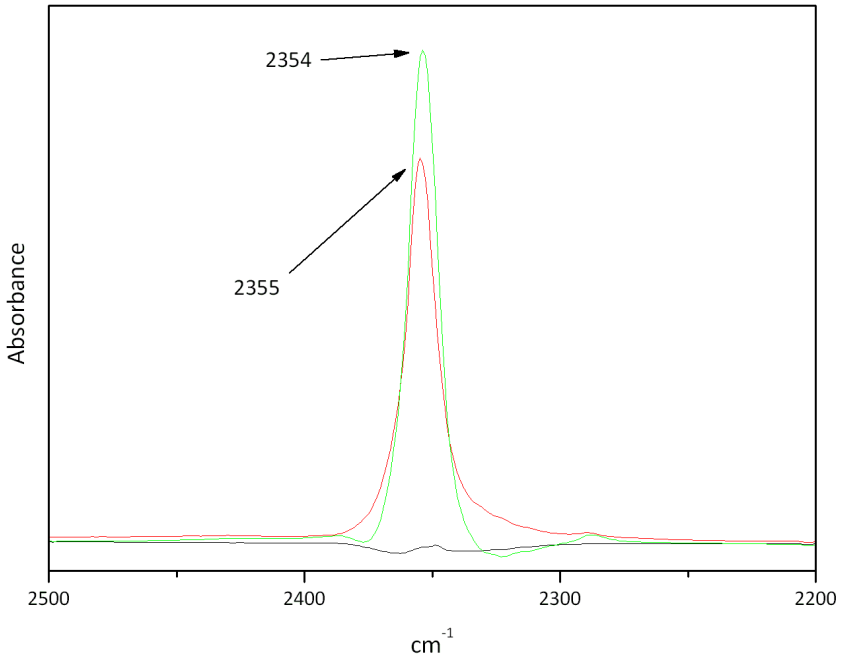

Figure 3.39 Infrared spectra of Conv-Zeolite during dosing with CO_2 in the CO_2 peak region. Spectra were subtracted from initial spectra in order to see only changes in peaks caused by the dosing

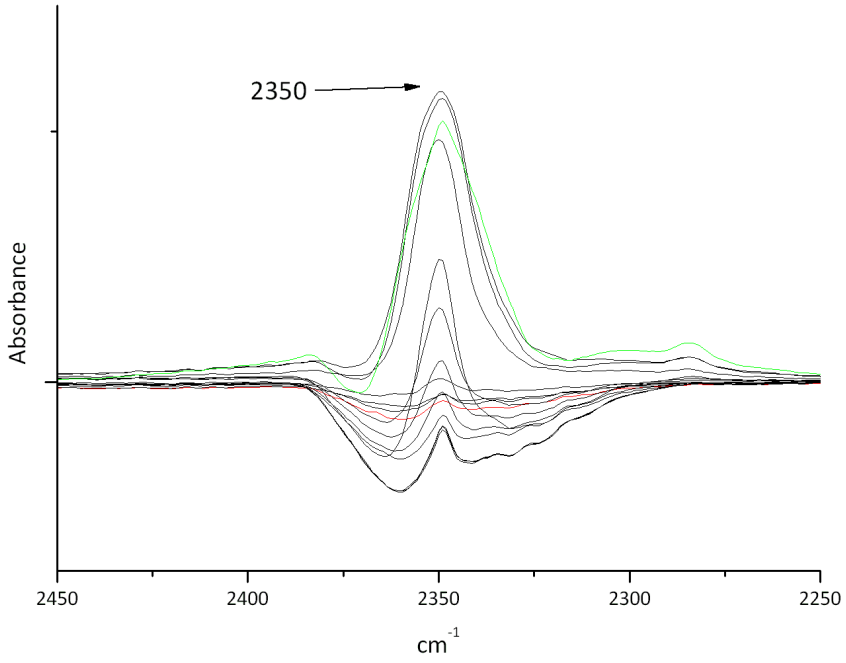

Figure 3.40 Infrared spectra of RHA-Zeolite (Lower Aluminium) during dosing with CO_2 in the CO_2 peak region. Spectra were subtracted from initial spectra in order to see only changes in peaks caused by the dosing

The shift in wavenumbers on higher dosing of CO_2 observed in the main CO_2 peak in the spectra for RHA-Zeolite could be due to multiple interactions occurring. These interactions could be either multiple CO_2 molecules interacting with a single sodium cation or multiple sodium cations interacting with a single CO_2 molecule (simplified diagram shown in Figure 3.41). Multiple CO_2 molecules interacting with a single sodium cation is more likely to occur on increased dosage of CO_2 gas (and thus higher concentration of CO_2 molecules in the pores) and this effect would decrease the electric field and therefore there would be a decrease in the magnitude shift. The electron density of a delta negative oxygen ($O^{\delta-}$) from a carbon dioxide molecule interacts with a delta positive sodium cation and thus reduces the positive charge on that sodium cation. The second carbon dioxide molecule that interacts with that sodium cation will encounter a reduced charge density and interact less with the sodium. Equilibration would then equalise the two interactions and the band associated with this effect would be lower in magnitude.

A high concentration of sodium cations would be needed for the second effect shown in Figure 3.41 and this is the case due to the high ratio of aluminium present in the materials. The single carbon dioxide molecule would then experience a larger electric field as both oxygen ends interacted with different delta positive sodium cations and the magnitude of the peak shift would increase. The symmetry of this effect would be important and depend on the location of the two sodium cations in the cage as if they were arranged such that the carbon dioxide molecule was linear then the intensity of the band could drop.

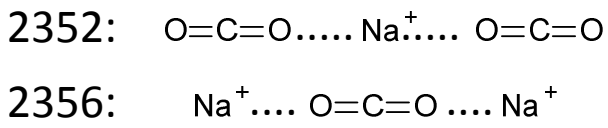

Figure 3.41 Schematic diagram of CO_2 / sodium cation interactions and their related IR peak locations

CO_2 also chemisorbs onto oxygen sites on the surface of zeolites to form carbonate species and these appear as peaks in the region 1800-1200 cm^{-1}. There are two doublets of peaks which relate to two species of carbonate shown in Figure 3.42; Species I is a carboxylate species described by Jacobs *et al* as CO_2 adsorbed in the end-on configuration polarised by a less shielded sodium cation and interacting with a lattice oxygen ion and is represented by peaks at 1365 cm^{-1} ($\nu_{C\text{-}O}$ asymmetric) and 1715 cm^{-1} (C=O stretching mode).[116] Species II is the true carbonate structure whereby the negative charge is delocalised over the three oxygen atoms and stabilised by the electrostatic field of the sodium cation.[116] The two peaks at 1431 cm^{-1} and 1488 cm^{-1} relate to the ν_3 carbonate vibration.[116] There is some asymmetry occurring for this interaction which causes the peak to split but as the difference is small the three oxygen atoms of the carbonate species should be practically equivalent.[117]

Table 3.12 Wavenumber values for two species of carbonate interactions as described by Jacobs *et al*[116]

Species I	**1711 cm^{-1}**	**C=O**
	1365 cm^{-1}	**O-C**
Species II	**1488 cm^{-1}**	**Delocalised C-O bond**
	1431 cm^{-1}	**Delocalised C-O bond**

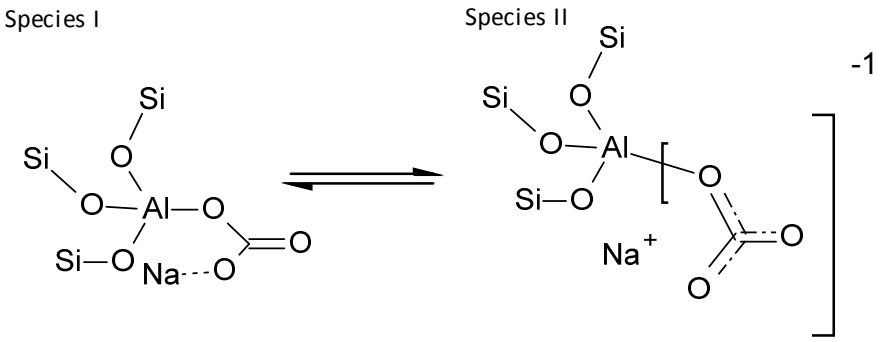

Figure 3.42 Diagram showing two species of CO_2 adsorbed onto hydroxyl groups on the surface of zeolitic matertials as described by Jacobs[116]

For the RHA-Zeolite, sample peaks appeared for Species I and negative peaks appeared for Species II on increased CO_2 dosages in the difference spectra (Figure 3.43). This implies carbonate species II existed on the sample under vacuum before any CO_2 was added to the environment and that this carbonate then underwent conversion to Species I as the CO_2 dosage increased. As the carbonate is forming in pores and coverage increases, it would seem to make sense that the nature of chemisorption would favour the formation that takes up less space over any other thermodynamic effects. There is a shoulder at around 1650 cm^{-1} which relates to a loss of symmetry of the carbonate perhaps due to the small pores in which the interactions occur.

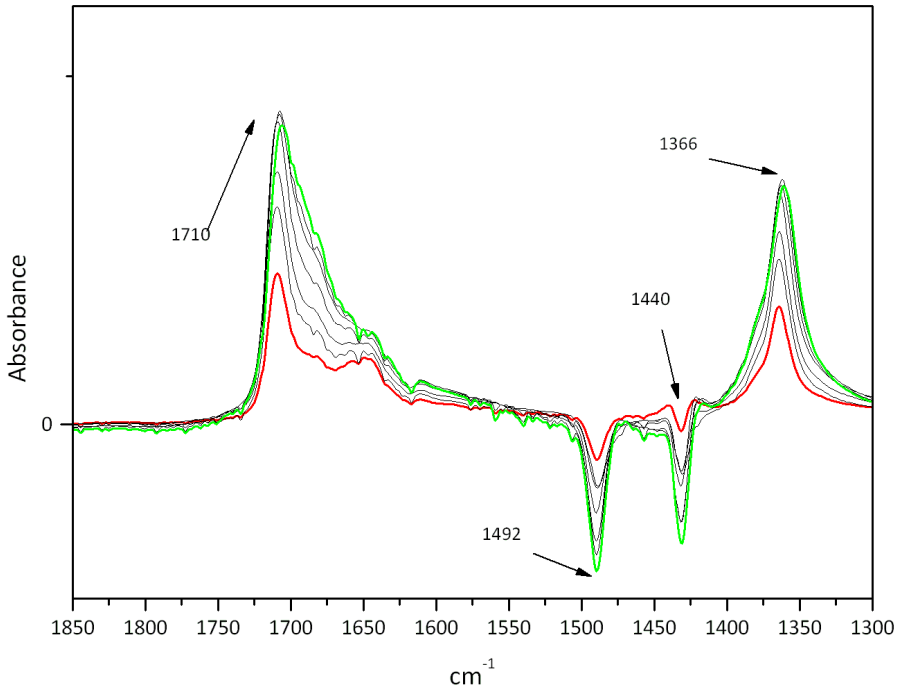

Figure 3.43 Infrared spectra of RHA-Zeolite during dosing with CO_2 in the carbonate region. Spectra were subtracted from initial spectra in order to see only changes in peaks caused by the dosing

For the Conv-Zeolite sample the four main peaks appeared (Figure 3.44) showing growth of both carbonated species in the pores. There are also some shoulders on the 1712 cm^{-1} peak at 1677 cm^{-1} and 1597 cm^{-1}. These extra peaks could be arising from further changes in the symmetry of the carbonate molecules formed in the pores as the concentration of CO_2 increases or due to multiple interactions of the CO_2 molecules on sodium cations.

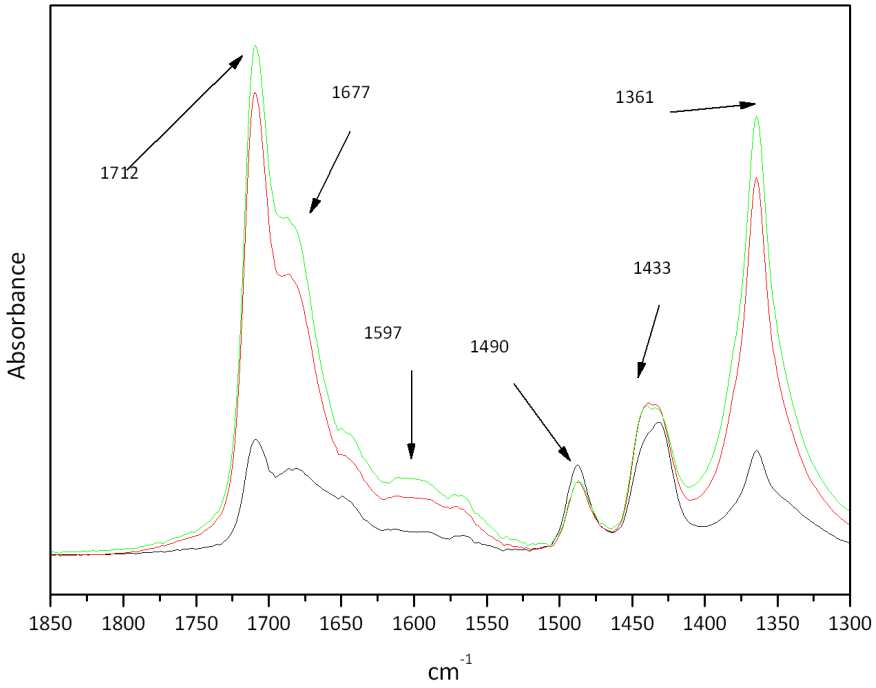

Figure 3.44 Infrared spectra of Conv-Zeolite during dosing with CO_2 in the carbonate region. Spectra were subtracted from initial spectra in order to see only changes in peaks caused by the dosing

The carbonate peak area of the FT-IR spectra for the RHA-Zeolite (lower aluminium) (Figure 3.45) is still more complex. There are the two negative peaks representing the Species II and the two positive peaks for Species I but there also are additional peaks at 1504 and 1400 cm^{-1} which disappear alongside the Species II peaks and shoulders on the 1695 cm^{-1} peak around 1630 cm^{-1} which grow alongside the Species I peaks. Again, these extra peaks could be arising from further changes in the symmetry of the carbonate molecules formed in the pores as the concentration of CO_2 increases or due to multiple interactions of the CO_2 molecules on sodium cations.

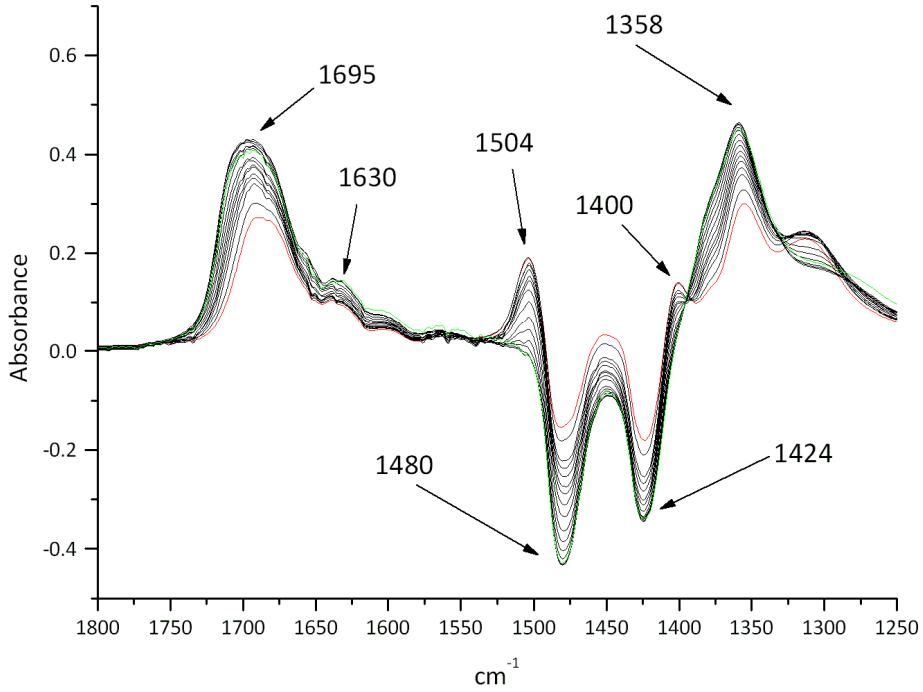

Figure 3.45 Infrared spectra of RHA-Zeolite (lower Aluminium) during dosing with CO_2 in the CO_2 peak region. Spectra were subtracted from initial spectra in order to see only changes in peaks caused by the dosing

3.5 Conclusion

In this chapter the synthesis for a bio-derived Faujasite Zeolite has been described and the process of optimisation shown. This included varied Si/Al ratios and methods of cooling. This optimised zeolite with Si/Al = 1.1 has been compared to a conventionally synthesised Zeolite X using all available techniques including XRD, porosimetry, Solid State NMR, TG-IR, and FT-IR. RHA-Zeolite was shown to have some crystalline phases of Faujasite as well as sodalite whereas Conv-Zeolite was solely Faujasite. The surface areas of both RHA-Zeolite and RHA-Zeolite (lower Al) were significantly lower than Conv-Zeolite which is likely due to the presence of strongly bound carbonate in the pores and the significant presence of the crystalline phase Sodalite which has negligible surface area when using N_2 porosimetry. An in-depth study has been presented on the comparison of the 'best' synthesised Zeolite X derived from alkali silicates from Rice Hull Ash and a Zeolite X synthesised from a commercial alkali silicate solution. Both materials exhibited surfaces which interacted with the probe molecules CO and CO_2 but there were additional interactions created by the presence of carbonate on the RHA-Zeolite. Given the

combustion process which forms the ashes creates CO_2 and occurs in the presence of basic ashes, it is likely that there will be relatively large quantities of carbonate in the ashes and therefore in the solutions. A further zeolite synthesised from ash with a higher Si/Al ratio was shown to more closely resemble the conventionally synthesised zeolite. The reduced concentration of aluminium created a structure which was closer to Faujasite and therefore showed surface properties similar to Conv-Zeolite, particularly in the *in situ* FT-IR studies.

4 Synthesis of Mesoporous MCM-41 from Biomass Ashes

4.1 Context

MCM-41, originally synthesised by Beck *et al* in 1992, was chosen as an ordered mesoporous silica to study the potential for synthesis from alkali silicates derived from biomass ashes.[46-47] MCM-41 has many applications as outlined in the Introduction (Section 1.7.2). Hui *et al* have shown that it is possible to synthesise MCM-41 materials from alkali silicate solutions from coal fly ash with properties comparable to those synthesised conventionally.[21] The synthesis methodology of Beck *et al* was mimicked and then developed in this work to obtain MCM-41 from Miscanthus bottom ash obtained from Ely Power Station. As there was a limited supply of ash, a synthesis for MCM-41 was optimised using a commercial sodium silicate (PQ Corp K120) which most closely matched the alkali silicate solution extracted from the ash (see Chapter 2 Section 2.5.1).[47] This included a study on the effect of pH in the synthesis mixture on the synthesised product.

Various methods were used to analyse the materials once synthesised. X-Ray Diffraction (XRD) patterns obtained prove that there is short-range ordering of the hexagonal structure. Nitrogen porosimetry results show the materials have high surface areas of around 1000 m^2g^{-1}. Transmission Electron Microscopy (TEM) was used to capture images of the hexagonal ordering. Thermogravimetric Analysis (TGA), in conjunction with Infrared Spectroscopy (TG-IR), illustrated the loss of water and the organic template from the structure and the further stability of the structures up to 1000 ˚C. The effect of the addition of different aluminium-containing compounds was studied using Nuclear Magnetic Resonance Spectroscopy (NMR). These aluminium-containing compounds included Red Clay, a waste product from the Bayer process, which was added to the synthesis as a raw material and was also studied as a potential source for aluminium extraction.

The synthesis of MCM-41 proceeds via a liquid crystal templating mechanism (LCT) and the organic template used is CTAB (cetyl trimethylammonium bromide) as shown in Figure 4.1.[46-47] Quarternary ammonium surfactants, such as CTAB, organise into hexagonal arrays of cylindrical micelles when in aqueous environments, organic ends in the centre and polar groups at the outside. Silicate species hydrolyse around these formations and once the material is calcined the template burns off and the hollow

hexagonal tubes are left as a stable mesoporous molecular sieve. This process is shown in Figure 4.2.

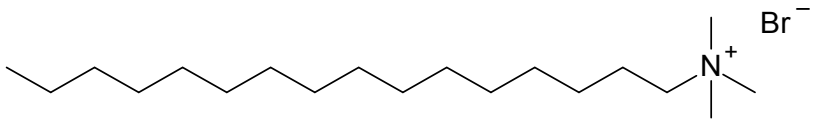

Figure 4.1 Chemical structure of CTAB

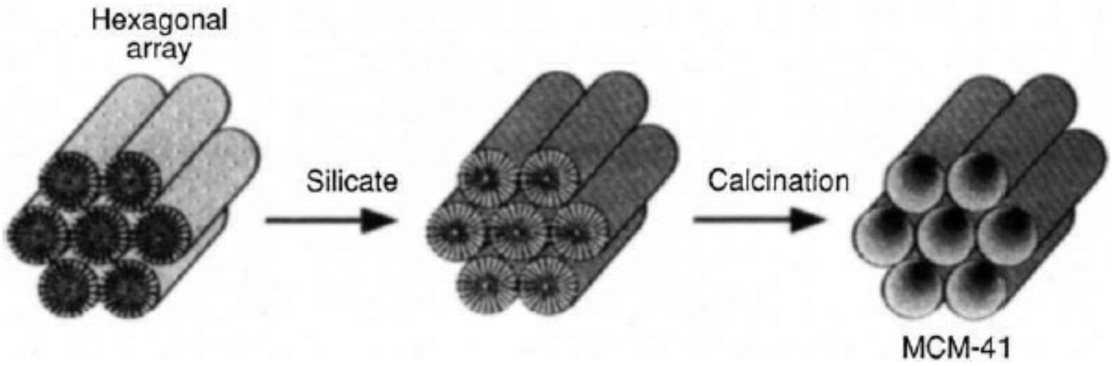

Figure 4.2 Schematic drawing of the LCT mechanism used in the synthesis of MCM-41[46]

4.2 X-Ray Diffraction and porosimetry analysis for mesoporous materials

X-Ray Diffraction analysis can provide information on whether a structure has order within its pore structure. Although many mesoporous materials such as MCM-41 show no long-range order they can exhibit short-range order and this appears as peaks in the low-angle region of an XRD pattern. MCM-41 originally synthesised by Beck *et al* showed XRD peak locations as shown in Table 4.1 with the corresponding lattice planes.[47]

Table 4.1 XRD Peaks and corresponding lattice planes for MCM-41 synthesised by Beck *et al*[47] d_{hkl} = [λ (Cu Kα radiation = 1.5406 Å)]/2 sin θ

hkl	2θ	d_{hkl} (Å)
100	2.22	39.8
110	3.85	22.9
200	4.46	19.8
210	5.92	14.9

Beck *et al*, and subsequent literature about the synthesis of MCM-41, assign the first XRD peak at around 2 2θ to the 100 plane and the successive peaks to 110, 200, and 210.[46-47] These numbers refer to planes in which there is repetition of the unit cell in the structure (Figure 4.3). The planes 100, 200, 110, and 210 are illustrated in Figure 4.4, Figure 4.5, and Figure 4.6. The lattice spacing, d_{hkl}, refers to the distance between planes (shown in Figure 4.4) and is related to the angle with which the X-Ray diffracts. D_{hkl} can be calculated for each plane using the XRD peak location 2θ value, the X-ray wavelength (for Cu K radiation X-ray diffractometer used in the work this is 1.5406 Å), and Equation 4.1. These values can provide information on the nature of ordering and crystallinity in the material.

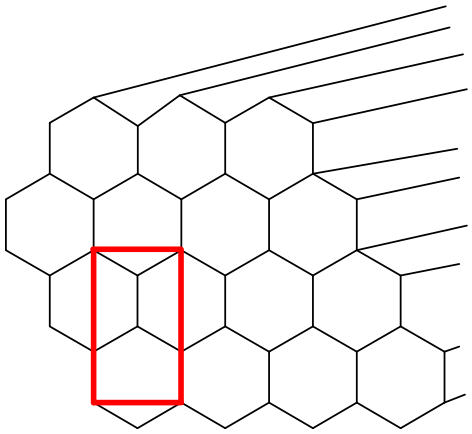

Figure 4.3 Schematic diagram showing repeating unit cell

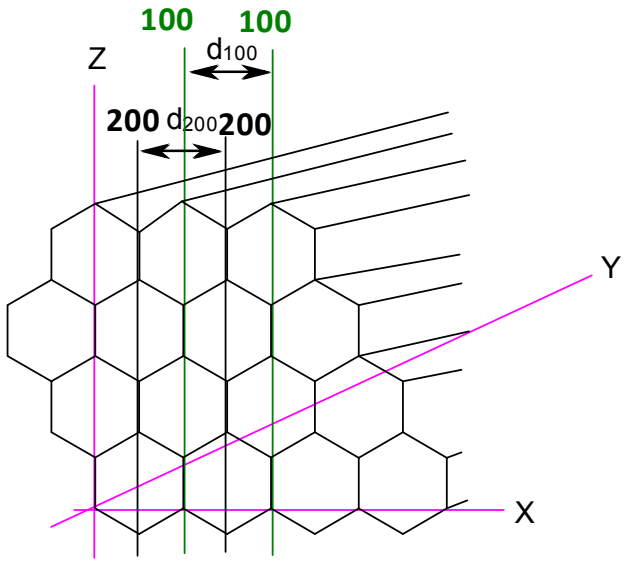

Figure 4.4 Schematic diagram of the 100 and 200 planes of MCM-41 and the d_{hkl} spacing measurement for d_{100} and d_{200}

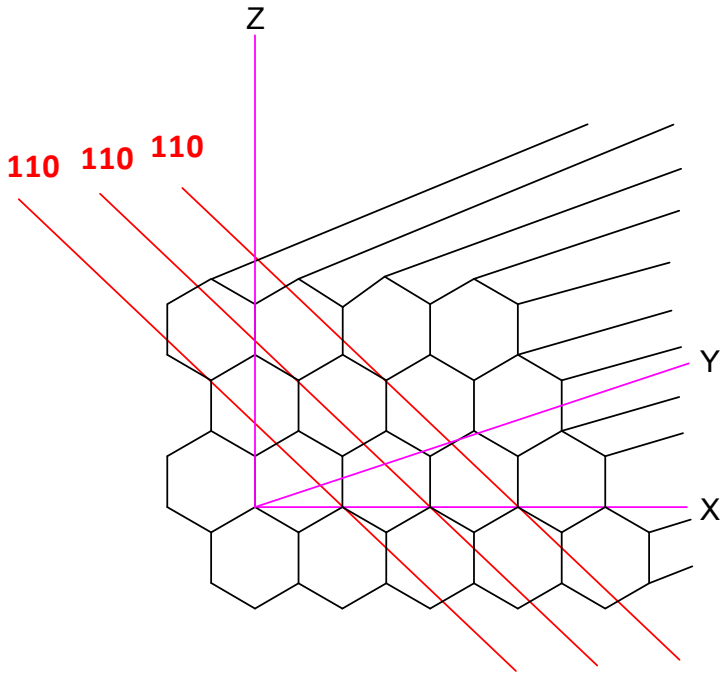

Figure 4.5 Schematic diagram of 110 planes of MCM-41

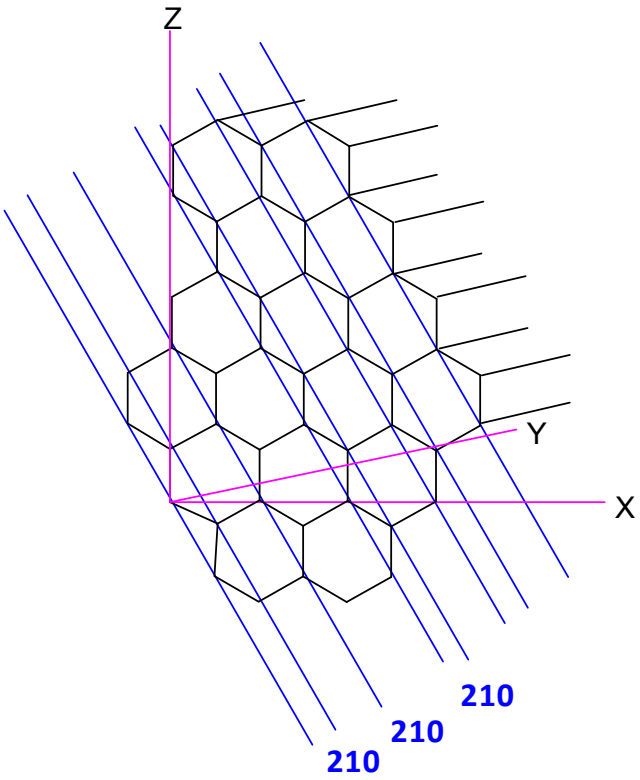

Figure 4.6 Schematic diagram of 210 planes of MCM-41

$$d_{hkl} = \frac{\lambda\ (= 1.5406\text{Å})}{2\sin\theta}$$

Equation 4.1 Lattice spacing calculation

Further pore information can be obtained by combining XRD results with porosimetry values. Shown in Figure 4.7 are the calculated pore size, average pore diameter, and pore wall thickness. The average pore diameter is calculated from porosimetry data and is an average of all pores detected by the technique. Pore size refers to diameter of each repeating pore in the lattice plane for which it is calculated (100 for all calculations in this thesis). This value combines the pore volume value from porosimetry and d_{100} value from XRD. Since the MCM-41 materials synthesised for this project should have a uniform pore structure, the pore size should remain consistent for whichever lattice plane is used. The 100 reflection was chosen as it is the first peak in the pattern and should be the most intense and thus the most straightforward to locate. Pore wall thickness is calculated using the lattice parameter (XRD) and the pore diameter (porosimetry).

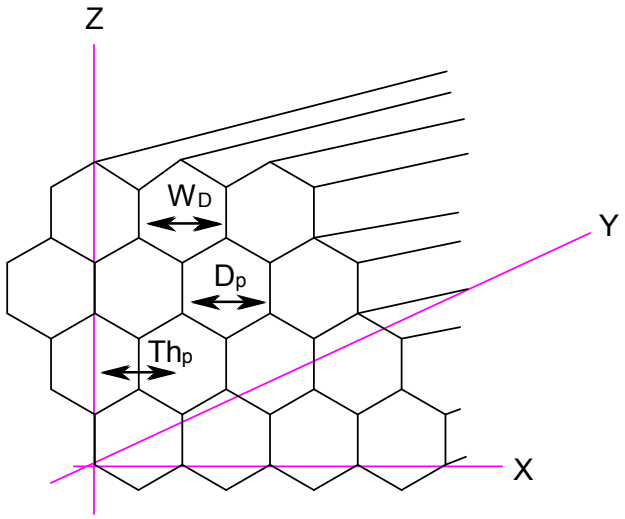

Figure 4.7 Schematic diagram showing Pore Size (W_D), Average Pore Diameter (D_P), and Pore Wall Thickness (Th_P)

4.3 Synthesis of MCM-41 in different pH environments and initial Synthesis of MCM-41 from biomass ash derived alkali silicate solution

Since the amount of bio-derived alkali silicate was limited, initial experiments were performed with a commercial alkali silicate solution which most closely resembled EBA alkali silicate from Miscanthus ash. Details of the ratios of potassium silicate solutions are described in Chapter 2 Section 2.6. The first experiments investigated the effect of pH of the initial synthesis mixture on the final crystallised product. This was in order to compare the results with those obtained by Hui & Chao who also investigated the synthesis of MCM-41 using Coal Fly Ash derived alkali silicates.[21]

4.3.1 X-Ray Diffraction Analysis (XRD)

XRD patterns obtained from MCM-41 materials synthesised for this work, shown in Figure 4.8, show peaks in a similar region of 2θ values between 2.2 and 2.6. There is a significant shoulder of high intensity at low 2θ (between 2 and 2.3 2θ) which raises the background of the 100 peak for all samples. Though this exists in the literature it seems more pronounced for patterns obtained in this work. This could be an instrumental effect as measurements were taken at very low angles at the limits of the diffractometer. The hypothesis that X-rays were travelling through the space above the sample was proven

wrong by raising the top level of the sample to above the holder and until it touched the upper sample slit and the shoulder remained in the subsequent pattern.

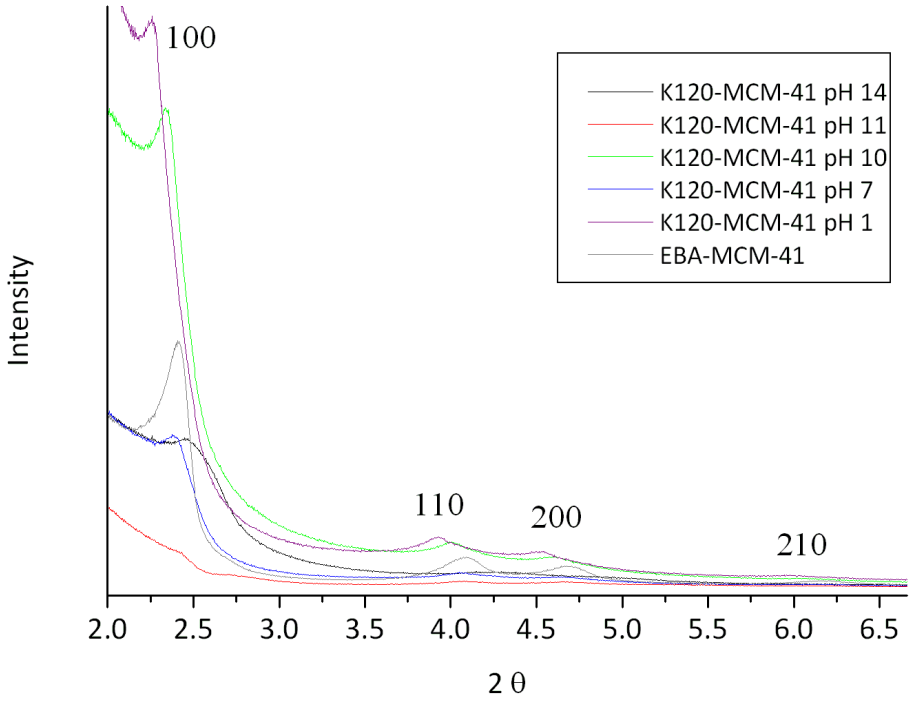

Figure 4.8 XRD Patterns for MCM-41 Synthesised at pH 14, 12, 10, 7, 1 from K120 and from EBA and their corresponding lattice planes[47]

All four peaks described in the literature for MCM-41 are apparent in Figure 4.9, a close up of the area between 3 and 6.5 2θ.

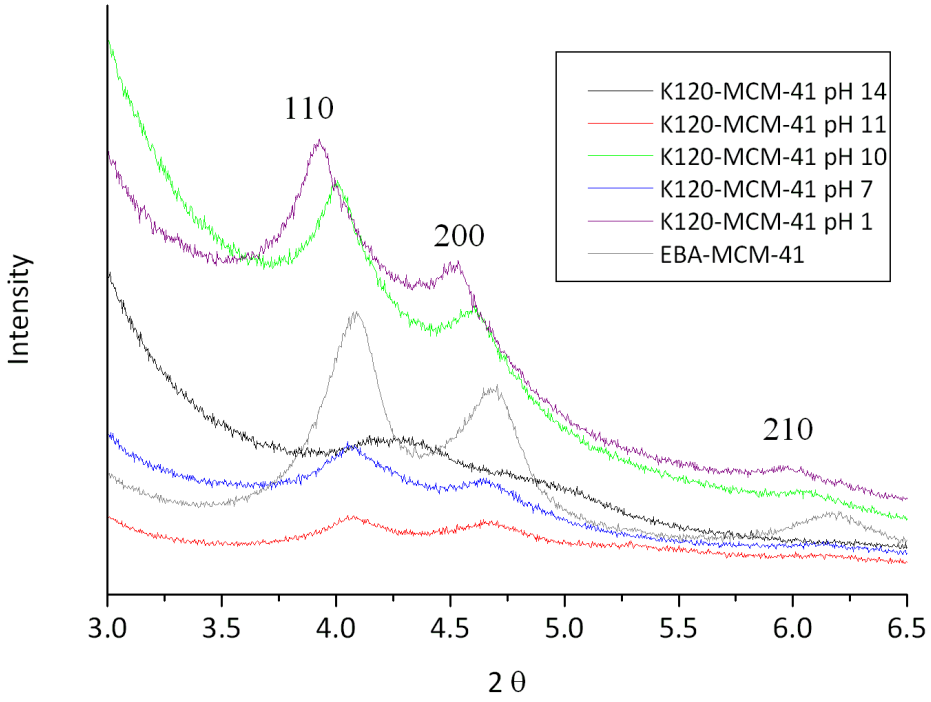

Figure 4.9 XRD Patterns for MCM-41 Synthesised at pH 14, 12, 10, 7, 1 from K120 and from EBA close up on peaks relating to lattice planes 110, 200, 210[47]

Of the K120 derived MCM-41 materials synthesised at different pH environments, those synthesised at pH 10 and pH 1 showed the most pronounced peaks for all lattice planes but nearly all samples showed at least three defined peaks (Table 4.2). MCM-41 synthesised from K120 at pH 14 had the least defined peaks which may have been due to the high pH causing redissolution and restructuring. Therefore, the K120-MCM-41 synthesised at pH 1 and pH 10 contained the most crystalline structure of the pH varied materials, K120-MCM-41 synthesised at pH 7 and pH 11 had less crystalline structure and K120-MCM41 synthesised at pH 14 had the least amount of ordered structure. That the MCM-41 synthesised at pH 1 created the same structure as those synthesised must mean a different mechanism is occurring as the environment pH is on the other side of the isoelectric point (pH ~ 2) and so cannot occur via $S^{+}I^{-}$ (Introduction Section 1.7.1).

There does not appear to be a clear correlation between pH synthesis and level of crystallinity for these MCM-41 materials as is the case for MCM-41 from coal fly ash.[21]

The MCM-41 synthesised from EBA derived bio-derived alkali silicate showed distinct peaks within the same range as those synthesised from K120. The EBA-MCM-41 was

synthesised without adjustment of pH in order to ascertain the potential for use 'as is'. The pH of the reaction mixture was 12.

All peaks for the EBA sample are at least as well defined as those for the K120-MCM-41 samples and therefore the synthesis appears to have produced a material with well ordered pores.

Overall these XRD patterns show the materials synthesised from K120 and EBA have comparable degrees of regularity.

The locations of the XRD peaks have been described in Table 4.2 and they have been matched with their appropriate lattice planes according to Beck *et al*.[47]

Table 4.2 XRD Peaks and corresponding lattice plane 2θ locations for MCM-41 synthesised from K120 at varied pH and from EBA

Si source	Synthesis pH	Lattice Plane 2θ location			
		100	110	200	210
K120	14	2.39	4.26	4.88	-
K120	11	2.42	4.07	4.67	-
K120	10	2.34	4	4.6	6.05
K120	7	2.26	4.07	4.64	6.12
K120	1	2.26	3.93	4.52	5.97
EBA	12	2.41	4.09	4.69	6.18

The calculated d_{hkl} values for K120-MCM-41 synthesised at pH 10 and EBA-MCM-41 are shown in Table 4.3 and Table 4.4 respectively.

Table 4.3 XRD Peaks and corresponding lattice planes for MCM-41 synthesised from K120 at pH 10

hkl	2θ	d_{hkl} (Å)
100	2.34	37.7
110	4	22.1
200	4.6	19.2
210	6.05	14.6

Table 4.4 XRD Peaks and corresponding lattice planes for MCM-41 synthesised from EBA

hkl	2θ	d_{hkl} (Å)
100	2.41	36.6
110	4.09	21.6
200	4.69	18.8
210	6.18	14.3

These values enable us to visualise the nature of porosity for these materials as shown in Figure 4.3. As the lattice structure in MCM-41 is two dimensional there are no lattice planes which intersect with the z-axis. The lattice planes 100 and 200 intersect the x-axis and the 110 and 210 planes intersect both the x- and y-axes. Using this knowledge and the d_{hkl} values it is possible to plot the unit cell in terms of these repeating planes and visualise the hexagonal linear pore structure. Since these values are comparable to those of the reference MCM-41 and MCM-41 structures in the literature, the structure will look similar to Figure 4.3.

4.3.2 Porosimetry

Porosimetry can provide useful and detailed information on the pore structure and surface area of MCM-41 materials. All materials synthesised for this work showed extremely high surface areas, of around 1000m^2g^{-1}, pore volumes of 0.7-1.12 cm^3g^{-1}, and pore diameters of 3.2-4.3nm which are comparable, and even larger than some of the values found in the literature using both commercial alkali silicate and other silicon sources (Table 4.5).

Table 4.5 Surface area values from porosimetry as found in the literature

	pH	Surface Area S_{BET}	Pore Volume V_p	Average Pore Diameter D_p
		m^2g^{-1}	cm^3g^{-1}	nm
Rice Hull Ash[69]		1100	0.869	2.95
Rice Hull Ash [71]		602		
Sodium Silicate [69]		1,180	0.91	2.95
Sodium Silicate (N brand, 27.8% silica, P.Q. Corp.) [47]		1040	not given	not given
Coal Fly Ash[21]	1.16	1149	0.6	not given
Coal Fly Ash[21]	6.9	953	0.9	not given
Coal Fly Ash[21]	11.06	996	0.7	not given
Power Plant Bottom Ash [64]	-	847	0.7	3.0

Porosimetry results for K120-MCM-41 and EBA-MCM-41 materials synthesised at different pH are shown in Table 4.6. MCM-41 synthesised at neutral pH from commercial alkali silicate K120 showed the lowest surface area at 880 m^2g^{-1} and MCM-41 materials synthesised in more basic conditions had the highest surface areas of between 1010 m^2g^{-1} and 1080 m^2g^{-1} although all surface area values fall within a similar range when considering error related to porosimetry measurement and calculations. It is also sometimes difficult to judge the accuracy of surface area values in the literature as there is no way to tell if the calculated values are corrected for BET linearity. There is no obvious correlation between synthesis pH and porosity of the samples and this was also the case for Hui *et al* and their coal fly ash samples.[21]

All samples showed similar pore diameters (Table 4.6) proving the synthesis to be reproducible despite changes in synthesis pH. This is confirmed by the consistency of XRD peak locations (Table 4.2). Literature values are also included in Table 4.5 and are comparable to the results shown.[64, 69-70]

Table 4.6 Porosimetry results for MCM-41 synthesised from K120 at varied pH and EBA

Si Source	pH	BET Surface Area S_{BET}	Pore Volume V_p	Average Pore Diameter D_p
		m^2g^{-1}	cm^3g^{-1}	nm
K120	14	1010	0.8	3.2
K120	12	1055	1.1	4
K120	10	1080	0.9	3.4
K120	7	880	0.7	3.4
K120	1	920	0.8	3.3
EBA	12	1043	1.12	4.3

Shown in Figure 4.10 is a typical isotherm for the materials synthesised from K120, in this case at pH 10. It shows a steep increase of nitrogen adsorption between 0.3 and 0.38 relative pressure of 100 cm^3g^{-1} (300 cm^3g^{-1} to 400 cm^3g^{-1}) N_2 which relates to mesopores with a small range of sizes.[80] There is also some micropore absorption shown in the initial steep rise at 0 relative pressure up to 150 cm^3g^{-1} and some further meso and macro porous adsorption at higher relative pressures. There is a Type B or H4 hysteresis loop shown by the desorption branch remaining at higher adsorbed volume than the adsorption branch for the same relative pressure over a range of relative pressures above 0.42 P/Po which then joins the adsorption branch and remains at the same values at lower relative pressures. This behaviour is evidence of narrow mesopores open at both ends.[81]

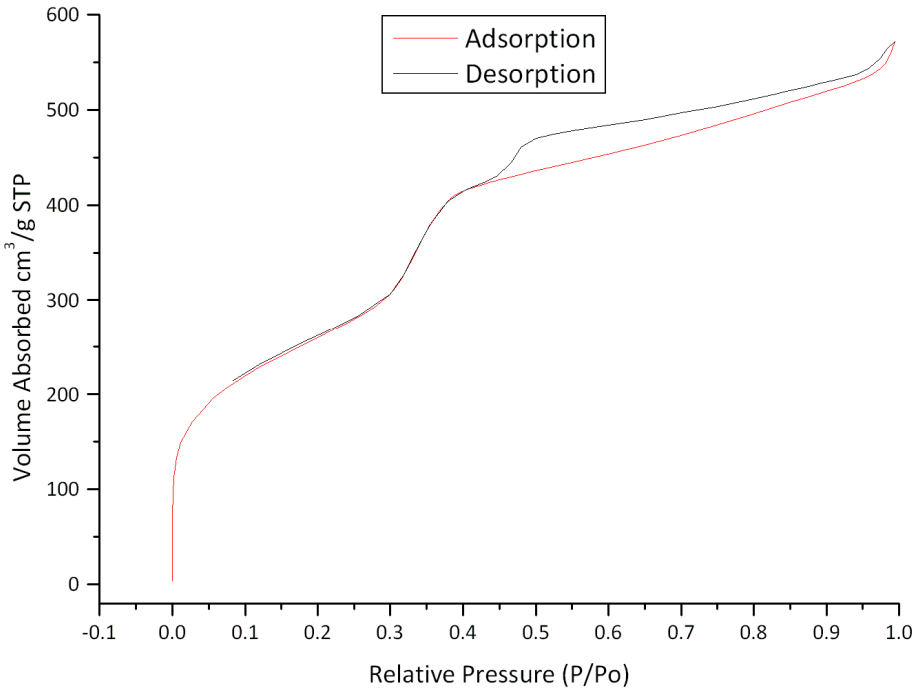

Figure 4.10 N_2 Adsorption Desorption Isotherm for K120-MCM-41 at pH 10

The bio-derived alkali silicate sample, EBA-MCM-41, which was also synthesised in a more basic environment (approximately pH 12), had a surface area of 1043 m^2g^{-1}. The isotherm is very similar to that of MCM-41-K120 (pH10) and displays the same features as described above (Figure 4.11). Both isotherms are similar to those found in the literature.[21, 55]

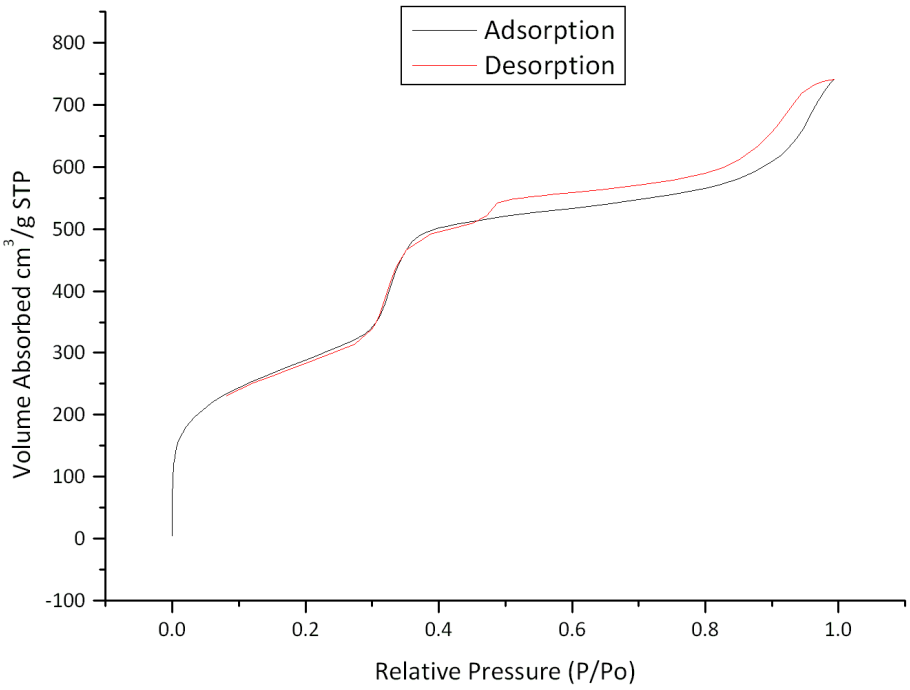

Figure 4.11 N_2 Adsorption Desorption Isotherm for EBA-MCM-41 at pH 12

Combining XRD 2θ peak locations with porosity data it is possible to calculate pore size and wall thickness.[21, 118]

The lattice spacing, d_{100} (from XRD peak location), value can be used, in conjunction with the pore volume, V_p (calculated using porosimetry), to calculate the pore size W_d of the ordered pores in the 100 lattice plane (Equation 4.2).

$$W_d = cd_{100}\left[\frac{\rho Vp}{1 + \rho Vp}\right]^{\frac{1}{2}}$$

Equation 4.2 Pore size calculation where constant c = 1.155 and silica wall density ρ = 2.2 g cm^{-3}.[21, 118]

The lattice parameter, a_0, can also be calculated from the lattice spacing as in Equation 4.3.

$$a_0 = \frac{2}{\sqrt{3}} d_{100}$$

Equation 4.3 Lattice parameter calculation[119]

Pore wall thickness, Th_p can be calculated by subtracting the pore diameter, D_p (obtained from porosimetry), from the lattice parameter, a_0 (obtained from XRD) (Equation 4.4).[119]

$$Th_p = a_0 - D_p$$

Equation 4.4 Pore wall thickness calculation[119]

The pore size distributions for EBA-MCM-41 and K120-MCM-41 (pH 12) are shown in Figure 4.12 and Figure 4.13 respectively. The pore size distribution for EBA-MCM-41 shows a symmetric peak with a range of 2.5 – 3.5 nm and peak around 2.85 nm. For the K120-MCM-41 (pH 12) sample the curve is asymmetric and the range and peak are lower, 2.25 – 3.25 nm and 2.8 nm respectively. Both materials have average pore sizes which fit within the range of the other materials and those in the literature.[21, 54-55, 71]

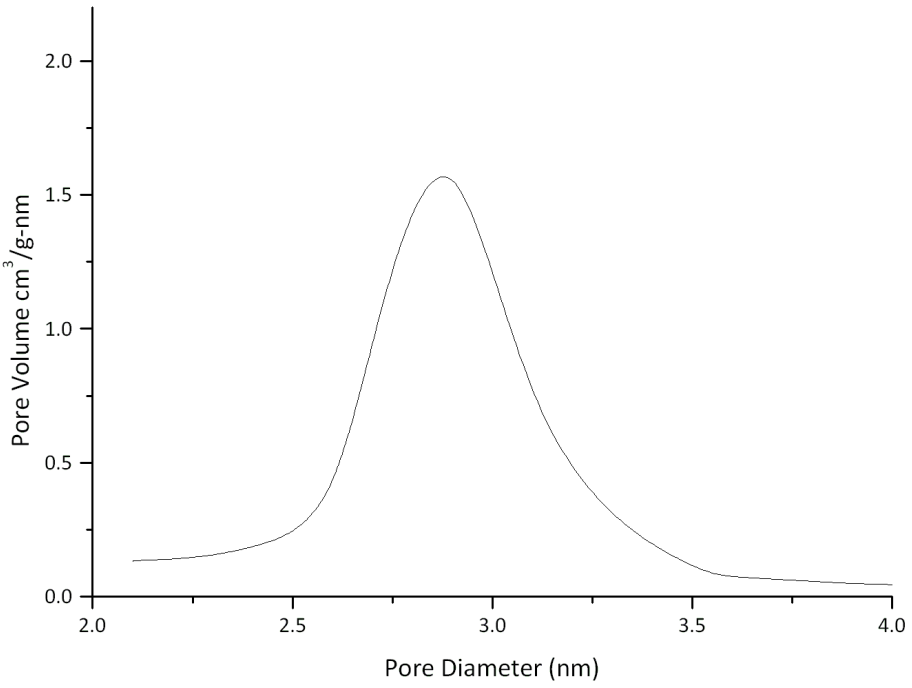

Figure 4.12 BJH adsorption pore size distribution for EBA-MCM-41

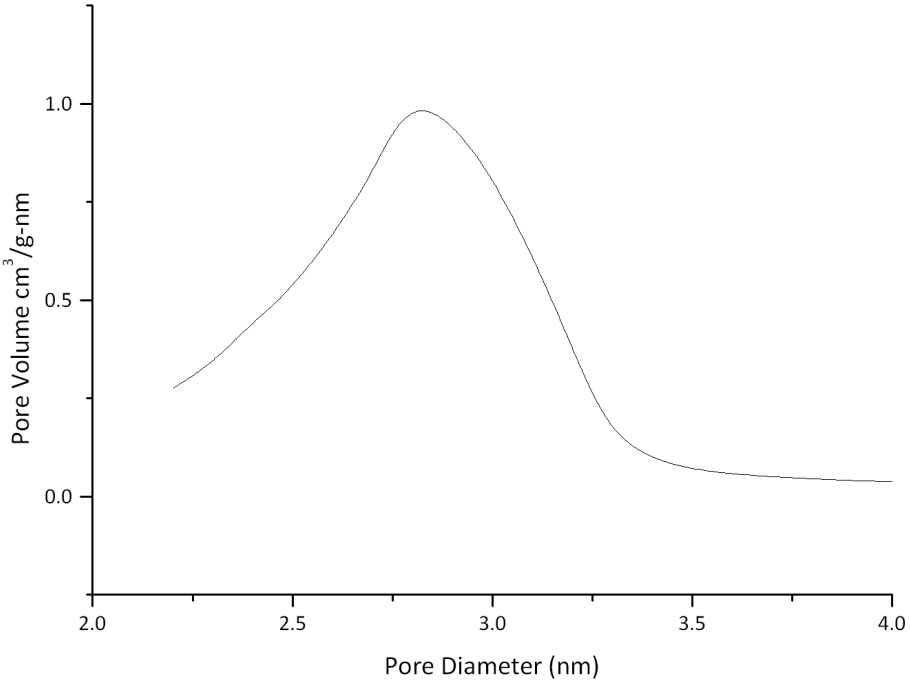

Figure 4.13 BJH adsorption pore size distribution for K120-MCM-41 (pH 12)

All MCM-41 materials synthesised from K120 had similar pore sizes (W_d) of around 33-36 Å and pore wall thicknesses (Th_p) of around 12-14 Å. Pore size and pore wall thickness values for EBA-MCM-41 also fell within this range (Table 4.7). Average pore diameter was taken as the mode.

Table 4.7 Porosimetry, XRD and calculated values for surface properties of synthesised MCM-41. Results are compared with values for Coal Fly Ash MCM-41 from Hui and Chao.[21]

Silica source	pH	2θ	d_{100}	Lattice Parameter a_0	S_{BET}	Average Pore Diameter D_p	Pore Size W_d	Pore Wall Thickness Th_p
			Å	Å	m^2g^{-1}	Å	Å	Å
K120	14	2.51	35.2	40.6	1010	27.5	32.4	13.1
	12	2.43	36.4	42.0	1055	28	35.3	14
	10	2.45	36	41.6	1080	30	33.9	11.6
	7	2.39	36.9	42.6	880	30.5	33.2	12.1
	1	2.26	39.1	45.1	920	30.5	36	14.6
EBA	12	2.36	37.4	43.2	1019	28.5	36.4	14.7
Coal Fly Ash[21]	1.16			36	1149		27	9
Coal Fly Ash[21]	6.9			39	953		32	7
Coal Fly Ash[21]	11.06			40	996		31	9

4.3.3 TEM

Transmission Electron Microscopy is a useful tool for obtaining images of structures at very high magnifications. TEM images, shown in Figure 4.14 and Figure 4.15, showed all samples contained evidence of hexagonal arrays and uniform pores. This is consistent with the literature which shows hexagonal arrays of ordered pores of diameter 20-100 Å.[21, 46-47] TEM pore sizes were measured to be approximately 3 nm in diameter. This confirms the porosimetry data and combined porosimetry and XRD calculations which gave pore diameters of around 3 nm and pore sizes of around 3.5 nm. Therefore there is no clear difference in the hexagonal pores of these materials synthesised at different pH values.

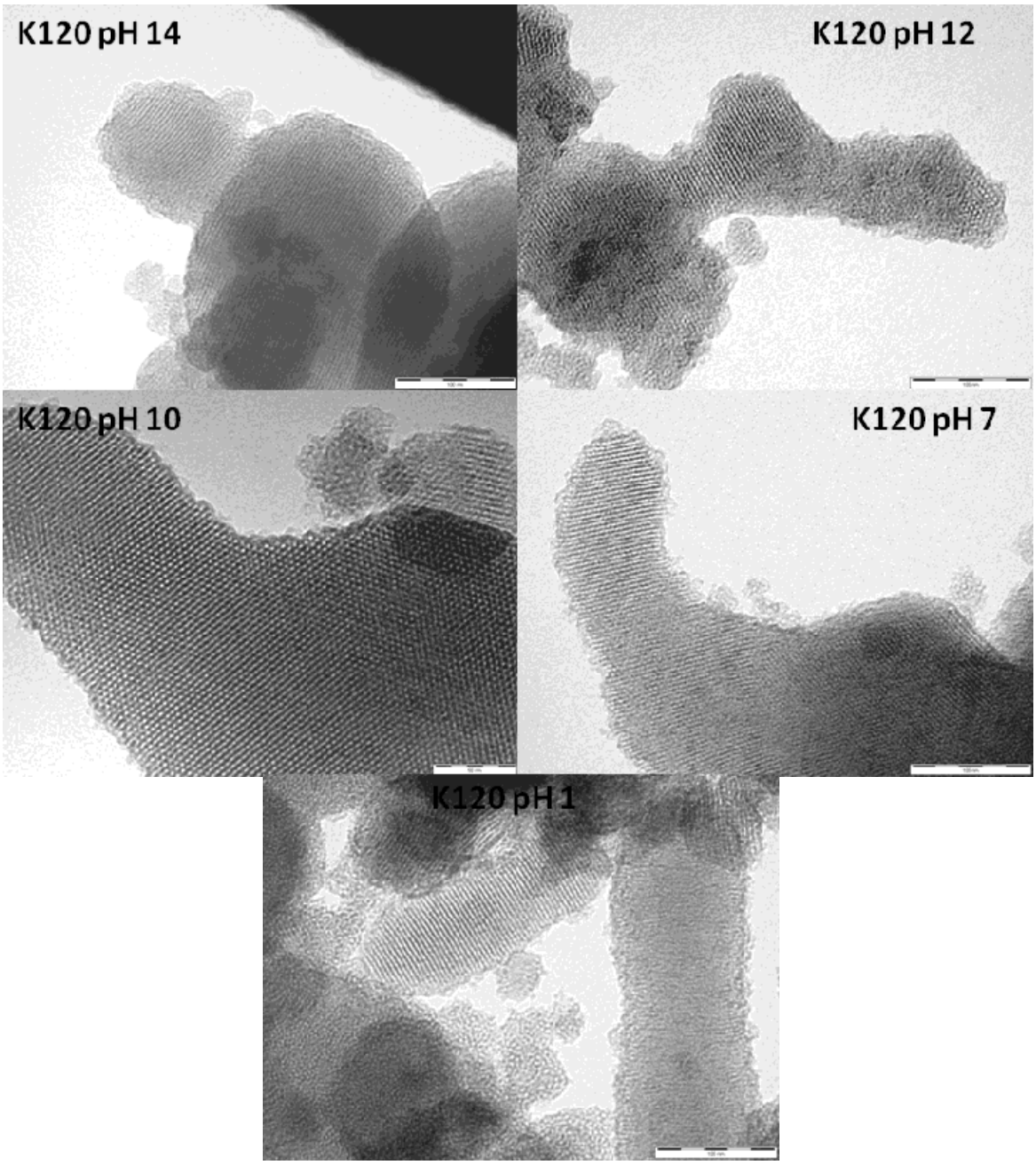

Figure 4.14 TEM Images of MCM-41 materials synthesised from K120 at different pH values. Whole scale bar is 100nm long.

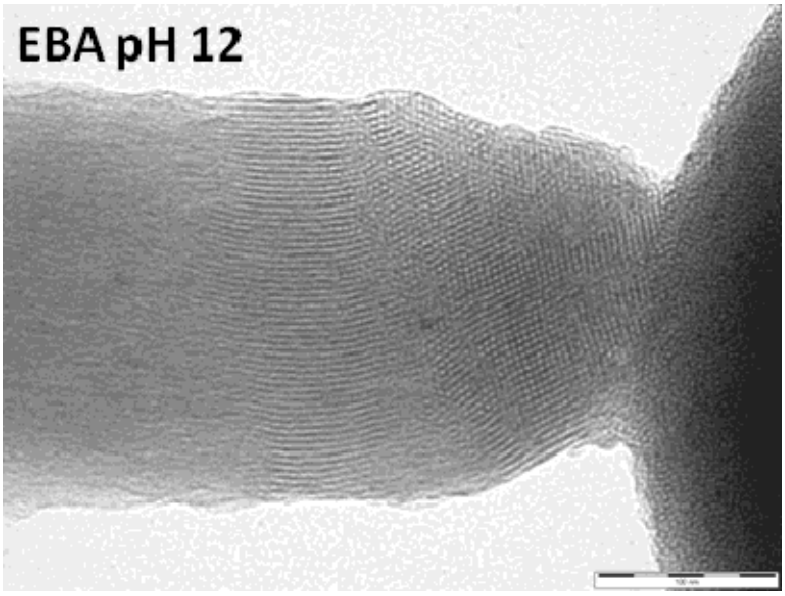

Figure 4.15 TEM Images of MCM-41 materials synthesised from EBA bio-derived alkali silicate at pH 12. Whole scale bar is 100nm long.

4.3.4 Thermogravimetric Analysis with Infrared Absorption Spectroscopy (TGA-IR)

Thermogravimetric analysis (TGA) is a useful technique for investigating a material as it highlights the temperatures at which the material rearranges and decomposes to form other compounds as gases. It can also provide information on the thermal stability of a material. Coupled with infrared spectroscopy (TGA-IR) it is possible to study these gases via their functional group absorption to determine what molecules are being expelled from the sample. This technique occurs under an atmosphere of nitrogen.

Schüth *et al* describe the decomposition of CTAB in air as follows.[120] The calcination should involve three steps in the decomposition of CTAB. An endothermic elimination occurs between 150 ˚C and 250 ˚C which removes 46% of the template through evaporation of hexadecene and trimethylamine (Hoffman Degradation, Figure 4.16). The second step involves exothermic successive fragmentation of the carbon chain and oxidation to form CO_2, NO_2, and H_2O gases between 250 ˚C and 300 ˚C. The final stage occurs between 300 ˚C and 350 ˚C although the template is not fully removed until a sustained period at 550 ˚C. Oxidation occurs and converts the remaining organic components to CO_2 and H_2O.[120] Sumiya *et al* studied the calcination and thermal degradation of CTAB in MCM-41 in air using FT-IR spectroscopic analysis of the sample and found peaks assigned to the various organic functional groups in CTAB disappear in

the infrared spectra after 400 ˚C.[121] It is likely that the process will be similar for analysis using TGA except there will be no oxidation by oxygen in the atmosphere.

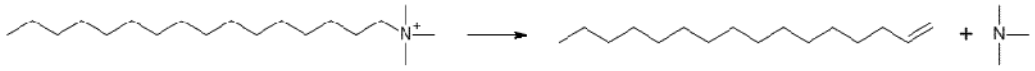

Figure 4.16 Initial step of degradation of CTAB[120]

A recent TGA study on fly ash derived MCM-41 reports three to four stages of mass loss.[122] These stages approximately consist of thermal desorption of adsorbed water (25 – 100 ˚C), decomposition of CTAB (breaking of hydrocarbon chain) (100 – 355 ˚C), residual CTAB decomposition and water loss associated with condensation of silanol groups (355 – 600 ˚C), and residual silanol condensation (600 – 840 ˚C).[122]

TGA-IR was conducted on the as-synthesised EBA-MCM-41 sample with the CTAB template present (Figure 4.17). Significant weight losses occurred up to 120 ˚C which can be assigned to water desorption.[122] There is then a continuous decrease of mass from 120 ˚C to 300 ˚C which can be designated as the degradation of the template (CTAB) followed by residual CTAB degradation and condensation of silanol groups from 300 ˚C to 500 ˚C. A further small mass loss occurs at higher temperature which can be assigned to residual condensation of silanols.[122]

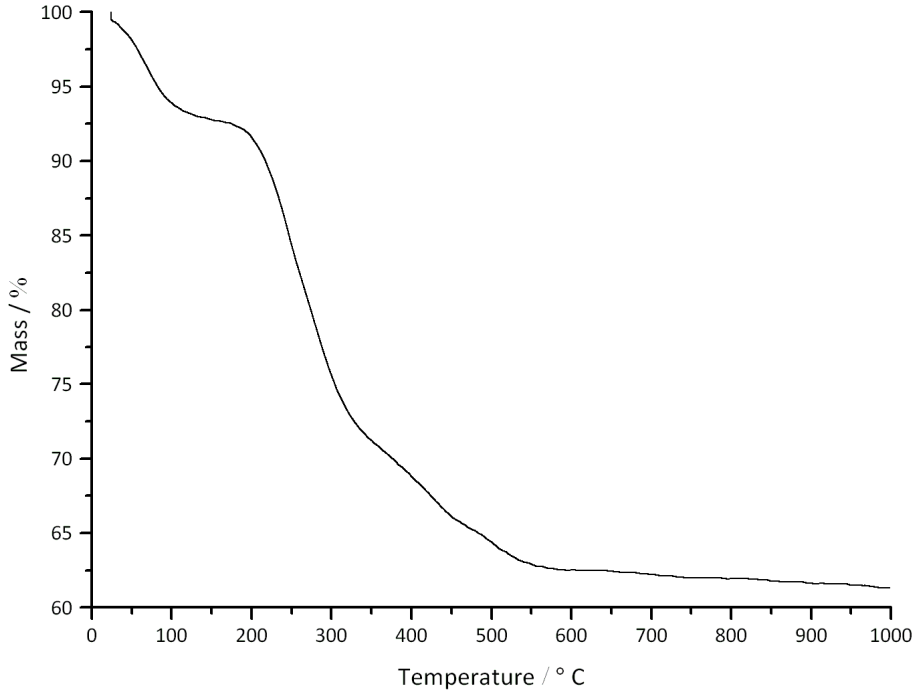

Figure 4.17 TGA of EBA-MCM-41 showing mass loss at increasing temperatures

In this study FT-IR was conducted on the gases produced from the sample and therefore there should be similar peaks as the products of the calcination leave the sample.

Shown in Figure 4.18 are three infrared spectra of the exit gases from the thermal analysis of EBA-MCM-41 at three temperatures.

At 250 ˚C there is the C-H stretching peaks at 2932 cm^{-1} and 2865 cm^{-1} and possibly an aldehyde (=C-H) peak at 2780 cm^{-1}, carbonyl (C=O) peak at 1773 cm^{-1}, and amine (C-N) peaks at 1050 cm^{-1} and 1246 cm^{-1}. At 400 ˚C the only molecules appear to contain only C-H stretching (2932 cm^{-1} and 2865 cm^{-1}). At 1000 ˚C CO_2 appears to be the main gas appearing in the spectra (2340 cm^{-1}). There are no peaks for water appearing from adsorbed water or condensation of silanol groups. This implies there was very little adsorbed water or silanol groups in the sample. It appears that the thermal degradation of the material solely relates to the degradation of CTAB, initially into nitrogen containing gases and latterly purely as alkanes and finally as CO_2.

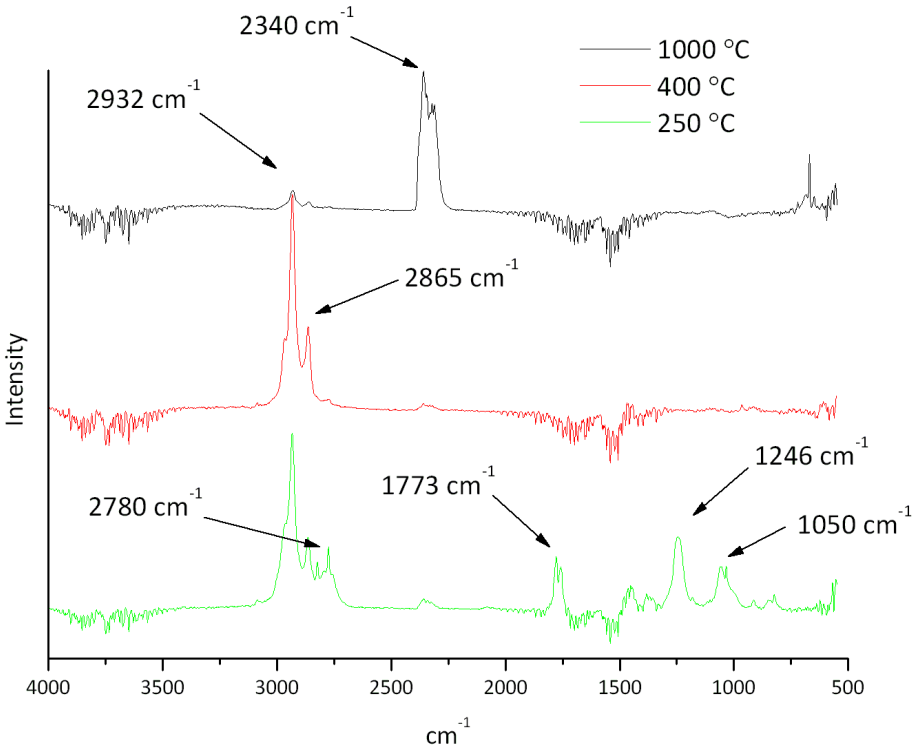

Figure 4.18 IR spectra at three temperatures of exit gases from thermal degradation of EBA-MCM-41

Combining results from XRD, porosimetry, TEM, and TGA-IR results it is clear that the MCM-41 pore structure can be synthesised over a range of pH values with only small changes to the physical properties occurring and with no clear trends. It has also been shown that it is possible to synthesise MCM-41 from alkali silicate derived from Miscanthus biomass ashes.

The synthesis is robust enough that the materials produced at different pH values and from different silicon sources have the same structure with the same pore shape and size, within instrumental error (Section 6.5).

4.4 Introduction of Aluminium into bio-derived MCM-41 synthesis

In order to make the bio-MCM-41 materials more useful for catalysis it is necessary to improve functionality on the surface of the pores. This can be done by introducing aluminium into the silica matrix. As aluminium has one fewer electron than silicon, when it bonds to four oxygens within the tetrahedral structure it creates a charge imbalance

which necessitates the presence of a counter cation such as sodium, potassium, or hydrogen.

Beck *et al*. introduced aluminium into their synthesis for MCM-41 using sodium aluminate, aluminium sulphate, and Catapul alumina.[47] In this work the addition of red clay is investigated as a waste product source of aluminium. Red Clay is described in the Introduction (Section 1.8) as a waste product which shows promise as a source of aluminium and other metals. This source of aluminium was compared with additions of sodium aluminate or aluminium hydroxide.

Red Clay was sourced from India (via Glasgow) and has been discussed in papers by Hargreaves *et al* including elemental composition and potential applications.[74-76] The published Initial Inductively Coupled Plasma Elemental Analysis (ICP-AES) results for a sample of red clay are shown in Table 4.8.[75] Also shown in this table are the XRF elemental component results of the sample received for use in this project. Both techniques show significant concentrations of aluminium, silicon, and sodium are contained in the Red Clay.

Table 4.8 Elemental composition (ICP-AES) of red clay samples (wt%) from Hargreaves *et al*. [75] and the XRF elemental analysis of the as received sample used in this project

Sample Code	Major Elements										
	SiO_2	Al_2O_3	Fe_2O_3	TiO_2	CaO	MgO	Na_2O	K_2O	P_2O_5	MnO	LOI
RM4[75]	16.4	10.44	42.7	6.44	2.85	1.56	3.72	0.05	0.02	-	15.3
RM6[75]	12.4	10.12	36.4	18.7	2.65	2.52	3.85	0.09	0.02	-	12.8
RM7[75]	14.6	23.51	36.79	0.74	1.18	0.07	6.08	0.02	0.15	0.12	16.47
Red Clay	15.7	27.7	39.2	1.62	1.39	0.0	12.7	0.07	0.0	0.11	1.51

Initially the red clay was tested in the synthesis as a raw material (without any treatment) alongside other aluminium sources. It was added to the synthesis 'as is' before the crystallisation stage (Section 6.3.2). The solutions were not adjusted to a certain pH and thus the syntheses occurred at the basic pH of the solutions (around pH = 12).

Si/Al ratios in the initial synthesis mixtures are detailed in Table 4.9. These are calculated using the silicon concentration method (detailed in Chapter 2 Section 2.5) in order to gain a specific mass of silicon contained in the volume of alkali silicate solution and calculations of the relative concentrations of aluminium in the compounds used. XRF data of red clay (Table 4.8) was used to calculate the weight of aluminium used in the synthesis. The higher Si/Al ratios for Red Clay were due to a lower concentration of aluminium within the red clay (same mass of aluminium source used for all three samples).

Table 4.9 Si/Al ratios of synthesis mixtures containing different Aluminium Sources

	Red Clay	Sodium Aluminate	Aluminium Hydroxide
K120	1.52	0.68	0.64
EBA	1.52	0.68	0.64

4.4.1 Nuclear Magnetic Spectroscopy (NMR)

NMR is a useful technique for ascertaining the nature of bonding of particular elements in a material. ^{27}Al-NMR of the MCM-41 samples will provide information on the level of incorporation of aluminium into the structure. A peak at 0 ppm represents the presence of extra-framework octahedral aluminium, i.e. aluminium which has not integrated into the structure. Peaks shifted to higher ppm (53-55 ppm) represent aluminium bonded tetrahedrally to the silica within the MCM-41 structure. A peak at 32 ppm is, thus, likely to be 5-coordinate bonded aluminium.[107]

On examination of the aluminium NMR results of the samples synthesised for this project, (Figure 4.19 and Figure 4.20) all aluminium sources integrated into the MCM-41 samples to make tetrahedrally bonded aluminium (53-55 ppm) but none of them did so completely as there was still the presence of extra-framework aluminium for all samples identified by the peaks at 0 ppm. Sodium aluminate was the most effective aluminium source for integration into the MCM-41 silica matrix for both EBA- and Conv- MCM-41 samples as the shifted peak had a much higher intensity than the extra-framework peak. Aluminium hydroxide and red clay both integrated into the structure but to a lesser degree than the sodium aluminate. Their two NMR peaks are more evenly split. The tetrahedrally bonded aluminium produces a more intense peak than the extra-framework

aluminium but the latter is a wider peak which may imply a significant presence. The two materials synthesised with aluminium hydroxide show the presence of a third peak at 32 ppm, a shoulder in the EBA-MCM-41 ($Al(OH)_3$) and a pronounced peak for the conv-MCM-41 ($Al(OH)_3$). This relates to a 5-coordinate orientation which may be due to an additional interaction with a hydroxyl group on the surface (Figure 4.21).[123]

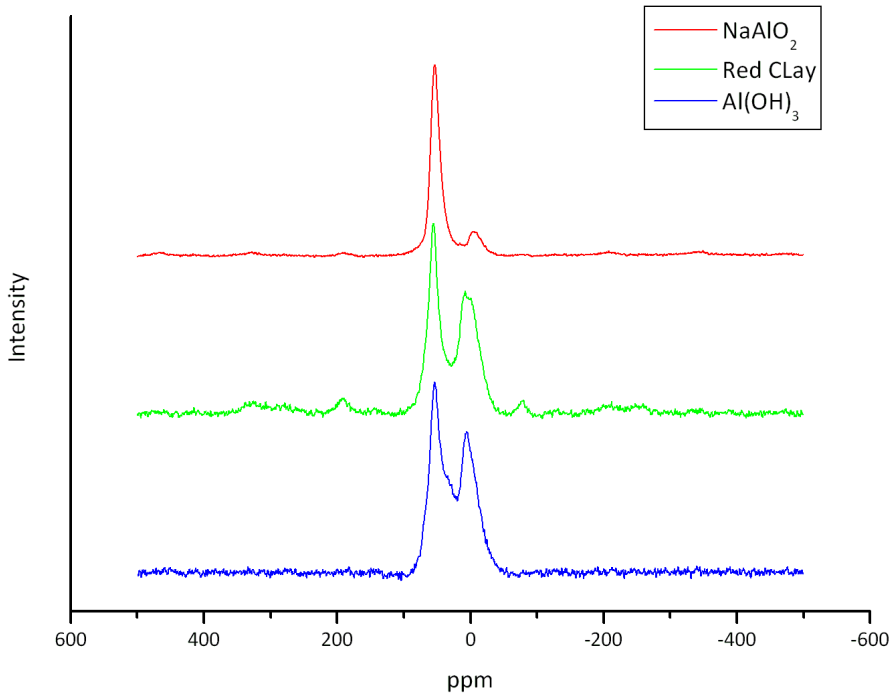

Figure 4.19 Aluminium NMR peaks of EBA-MCM-41 synthesised with different aluminium sources

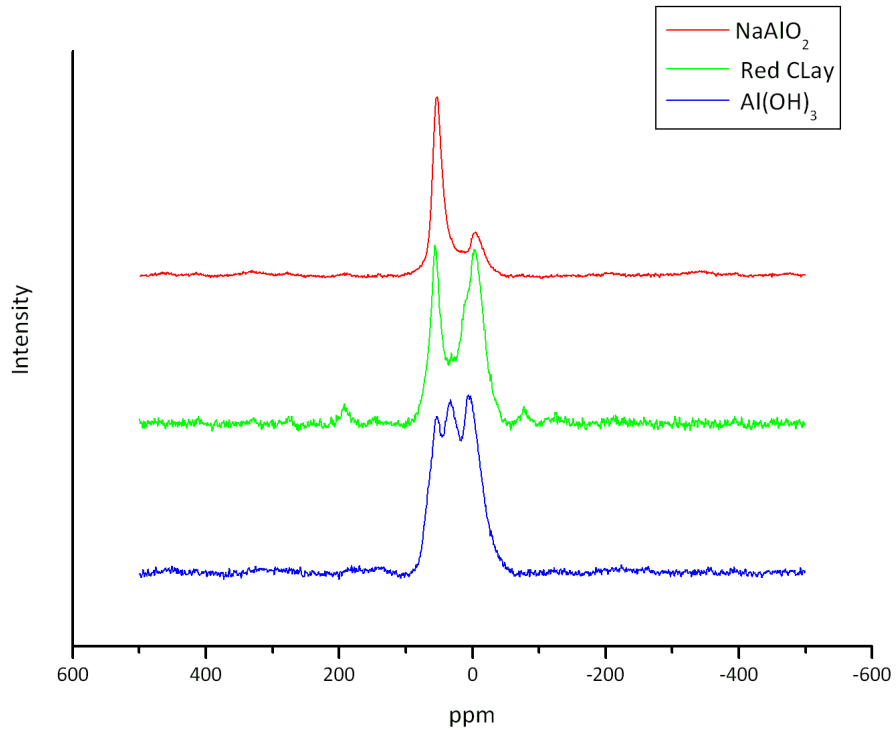

Figure 4.20 Aluminium NMR peaks of Conv-MCM-41 synthesised with different aluminium sources

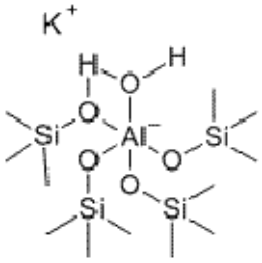

Figure 4.21 Diagram of 5 coordinate aluminium within MCM structure[123]

4.4.2 Transmission electron microscopy (TEM)

TEM can enable an image to be taken of the materials on a nanometer scale. Such an image was taken of EBA-MCM-41 (Red Clay) and there is clearly linearity within the pore system and an ordered array of hexagonal pores (Figure 4.22).

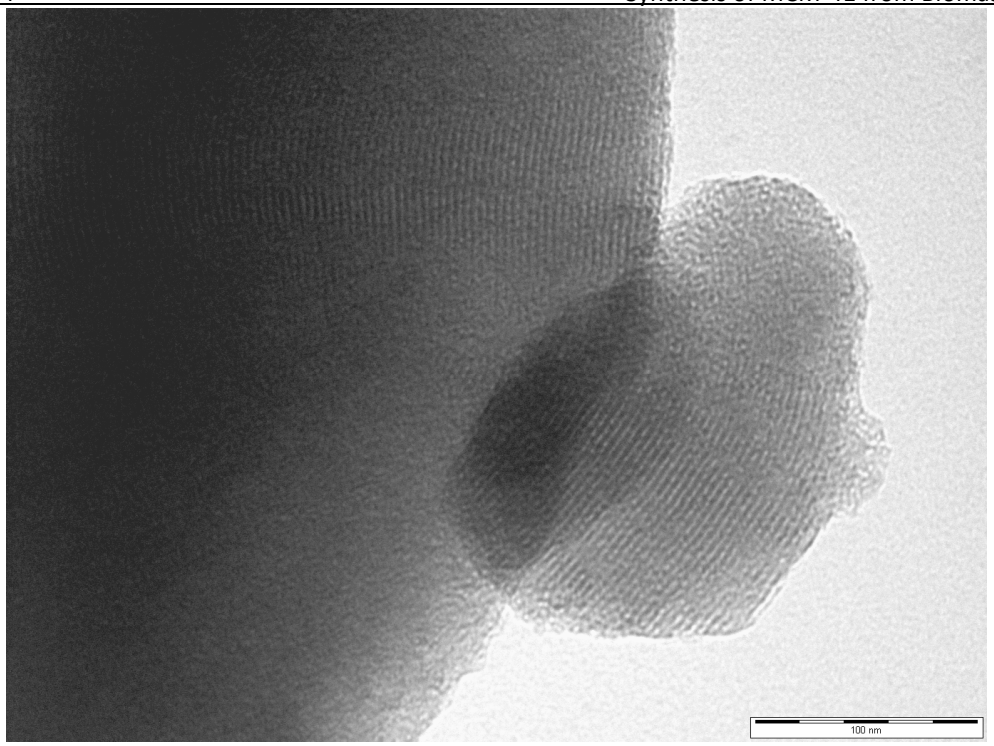

Figure 4.22 TEM image of EBA-MCM-41 (Red Clay). Scale bar in 100 nm sections

4.4.3 N_2 Porosimetry

Porosimetry results (Table 4.10) showed all materials had reasonably high surface areas. There was a drop in surface area for samples on addition of the aluminium sources of around 100 m^2g^{-1} – 200 m^2g^{-1} except for EBA-MCM-41 (Sodium Aluminate) which lost around 400 m^2g^{-1}. This is likely to be due to the presence of aluminium weakening or collapsing the structure.

All pore diameters fall within the range 2.5 – 3.5 nm (Figure 4.23) and so the effect of aluminium has not been on the nature of the pore structure but on the level of crystallinity. The structures may be less stable at higher temperatures and collapse during the calcination step of the synthesis.

The difference in pore volumes of the samples reflects that for surface areas with a marked decrease for all materials containing aluminium and a significant decrease for EBA-MCM-41 (Sodium Aluminate).

Table 4.10 Porosimetry Table for MCM-41 synthesised with different aluminium sources

		Aluminium Source	Surface Area	Pore Volume	Average Pore Diameter
			m^2g^{-1}	cm^3g^{-1}	nm
EBA	0	None	1025	1.07	2.9
	1	Sodium Aluminate	607	0.54	3.1
	2	Red Clay	812	0.79	3.1
	3	Aluminium Hydroxide	913	1.06	2.9
K120	0	None	966	1.08	2.7
	1	Sodium Aluminate	823	0.81	3.0
	2	Red Clay	852	0.72	2.8
	3	Aluminium Hydroxide	930	0.67	3.1

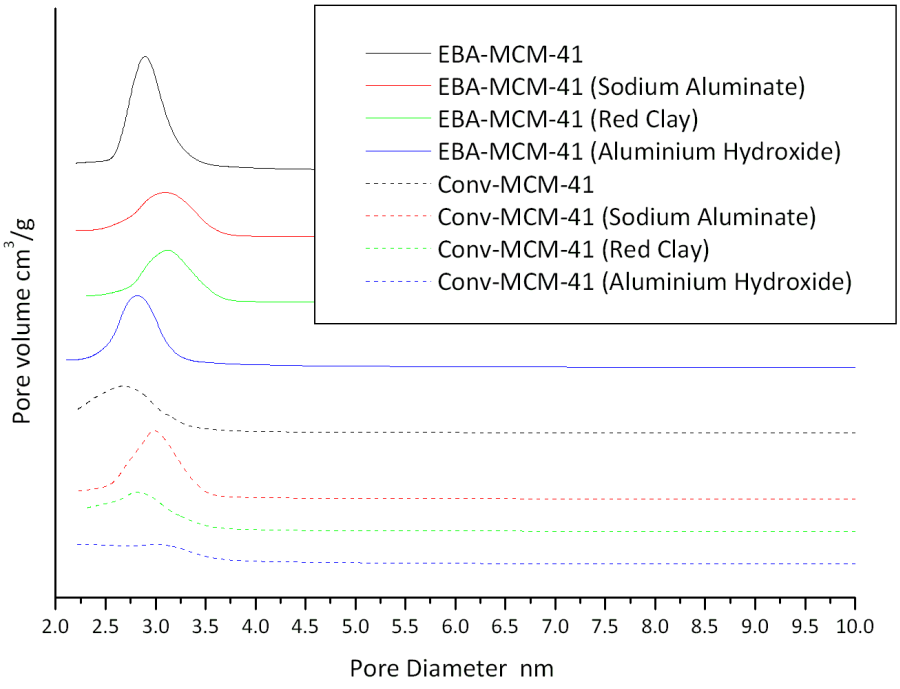

Figure 4.23 BJH Adsorption Pore size distribution for EBA-MCM-41 and Conv-MCM-41 with aluminium sources (sodium aluminate, red clay, and aluminium hydroxide)

It is important to consider the potentially significant effect of undissolved red clay residue on the porosimetry results. There may be some presence of precipitated or undissolved sodium aluminate or aluminium hydroxide but these will be at a much lower magnitude than that of red clay.

4.4.4 Effect of red clay residue on Porosimetry results

In order to examine the effect of red clay residue on the porosimetry results of the MCM-41 materials, red clay was subjected to conditions similar to those which occur during the MCM-41 synthesis. These include a strongly basic pH environment and the presence of the surfactant organic template CTAB (Section 6.3.2.1). The red clay was then analysed before and after to investigate the effect on the material. Red clay was tested using porosimetry and showed a very small amount of porosity initially and following treatment described with NaOH (Figure 4.24 and Table 4.11). The surface area and pore volume was found to double on treatment with KOH and CTAB. Since the values for red clay are below 5% of the surface areas of MCM-41 and are mainly textural, the level of porosity is negligible in comparison. Therefore the presence of significant mass of this material along with the synthesised MCM-41 in samples will have a negative effect on the recorded porosity for MCM-41 materials synthesised in this way.

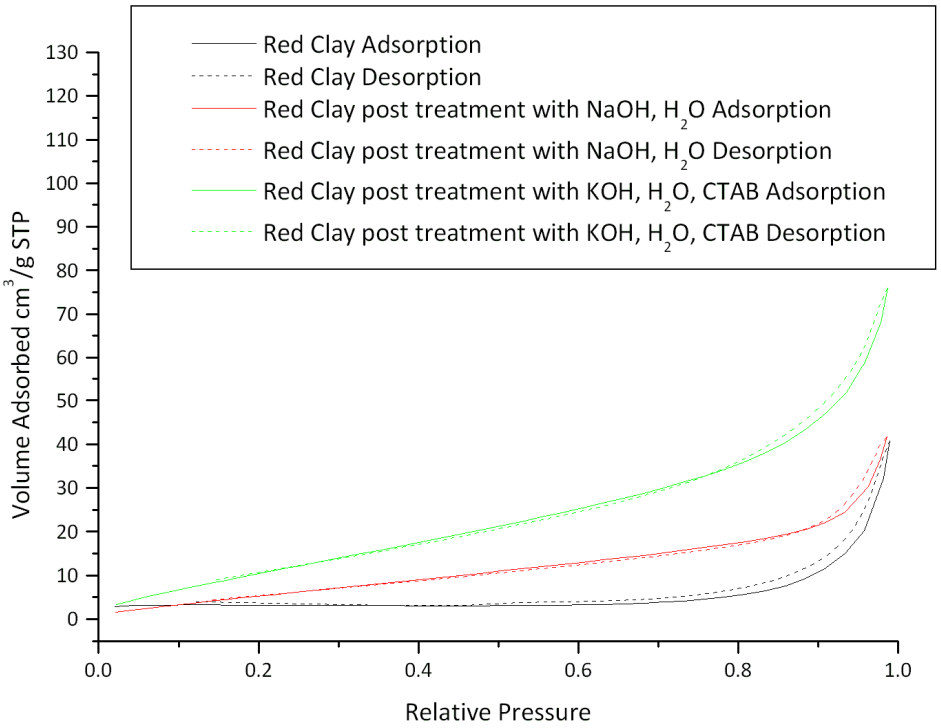

Figure 4.24 N_2 Adsorption/Desorption Isotherm of Red Clay and post treatments with base, water, and CTAB

Table 4.11 Porosity Results for Red Clay and post treatments with base, water, and CTAB

	Treatment	Surface Area	Pore Volume	Average Pore Diameter
		m^2g^{-1}	cm^3g^{-1}	nm
Red Clay	**Initial**	**13**	**0.05**	**15**
	5M NaOH	**14**	**0.066**	**16**
	5M KOH and CTAB	**29**	**0.11**	**15**

XRF elemental analysis of the red clay material before and after treatments (Table 4.12) showed adsorption of some the sodium cations when treated with sodium hydroxide (increase from 12.7 to 17.1%) and potassium cations when treated with potassium hydroxide (0.07 to 8.46%).

Some silicon and aluminium is extracted into the solution during the process which is evidenced by a decrease in percent concentration of the red clay (27% and 20% decrease of Silica and 14% and 12% decrease of aluminium oxide for NaOH and KOH respectively) and an increase in concentration within the filtrate solutions (1880 ppm Al_2O_3 and 926 ppm SiO_2 after treatment with NaOH and 2840 ppm Al_2O_3 and 1290 ppm SiO_2 after treatment with KOH in the presence of CTAB) (Table 4.13).

The concentration of iron decreases by less than 1% on treatment with NaOH and KOH which implyies very little is extracted into the solutions which decreases the possibility of uptake by the MCM-41 materials. Not all values match for XRF analysis of the solid residues and filtrate as the calculations and assumptions were different for solids and liquids in this technique.

Table 4.12 XRF Elemental analysis of red clay pre and post treatment with conditions similar to MCM-41 synthesis wt%

Sample Code	Major Elements								
Red Clay	SiO_2	Al_2O_3	Fe_2O_3	TiO_2	CaO	Na_2O	K_2O	MnO	LOI
Pre	**15.70**	**27.70**	**39.20**	**1.62**	**1.39**	**12.70**	**0.07**	**0.11**	**1.51**
Post NaOH / H_2O	**11.50**	**23.90**	**38.40**	**1.47**	**1.40**	**17.10**	**0.05**	**0.10**	**6.09**
Post KOH / H_2O / CTAB	**12.50**	**24.70**	**38.60**	**1.43**	**1.23**	**2.27**	**8.46**	**0.11**	**10.71**

Table 4.13 XRF Elemental analysis of filtrate from treatment with conditions similar to MCM-41 synthesis of red clay ppm

	Br	Ag	MgO	K_2O	CaO	Fe_2O_3	CuO
NaOH H_2O	0	126	0	50.8	35.1	15.4	9.07
KOH H_2O CTAB	4540	185	620	59400	178	150	6.9
	Al_2O_3	SiO_2	P_2O_5	SO_3	Na_2O	V_2O_5	ZnO
NaOH H_2O	1880	926	37.1	45.2	179000	4.92	1.84
KOH H_2O CTAB	2840	1290	26.2	42	0	0	0

The extraction by basic solutions appears to be unaffected by the type of alkali (NaOH or KOH) or the presence of CTAB. The presence of CTAB appears to have increased the surface area from 13 m^2g^{-1} to 29 m^2g^{-1}. The surfactant interacting in a small way with the red clay could produce the slightly higher level of textural porosity.

Returning to the study of MCM-41 materials synthesised from EBA bio-derived alkali silicate and K120 with different types of aluminium source (sodium aluminate, red clay, and aluminium hydroxide), below is a discussion on the porosimetry results of these materials.

N_2 adsorption/desorption isotherms are shown for MCM-41 materials synthesised from the bio-derived alkali silicate 'EBA' in Figure 4.25. All materials showed a steep rise in the Isotherm between 0.3 and 0.4 relative pressure which relates to a small range of mesoporosity. Also present is the Type B or H4 hysteresis loop which implies the pores are narrow and open at both ends.[80] The isotherm of the bio-derived MCM-41 with aluminium hydroxide most closely resembled the isotherm with no aluminium source. The EBA-MCM-41 materials with sodium aluminate and red clay had isotherms with less adsorption at high relative pressure.

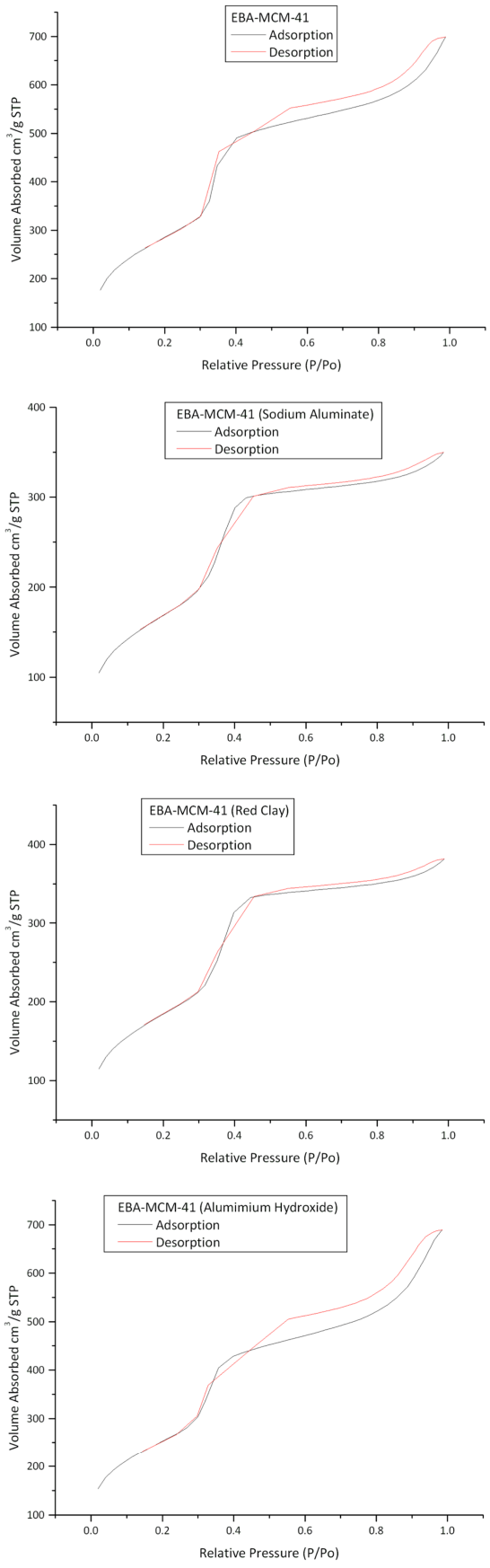

Figure 4.25 N_2 Adsorption/Desorption Isotherms for EBA-MCM-41 materials with aluminium

N_2 adsorption/desorption isotherms are shown for MCM-41 materials synthesised from the commercial alkali silicate 'K120' in Figure 4.26. All materials show the characteristic shape and hysteresis loop of a small range of narrow mesopores open at both ends.[80] The MCM-41 with no additional aluminium has adsorption at high relative pressures which is reduced for the samples with aluminium. Conv-MCM-41 (Aluminium Hydroxide) appears to have a slightly wider range of pore sizes as the increase in volume adsorbed occurs over a wider range of relative pressures. This is confirmed by the less pronounced peak in the pore size distribution graph (Figure 4.23).

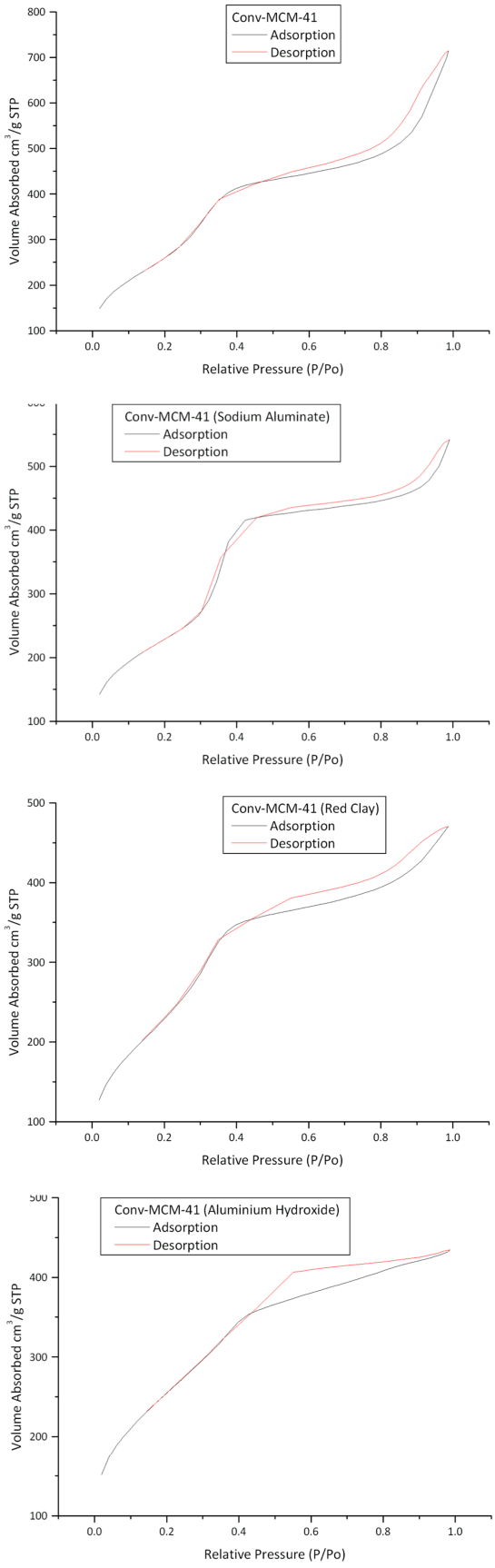

Figure 4.26 N_2 Adsorption/Desorption Isotherms for Conv-MCM-41 materials with aluminium

There is no clear effect on the porosity of these materials synthesised from different alkali silicate solutions.

4.4.5 X-Ray Diffraction Analysis

XRD patterns (Figure 4.27) showed all materials except for conv-MCM-41 synthesised with $Al(OH)_3$ exhibited the 100 plane between 2 and 3 2θ as either a shoulder or a peak. All other materials showed the further diffraction peaks for 110, 200, 210 planes at varied levels of intensity. This shows these materials had high crystallinity and short-range order. These crystalline properties are also consistent with the MCM-41 pore structure.[54-55] The all-silica material, EBA-MCM-41 exhibits the most intense and well-defined peaks of all the samples. The other all-silica material, Conv-MCM-41, has much less well defined peaks, and lower than some of the materials containing aluminium. Both samples containing sodium aluminate have barely observable peaks in this region, as does Conv-MCM-41 ($Al(OH)_3$). As can be seen from its isotherm in Figure 4.26, Conv-MCM-41 (aluminium hydroxide) has the least well defined pore size distribution as well as the XRD pattern with no peaks and therefore the least crystalline structure relating to the ordered mesopores. The locations of the peaks shift slightly and this may refer to slight changes in the unit cell due to introduction of aluminium into the structure. The peak locations for Conv-MCM-41 and EBA-MCM-41 ($Al(OH)_3$) are similar and both at higher 2θ values than EBA-MCM-41 but the level of aluminium integration into EBA-MCM-41 ($Al(OH)_3$) is less than the other materials and thus it appears from the XRD patterns that order is significantly decreased on addition of sodium aluminate for both Conv-MCM-41 and EBA-MCM-41 and addition of aluminium hydroxide on Conv-MCM-41.

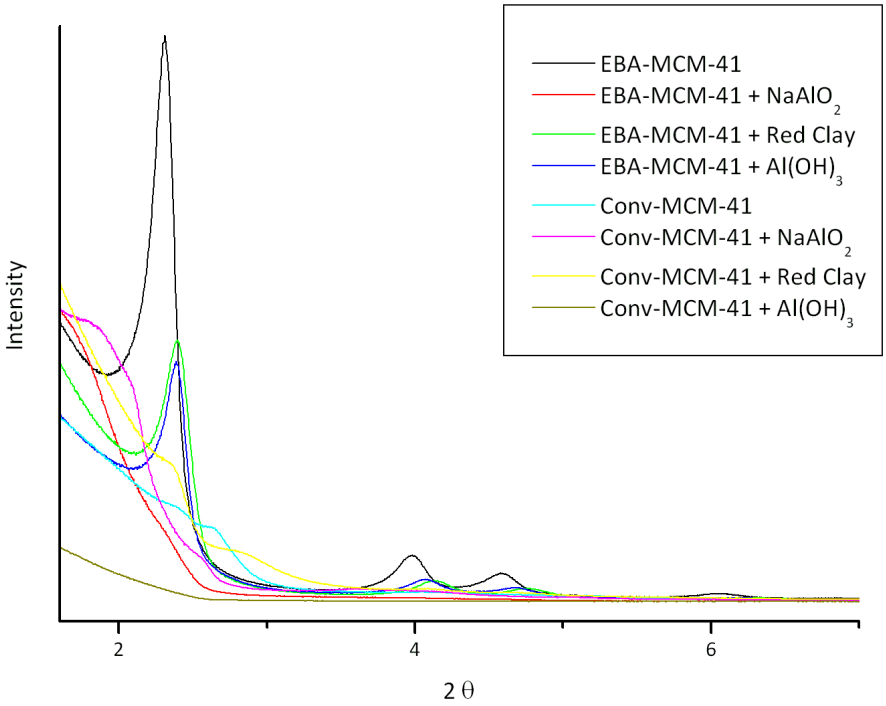

Figure 4.27 XRD patterns of MCM-41 synthesised with different aluminium sources

4.4.6 FT-IR Spectroscopy

On the surface of MCM-41 without aluminium, there can be Si-OH groups and siloxane groups (Si-O-Si). Once aluminium is bonded in the structure there can also be Al-OH and Si-O-Al groups.

Solid state FT-IR analysis (Figure 4.28) showed mainly silica-oxygen interactions with peaks at 1050 cm^{-1} and 810 cm^{-1} relating to the asymmetric and symmetric stretching vibrations respectively.[21] On addition of sodium aluminate to the synthesis mixture of MCM-41 a shift is observed in these peaks to lower wavenumber (-8 cm^{-1} and -7 cm^{-1} for Conv and -16 cm^{-1} and -7 cm^{-1} for EBA respectively) (Figure 4.29). The effect is observed to a lesser extent for the MCM-41 materials synthesised in the presence of Red Clay and Aluminium Hydroxide. This shift could indicate an increase in the mean Si–O distance in the walls caused by the substitution of silicon by aluminium.[21]

Very little adsorbed water or surface silanols was shown to be present as there was a lack of band around 3500 cm^{-1} although there is a small peak at 3746 cm^{-1} signalling the presence of some silanol groups. There is a small shoulder at 975 cm^{-1} which relates to

the stretching vibration of Si-O$^-$ groups. The shoulder at 1246 cm^{-1} could relate to the asymmetric stretching vibrations of the Si–O–Si bridges as this was assigned by Hui and Chao to be at 1223 cm^{-1} for their samples.[21]

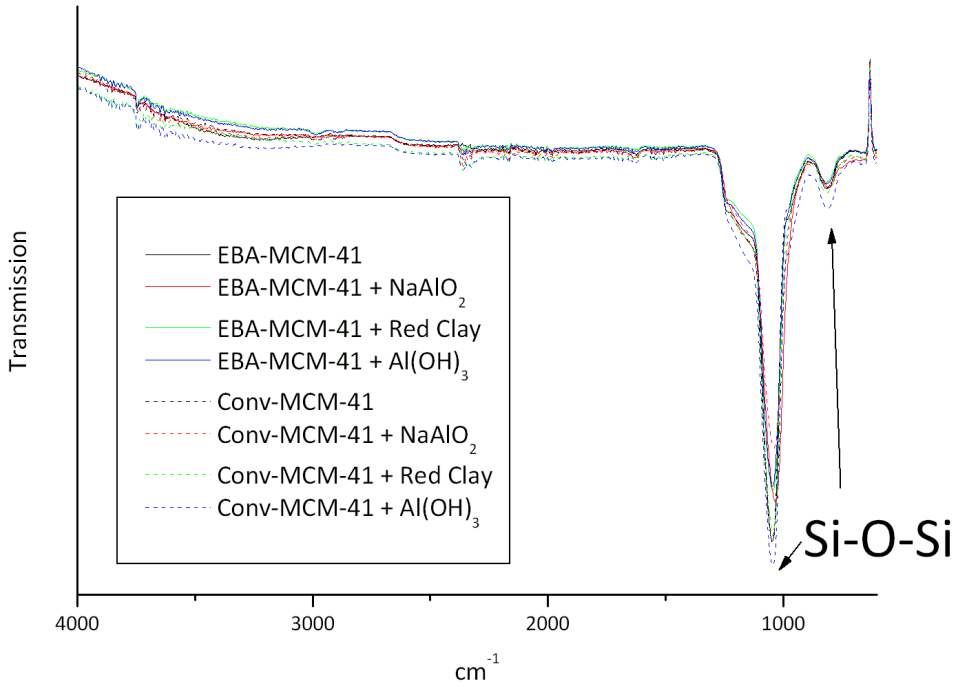

Figure 4.28 IR spectra of MCM-41 synthesised with different aluminium sources

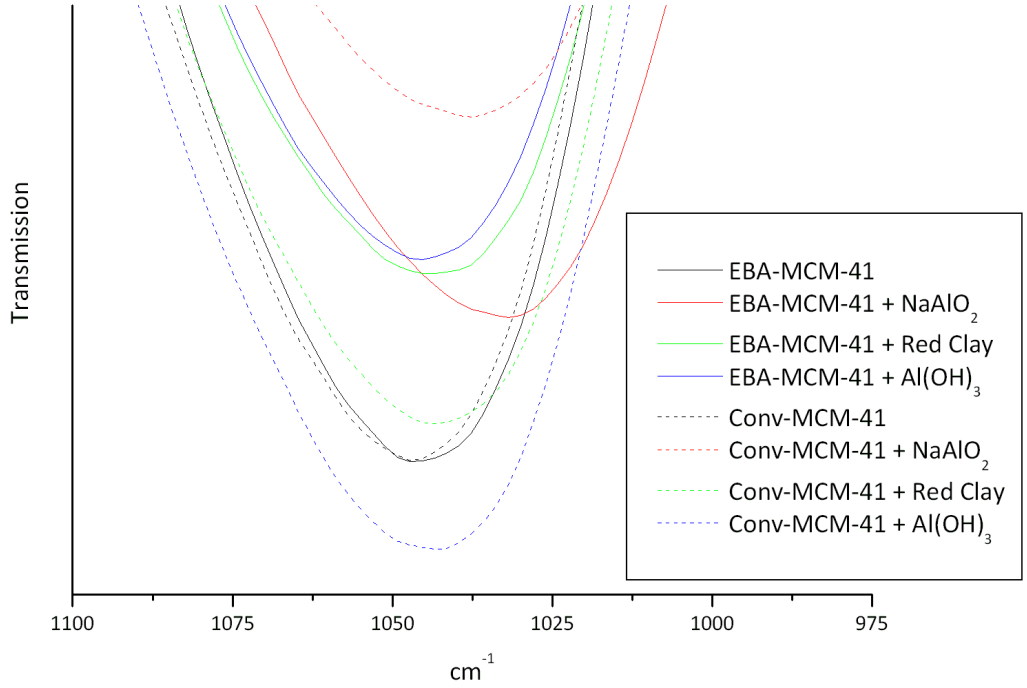

Figure 4.29 IR spectra of Si-O peak shift of MCM-41 materials synthesised with different aluminium sources

4.4.7 Varied Si/Al ratios of MCM-41 with Red Clay

As the addition of Red Clay showed promise as a source for aluminium in the MCM-41 synthesis, the amount added was varied for MCM-41 from K120 and EBA alkali silicates.

Porosimetry results (Table 4.14) showed a clear decrease in surface area and pore volume on increase of red clay into the synthesis. This occurred for both sources of silica. The change in porosity may be due to the collapse of the structure, less structure crystallization, or the presence of impurities. Red Clay was added to the synthesis in weights ranging from 0.01 g to 0.4 g relative to alkali silicate solutions corresponding to 0.446 g of silica. Therefore there may be an effect of the 85.30% of red clay which is not an aluminium-containing compound, some of which remains as a solid during the synthesis process and is collected alongside the synthesised MCM-41 but has no porosity (Figure 4.24 and Table 4.11). Since the pore diameter (Table 4.14) is unchanged this

would seem likely. One way to avoid this would be to extract aluminium prior to the synthesis and perhaps even in the same vessel as the biomass ash extraction.

Table 4.14 Porosimetry results for MCM-41 synthesised from EBA and K120 with varied addition of red clay to the synthesis

Si source	Red Clay	Si/Al (wt)	BET Surface Area	Pore Volume	Average Pore Diameter
(0.446g Si)	g		m^2g^{-1}	cm^3g^{-1}	nm
EBA	0.01	573	977	0.96	2.9
EBA	0.05	115	1004	1.04	2.9
EBA	0.1	57	842	0.81	2.8
EBA	0.4	14	660	0.61	2.7
K120	0.01	573	941	0.82	2.6
K120	0.05	115	890	0.88	2.6
K120	0.1	57	568	1.2	2.6
K123	0.4	14	645	0.63	2.9

All EBA-MCM-41 samples showed similar N_2 isotherms (Figure 4.30) with the previously identified steep rise in curve and hysteresis loop. There is a decrease in the amount of volume of N_2 adsorbed from around 650 cm^3g^{-1} for Si/Al values of 573 and 115 to 500 cm^3g^{-1} and 400 cm^3g^{-1} for Si/Al values of 57 and 14 respectively. Therefore, as the relative amount of red clay is added to the synthesis, the level of adsorption of nitrogen decreases.

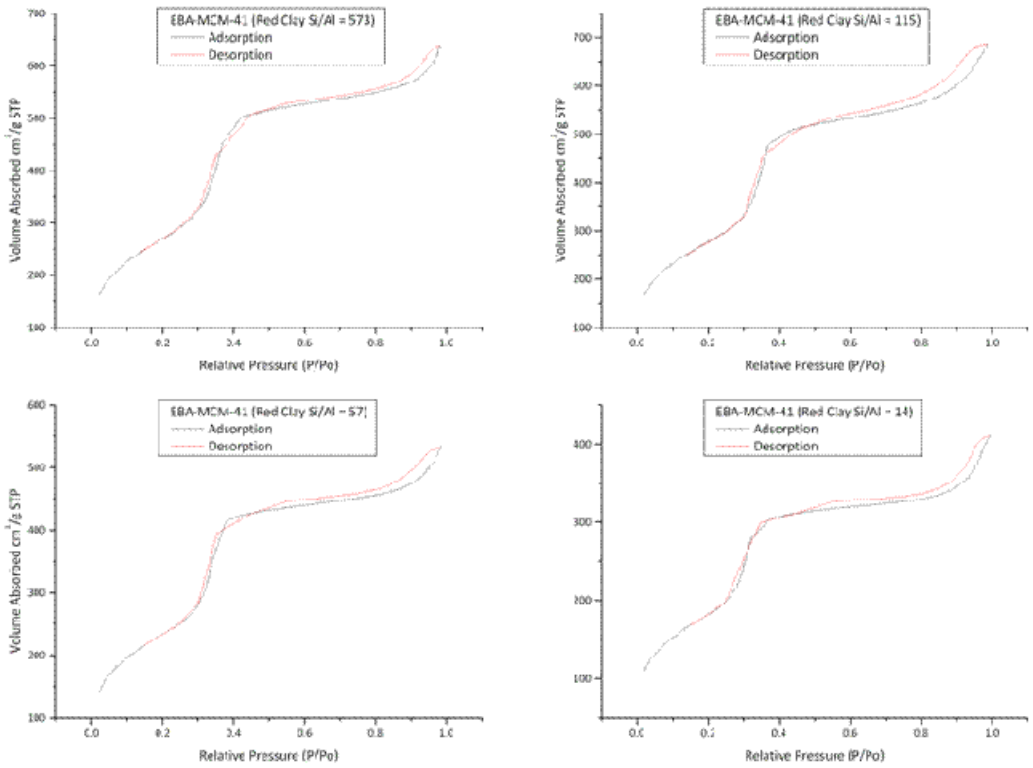

Figure 4.30 N_2 Adsorption/Desorption Isotherms for EBA-MCM-41 materials with different amounts of Red Clay added during synthesis. Si/Al ratios described in the legends.

The N_2 isotherms for Conv-MCM-41 with increasing amounts of red clay (Figure 4.31) are more complex. The MCM-41 samples synthesised with Si/Al of 573 and 115 exhibit normal isotherms for these materials but the sample with Si/Al = 57 shows a very different isotherm. The steep increase of absorbed N_2 is very low, approximately 50 cm^3g^{-1}, compared to the Conv-MCM-41 with Si/Al = 573 which absorbs 125 cm^3g^{-1}. The isotherm then absorbs over 500 cm^3g^{-1} N_2 over 0.4 – 1 relative pressure which relates to the large meso- and macro- porous regions. The Conv-MCM-41 (Si/Al = 14) has an isotherm which has similar properties but is also more similar to the isotherms for Si/Al = 573, 115. This could be due to the collapse of a lot of the mesoporous pore structure or synthesis of a larger secondary porous structure. The Conv-MCM-41 (Si/Al = 14) has the largest pore volume recorded of the materials (Table 4.14) which would confirm the hypothesis of secondary larger meso and macro pore structures.

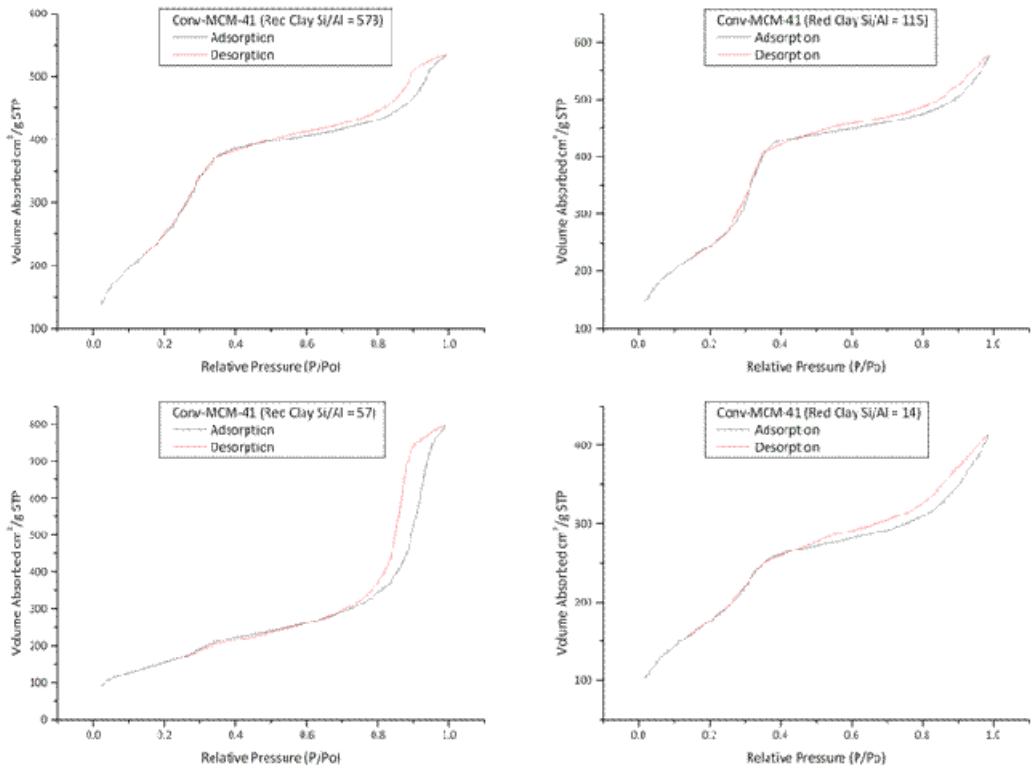

Figure 4.31 N_2 Adsorption/Desorption Isotherms for Conv-MCM-41 materials with different amounts of Red Clay added during synthesis. Si/Al ratios described in the legends.

Conv-MCM-41 synthesised with a Si/Al = 57 showed an unusual pore size distribution curve as shown in Figure 4.32. This distribution shows a significant amount of pore structure with pores diameters in the region 10-35 nm as well as a clear peak relating to the MSM-41 pore structure at around 2.8 nm.

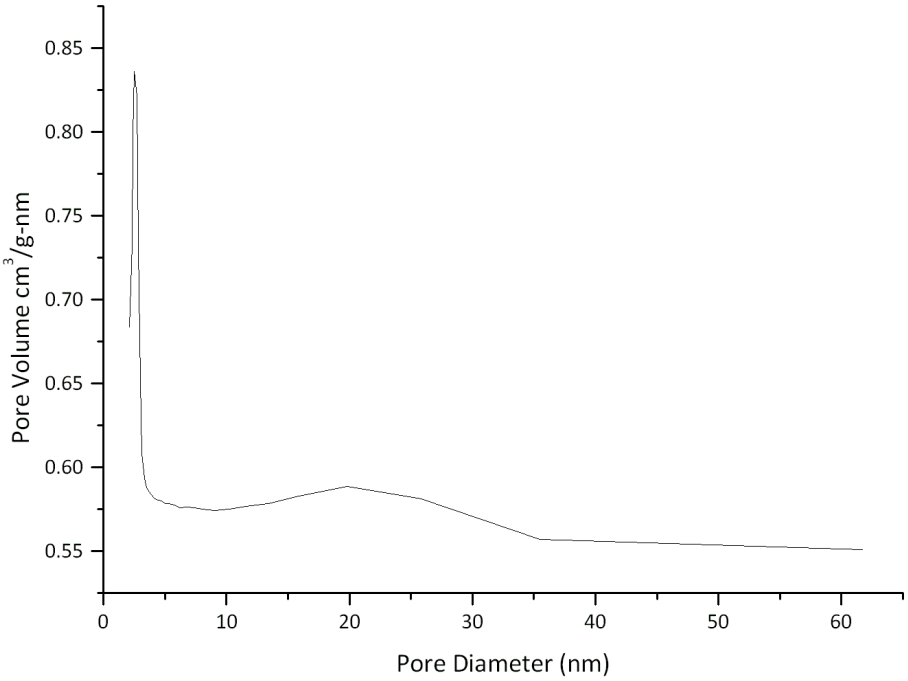

Figure 4.32 Pore Size Distribution of Conv-MCM-41 synthesised 0.1 g Red Clay. Si/Al = 57

Pore size distributions for all other MCM-41 materials synthesised from red clay showed a normal curve with a peak between 2.5 and 3 nm (Figure 4.33 and Figure 4.34).

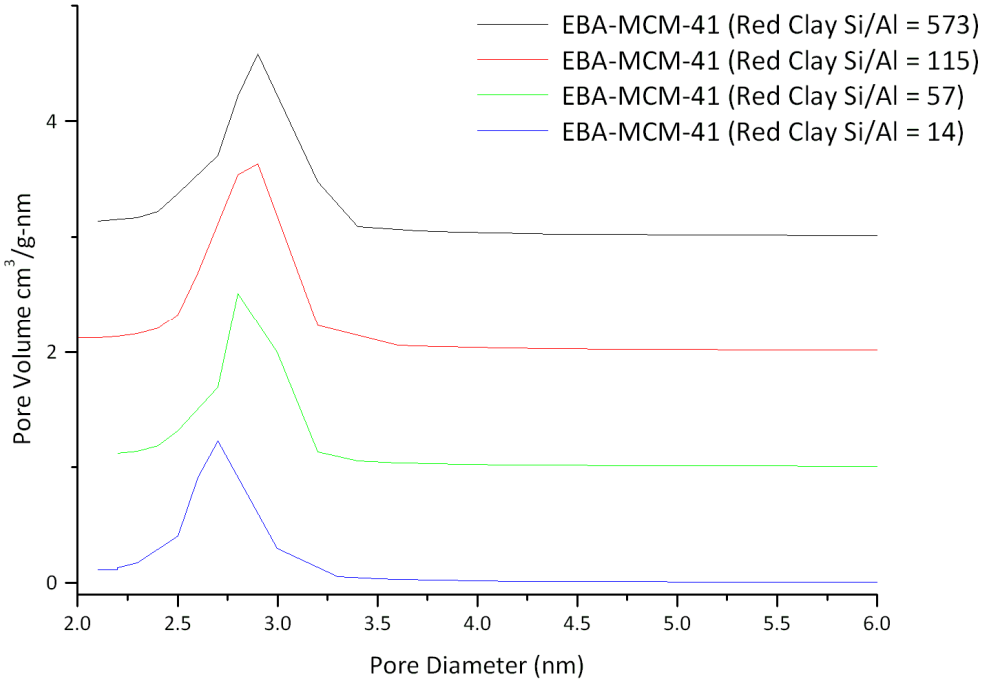

Figure 4.33 Pore Size Distribution of EBA-MCM-41 materials synthesised with increasing amounts of Red Clay. Si/Al ratios shown in legend

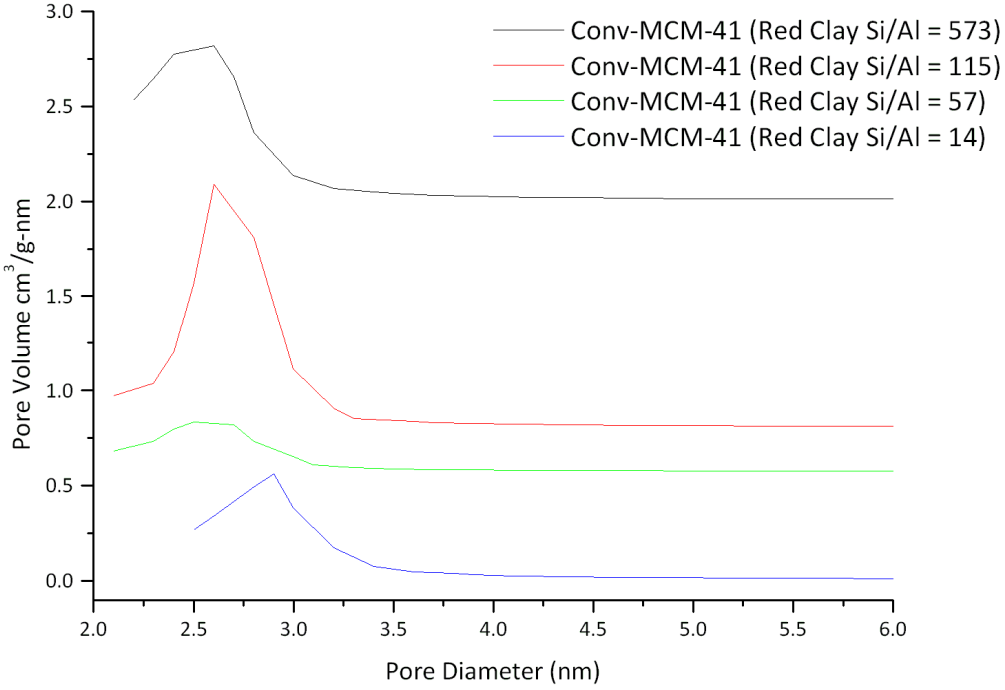

Figure 4.34 Pore Size Distribution of Conv-MCM-41 materials synthesised with increasing amounts of Red Clay. Si/Al ratios shown in legend

XRD patterns show peaks relating to short-range order for both MCM-41 materials synthesised from K120 and EBA (Figure 4.35 and Figure 4.36). The EBA-MCM-41 materials all show a peak around 2.3 2θ which relates to the 100 plane and can be used to calculate values for pore size and pore wall thickness. The sample with Si/Al = 14 shows the further 110 and 200 peaks. There is a major shoulder at around 1.2 2θ which could be an artifact of the X-Ray Diffractometer.

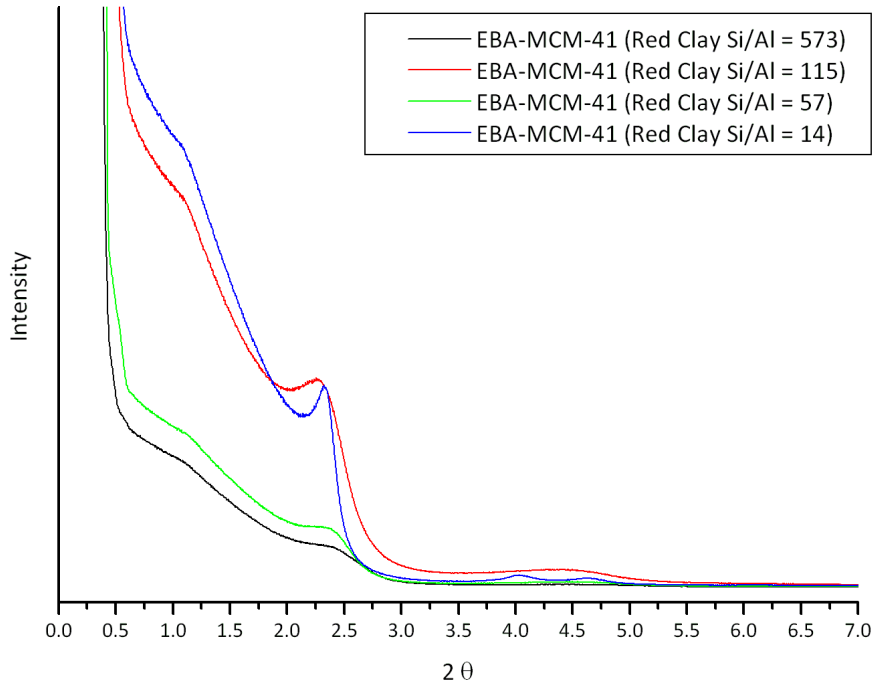

Figure 4.35 XRD Patterns of EBA-MCM-41 (Red Clay) with varied Si/Al ratios showing peaks representing short-range order

The Conv-MCM-41 samples have more complex XRD patterns. The materials with Si/Al = 573 and 57 have peaks similar to the reference MCM-41. Conv-MCM-41 with Si/Al = 14 shows no discernible peaks, merely a subtle shoulder meaning there is very little crystallinity in the material. This information combined with porosimetry data which describes the sample as having the lowest porosity and surface area would imply any porosity in the material has not formed or collapsed at some point in the synthesis. The material Conv-MCM-41 with Si/Al = 115 uniquely has a double peak at its 100 peak location. This could be due to an additional reflection plane within the structure or two lengths of the same plane.

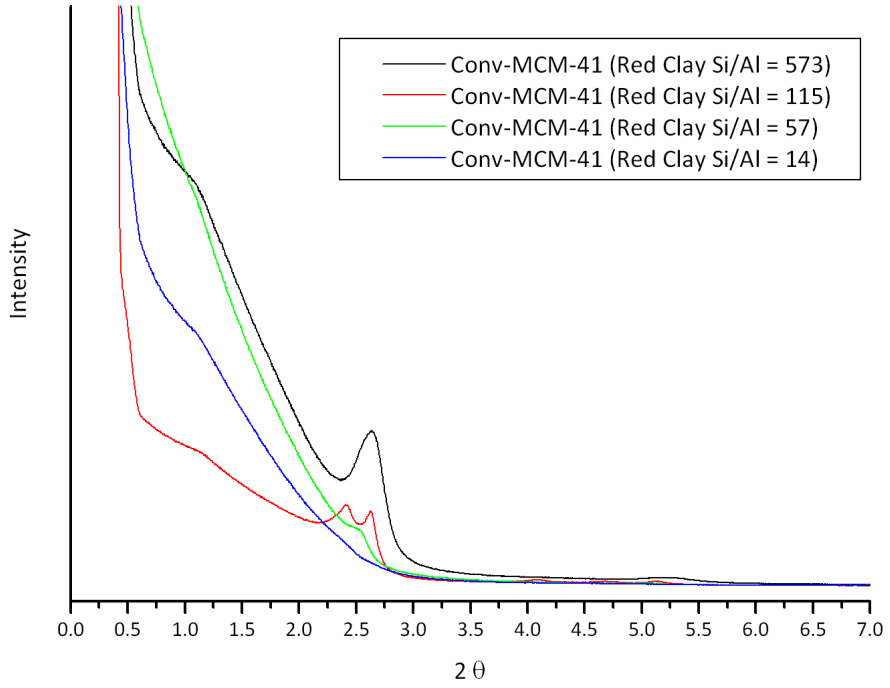

Figure 4.36 XRD Patterns of Conv-MCM-41 (Red Clay) with varied Si/Al ratios showing peaks representing short-range order

Calculated pore wall thickness is reasonably consistent for all samples as they fall within a range of 12.6 Å to 16.7 Å. Therefore there is no correlation between Si/Al ratio and pore size. There is no data for Conv-MCM-41 with Si/Al = 14 as it did not have distinct enough peaks to assign a 2θ value (Table 4.15).

Table 4.15 Combined XRD and porosimetry calculations

Si source	Si/Al		d_{100}	Unit Cell Parameter a_0	Pore Size	Pore Wall Thickness
(0.446g Si)		2θ	Å	Å	Å	Å
EBA	573	2.37	37.2	43.0	35.4	14.0
EBA	115	2.26	39.0	45.1	37.6	16.1
EBA	57	2.35	37.5	43.4	34.7	15.4
EBA	14	2.33	37.9	43.7	33.1	16.7
K120	573	2.63	33.6	38.7	31.1	12.7
K120	115	2.41	36.6	42.3	34.3	16.3
K120	57	2.54	34.7	40.1	34.2	14.1
K120	14	-				

NMR results for both EBA-MCM-41 and Conv-MCM-41 showed the presence of both extra-framework octahedral aluminium and tetrahedrally bonded aluminium within the MCM-41 framework. The ratios of these two species remain approximately constant with respect to the amount of Red Clay added. Therefore there is an increased uptake into the MCM-41 material.

There is a peak at 39 ppm which lies between the two peaks at 2 ppm (octahedral) and at 54 ppm (tetrahedral) for EBA-MCM-41 with Si/Al = 573. This implies more complicated bonding of a significant amount of the aluminium in the structure. A peak between the two peaks described would normally relate to a 5-coordinate system. There is a shoulder in the spectrum for EBA-MCM-41 with Si/Al = 115 which also falls in this region. Also of note is an increasing positive shift which occurs for the octahedral peak from 2 ppm for EBA-MCM-41 with Si/Al = 573 to 7.5 ppm for EBA-MCM-41 with Si/Al = 14. These effects may be due to aluminium bonding in the residue red clay and not integrated in the MCM-41.

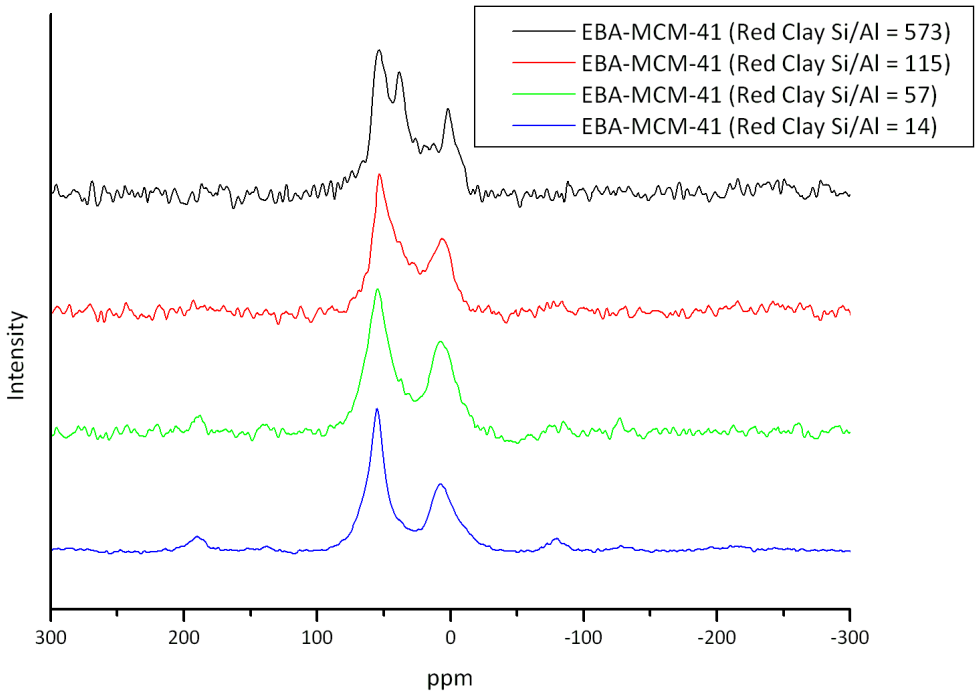

Figure 4.37 Solid state ^{27}Aluminium NMR spectra for EBA-MCM-41 with addition of Red Clay at varied Si/Al ratios as specified in the legend

The Conv-MCM-41 materials with higher Si/Al show similar peaks in between the octahedral and tetrahedral peaks. These peaks are most pronounced for Conv-MCM-41 with Si/Al = 573. For this sample there are two observable peaks at 6.9 ppm and 38 ppm which become shoulders for Conv-MCM-41 with Si/Al = 115. There is also a shift of the octahedral peak on decreasing Si/Al from -11.4 ppm to 8 ppm. This may just be due to background noise as the signals for Si/Al = 573 and 115 are significantly lower than Si/Al = 57 and 14.

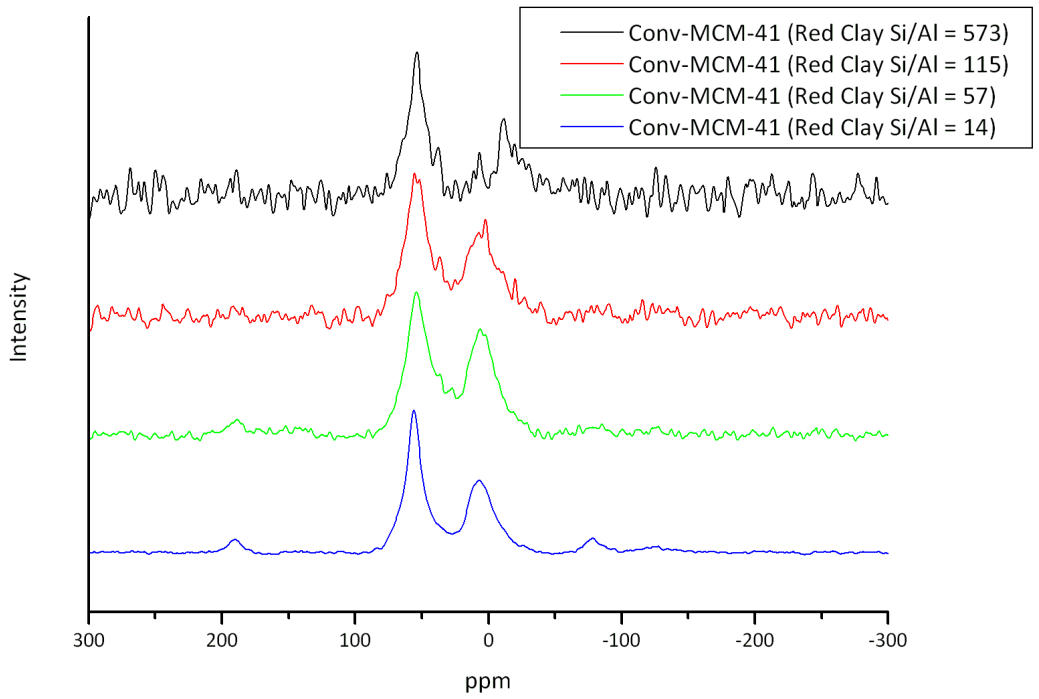

Figure 4.38 Solid State ^{27}Aluminium NMR spectra for Conv-MCM-41 with addition of Red Clay at varied Si/Al ratios as specified in the legend

Since there is a residue of red clay in the MCM-41 samples after synthesis it is difficult to ascertain whether any metals have been absorbed into the structure alongside the aluminium. It is clear from XRF analysis that on increased addition of red clay there is additional presence of iron and aluminium in the samples (Table 4.16).

Table 4.16 XRF analysis of MCM-41 materials synthesised with different amounts of Red Clay

Si Source	Si/Al	Br	K_2O	CaO	Fe_2O_3	Al_2O_3	SiO_2	SO_3	MnO	Co_2O_3
EBA	573	0.00	0.12	0.01	0.23	0.28	65.90	0.00	0.00	0.00
EBA	115	0.02	0.37	0.06	2.04	0.70	96.70	0.05	0.01	0.01
EBA	57	0.05	0.57	0.09	3.48	1.30	94.40	0.05	0.01	0.02
K120	573	0.17	0.49	0.02	0.45	0.35	97.90	0.01	0.01	0.00
K120	115	0.02	0.23	0.04	1.53	0.80	87.10	0.02	0.01	0.01
K120	57	0.00	0.53	0.07	3.00	1.75	74.10	0.04	0.01	0.00

4.4.8 Conclusion

MCM-41 materials have been successfully synthesised using a bio-derived alkali silicate solution (EBA) and a commercially available alkali silicate solution (K120). These materials have been compared using appropriate analytical techniques such as XRD, N_2 adsorption porosimetry, and FT-IR and found to be similar in their properties of crystallinity, porosity and elemental composition. The materials were found to be similar and reproducible despite certain reaction conditions such as a change in pH. The introduction of aluminium, and more specifically the use of red clay as an aluminium source, was explored and discussed. Sodium aluminate was found to incorporate most effectively into the material but this led to a weakening of the pore structure whereas aluminium hydroxide integrated least well which meant the pore structure remained stable. The introduction of aluminium from red clay into the structure was successful and, again, led to a weakening of the pore structure. The presence of the undissolved red clay also had an effect on the porosity results.

5 Synthesis of SBA-15 from Miscanthus Alkali Silicate Solutions

5.1 Context

Further to the investigation into the synthesis of Zeolite X from RHA bio-derived alkali silicate, and MCM-41 from EBA bio-derived alkali silicate, other porous silica materials were considered for the adaptation of the silica source to bio-derived alkali silicate. One that has many useful applications is SBA-15 and this was initially synthesised according to a recipe devised by Zhao *et al*.[54] SBA-15 has the same hexagonal pore structure as MCM-41 with the difference that the pores are bigger. This is due to a change in template leading to larger micelles. Due to its stability and pore structure, SBA-15 has many applications, as described in the Introduction Section 1.7.3, such as in catalysis, drug delivery, and ion exchange.

The synthesis is traditionally carried out using tetraethyl orthosilicate (TEOS) as the silicon source whose own energy and resource intensive synthesis is outlined in the Introduction Section 1.3.1. TEOS was used to synthesise a conventional SBA-15 as described in Section 6.4.1 to function as a reference material. The synthesis was then adapted in several ways with the objective of refining the method for alkali silicates extracted from Miscanthus combustion ashes. This would be a cheaper and more environmentally benign method of synthesising SBA-15.

Described in the Introduction (Section 1.7.4) is the work done already in synthesising SBA-15 from ashes. Coal ashes and rice hull ashes have been used but often with an addition of a secondary silicon source such as sodium metasilicate. This work uses no other silicon source and synthesises SBA-15 from a novel power plant biomass ash (Miscanthus Bottom Ash from Ely Power Station).

The main challenge in this work is the alkaline pH of the bio-derived alkali silicate reaction mixture. Conventionally TEOS is used as the silicon source for this synthesis. TEOS is a neutral compound which precipitates to SiO_2 in the presence of water (and acid) and ethanol is produced as a by-product (Figure 5.1). These SiO_2 monomers are a notional intermediate. In solution the monomers polymerise to form dimers, trimers, and more complex polymers.

Sodium or potassium silicate solutions are strongly basic and hydrolyse under different conditions. If a bio-derived alkali silicate solution is to replace TEOS then there needs to be careful consideration of the pH environment as well as the presence of salts.

SBA-15 is formed from TEOS in acid media below pH 1. Above the isoelectric point of silica (pH > 2) no precipitation occurs. At neutral pH amorphous silica is obtained.[55]

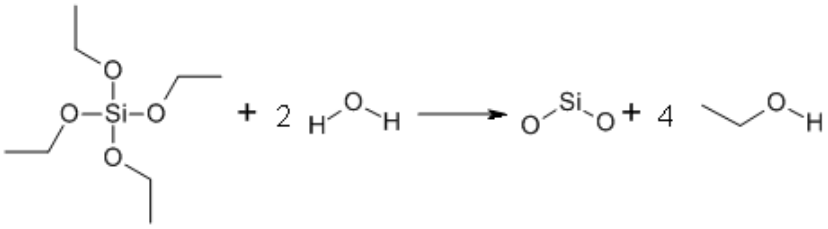

Figure 5.1 Schematic diagram of hydrolysis of TEOS

The synthesis of SBA-15 occurs via a micelle templated method as described in the Introduction Section 1.7.1. The surfactant used is Pluronic P123 which is a triblock copolymer based on the structure poly(ethylene glycol)-poly(propylene glycol)-poly(ethylene glycol). Micelles form a template that the silicon can condense around and, in this case, form the two dimensional hexagonal SBA-15 pore structure.

5.2 Replacement of TEOS with EBA alkali silicate

Firstly, a straightforward substitution of silicon source was performed in order to check whether the synthesis was directly transferable. EBA alkali silicate solution (from Miscanthus ash, 1.14 x10^5 ppm Silicon, SiO_2/KOH = 0.035) was used as the novel bio-derived silicon source instead of tetraethyl orthosilicate (TEOS). This SBA-15 material was named EBA-SBA-15 and the reference sample, TEOS-SBA-15. The organic triblock copolymer Pluronic P123 was used as the template for all samples.

The XRD pattern for the reference material, TEOS-SBA-15 (Figure 5.2), showed a clear reflection at around 1.1° 2θ (d(10)) and two shoulders after this reflection up to around 2° 2ϑ. If the reflection at 1.1° 2θ is the d(10) reflection and the material is hexagonal, then there should be further reflections at 1.9° 2θ and 2.2° 2θ (corresponding to the d(11) and d(20) reflections, respectively). The shoulders are located at approximately 1.75 ° 2θ and 2.05° 2θ which, within error and given the broad nature of the shoulders, supports the

hexagonal nature of the material. The reflections are consistent with observations in the literature and give a *d*-spacing of around 8.03 nm.[54-55] This XRD pattern will be used for comparison with the bio-derived SBA materials synthesised below.

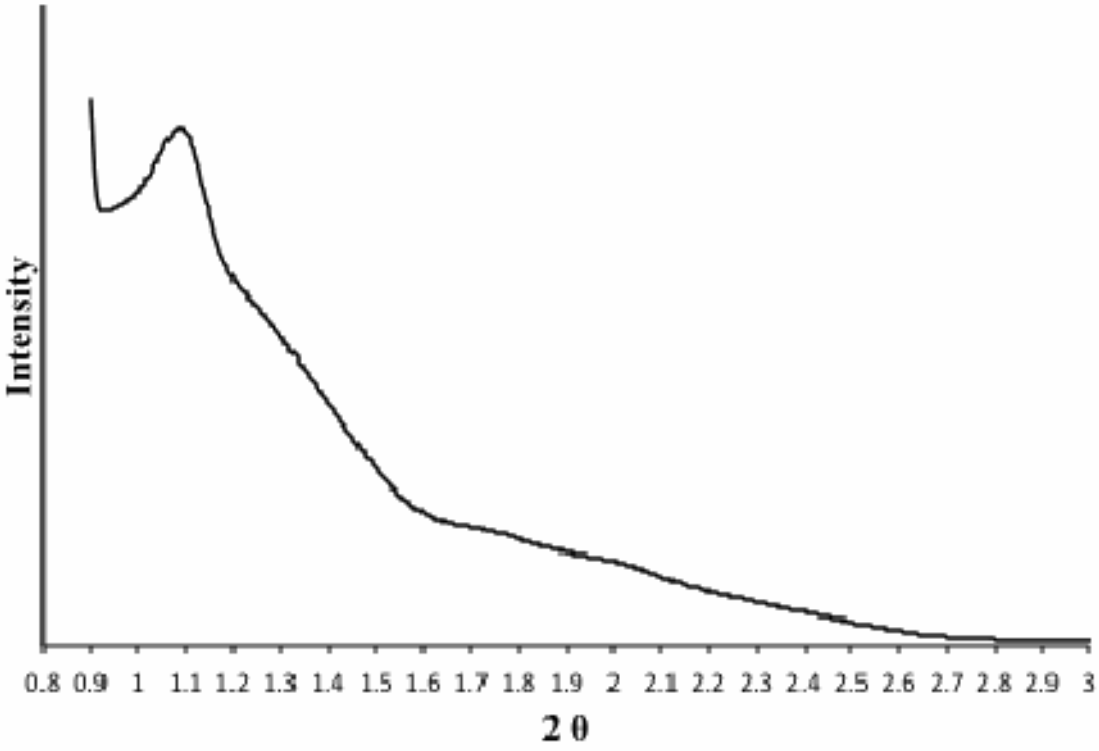

Figure 5.2 Low angle, high-resolution XRD pattern of calcined TEOS-SBA-15

When comparing the XRD patterns of the reference material TEOS-SBA-15 with the initial bio-derived EBA-SBA-15, it is clear there are no reflections at all (Figure 5.3), implying that there is no order in the material.

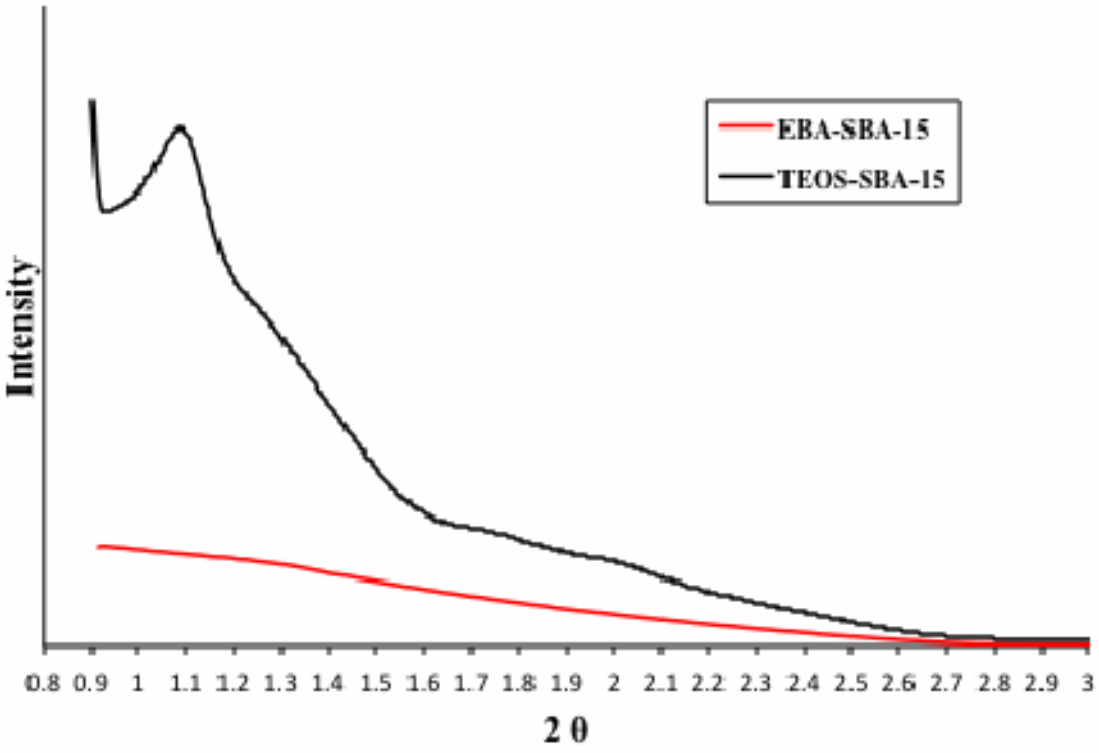

Figure 5.3 Low-angle XRD pattern of calcined EBA-SBA-15 and TEOS-SBA-15

Transmission electron micrographs (TEM) (Figure 5.4) showed both samples contained pores. There is clearly a parallel pore arrangement present in the TEOS-SBA-15 sample whereas there is no such evidence for the EBA-SBA-15 material which has visible pores but no order.

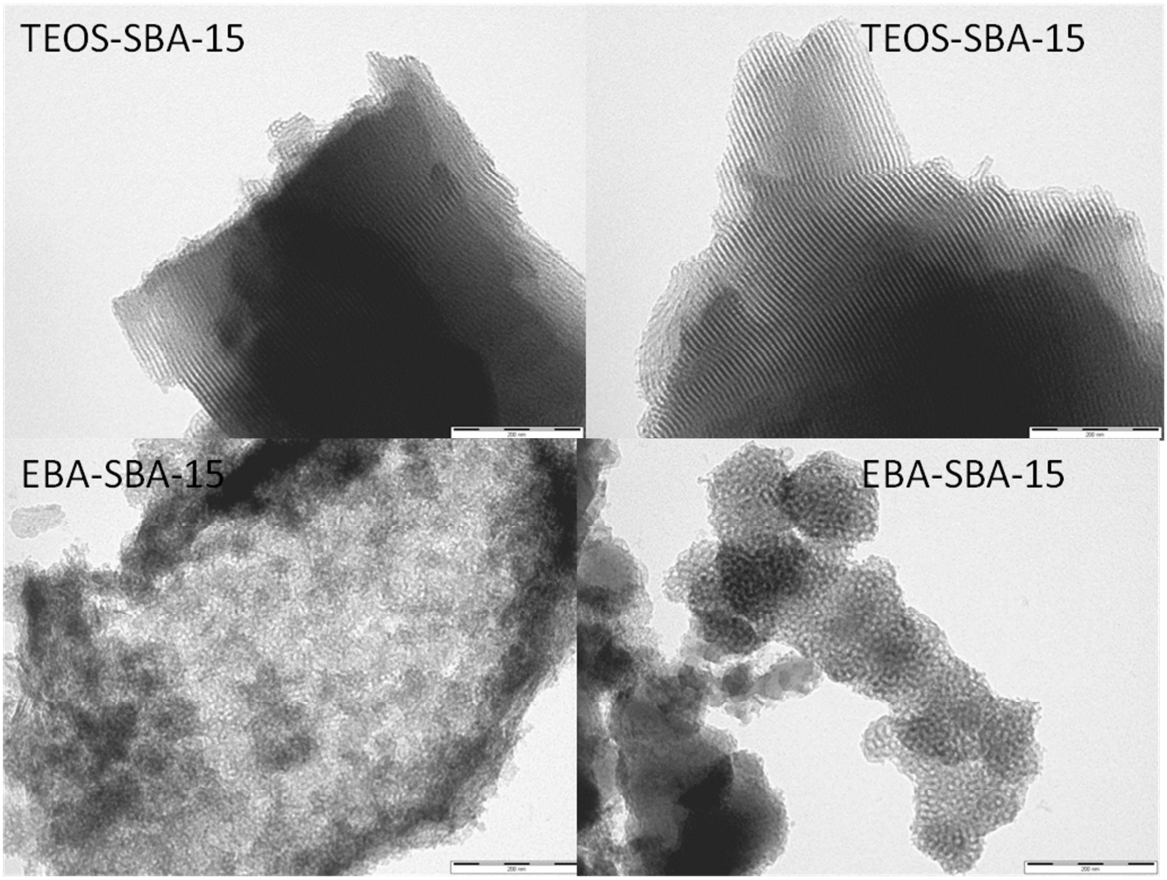

Figure 5.4 TEM images of TEOS-SBA-15 and EBA-SBA-15. Scale bar is 1 µm in length (1000 nm)

Porosimetry results for the two materials (Table 5.1) show significant differences. There is approximately half the surface area and pore volume for EBA-SBA-15 when compared to TEOS-SBA-15, which implies that either there is something blocking the pores of the bio-derived sample or that less pore structure has formed. The latter conclusion is confirmed by the XRD and TEM results described above which show there is no order in the material. The average pore diameters are similar but there is significantly less pore volume. Other bio-derived SBA-15 materials also showed lower surface areas of 483 m^2g^{-1} and 645 m^2g^{-1} but not as low as that found for EBA-SBA-15.[62, 67]

Table 5.1 Porosimetry data for TEOS-SBA-15 and EBA-SBA-15

	Surface Area	Pore Volume	Average Pore Diameter
	m^2g^{-1}	cm^3g^{-1}	nm
TEOS-SBA-15	**840**	**0.8**	**4.1**
EBA-SBA-15	**300**	**0.39**	**5.2**

N_2 adsorption/desorption isotherms (Figure 5.5) show a significant difference in the nature of the porosity for the two materials. The TEOS-SBA-15 sample shows the characteristic sharp steep rise of the isotherm at around 0.6 relative pressure. This signifies a mesopore system with a consistent pore size. The Type B or H4 hysteresis loop is present which, like the MCM-41 materials, indicates that narrow mesopores open at both ends are formed.[81] The EBA-SBA-15 sample also has a hysteresis loop and so has the same shape mesopores but, as there is more of a gradual increase in volume of adsorbed N_2 over a much wider range of relative pressure, there is a much wider range of pore size in the material.[80]

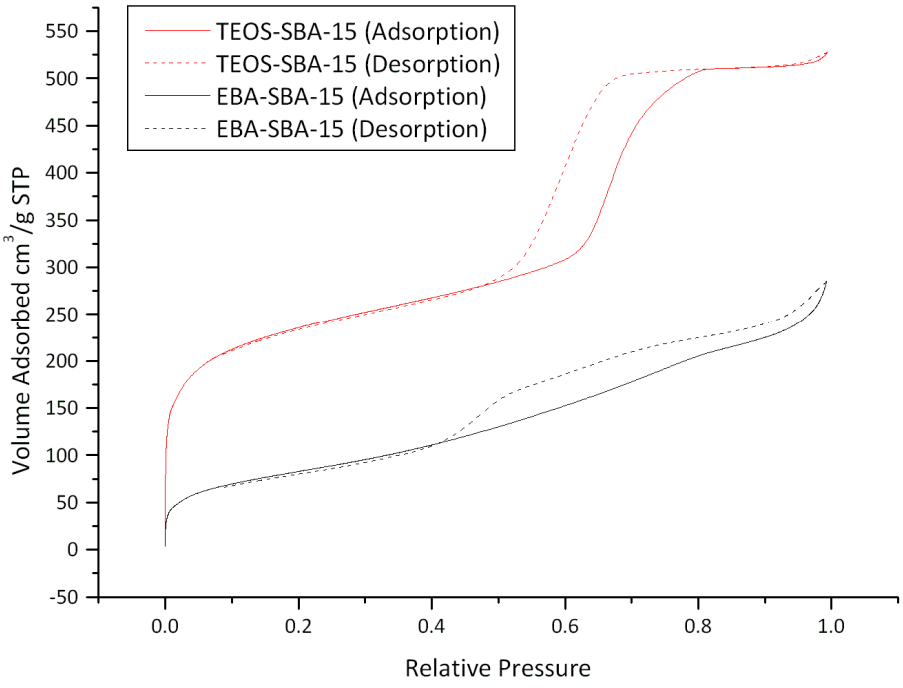

Figure 5.5 N_2 Adsorption / Desorption Isotherms of TEOS-SBA-15 and EBA-SBA-15

This effect is clearly shown in the pore size distribution of the two materials (Figure 5.6). There is a clear peak for the TEOS-SBA-15 sample which represents a small range of pore sizes nearly all falling within the region 3-7 nm whereas the pore size distribution for the EBA-SBA-15 sample is over a much wider range of 2-100 nm. There is a sharply defined pore size peak at around 3.5 nm which is lower than that for TEOS-SBA-15 which is around 5-5.5 nm.

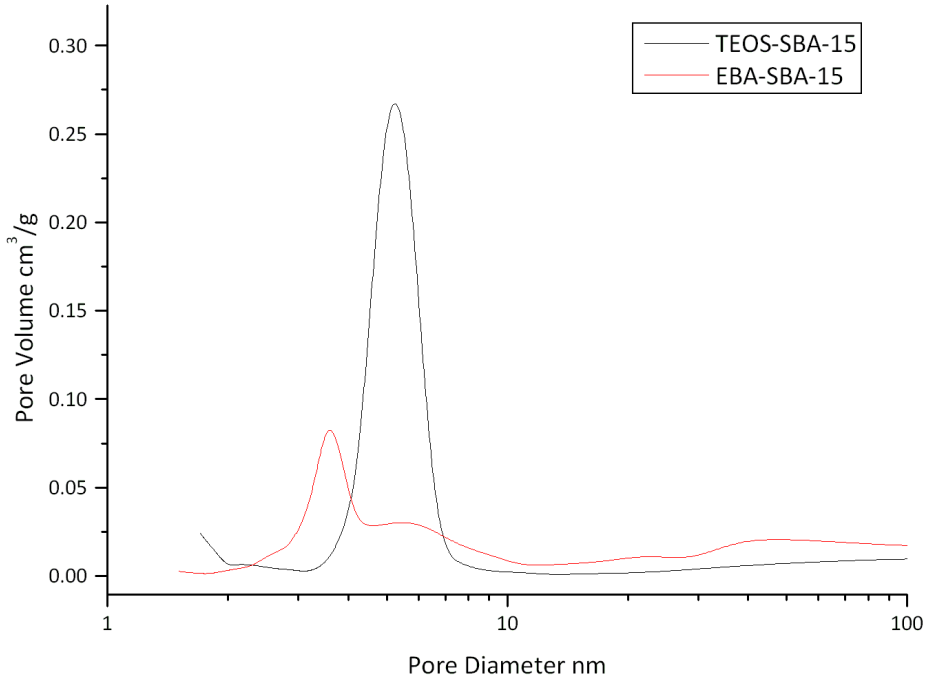

Figure 5.6 BJH calculated Pore size distribution for TEOS-SBA-15 and EBA-SBA-15

Integrating the results from these three techniques it appears that replacing the silicon source of TEOS with EBA bio-derived alkali silicate has caused the material to lose its linearity and order. There is still significant porosity despite the lack of linearity of the pores and this implies that the material may have formed wormhole pores *via* a neutral template method (S^0I^0 mechanism) described in section 1.7.1. This would imply a higher pH environment in the synthesis solution which would be expected as the basic silicate solution mixes with the acidic solution containing the template.

It appears that the first step of micelle formation occurs for both materials and that the alkali silicate in solution does hydrolyse around the template formed. The difference in properties of the materials formed appears to occur due to the difference in structure of the aligned micelles and the mechanism of interaction of silicate with template. This difference could be due to some difference in synthesis environment such as pH or the presence of other ions in solution.

5.3 Effect of KOH on synthesis environment

In order to investigate whether the presence of KOH in the synthesis solution could be the cause of this problem in formation of the SBA-15 structure in EBA-SBA-15, TEOS-SBA-15 was synthesised in the presence of potassium hydroxide which had the dual effect of increasing the pH to a more basic environment similar to the alkali silicate solutions used in the EBA syntheses and to introduce the presence of potassium cations in the solution which were also present in the alkali silicate solution. An increased pH would have the effect of decreasing the level of protonation of the template surface and silicate ions. The extra potassium cations could interact with chloride ions and thus remove them from the traditional SBA-15 synthesis mechanism (Figure 1.14 and Figure 1.16).

The XRD pattern of the TEOS-SBA-15 material synthesised in the presence of potassium hydroxide shows a similar location and intensity of the main reflection when compared to the reference sample (Figure 5.7), but does nothing to induce order into the EBA sample.

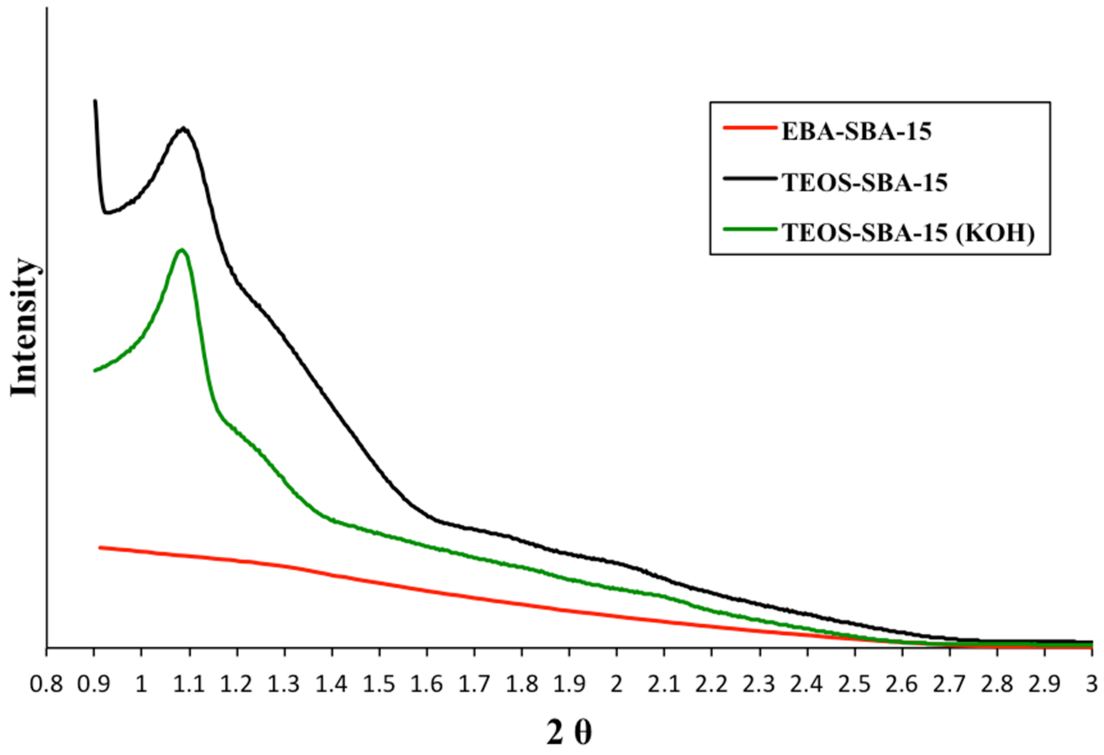

Figure 5.7 XRD patterns of TEOS-SBA-15, EBA-SBA-15, and TEOS-SBA-15 synthesised in the presence of KOH

Porosimetry results (Figure 5.2) showed the effect of addition of potassium hydroxide to the solution was a reduction in surface area and pore volume of approximately one third. The pore sizes remained consistent.

Table 5.2 Porosimetry results for TEOS-SBA-15 (KOH) and TEOS-SBA-15 as a comparison

	Surface Area	Pore Volume	Average Pore Diameter
	m^2g^{-1}	cm^3g^{-1}	nm
TEOS-SBA-15	**769**	**0.8**	**4.1**
TEOS-SBA-15 (KOH)	**592**	**0.53**	**3.4**
EBA-SBA-15	**300**	**0.39**	**5.2**

The isotherm for this material (Figure 5.8) showed the presence of KOH did not affect the nature of the mesoporosity as the shape of the isotherm clearly resembles the reference sample (TEOS-SBA-15), but there is a significant loss in the extent of the porosity. There is some microporous structure present for all materials and this is due to silica forming around and within the template as described in the Introduction Section 1.7.1.

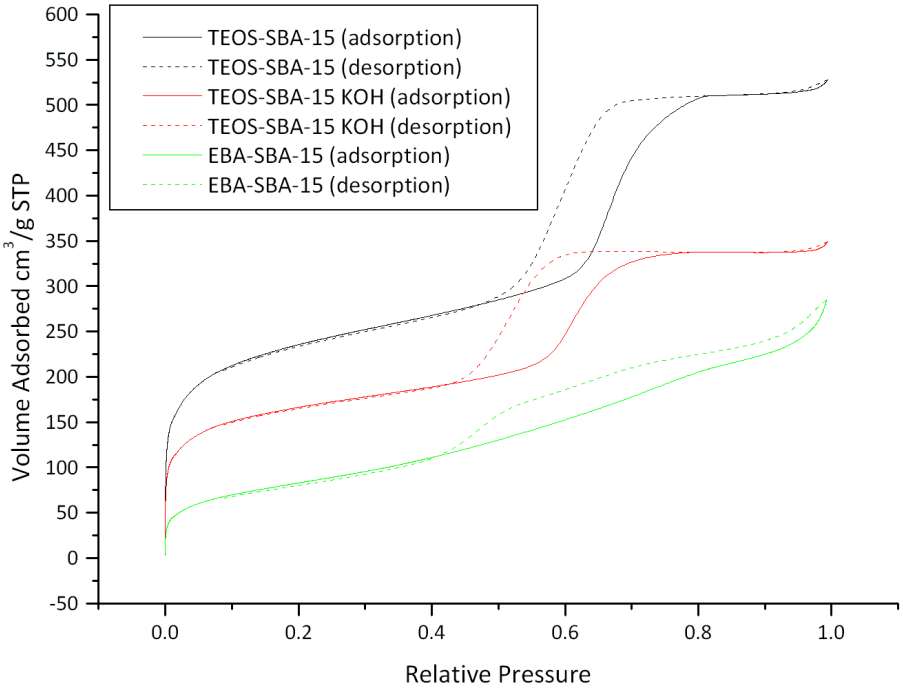

Figure 5.8 N_2 Adsorption / Desorption Isotherms of TEOS-SBA-15 with KOH and TEOS-SBA-15 and EBA-SBA-15 for comparison

The pore size distribution (Figure 5.9) showed that the pores had formed within a small range as with the reference sample. The peak is marginally sharper for the sample synthesised in the presence of KOH, with a marginally smaller range and a smaller average pore size.

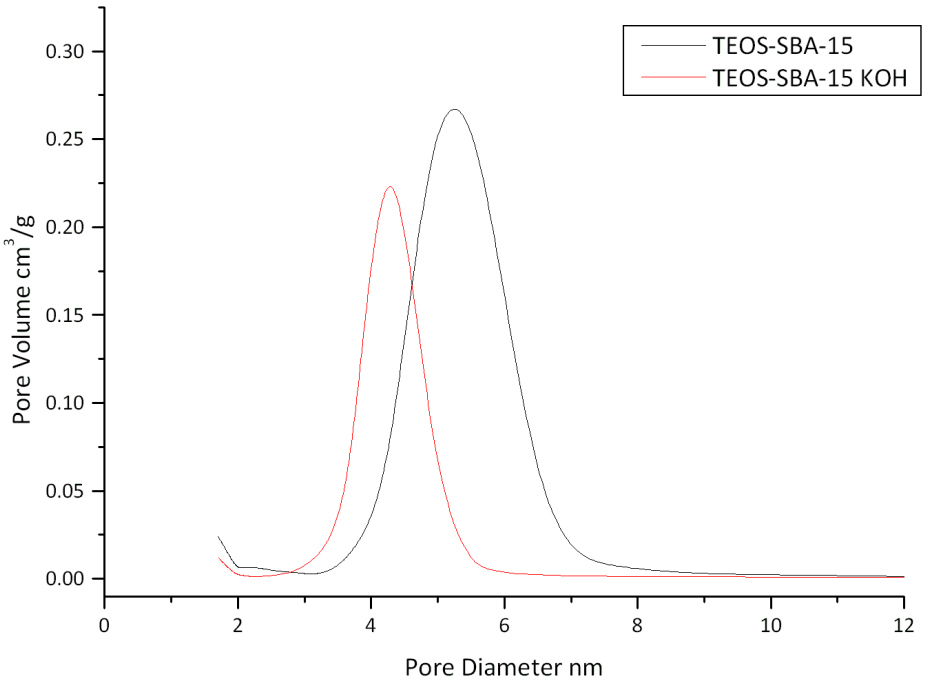

Figure 5.9 BJH calculated Pore size distribution for TEOS-SBA-15 and TEOS-SBA-15 with KOH

TEM images for the sample (Figure 5.10) show the presence of ordered hexagonal pores and also linearity of the pores not present in the EBA-SBA-15 material.

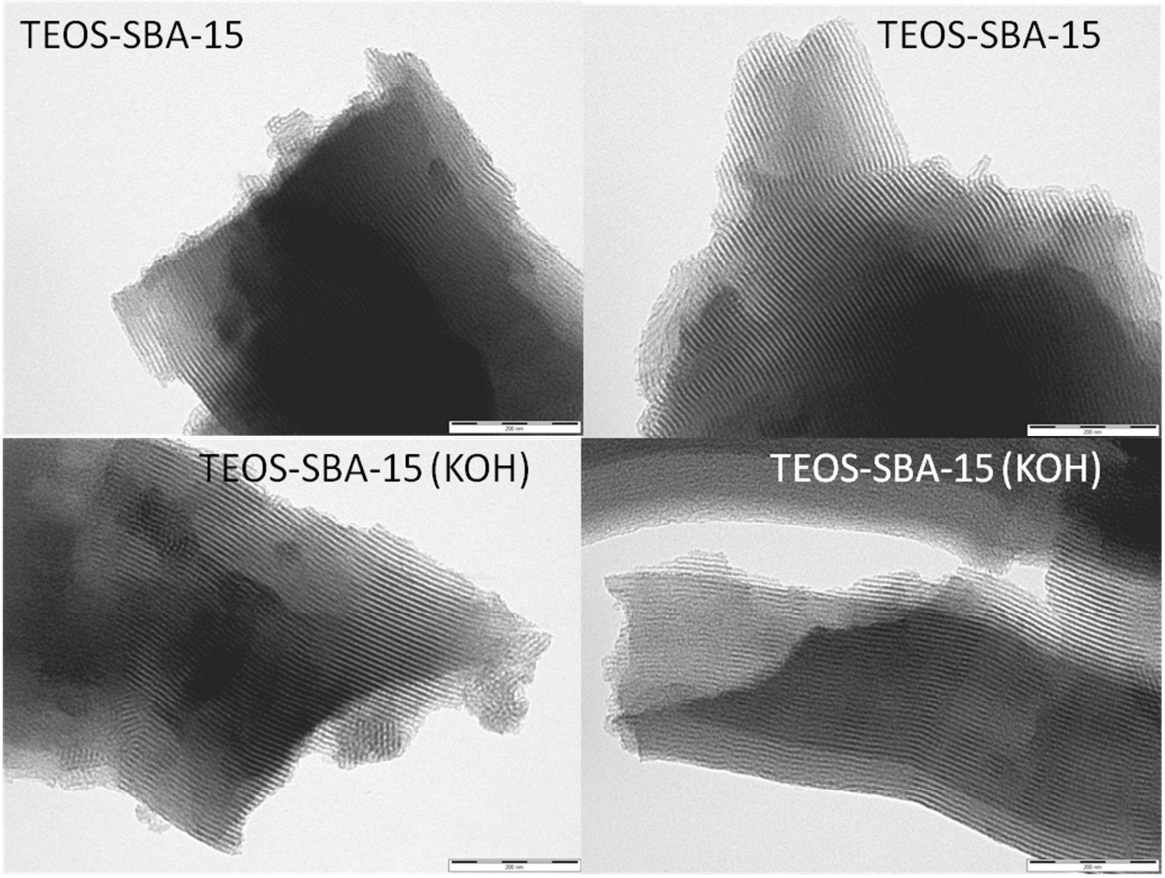

Figure 5.10 TEM images of TEOS-SBA-15 and TEOS-SBA-15 with KOH. Scale bar is 1 µm in length (1000 nm)

It appears, after examining the analysis of the TEOS-SBA-15 synthesised in the presence of KOH that this change in synthesis environment has had the effect of reducing the porosity but not to the same extent or in the same way as the substitution of TEOS for EBA alkali silicate. The isotherms are similar in shape although for the TEOS-SBA-15 less nitrogen is adsorbed into the pores. There may have been some increase in wall thickness due to the introduction of KOH into the synthesis environment as the average pore diameter is smaller. If potassium cations had interacted with chloride ions and the pH had been raised removing protonating species, some neutral templating may have occurred instead of the ionic templating route described in the introduction (Section 1.7.1) but this appears unlikely from the TEM images. The TEM images show clear parallel ordered pores as confirmed by the XRD reflection at 1.1° 2θ which was present for both TEOS derived samples but not for the EBA derived sample (Figure 5.3). Therefore the presence of KOH appears to have decreased the level of order achieved within the material.

5.4 Effect of ethanol on synthesis environment

The observation that when TEOS hydrolyses, ethanol is produced, led to an experiment to test whether the presence of ethanol enabled the formation of the SBA structure. Ethanol was, therefore, introduced into the EBA-SBA-15 synthesis environment and the resultant material compared to EBA-SBA-15.

The effect of introducing an amount of ethanol into the synthesis mixture for EBA-SBA-15 seems to have had a very significantly detrimental effect on the order of the material. The XRD patterns (Figure 5.11) appear to be comparable for both materials in that the reflection at 1.1° 2 θ is absent.

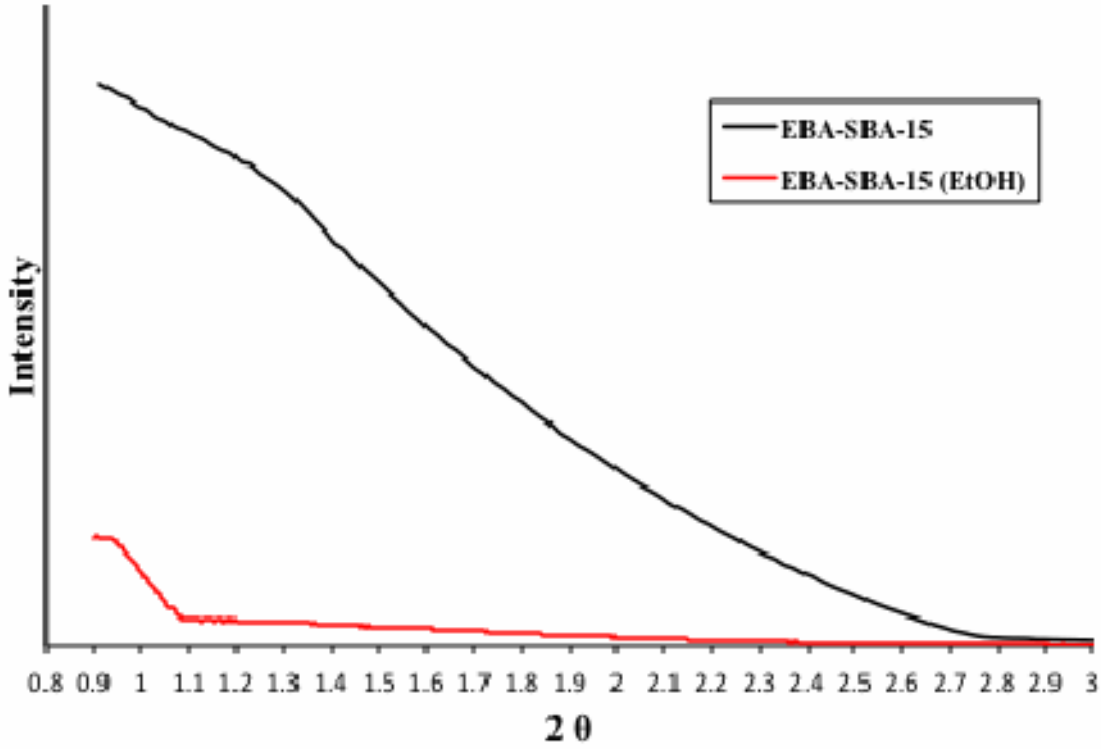

Figure 5.11 XRD patterns of calcined EBA-SBA-15 with and without the presence of Ethanol in the synthesis environment

Examining the porosimetry results (Table 5.3, Figure 5.12, and Figure 5.13) it would appear that the porosity is significantly decreased. There is a small amount of mesoporosity and the characteristic hysteresis loop, representative of the narrow mesopores open at both ends created by the micelle template, is present. The pore size

distribution shows a much smaller range of pore sizes for the sample synthesised in the presence of ethanol.

Table 5.3 Porosimetry results for EBA-SBA-15 (EtOH) and TEOS-SBA-15 and EBA-SBA-15 as a comparison

	Surface Area	Pore Volume	Average Pore Diameter
	m^2g^{-1}	cm^3g^{-1}	nm
TEOS-SBA-15	**769**	**0.8**	**4.1**
EBA-SBA-15	**300**	**0.39**	**5.2**
EBA-SBA-15 (EtOH)	**146**	**0.11**	**3.1**

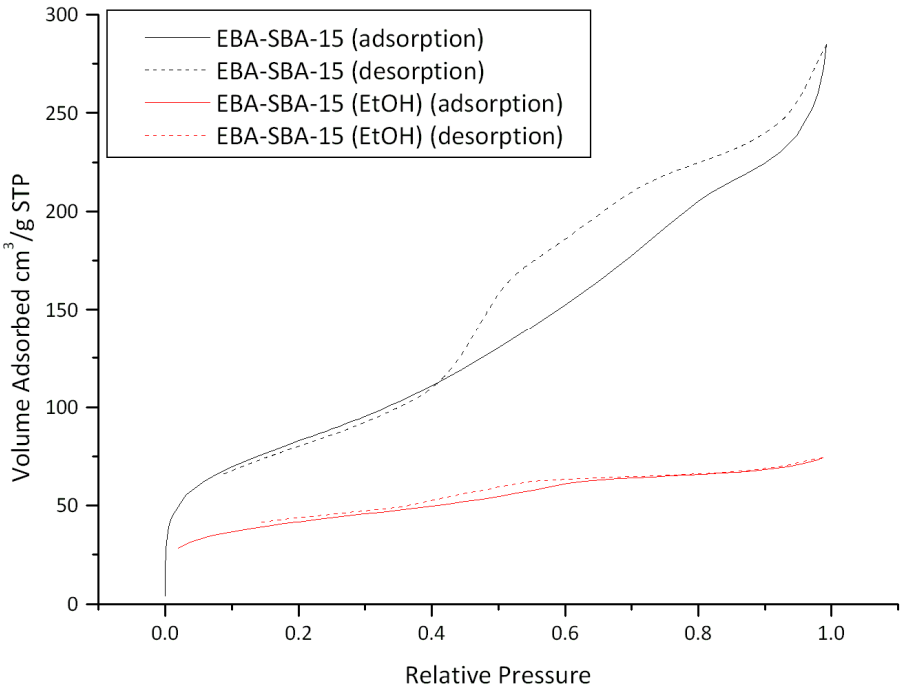

Figure 5.12 N_2 Adsorption / Desorption Isotherms of EBA-SBA-15 with and without the presence of Ethanol in the synthesis environment

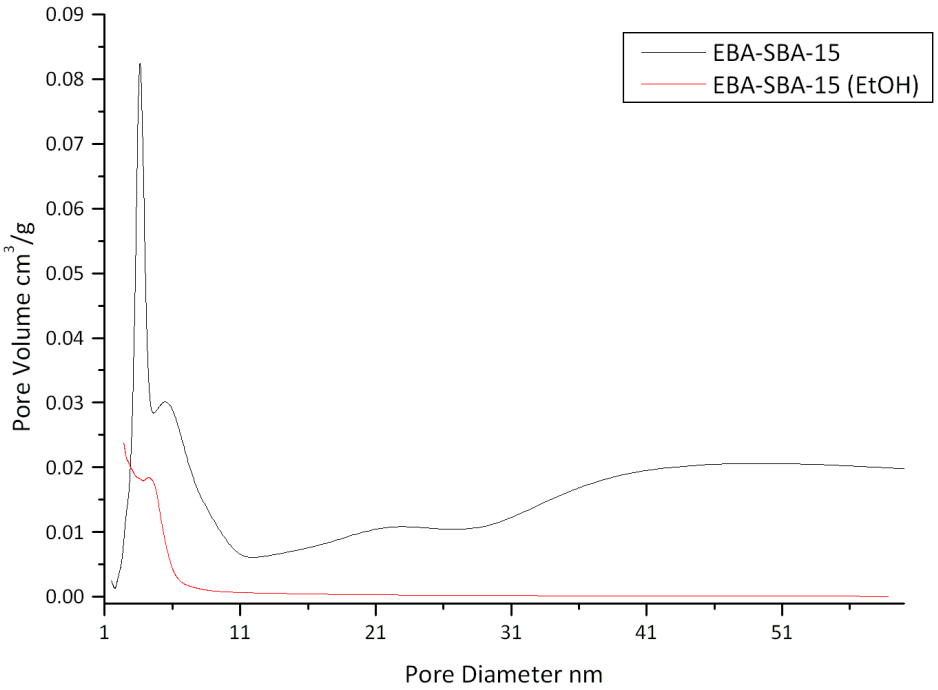

Figure 5.13 BJH calculated Pore size distribution for EBA-SBA-15 with and without the presence of Ethanol in the synthesis environment

Transmission electron micrographs (Figure 5.14) show no pore structure for either material.

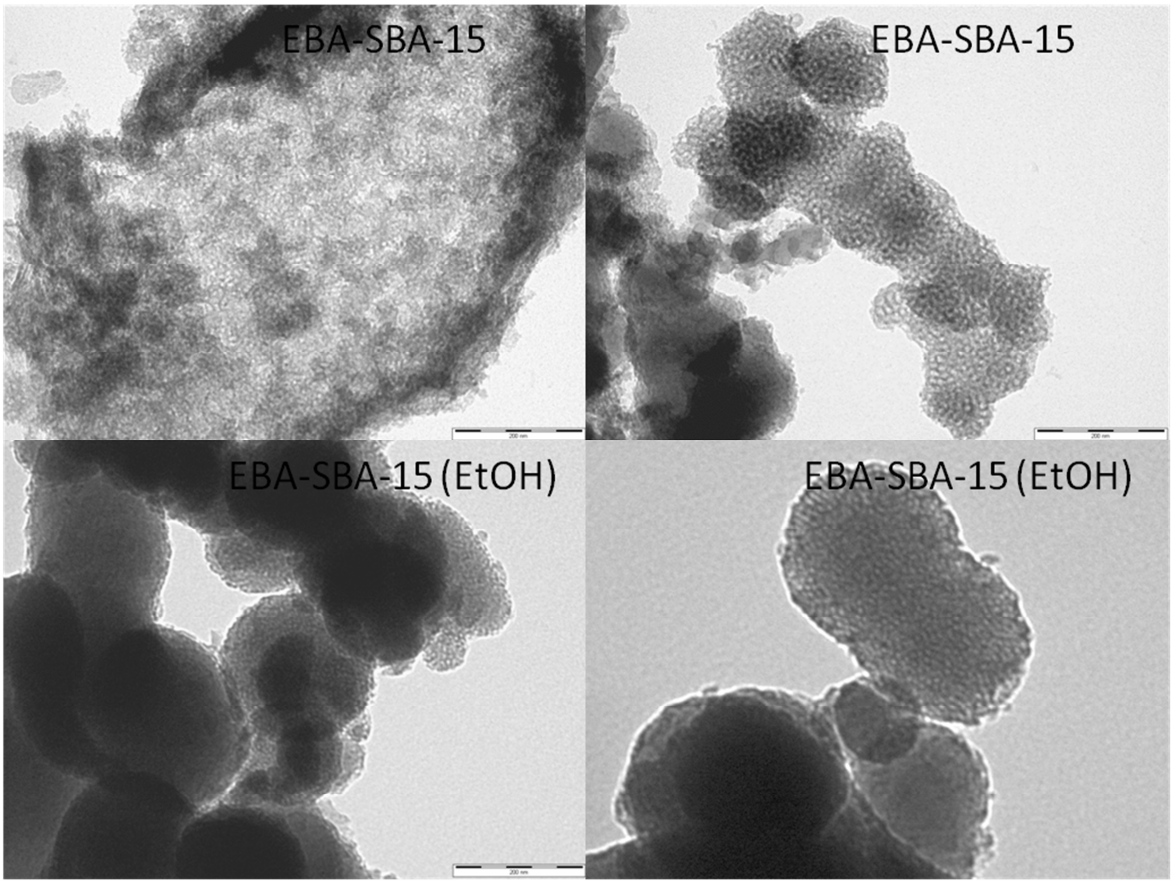

Figure 5.14 Transmission electron microscopy images of the materials. Scale bar is 1 µm in length (1000 nm)

These results show the presence of ethanol is not the factor which is inhibiting the organisation of the micelles, in fact it appears to reduce it further. This has had the effect of reducing the porosity and order within the material for an EBA derived SBA-15.

In order to further investigate the main problem with the synthesis and how to solve it in order to synthesise SBA-15 from a bio-derived alkali silicate more experiments were done using commercial alkali silicate solutions. This was in order to simplify the level of variables, eliminate any effects of the unique properties of the ash derived alkali silicates and to focus on the transition to alkali silicate solutions from TEOS.

5.5 Optimisation of SBA-15 synthesis using commercial alkali silicate solutions

Two alkali silicate solutions were chosen to be investigated in the synthesis of SBA-15. These were named C501, a sodium silicate solution which was used in the synthesis of Zeolite X (Chapter 3), and K120, a potassium silicate solution which is similar to EBA alkali silicate solution and was used for the reference MCM-41 sample synthesised in Chapter 4. More information on these alkali silicate solutions can be found in Chapter 2. Since pH is likely to be a significant factor, these alkali silicate solutions were treated with 1M HCl overnight in order to change the pH from strongly basic to acidic. The silicate would precipitate on addition of the HCl and proceed to redissolve after 12 hours. The silicate would then re-precipitate and crystallise on addition of the template in dilute acid.

XRD patterns of the SBA-15 materials synthesised form commercial alkali silicates K120 and C501 (Figure 5.15) have no reflections and therefore have no long-range order.

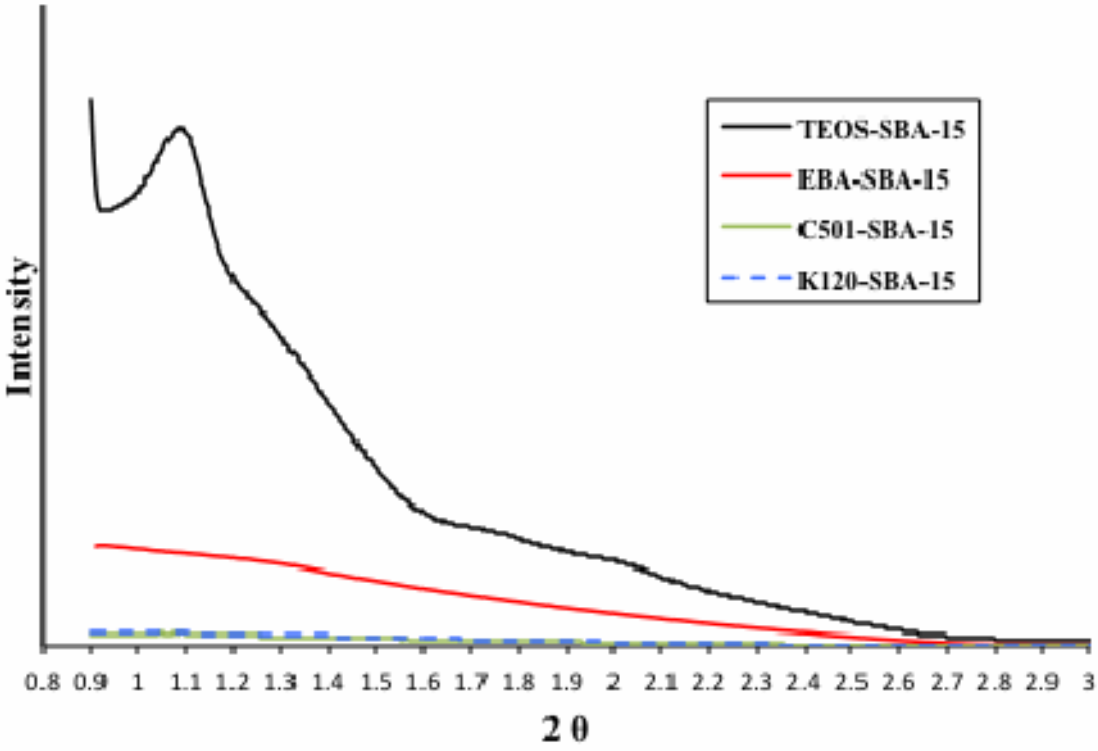

Figure 5.15 XRD patterns of C501-SBA-15 and K120-SBA-15 and, for comparison, TEOS-SBA-15 and EBA-SBA-15

On closer inspection of the patterns there is a slight peak/shoulder visible at 1.1° 2θ for the C501-SBA-15 sample which could signal some ordering of pores pores (Figure 5.16). There is a slight shoulder at this angle for the K120-SBA-15 sample.

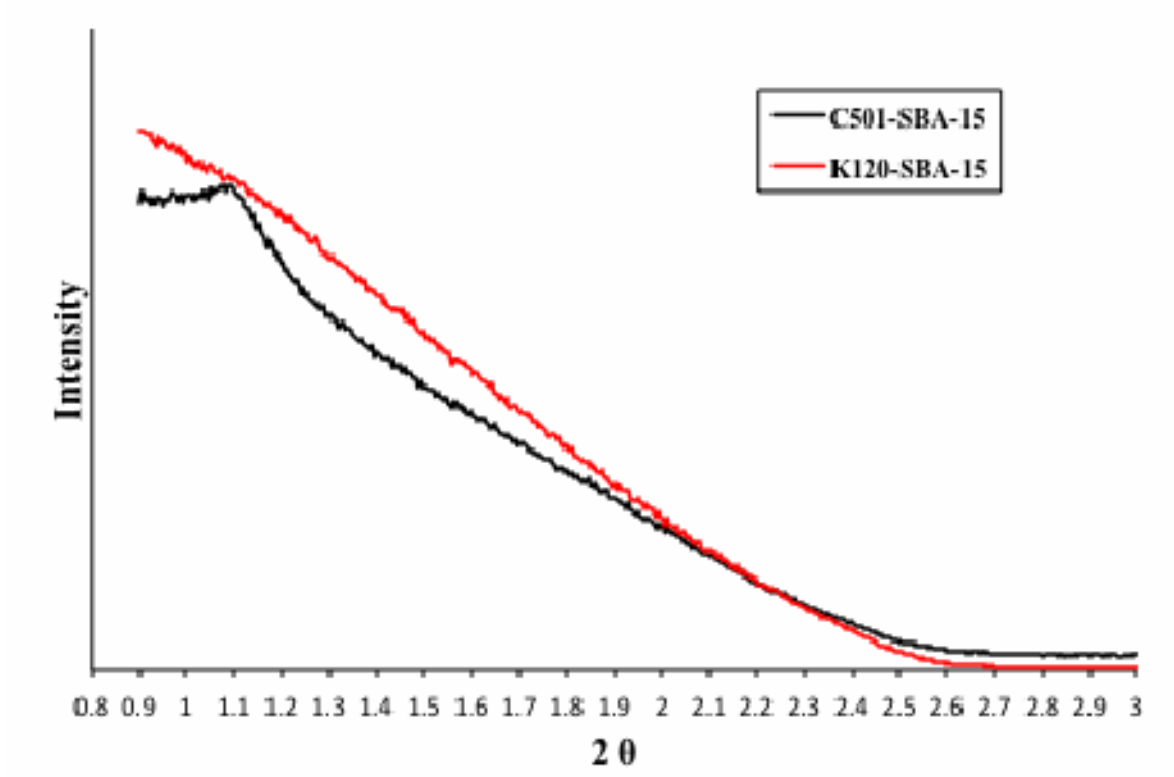

Figure 5.16 XRD patterns of C501-SBA-15 and K120-SBA-15

The porosimetry analysis shows isotherms are more comparable with the TEOS-SBA-15 (Figure 5.17). There is clearly a small region of porosity signified by the steep increase in volume of adsorbed N_2 over a short-range in relative pressure. The hysteresis loop is also similar to the reference sample signifying the presence of narrow mesopores open at both ends. The pore size distribution is also similar to the reference material (Figure 5.18). The range has shifted from 3-8 nm for the reference material to 5-9 nm for the two alkali silicate derived materials.

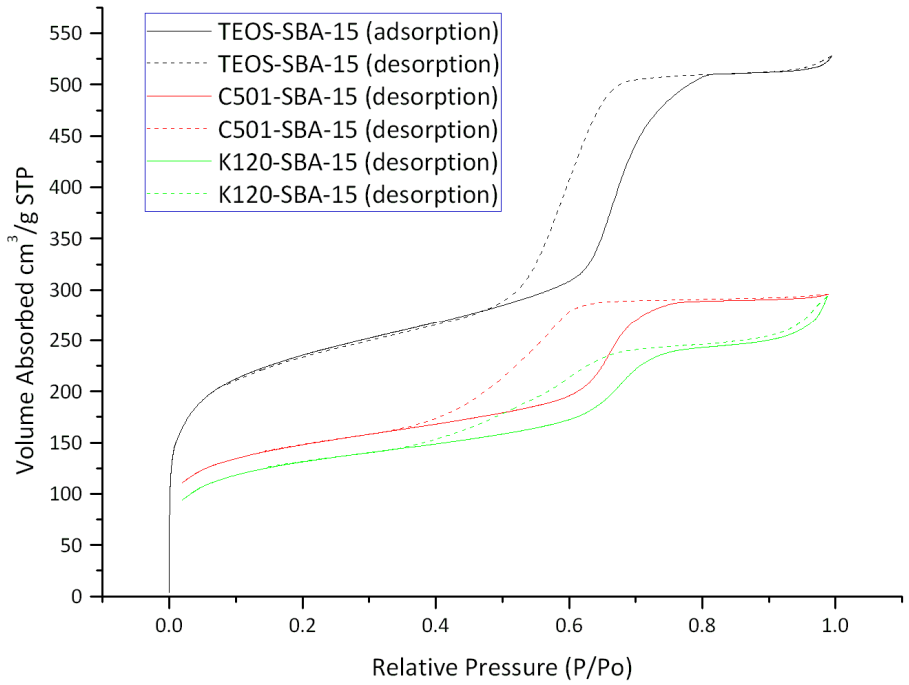

Figure 5.17 N_2 Adsorption / Desorption Isotherms of TEOS-SBA-15, C501-SBA-15 and K120-SBA-15

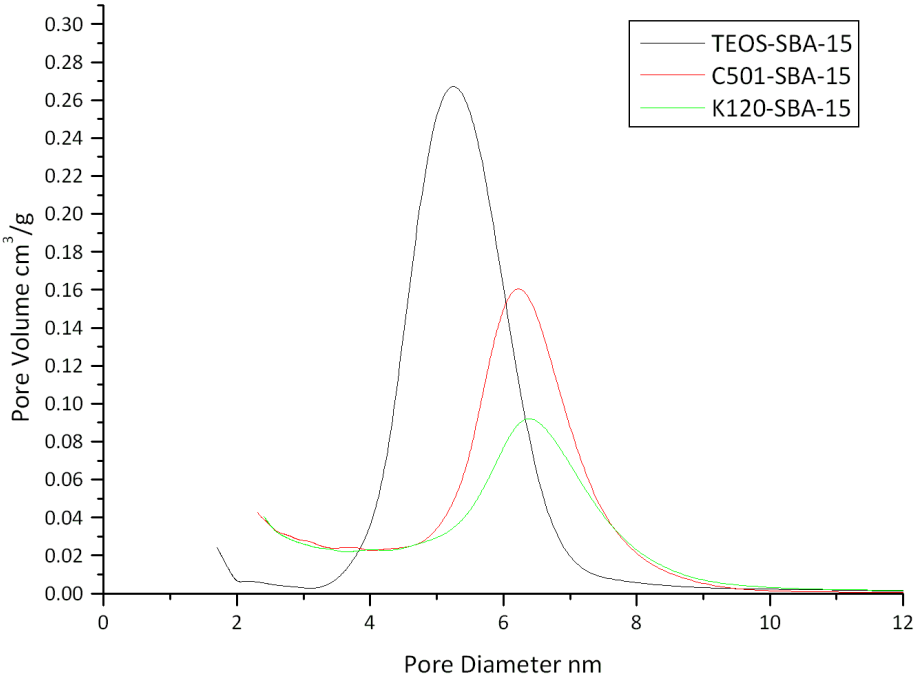

Figure 5.18 BJH calculated Pore size distribution for C501-SBA-15 and K120-SBA-15

As can be seen from the summary of the porosimetry results below (Table 5.4) there is a decrease of around one third in the surface area and pore volume. The average pore diameters remain similar. Therefore there is a decrease in the amount of porosity.

Table 5.4 Porosimetry results for C501-SBA-15 and K120-SBA-15, and TEOS-SBA-15 as a comparison

	Surface Area	Pore Volume	Average Pore Diameter
	m^2g^{-1}	cm^3g^{-1}	nm
TEOS-SBA-15	**769**	**0.8**	**4.1**
C501-SBA-15	**510**	**0.45**	**3.6**
K120-SBA-15	**465**	**0.43**	**3.7**

TEM images of SBA-15 synthesised from the commercial alkali silicates ‘C501’ and ‘K120’ (Figure 5.19) show the presence of ordered hexagonal pores and some linear pore structures. This would imply the synthesis with these alkali silicate solutions is more successful than that for prior EBA alkali silicate derived SBA-15 materials.

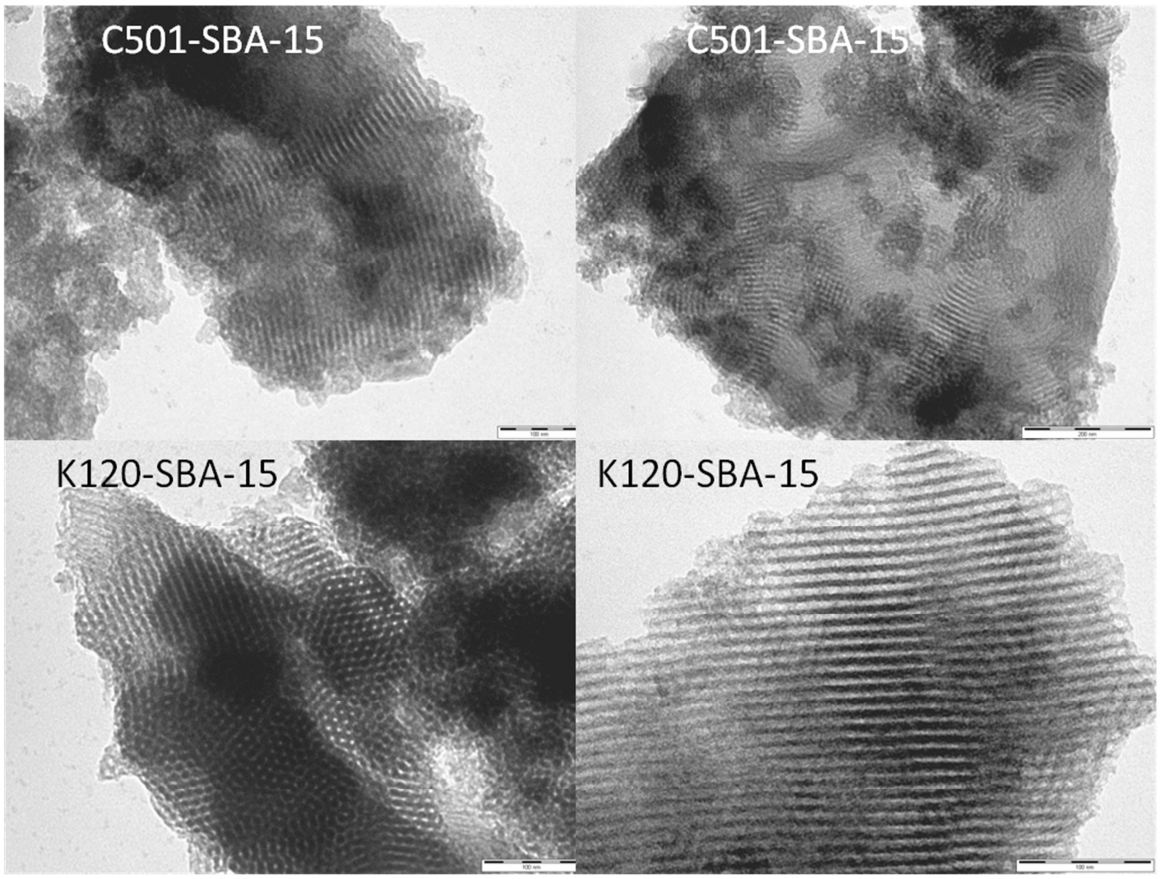

Figure 5.19 TEM images of C501-SBA-15 and K120-SBA-15. Scale bar is 1 µm in length (1000 nm)

It appears that the SBA-15 synthesised from commercial alkali silicate solutions crystallised into the SBA-15 structure well. The XRD, porosimetry, and TEM data confirm the presence of ordered linear hexagonal pores. The XRD patterns appear to contradict these observations although this may be due to the fact that less of the structure has crystallised and this can be seen from the porosimetry isotherms and TEM. Therefore there has been successful synthesis of the SBA-15 structure over a shorter range but the long-range order obtained using TEOS has failed for these materials synthesised from alkali silicate solutions. The key improvement in this synthesis was a transfer from basic to acidic pH of the alkali silicate solutions prior to the addition of the template and crystallisation period.

5.6 Acidic EBA Silicate Solution in Synthesis of SBA-15

The conclusions made in Section 1.4 were applied to the bio-derived alkali silicate solution 'EBA' by adding a dilute mineral acid to the basic silicate solution to obtain a low pH value. This solution was stirred for 24 hours in order to allow any silica which may

have precipitated during the decrease in pH to re-dissolve into solution. The synthesis then followed the conventional recipe with addition of Pluronic P123 and a crystallisation period at 80 ˚C. The material synthesised was washed with water and calcined at 550 ˚C and named 'EBA-SBA-15 (acidic)'.

The XRD pattern of EBA-SBA-15 (acidic) (Figure 5.20) shows a very slight shoulder at 1.1° 2θ which shows that the sample could contain a small amount of the ordered pore structure of the standard SBA-15 but this order is minimal and short range. The surface area and pore volume of EBA-SBA-15 (acidic) are 753 m^2g^{-1} and 1.03 cm^3g^{-1} respectively, which is significant but lower than that for TEOS-SBA-15 (840 m^2g^{-1} and 0.8 cm^3g^{-1}) (Table 5.5).

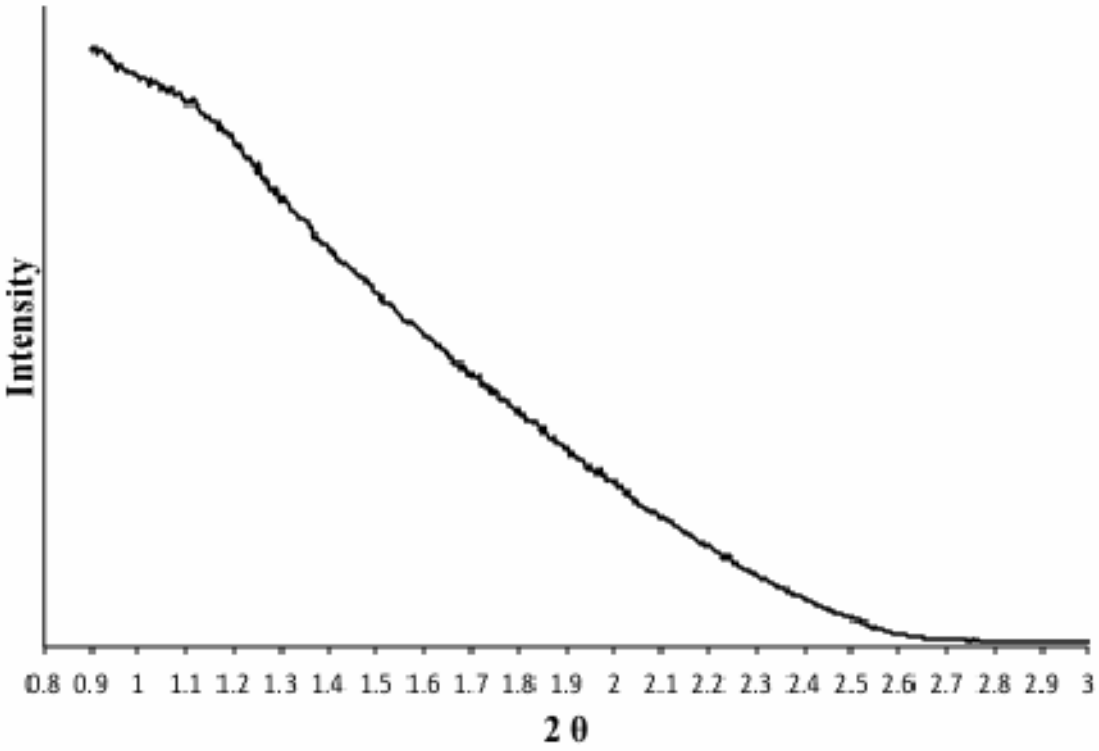

Figure 5.20 XRD pattern of EBA-SBA-15 (acidic)

Table 5.5 Porosimetry results for EBA-SBA-15 (acidic)

	Surface Area	Pore Volume	Average Pore Diameter
	m^2g^{-1}	cm^3g^{-1}	nm
EBA-SBA-15 (acidic)	**753**	**1.03**	**6.9**

The N_2 adsorption / desorption isotherm for EBA-SBA-15 (Figure 5.21) is significantly different to that of the TEOS-SBA-15 material. There is clearly a range of pore systems present. There is adsorption of up to 200 cm^3g^{-1} in the microporous region and this is likely due to the interconnecting micropores which form from silica condensing within the micelles around the Pluronic P123 chains (Section 1.7.1). A steep rise occurs at 0.65 relative pressure which relates to the small range of mesopores formed around the Pluronic P123 micelle template. There is then a steep rise at much higher relative pressure which is due to textural porosity within the material.

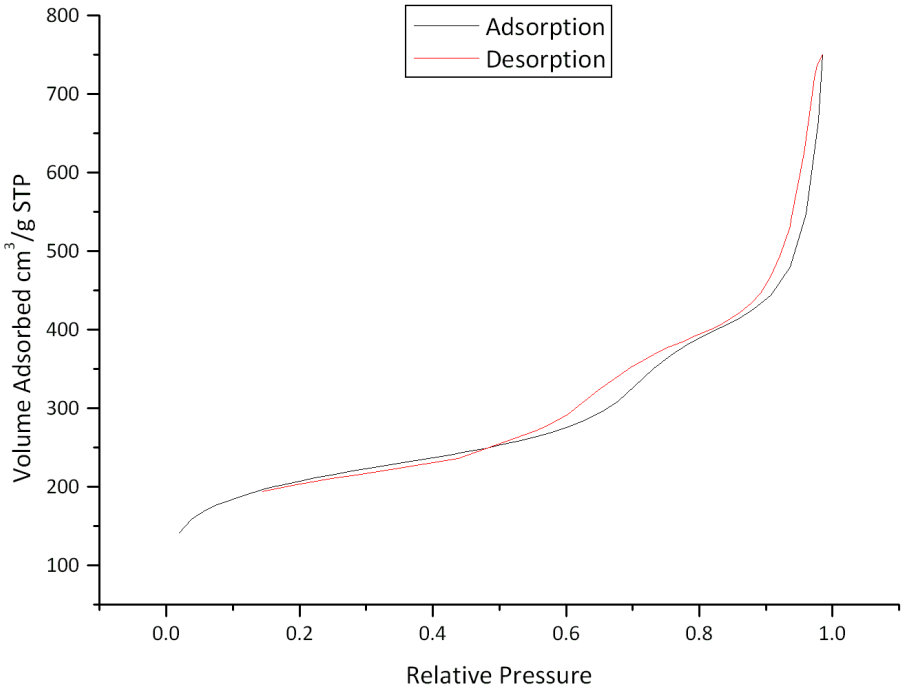

Figure 5.21 N_2 Adsorption / Desorption Isotherm of EBA-SBA-15 (acidic)

The BJH calculated pore size distribution (Figure 5.22) clearly shows a peak at 6.9 nm which is concurrent with the mesoporous template pore structure. There is also a shoulder of a large peak in the microporous region as described above.

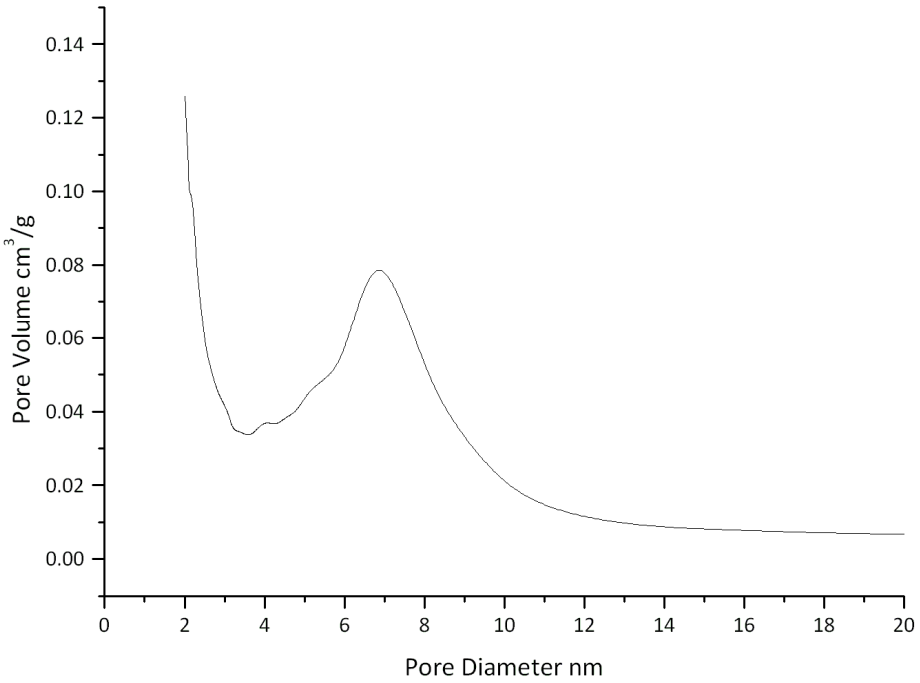

Figure 5.22 BJH calculated pore size distribution of EBA-SBA-15 (acidic)

TEM images (Figure 5.23) show more linear and ordered hexagonal pore structures than have been seen for any EBA-SBA-15 so far in this work but it is still difficult to ascertain the extent of the level of order. There are clearly visible elongated pores and ordered hexagonal arrays present in the material.

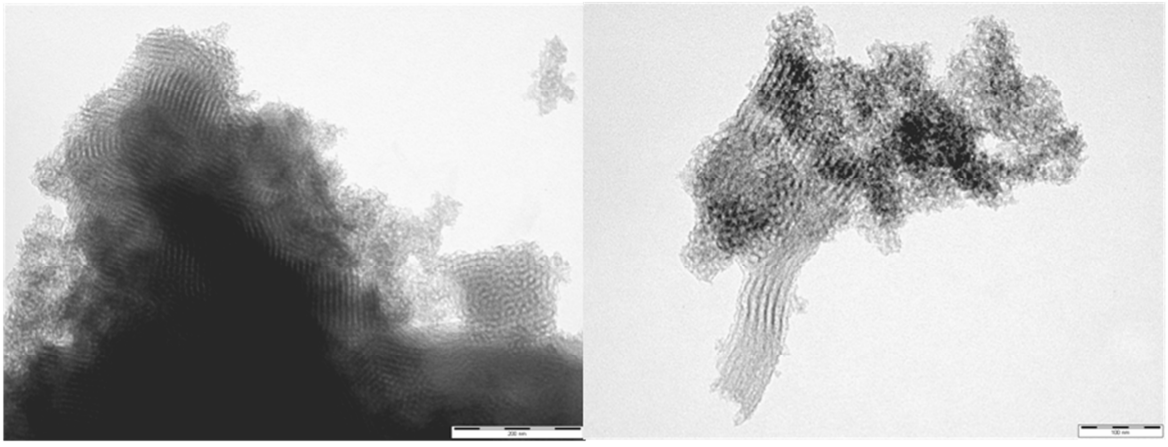

Figure 5.23 TEM images of EBA-SBA-15 (acidic) Scale bar is 1 µm (1000 nm) on left and 500 nm on right

Combining analysis from porosimetry, XRD, and TEM, it is clear that the SBA-15 structure was not synthesised from an acidified silicate solution from Miscanthus ash but that there may the potential for the successful synthesis of the structure in the future.

5.7 Conclusion

A reference SBA-15 was synthesised from TEOS for comparison with materials synthesised from bio-derived silicate solutions. Initially, it was not possible to prepare SBA-15 using a bio-derived alkali silicate solution, despite attempts to liken the synthesis environment to that of the conventional synthesis by addition of ethanol. It was found that the pH of the synthesis environment was the most important factor. After the acidification of the commercial alkali silicate solutions, C501 and K120, was successful in producing the ordered SBA-15 structure, the synthesis was attempted using EBA potassium silicate solution. The process of acidifying the alkali silicate solution before addition to the synthesis was applied to the bio-silicate solution. Analysis showed a lack of order as there was no reflection at 1.1° 2θ in the XRD pattern and although there was substantial surface area, this was over a range of pore sizes. There was minimal evidence of order in the TEM images. These results prove it is possible to synthesise ordered mesoporous silica materials which are normally derived from neutral silica sources such as TEOS from alkali silicates and that there is potential to synthesise the materials from bio-derived alkali silicates. This widens the potential array of materials which can be synthesised by a silicate solution extracted from waste ashes.

6 Materials and Methodology

6.1 Biomass Ashes and Alkali Silicate Extraction and Analysis

6.1.1 Alkali Silicate Extraction

Once ashes had been obtained it was necessary to extract the silicon in the form of alkali silicates and this can be done using either microwaves or conventional heating using, for example, a heating mantle and oil bath.

Alkali silicate solutions and all synthesised materials were stored in propylene bottles and sealed using lab film.

All chemicals were purchased from Sigma-Aldrich and Fisher and used without purification. Commercial alkali silicate solutions were obtained from PQ Corporation.

6.1.1.1 Microwave Extraction

A method was followed from Dr. Jennie Dodson and is as follows; rice hull ash (0.32 g) was mixed with NaOH pellets (0.12 g) and water (2.4 g) in a microwave tube. The microwave was set to 150 °C and ran for durations of between 2 and 10 minutes.[5] Extraction was conducted in a CEM Discover single mode microwave reactor.

The method was then scaled up to enable a larger amount of alkali silicate to be extracted. Rice hull ash (16.14 g) was mixed with NaOH pellets (38.23 g) and water (153 g) in a propylene bottle, which was then placed in a glass container. This container then span within the microwave in order to mix the contents. The microwave was set to 500 Watts for between 2 and 10 minutes. Extraction was conducted in a Milestone RotoSynth multi mode microwave reactor.

6.1.1.2 Hydrothermal extraction

In order to extract the alkali silicate solution hydrothermally, Ely Bottom Ash (75g) and 5M KOH (125ml) or rice hull ash (16.14 g), NaOH pellets (38.23 g) and water (153 g) were mixed in a Teflon round bottomed flask and refluxed for 24 hours using a temperature controlled oil bath and heating mantle.

6.2 Synthesis of Zeolites from Biomass Ashes

6.2.1 Synthesis of reference zeolite

The commercial sodium silicate solution 'PQ Corp. C501' was used throughout this chapter. C501 had a given SiO_2 / M_2O ratio of 1.6 and a calculated ratio of 1.4 using XRF (Chapter 2 Section 2.4).[5]

The synthesis of the reference Zeolite X followed the recipe from the IZA.[27] Water (12.5 g) was mixed with NaOH (12.5 g) in a propylene bottle and sodium aluminate (12.2 g) was added to this solution and stirred at 100 °C in an oil bath. The solution was then allowed to cool to room temperature. Water (25.3 g) was added and stirred. This solution (12.5 g) was weighed out and added to water (76.5 g) and NaOH (7.39 g) in a propylene bottle. In a separate propylene bottle 'C501' sodium silicate (27.46g) was added to water (76.5 g) and NaOH (7.39 g). The two solutions were then mixed together and stirred for 30 minutes. This solution was left in an oil bath at 90 °C for 8 hours. The solution was washed and filtered using a sintered funnel. The sample was then dried in an oven at 150 °C for 2 hours and calcined in a furnace at 600 °C for 4 hours.

6.2.2 Synthesis of Zeolites from Biomass Ash

6.2.2.1 Initial Synthesis

The synthesis was then adjusted for alkali silicates extracted from rice hull ash (Chapter 2 Section 2.5.1) as follows.

NaOH (25 g) was added to water (25 g) and sodium aluminate (24.375 g) and stirred at 100 °C until the sodium aluminate had dissolved. Water (50.625 g) was then added to the solution. This solution (25 g) was then mixed with water (153 g) and NaOH (14.75 g). This solution was then mixed with RHA alkali silicate solution (30 g) and stirred at room temperature for 40 minutes. The solution was then left in an oil bath for 8 hours at 90 °C. Samples were filtered and washed with water then dried in an oven at 150 °C for 2 hours and calcined in a furnace at 600 °C for 4 hours.

6.2.2.2 Synthesis of RHA Zeolites with Different Si/Al ratios

Since the synthesis described above (Section 6.2.2.2) produced more mass of zeolite than necessary for the analysis, it was scaled down as follows.

NaOH (5 g) was added to water (5 g) and a specified amount of sodium aluminate (Table 6.1) and stirred at 100 °C until the sodium aluminate had dissolved. Water (10.125 g) was then added to the solution. This solution (5 g) was then mixed with water (30.6 g) and NaOH (2.95 g). This solution was then mixed with RHA alkali silicate solution (6 g - 16.14 g RHA, 153 g water, 38.23 g NaOH) and stirred at room temperature for 40 minutes. The solution was then left in an oil bath for 8 hours at 90 °C. Samples were filtered and washed with water then calcined in a furnace at 600 °C for 4 hours.

Table 6.1 Ratio of silica to aluminium and amount of sodium aluminate for addition in the synthesis

Si/Al	Sodium Aluminate g / 16.14 g RHA
6.3	2.10
3	4.88
1.7	10.27
1.2	20.55
0.9	41.10

6.2.2.3 Synthesis of RHA Zeolites with Further Different Si/Al ratios

Synthesis was carried out as described in Section 6.2.2.2 but with sodium aluminate amounts as shown in Table 6.2.

Table 6.2 Ratio of silica to aluminium and amount of sodium aluminate for addition in the synthesis

Si/Al	Sodium Aluminate g / 16.14 g RHA
2.7	4.88
3.6	3.41
4.6	2.56
5.6	2.05
6.6	1.71

6.2.2.4 Investigation into methods of cooling

Synthesis was carried out as described in Section 6.2.2.2 for Si/Al = 4.6.

After samples had been in an oil bath for 8 hours at 90 °C, they were either cooled in an ice bath and filtered with ice cold water, filtered hot and washed with hot water, or left to cool slowly in the oil bath and then filtered. The samples were then calcined in a furnace at 600 °C for 4 hours as described above.

6.2.3 Optimised RHA-Zeolite Synthesis and comparison with Conv-Zeolite

The zeolite filtered hot from Section 6.2.2.4 was used as the RHA-Zeolite and the Conv-Zeolite was that synthesised as in Section 6.2.1.

6.3 Synthesis of Mesoporous MCM-41 from Biomass Ashes

6.3.1 Synthesis of MCM-41 in different pH environments and initial Synthesis of MCM-41 from biomass ash derived alkali silicate solution

A synthesis was based on the research by Hui *et al* as follows.[21] Since Hui *et al* used alkali silicate solution (82ml) with a silica concentration of 5470 mgl^{-1} (analyzed by ICP-AES) and K120 and EBA had silica concentrations of 272,000 ppm and 114,000 ppm respectively (calculated using technique described in Chapter 2 Section 2.5 with K120 calibration curve since EBA resembles K120 in speciation and thus in IR spectra curve), K120 (1.64 ml) and EBA alkali silicate solution (3.91 ml) was used in the synthesis. A suitable amount of water was added to the alkali silicate solutions to dilute them to a similar concentration to that used by Hui *et al*.

K120 (1.64 ml) or EBA alkali silicate solution (3.91 ml) were mixed with CTAB (1 g) and H_2O (40 ml) at 85 °C. Ethyl acetate (3.1 ml) was added to this mixture with rapid stirring for 10 minutes. The solutions were left cool to room temperature. The RXN mixture (10ml) was adjusted to pH with concentrated H_2SO_4 or concentrated NaOH. The solutions were then left to age at room temperature for 24 hours. Following this the precipitates were filtered and washed with water. They were then dried for 2 hours at 100 °C and calcined at 550 °C for 4 hours.

6.3.2 Introduction of aluminium into bio-derived MCM-41 synthesis

EBA alkali silicate solution (3.91ml) or K120 alkali silicate solution (1.64ml) was used as in the synthesis described in Section 6.3.1. Before the addition of ethyl acetate, sodium aluminate (0.2g), aluminium hydroxide (0.2g), or Red Clay (0.2g) and concentrated NaOH solution (2 drops) was added.

6.3.2.1 Effect of red clay residue on Porosimetry results

Red clay (2 g) was added to a solution of sodium hydroxide and potassium hydroxide (both at pH = 12) and stirred at room temperature for 24 hours. The potassium hydroxide solution also contained the CTAB template (1 g). Solutions were then filtered and the solid and liquid analysed.

6.3.2.2 Varied Si/Al ratios of MCM-41 with Red Clay

Synthesis was as described in Section 6.3.2 but with additions of red clay as shown in Table 6.3.

Table 6.3 Ratio of silica to aluminium and amount of red clay added in the synthesis

Si/Al (wt)	Red Clay
	g
573	0.01
115	0.05
57	0.1
14	0.4

6.4 SBA-15

6.4.1 Synthesis of SBA-15 using TEOS and EBA derived alkali silicate solution

The synthesis from Zhao *et al* was followed for the initial synthesis using TEOS and K120 as follows.[54-55] Pluronic P123 (4.0 g) was dissolved in water (29.8 ml) and 1M HCl (116.5 ml) at 35 ˚C under stirring. Once the template was completely dissolved (approximately 2 hours), tetraethylorthosilicate (TEOS) (9.05 ml) was added to the mixture and the solution

left to stir for 20 hours at 35 ˚C. The white solution formed from this process was aged at 80 ˚C, for 24 hours, in a sealed bottle (propylene bottles are best and the complete synthesis can be carried out in them) in an oil bath without stirring. The resulting solution was filtered under vacuum, washed with water, dried at room temperature overnight, and calcined at 500 ˚C for 6 hours in air.

This synthesis was adapted for the EBA alkali silicate solution by replacing TEOS (9.05ml) with EBA alkali silicate solution (10ml). All other elements of the thesis remained the same.

6.4.2 Effect of KOH on synthesis environment

The synthesis was carried out as above (Section 6.4.1) with TEOS but with the addition of KOH (2.5 g) before the solution set to stir for 20 hours.

6.4.3 Effect of ethanol on synthesis environment

The synthesis was carried out as above (Section 6.4.1) with EBA but with the addition of ethanol (29.8 ml) instead of water.

6.4.4 Optimisation of SBA-15 synthesis using commercial alkali silicate solutions

The synthesis was carried out as above (Section 6.4.1) with the following adjustment. C501 (10 ml) and K120 (10 ml) were stirred with 1 M HCl (50 ml) at room temperature for 24 hours prior to addition to the synthesis.

6.4.5 Use of Acidic EBA Silicate Solution in Synthesis of SBA-15

1 M HCl (50 ml) was stirred with EBA (9.35 ml) at room temperature overnight prior to addition of Pluronic P123 (2.3 g) and stirred at 35 ˚C for 24 hours. The mixture was then aged at 80 ˚C for 24 hours. The resulting solution was filtered under vacuum, washed with water, dried at room temperature overnight, and calcined at 500 ˚C for 6 hours in air.

6.5 Analysis Techniques

6.5.1 pH Analysis

pH values were taken using Fisherbrand pH indicator paper.

6.5.2 Infrared Spectroscopy (IR)

A Bruker Vertex 70 FTIR spectrometer equipped with a MKII Golden Gate Single Reflection ATR System with a 45° diamond crystal was used to obtain infrared spectra. Solid powder samples were placed on the crystal surface and then clamped using a sapphire anvil. A drop of a liquid sample was placed on the crystal surface for analysis. Spectra were taken from 4000 cm^{-1} to 600 cm^{-1} at 64 scans with a spectral resolution of 4 cm^{-1}. A water or blank spectrum was used for the background. Bruker OPUS software was used for analysis of spectra.

6.5.3 *In Situ* IR experiments

Dry ground powder samples were pressed into a disc under high pressure and placed in a foil envelope. The envelope was then placed in a sealed glass tube for heat treatment. Samples were exposed to heat treatments of 150 ˚C, 300 ˚C, or 500 ˚C under vacuum for three hours. The samples were then kept in a vacuum until they were dosed with gas or analysis was over. Spectra were recorded using a Bruker Equinox 55 spectrometer using a resolution of 2 cm^{-1}.

6.5.4 Porosimetry

Nitrogen adsorption analyses were carried out at 77 K using a Micromeritics Tristar volumetric adsorption analyser. Prior to analysis, finely ground samples were outgassed at 180 °C for 1 h under nitrogen flow. Specific surface areas (S_{BET}) were analysed using the Brunauer, Emmett and Teller (BET) method and pore size was analysed using the Barrett, Joyner and Halenda method (BJH) method.

6.5.5 XRD

X-ray diffraction patterns were obtained using a Bruker-AXS D8 Advance diffractometer with a Kristalloflex 760 X-ray generator which produces monochromatic Kα X-rays from a

copper source. A powder sample was placed and levelled within a small round hole bevelled out of an aluminium sample holder. Scans were taken across the range 5 - 50 2θ for materials in Chapter 3 and 0.3 – 8 2θ for those in Chapters 4 and 5. A 45 kV voltage and 20 mA current were used during analysis. The software EVA and the Chemical Database Service were used to identify the phases present in the samples.

6.5.6 XRF

A Rigaku NEX-CG X-ray fluorescence spectrometer was used to obtain non organic elemental analysis of solid and liquid samples. Samples were analysed in a Helium atmosphere.

6.5.7 XPS

A Kratos Axis Ultra-DLD X-Ray Photon Spectrometer was used to obtain elemental analysis of the top surface layers of solids by Dr David J Morgan at Cardiff University. Samples were analysed under vacuum.

6.5.8 TEM

Transmission electron microscopy was carried out by Dr Meg Stark at the Department of Biology, University of York. A small sample was suspended in ethanol and dropped onto a carbon grid to evaporate before analysis under vacuum.

6.5.9 NMR

Solid state ^{27}Al NMR was carried out by the Solid State NMR Research Service at the University of Durham using a Varian Unity Inova spectrometer operating at 59.56 MHz.

6.5.10 TGA

Thermo gravimetric analysis was conducted using a Netsch STA 409 under nitrogen. Exit gases were analysed using a Bruker Equinox 55 IR spectrometer.

7 Conclusion and Further Work

7.1 Conclusion

The objectives of this project were to synthesise zeolites and aluminosilicate materials from silicon sources derived from biomass ashes. In particular, Zeolite X from the Faujasite family, MCM-41, and SBA-15 were studied with a view to proving the concept of successful synthesis from waste products of both micro- and meso-porous materials, *via* templated and untemplated routes, and in both basic and neutral pH environments. Included in this study was the first synthesis of mesoporous materials from alkali silicate solutions derived from power plant biomass ashes, in this case from the large-scale combustion of miscanthus. This research is important as it is the first stage in proving the synthesis can be scaled up for industrial use.

For the synthesis of all the materials in this project it was necessary to have stock solutions of bio-derived alkali silicates and analysis of the ashes and these extracted alkali silicate solutions. Initially a method was optimised to extract alkali silicate solutions from biomass ashes. This involved hydrothermal treatment overnight with addition of sodium or potassium hydroxide. A quick, accurate, and straightforward analysis technique was developed in collaboration with Dr Jennie Dodson to obtain concentrations of silicon from alkali silicate solutions. The technique involved the use of integrals of infrared spectra between 1250 cm^{-1} and 650 cm^{-1} and calibration curves from a range of commercial alkali silicate solutions. This novel method was compared with a commonly used analysis technique, atomic absorption spectroscopy, and found to be comparable in accuracy and reliability as well being as much easier to use.

The first material to be synthesised from a bio-derived alkali silicate was Zeolite X, a commonly used zeolite synthesised commercially on a large-scale from alkali silicates, which does not require a template in its synthesis. The synthesis was developed and compared to a commercial alkali silicate derived equivalent. It was found to be less pure in its crystalline phases including impurities such as Sodalite. It also had significantly less porosity. These results showed it was possible to synthesise a specific phase from the bio-derived alkali silicate but in order to refine the material to obtain the pure phase would require significantly more research. An in-depth *in situ* probe FT-IR study concluded there was a significant amount of strongly bonded carbonate within the pores which affected the porosity measurements. This carbonate is likely to have come from carbonate

materials in the ashes, The two materials were found to have some similarities in their interactions with the probe molecules CO and CO_2 such as the location of sodium cations within the structure and a lack of hydroxyl groups on the surface. This is the first study of a bio-derived zeolite using this technique.

The second material to be synthesised was the mesoporous silica MCM-41, which is synthesised commercially from alkali silicates using an amine-based template. MCM-41 was synthesised successfully from a bio-derived alkali silicate. The transfer from commercial alkali silicate to bio-derived alkali silicate was straightforward and successful. In this case it was found that the synthesis pH environment did not affect the overall properties of the material in any consistent way. The bio-derived MCM-41 was compared to a commercial alkali silicate derived MCM-41 and found to have a similar surface area, pore volume, and pore structure as shown by XRD, N_2 adsorption porosimetry, and TEM. The addition of three types of aluminium source into the bio-derived MCM-41 structure was investigated in order to improve the catalytic activity of the materials. It was found that sodium aluminate was the aluminium source which was most incorporated into the structure, but this increased incorporation led to a decrease in crystallinity and stability of the material. Red clay, a waste product containing aluminium, iron, and silicon, was described, characterised and found to leach aluminium which was incorporated into the structure during the synthesis. As with sodium aluminate, there was a correlation between the level of aluminium added to the structure and the instability of the pore structure. These results show a clear advantage in synthesising MCM-41 commercially from waste biomass ashes as the change is silica source has no discernable effect on the final product and is a lot more environmentally friendly and potentially more economical. The potential use of red mud, a large-scale waste source, to provide aluminium for introduction to the MCM-41 structure has been shown. This modification could improve the properties of the material whilst also providing a use for a waste product.

The most significant difference in synthesis was found for the third type of material synthesised, SBA-15, a mesoporous silica which is conventionally synthesised from the neutral silicon source, TEOS, with a triblock copolymer template. Initially the synthesis was attempted in basic solution and, since the template Pluronic P123 was dissolved in acid, this led to a near neutral pH environment in which templating occurred producing wormhole porosity within the silica structure. In order to adapt the synthesis for an alkali

silicate solution it was necessary to lower the pH of the solution using mineral acids to values <7. This modification was successful in synthesising the SBA-15 structure from commercial alkali silicates but unsuccessful for the bio-derived alkali silicate. These results show the potential to synthesis SBA-15 from bio-derived acidic silicate solutions but that more research needs to be done to obtain the ordered SBA-15 structure.

MCM-41 and SBA-15 materials synthesised in this project are the first mesoporous silica materials to have been synthesised from Miscanthus ashes and more generally from a biomass ash from large-scale combustion. These materials show promise as suitable replacements for their conventionally synthesised counterparts and, as such, are a greener alternative. These materials have wide ranging applicability, particularly in catalysis and sorption.

7.2 Further Work

There are various strands of work which could occur based on the results from this project. One important opportunity would be to find applications for the bio-derived materials synthesised. There is already ongoing work at the Green Chemistry Centre of Excellence in testing these materials as catalysts in various reactions.

It would also be important to prove the syntheses can be carried out on a larger scale whilst retaining consistency and reliability in properties of the final product. This will become easier to carry out once an industrial partner tests the extraction of ashes to produce alkali silicate solutions on an industrial scale which is imminent.

There are also many other zeolites and mesoporous aluminosilicate materials which have numerous applications and would benefit from being derived from waste products such as biomass ashes.

An exciting development of the work described here would be to incorporate the extraction of aluminium and other metals from red clay simultaneously with the extraction of silicon from the biomass ashes for synthesis of zeolies and mesoporous aluminosilicate materials.

8 Abbreviations

AAS	Atomic Absorption Spectroscopy
a_0	Lattice Parameter
BET	Brunauer, Emmett and Teller
BJH	Barrett, Joyner and Helenda
CTAB	Cetyl Trimethylammonium Bromide
D_p	Average Pore Diameter
EBA	Ely Bottom Ash
EU	European Union
FT-IR	Fourier Transform Infrared spectroscopy
ICP-AES	Inductively Coupled Plasma Atomic Emission Spectroscopy
IUPAC	International Union of Pure and Applied Chemistry
ND	Not Detected
NMR	Nuclear Magnetic Resonance
ppm	parts per million
RHA	Rice Hull Ash
S_{BET}	BET Surface Area
TEM	Transmission Electron Microscopy
TEOS	Tetraethyl Orthosilicate

TGA	Thermogravimetric Analysis
Th_p	Pore Wall Thickness
V_p	Pore Volume
W_d	Pore Size
wt%	Weight in %
XPS	X-Ray Photoelectron Spectroscopy
XRD	X-Ray Diffraction
XRF	X-Ray Fluorescence Spectroscopy

9 References

1. P. T. Anastas and J. C. Warner, *Green Chemistry: Theory and Practice*, Oxford University Press, USA, 2000.
2. E. Audsley and J. E. Annetts, *Agr. Syst.*, 2003, **76**, 39-59.
3. J. H. Clark, V. Budarin, F. E. I. Deswarte, J. J. E. Hardy, F. M. Kerton, A. J. Hunt, R. Luque, D. J. Macquarrie, K. Milkowski, A. Rodriguez, O. Samuel, S. J. Tavener, R. J. White and A. J. Wilson, *Green Chemistry*, 2006, **8**, 853-860.
4. F. E. I. Deswarte, J. H. Clark, A. J. Wilson, J. J. E. Hardy, R. Marriott, S. P. Chahal, C. Jackson, G. Heslop, M. Birkett, T. J. Bruce and G. Whiteley, *Biofuel Bioprod Bior*, 2007, **1**, 245-254.
5. J. R. Dodson, Wheat straw ash and its use as a silica source, PhD, University of York, 2011.
6. M. Maughan, G. Bollero, D. K. Lee, R. Darmody, S. Bonos, L. Cortese, J. Murphy, R. Gaussoin, M. Sousek, D. Williams, L. Williams, F. Miguez and T. Voigt, *GCB Bioenergy*, 2012, **4**, 253-265.
7. Department of Energy and Climate Change, *Guidance on carbon neutrality,* 30 September 2009
8. *Ely Power Station*, http://www.eprl.co.uk/assets/ely/overview.html, 2012.
9. SSE, *Use of Biomass at Ferrybridge Power Plant,* 2012
10. European Parliament, *Promotion of the use of energy from renewable sources, 2009/28/EC,* 2009
11. Department for Environment Food and Rural Affairs, *UK Biomass Strategy,* 2007
12. Department of Energy & Climate Change, *The UK Renewable Energy Strategy 2009,* 2009
13. US Department of Energy, *Replacing the Whole Barrel To Reduce U.S. Dependence on Oil, Biomass Program,* 2012
14. R. K. Iler, *The Chemistry of Silica*, Wiley & Sons: New York, 1979.
15. N. Baccile, F. Babonneau, B. Thomas and T. Coradin, *J. Mater. Chem.*, 2009, **19**, 8537-8559.
16. R. E. Kirk, D. F. Othmer, M. Grayson and D. Eckroth, *Encyclopedia of Chemical Technology*, Wiley, 1982.
17. J. S. Falcone, J. L. Bass, M. Angelella, E. R. Schenk and K. A. Brensinger, *Ind. Eng. Chem. Res.*, 2010, **49**, 6287-6290.
18. H. L. Chang and W. H. Shih, *Ind. Eng. Chem. Res.*, 1998, **37**, 71-78.

19. H.-L. Chang, C.-M. Chun, I. A. Aksay and W.-H. Shih, *Ind. Eng. Chem. Res.*, 1999, **38**, 973-977.
20. H.-L. Chang and W.-H. Shih, *Ind. Eng. Chem. Res.*, 2000, **39**, 4185-4191.
21. K. S. Hui and C. Y. H. Chao, *J. Hazard. Mater.*, 2006, **137**, 1135-1148.
22. V. Polshettiwar and R. S. Varma, in *Aqueous Microwave Assisted Chemistry: Synthesis and Catalysis*, The Royal Society of Chemistry, 2010, pp. 1-9.
23. V. Budarin, 2012, personal communication.
24. B. C. Gates, *Catalytic chemistry*, Wiley, 1992.
25. J. B. Nagy, *Synthesis, Characterization and Use of Zeolitic Microporous Materials*, DecaGen, 1998.
26. *US Pat.*, 2882244, 1953.
27. I. Z. A. (IZA), in *International Zeolite Association (IZA)*, 2012.
28. S. Wang, *Environ. Sci. Technol.*, 2008, **42**, 7055-7063.
29. O. Babajide, N. Musyoka, L. Petrik and F. Ameer, *Catal. Today*, 2012, **190**, 54-60.
30. C. F. Lin and H. C. Hsi, *Environ. Sci. Technol.*, 1995, **29**, 1109-1117.
31. B. S. Shin, S. O. Lee and N. P. Kook, *Korean J. Chem. Eng.*, 1995, **12**, 352-357.
32. X. Querol, A. Alastuey, J. L. Fernandezturiel and A. Lopezsoler, *Fuel*, 1995, **74**, 1226-1231.
33. X. Querol, A. Alastuey, A. LopezSoler, F. Plana, J. M. Andres, R. Juan, P. Ferrer and C. R. Ruiz, *Environ. Sci. Technol.*, 1997, **31**, 2527-2533.
34. X. Querol, F. Plana, A. Alastuey and A. LopezSoler, *Fuel*, 1997, **76**, 793-799.
35. N. Shigemoto, H. Hayashi and K. Miyaura, *J. Mater. Sci.*, 1993, **28**, 4781-4786.
36. N. Shigemoto, S. Sugiyama, H. Hayashi and K. Miyaura, *J. Mater. Sci.*, 1995, **30**, 5777-5783.
37. C. Amrhein, G. H. Haghnia, T. S. Kim, P. A. Mosher, T. Amanios and L. DelaTorre, *Environ. Sci. Technol.*, 1996, **30**, 735-742.
38. W.-H. Shih and H.-L. Chang, *Mater. Lett.*, 1996, **28**, 263-268.
39. C. A. Rios, C. D. Williams and C. L. Roberts, *Fuel*, 2009, **88**, 1403-1416.
40. A. Molina and C. Poole, *Miner. Eng.*, 2004, **17**, 167-173.
41. D. Wu, Y. Lu, H. Kong, C. Ye and X. Jin, *Ind. Eng. Chem. Res.*, 2007, **47**, 295-302.
42. A. K. Dalai, M. S. Rao and K. Gokhale, *Ind. Eng. Chem. Prod. RD.*, 1985, **24**, 465-468.
43. P. K. Bajpai, M. S. Rao and K. Gokhale, *Ind. Eng. Chem. Prod. RD.*, 1981, **20**, 721-726.

44. A. V. Rawtani, M. S. Rao and K. Gokhale, *Ind. Eng. Chem. Res.*, 1989, **28**, 1411-1414.

45. D. Prasetyoko, Z. Ramli, S. Endud, H. Hamdan and B. Sulikowski, *Waste Manage.*, 2006, **26**, 1173-1179.

46. C. T. Kresge, M. E. Leonowicz, W. J. Roth, J. C. Vartuli and J. S. Beck, *Nature*, 1992, **359**, 710-712.

47. J. S. Beck, J. C. Vartuli, W. J. Roth, M. E. Leonowicz, C. T. Kresge, K. D. Schmitt, C. T. W. Chu, D. H. Olson, E. W. Sheppard, S. B. McCullen, J. B. Higgins and J. L. Schlenker, *J. Am. Chem. Soc.*, 1992, **114**, 10834-10843.

48. A. Taguchi and F. Schüth, *Microporous Mesoporous Mater.*, 2005, **77**, 1-45.

49. S. Hudson, J. Cooney and E. Magner, *Angew. Chem. Int. Ed.*, 2008, **47**, 8582-8594.

50. A. Corma, *Chem. Rev.*, 1997, **97**, 2373-2420.

51. L. Mercier and T. J. Pinnavaia, *Adv. Mater.*, 1997, **9**, 500-503.

52. M. Grün, A. A. Kurganov, S. Schacht, F. Schüth and K. K. Unger, *J. Chromatogr. A*, 1996, **740**, 1-9.

53. M. Bhagiyalakshmi, L. J. Yun, R. Anuradha and H. T. Jang, *J. Hazard. Mater.*, 2010, **175**, 928-938.

54. D. Zhao, Q. Huo, J. Feng, B. F. Chmelka and G. D. Stucky, *J. Am. Chem. Soc.*, 1998, **120**, 6024-6036.

55. D. Y. Zhao, J. L. Feng, Q. S. Huo, N. Melosh, G. H. Fredrickson, B. F. Chmelka and G. D. Stucky, *Science*, 1998, **279**, 548-552.

56. R. Ryoo, C. H. Ko, M. Kruk, V. Antochshuk and M. Jaroniec, *J. Phys. Chem. B*, 2000, **104**, 11465-11471.

57. P. T. Tanev and T. J. Pinnavaia, *Science*, 1995, **267**, 865-867.

58. P. T. Tanev and T. J. Pinnavaia, *Chem. Mat.*, 1996, **8**, 2068-2079.

59. D. J. Macquarrie, D. B. Jackson, J. E. G. Mdoe and J. H. Clark, *New J. Chem.*, 1999, **23**, 539-544.

60. D. J. Macquarrie, D. B. Jackson, S. Tailland and K. A. Utting, *J. Mater. Chem.*, 2001, **11**, 1843-1849.

61. T. G.J.T, *Phys. Rep.*, 1980, **57**, 1-46.

62. P. Kumar, N. Mal, Y. Oumi, K. Yamana and T. Sano, *J. Mater. Chem.*, 2001, **11**, 3285-3290.

63. H. Misran, R. Singh, S. Begum and M. A. Yarmo, *J. Mater. Process. Technol.*, 2007, **186**, 8-13.

64. G. Chandrasekar, K.-S. You, J.-W. Ahn and W.-S. Ahn, *Microporous and Mesoporous Materials*, 2008, **111**, 455-462.

65. G. Chandrasekar and W.-S. Ahn, *J. Non-Cryst. Solids*, 2008, **354**, 4027-4030.

66. G. Chandrasekar, W.-J. Son and W.-S. Ahn, *J. Porous Mater.*, 2009, **16**, 545-551.

67. C. Chen, K.-S. You, J.-W. Ahn and W.-S. Ahn, *Korean J. Chem. Eng.*, 2010, **27**, 1010-1014.

68. I. Majchrzak-Kuceba and W. Nowak, *Int. J. Miner. Process.*, 2011, **101**, 100-111.

69. N. Grisdanurak, S. Chiarakorn and J. Wittayakun, *Korean J. Chem. Eng.*, 2003, **20**, 950-955.

70. S. Chiarakorn, T. Areerob and N. Grisdanurak, *Sci. Technol. Adv. Mater.*, 2007, **8**, 110-115.

71. A. Boonpoke, S. Chiarakorn, N. Laosiripojana, S. Towprayoon and A. Chidthaisong, *JSEE*, 2011, **2**, 88-81.

72. Technology Roadmap for Bauxite Residue Treatment and Utilization, The Alumnium Association, 2000.

73. Alumina Technology Roadmap 2010 Update, International Aluminium Institute, Bauxite and Alumina Committee, 2010.

74. M. Balakrishnan, V. S. Batra, J. S. J. Hargreaves and I. D. Pulford, *Green Chemistry*, 2011, **13**, 16-24.

75. M. Balakrishnan, V. S. Batra, J. S. J. Hargreaves, A. Monaghan, I. D. Pulford, J. L. Rico and S. Sushil, *Green Chem.*, 2009, **11**, 42-47.

76. S. Sushil, A. M. Alabdulrahman, M. Balakrishnan, V. S. Batra, R. A. Blackley, J. Clapp, J. S. J. Hargreaves, A. Monaghan, I. D. Pulford, J. L. Rico and W. Zhou, *J. Hazard. Mater.*, 2010, **180**, 409-418.

77. P. W. Atkins, *Physical chemistry*, Oxford University Press, Oxford, 2002.

78. R. E. Dinnebier and S. J. L. Billinge, *Powder Diffraction: Theory and Practice*, Rsc, 2008.

79. P. Brouwer, *Theory of XRF*, 3rd edn., PANalytical B.V., 2010.

80. S. J. Gregg and K. S. W. Sing, *Adsorption, surface area, and porosity*, Academic Press, 1991.

81. K. S. W. Sing, *Pure Appl. Chem.*, 1985, **57**, 603-619.

82. Micromeritics, *Tristar Manual, 6.08,* 2007

83. E. P. Barrett, L. G. Joyner and P. P. Halenda, *J. Am. Chem. Soc.*, 1951, **73**, 373-380.

84. J. H. van der Maas, *Basic infrared spectroscopy*, Heyden, in co-operation with Sadtler Research Laboratories, Philadelphia, 1969.

85. J. C. Lavalley, *Catal. Today*, 1996, **27**, 377-401.

86. G. Ramis, G. Busca and V. Lorenzelli, *Mater. Chem. Phys.*, **29**, 425-435.

87. G. Busca and V. Lorenzelli, *Mater. Chem.*, 1982, **7**, 89-126.

88. I. Salla, T. Montanari, P. Salagre, Y. Cesteros and G. Busca, *J. Phys. Chem. B*, 2005, **109**, 915-922.

89. P. Kozyra, I. Salla, T. Montanari, J. Datka, P. Salagre and G. Busca, *Catal. Today*, 2006, **114**, 188-196.

90. T. G. Rochow and P. A. Tucker, *Introduction to Microscopy by Means of Light, Electrons, X-Rays, or Acoustics*, Springer, 1994.

91. PerkinElmer, *Thermogravimetric Analysis: A Beginner's Guide*, 2010.

92. in *Spectrochemical Analysis by Atomic Absorption and Emission (2)*, eds. L. H. J. Lajunen and P. Peramaki, The Royal Society of Chemistry, 2004, vol. 0, pp. 16-77.

93. FAO, Food and Agriculture Organisation of the United Nations, 2012.

94. IRRI, International Rice Research Institute, 2012.

95. A. S.-F. Norma, P.-M. Graciela, P.-R. Patricia, A. Héctor, L. G.-C. María de, M. S. José and J. F. Jose, *J. Chem. Technol. Biotechnol*, 2007, **82**, 614-619.

96. X. C. Baxter, L. I. Darvell, J. M. Jones, T. Barraclough, N. E. Yates and I. Shield, *Fuel*, 2012, **95**, 50-62.

97. T. R. Miles, T. R. Miles Jr, L. L. Baxter, R. W. Bryers, B. M. Jenkins and L. L. Oden, *Biomass Bioenergy*, 1996, **10**, 125-138.

98. J. R. Dodson, E. C. Cooper, A. J. Hunt, A. Matharu, J. Cole, A. Minihan, D. Macquarrie and J. H. Clark, *Green Chem*, 2013, **(In Press)**.

99. *Eccleshall Power Station*, http://www.eccleshallbiomass.co.uk/?page=environment, 2012.

100. B. Beagley, J. Dwyer, N. P. Evmerides, A. I. F. Hawa and T. K. Ibrahim, *Zeolites*, 1982, **2**, 167-174.

101. H. W. Langmi, D. Book, A. Walton, S. R. Johnson, M. M. Al-Mamouri, J. D. Speight, P. P. Edwards, I. R. Harris and P. A. Anderson, *J. Alloys Compd.*, 2005, **404–406**, 637-642.

102. X. Du and E. Wu, *J. Phys. Chem. Solids*, 2007, **68**, 1692-1699.

103. R. M. Barrer and D. E. W. Vaughan, *J. Phys. Chem. Solids*, 1971, **32**, 731-&.

104. A. Bondi, *J. Phys. Chem.*, 1964, **68**, 441-451.

105. I. Hassan and H. D. Grundy, *Acta Crystallogr. C*, 1983, **39**, 3-5.

106. D. A. Fletcher, R. F. McMeeking and D. Parkin, J. , *Chem. Inf. Comput. Sci.* , 1996, **36**, 746-749.

107. *EPSRC National Solid-state NMR Service at Durham*, 2010-2012.

108. P. Komadel, J. Madejova, M. Janek, W. P. Gates, R. J. Kirkpatrick and J. W. Stucki, *Clays Clay Miner.*, 1996, **44**, 228-236.

109. V. C. Farmer, *The Infrared spectra of minerals*, Mineralogical Society, 1974.

110. E. Garrone, B. Fubini, B. Bonelli, B. Onida and C. Otero Arean, *Phys. Chem. Chem. Phys.*, 1999, **1**, 513-518.

111. T. Montanari, P. Kozyra, I. Salla, J. Datka, P. Salagre and G. Busca, *J. Mater. Chem.*, 2006, **16**, 995-1000.

112. G. Martra, R. Ocule, L. Marchese, G. Centi and S. Coluccia, *Catal. Today*, 2002, **73**, 83-93.

113. S. Huber and H. Knözinger, *Appl. Catal., A-Gen*, 1999, **181**, 239-244.

114. O. V. Manoilova, M. Peñarroya Mentruit, G. Turnes Palomino, A. A. Tsyganenko and C. Otero Areán, *Vib. Spectrosc*, 2001, **26**, 107-111.

115. Y. Pekounov, K. Chakarova and K. Hadjiivanov, *Mater. Sci. Eng., C*, 2009, **29**, 1178-1181.

116. P. A. Jacobs, F. H. van Cauwelaert and E. F. Vansant, *J. Chem. Soc., Faraday Trans 1*, 1973, **69**, 2130-2139.

117. P. A. Jacobs, F. H. van Cauwelaert, E. F. Vansant and J. B. Uytterhoeven, *J. Chem. Soc. Farad. Trans. 1*, 1973, **69**, 1056-1068.

118. P. Yang, *The Chemistry of Nanostructured Materials*, World Scientific, 2003.

119. O. Muraza, E. V. Rebrov, M. H. J. M. de Croon and J. C. Schouten, *Microporous Mesoporous Mater.*, 2009, **124**, 20-29.

120. F. Kleitz, W. Schmidt and F. Schüth, *Microporous Mesoporous Mater.*, 2001, **44–45**, 95-109.

121. S. Sumiya, Y. Kubota, Y. Oumi, M. Sadakane and T. Sano, *Appl. Catal., A-Gen*, 2010, **372**, 82-89.

122. I. Majchrzak-Kuceba, *J. Therm. Anal. Calorim.*, 2012, **107**, 911-921.

123. D. Trong On, S. M. J. Zaidi and S. Kaliaguine, *Microporous Mesoporous Mater.*, 1998, **22**, 211-224.

124. D. Macquarrie, 2013, personal communication.